Thèse présentée pour obtenir le titre de
Docteur de l'Université Louis Pasteur
Strasbourg I

Discipline : Physique

Structure et relaxation structurale des fondus de polymères vitrifiables en couches minces

Simone Peter

Thèse soutenue publiquement le 21 juin 2007

Membres du Jury :

Directeur de thèse :	**J. Baschnagel** Professeur ULP, ICS, Strasbourg
Co-encadrant :	**H. Meyer** Chargé de recherche, ICS, Strasbourg
Rapporteur interne :	**Y. Holl** Professeur ULP, ICS, Strasbourg
Rapporteur externe :	**M. Müller** Professeur, Fachbereich Physik, Göttingen
Rapporteur externe :	**W. Kob** Professeur, UM2, LCVN, Montpellier
Examinateur :	**G. Reiter** Directeur de recherche, ICSI, Mulhouse

Institut Charles Sadron
Strasbourg
CNRS

Acknowledgements

The work on this thesis has been made possible by many other people who have supported me. First of all I would like to express my gratitude to my supervisor Jörg Baschnagel who has helped me with his encouragement and many fruitful discussions. I owe a lot to my co-advisor Hendrik Meyer who was always available to help out solving physical as well as computational problems. I really appreciate that they gave me the liberty to follow my own ideas. I also would like to thank all the members of the RTN PolyFilm for the interesting discussions and incentives they have given throughout the meetings and visits I could make in other groups. Last but not least I would like to convey my gratefulness to my family and friends for the support they provided me throughout my life.

Contents

Résumé

Introduction

Récemment, des expériences [1–11], des simulations numériques [12–21] ainsi que des approches théoriques [22–27] ont été utilisées afin d'explorer le phénomène de la transition vitreuse en milieu confiné, de même que les méchanismes sous-jacents. Ces études mettent en évidence des déviations par rapport au comportement en volume si le système est confiné à l'échelle nanoscopique.

Un liquide de polymères formant un verre présente des propriétés que l'on retrouve également dans le cas d'autres liquides sujets à une transition vitreuse; par exemple, une forte augmentation (de type non Arrhenius) du temps de relaxation structurale lors du refroidissement au voisinage de la température de transition vitreuse T_{g} [28, 29]. L'hypothèse selon laquelle cette augmentation est liée à une croissance de la longueur de corrélation ξ_{g} existe de longue date. ξ_{g} est sensé correspondre à la taille moyenne de la zone de réarrangement coopératif (cooperatively rearranging region, CRR), c'est-à-dire d'un sous-ensemble de particules susceptible de se réarranger en une nouvelle configuration indépendament des autres particules dans leur entourage [29]. Une approche tentante pour mettre en évidence l'existence de telles CRR et estimer leur taille consiste en une étude de la transition vitreuse en milieu confiné. L'augmentation de ξ_{g} devrait alors être tronquée par la taille finie du système confiné, ce qui devrait conduire à une diminution de T_{g} [29].

De récents travaux expérimemtaux et numériques ont en effet rapporté des écarts dans la valeur de T_{g} pour des liquides confinés et des films de polymères. Cependant, ces déviations peuvent être aussi bien des augmentations que des diminutions par rapport à la valeur observée en volume (cf. [2, 30, 31] pour des revues et [24, 25, 27] pour des approches théoriques récentes). Ceci implique qu'en plus des effets dûs au confinement, d'autres facteurs jouent un rôle important. L'un des facteurs clé devrait être l'interaction du liquide avec le substrat le confinant [11]. Les simulations suggèrent que cette interaction liquide-substrat se décompose en deux contributions, l'une énergétique et l'autre stérique. Par exemple, une forte attraction liquide-substrat peut piéger temporairement des particules proches des parois et contribuer à ralentir la dynamique par rapport à celle observée en volume [16, 17]. Par ailleurs, même en l'absence d'attraction préférentielle, la dynamique peut se trouver ralentie si des

particules sont emprisonnées dans des cavités du substrat [19, 32–34]. Dans les deux cas, les particules lentes proches des parois ralentissent partiellement leur voisines qui à leur tour gênent le mouvement de leurs voisines, etc. Ceci permet au ralentissement induit par les parois de se propager vers le centre du système. Ceci résulte en une augmentation de T_{g}, particulièrement dans le cas de confinements importants (pores très étroits, films ultra fins). A contrario, on peut s'attendre à ce que des parois lisses facilitent le mouvement des particules les plus proches, et ainsi conduisent à une diminution de T_{g} [35, 36].

La plupart des études expérimentales de la transition vitreuse en géométrie confinée ont porté sur la réponse moyenne du liquide confiné. On trouve parmi les exceptions notables les travaux récents de Nugent et al. [37] et ceux de Ellison et Torkelson [9, 10]. Ellison et al. utilisent une technique de fluorescence sur multicouches dans laquelle une couche mince fluorescente de polystyrène (PS) est incorporée dans un film de PS non marqué. Ceci permet de mesurer T_{g} localement en différents endroits du film. Ils obtiennent une forte réduction de T_{g} à l'interface libre des films de PS et une atténuation continue de l'effet quand la couche fluorescente est située de plus en plus profond dans le film. Il est possible de mesurer une diminution de T_{g} dans une couche marquée située jusqu'à 30 nm de la surface libre du film. Cette distance excède largement la valeur de ξ_{g} estimée à 2-3 nm. Egalement, de récentes simulations numériques indiquent l'existence d'une dynamique hétérogène [17, 35, 38] et une distribution continue de T_{g} dans les couches minces de polymères [15, 21, 39].

Films de polymères libres et supportés

Dans cette thèse, nous apportons de nouvelles preuves de la diminution de T_{g} dans les couches minces de polymères avec une surface libre et des éléments en faveur de l'existence d'une température de transition vitreuse locale. Nous avons utilisé des simulations de dynamique moléculaire de films libres et supportés pour des chaînes non enchevêtrées. Dans le cas du film supporté, le substrat est modélisé par un mur attractif lisse. Pour ces deux géométries différentes, nous avons étudié l'influence du confinement sur les propriétés statiques et dynamiques du fondu.

Nous avons mis en évidence une structure en couche de la densité de monomères à l'interface supportée, tandis que le profil de densité au voisinage de la surface libre décroît vers zéro de façon monotone comme on peut l'observer sur la figure 1.

Cette structure en couches s'accentue lors d'un refroidissement et se propage vers l'intérieur du film. La dynamique dans nos systèmes est également modifiée de par l'existence des interfaces. Une analyse résolue en couches démontre clairement que les monomères aux interfaces libre et solide sont plus rapides que ceux situés au centre du film, qui conservent les propriétés observées en volume. De plus, les monomères à l'interface libre sont plus rapides que ceux proches du mur. Ces monomères de surface très mobiles transmettent une partie de leur mobilité élevée à

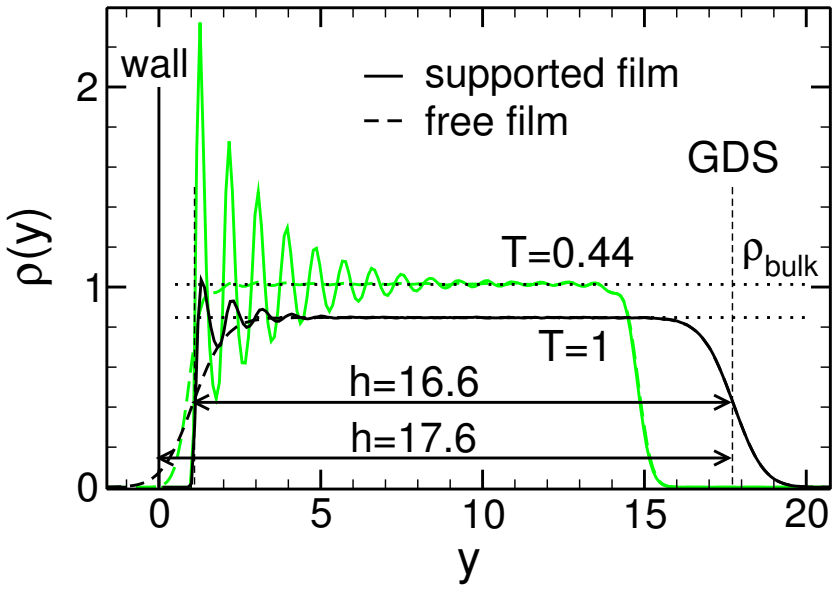

Figure 1: Profil de densité $\rho(y)$ pour un film supporté (trait plein) et un film libre (trait pointillé) à $T = 1$ et $T = 0.44$. Chacun des deux systèmes contient $n = 576$ chaînes. La ligne verticale marquée “wall” indique la position de la paroi dans la simulation du film supporté. La ligne pointillée verticale indique les positions des surfaces de Gibbs (GDS). Comme la surface de gauche du film supporté y_-^{G} est située à une distance valant environ 1 de la paroi, la définition $h = y_+^{\mathrm{G}} - y_-^{\mathrm{G}}$ donne une valeur de h inférieure à la définition $h = y_+^{\mathrm{G}}-$ (position de la paroi), c'est-à-dire $h = 16.6$ au lieu de $h = 17.6$ à $T = 1$ par exemple. La première définition $h = y_+^{\mathrm{G}} - y_-^{\mathrm{G}}$ sera toujours employée par la suite. Les lignes pointillées horizontales correspondent aux densités moyenne en volume à $T = 1$ et $T = 0.44$ ($\rho_{\mathrm{bulk}}(T = 1) = 0.85$ et $\rho_{\mathrm{bulk}}(T = 0.44) = 1.013$).

la couche suivante située plus en profondeur, qui à son tour peut accélérer la couche suivante, et ainsi de suite jusqu'à ce que l'effet se trouve amorti dans le cas où le film est suffisamment épais (pour des couches minces et/ou une basse température, les perturbations créées par les deux surfaces interagissent l'une avec l'autre au centre du film). Ceci est illustré par la figure 2, où les déplacements carrés moyens résolus par couches au sein d'un film libre sont présentés.

Ainsi, à une température donnée, la dynamique des films (moyenne pour l'ensemble du film) est plus rapide que celle observée en volume comme on peut le voir sur la figure 3 où les déplacements carrés moyens et la fonction de structure incohérente pour des films d'épaisseurs et de géométries différents sont comparées. Qui plus est, on observe que les films libres relaxent plus rapidement que les films supportés (qui n'ont qu'une seule interface libre au lieu de deux dans le cas des précédents).

Ces résultats ont un effet sur les températures caractéristiques telles que la température de transition vitreuse et la température critique de la théorie du couplage de

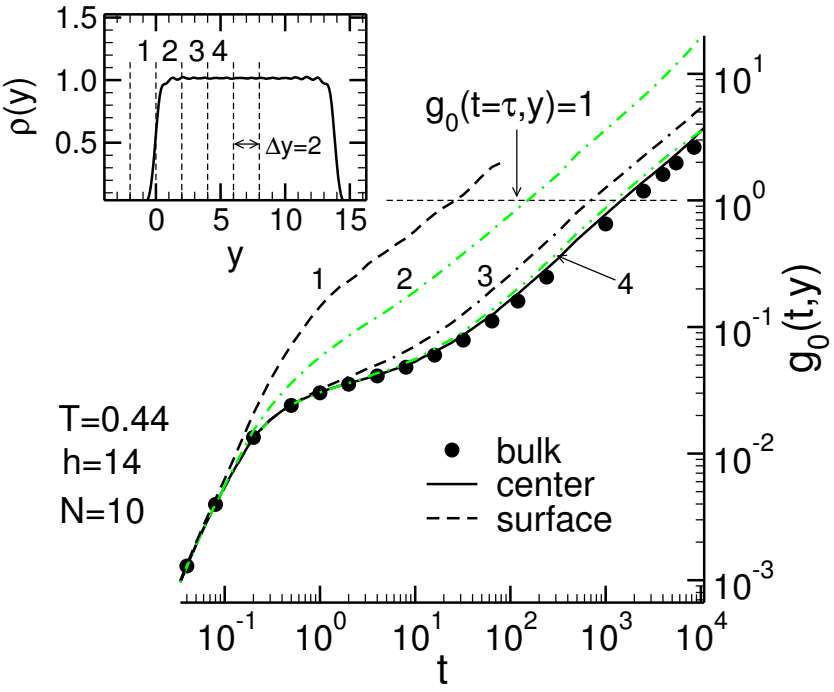

Figure 2: FIGURE PRINCIPALE: Déplacements carrés moyens résolus en couches $g_0(t,y)$ à $T = 0.44$ pour un film libre d'épaisseur $h = 14$. y représente la distance à la surface de Gibbs (située en $y = 0$). Seuls les déplacements parallèles à la paroi sont considérés pour le film (lignes pleines); les données pour la situation en volume (•) ont été multipliées par $2/3$ afin d'obtenir la même échelle que pour le film. $g_0(t,y)$ est obtenu après une moyenne sur l'ensemble des monomères d'une chaîne restant durant le temps considéré dans une couche d'épaisseur $\Delta y = 2$ centrée en y (equation (4.10)). Finalement, les monomères quittent la couche dans laquelle ils se trouvent initialement, donnant lieu à une baisse de la précision statistique pour les temps longs; les données sont donc parfois tronquées lorsque le bruit statistique est très fort. La ligne pointillée horizontale indique la définition du temps de relaxation locale $\tau(y,T)$ ((4.12)). ENCART: Profil de densité de monomères correspondant $\rho(y)$ en fonction de y. Les couches pour lesquelles $g_0(t,y)$ est présenté dans la figure principale sont indiquées par des nombres (1, 2, 3, 4).

modes (Mode Coupling Theory). T_g a été déterminée à partir de la dépendence en température de l'épaisseur du film h au cours du refroidissement; T_c est obtenue à partir d'une analyse des temps de relaxation dans les films. Qualitativement, $T_g(h)$ et $T_c(h)$ ont les mêmes caractéristiques. Les valeurs des deux températures sont abaissées par rapport à la situation en volume, et la diminution devient plus prononcée lorsque h décroît. La dépendence de T_c (ou T_g) en épaisseur est bien décrite par $T_c(h) = T_c^{\text{bulk}}/(1 + h_0/h)$. Un fit des données à l'aide de cette expression donne une hauteur caractéristique h_0 qui est approximativement deux fois plus grande dans le cas des films libres que dans celui des films supportés. Les résultats obtenus dans nos simulations sont comparés aux prédictions de Herminghaus dans la figure 4. Ils se

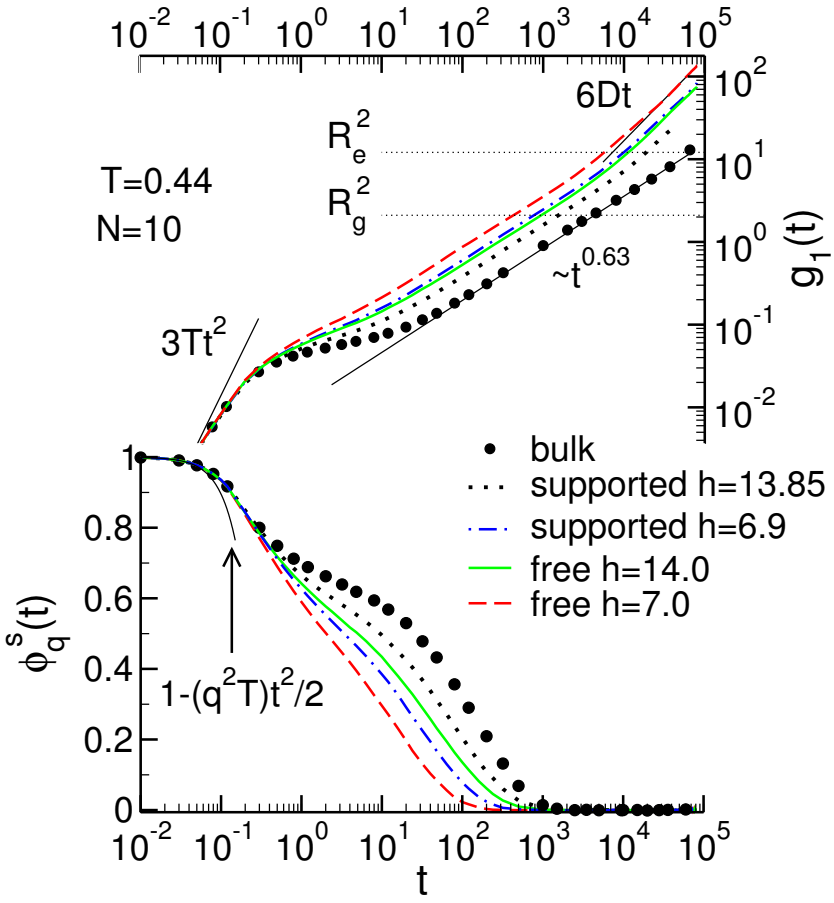

Figure 3: Déplacements carrés moyens des monomères intérieurs ($g_1(t)$) et facteur de structure dynamique incohérent ($\phi_q^s(t)$) dans le film et en volume à $T = 0.44$. ORDONNÉES DE DROITE : Tracé logarithmique de $g_1(t)$ en fonction de t; les déplacements carrés moyens sont mesurés dans la direction parallèle à la paroi et multiplié par $3/2$ afin de prendre en compte la différence de dimension par rapport à la situation en volume. Les lignes pointillées horizontales représentent la valeur du rayon de giration en volume $R_g^2 \simeq 2.09$ ainsi que la distance bout-à-bout $R_e^2 \simeq 12.3$. Les régimes ballistiques ($\sim t^2$), subdiffusif ($\sim t^{0.63}$), et diffusif ($\sim t$) sont indiqués (D est le coefficient de diffusion d'une chaîne). ORDONNÉES DE GAUCHE : Facteur de structure dynamique incohérent $\phi_q^s(t)$ à $q = 6.9$ ($\approx q^* =$ maximum du facteur de structure statique $S(q)$). Le régime ballistique ($\sim t^2$) est également indiqué.

retrouvent sur une courbe maîtresse si l'on redimensionne l'épaisseur par h_0 et T_c par T_c^{bulk}.

Cette observation est qualitativement en accord avec les résultats expérimentaux pour la diminution de T_g dans les films de PS libres et supportés [4, 40, 41]. Ces expériences suggèrent que T_g pour un film libre d'épaisseur h est en accord dans les barres d'erreurs avec la valeur de T_g pour un film supporté d'épaisseur $h/2$. D'après

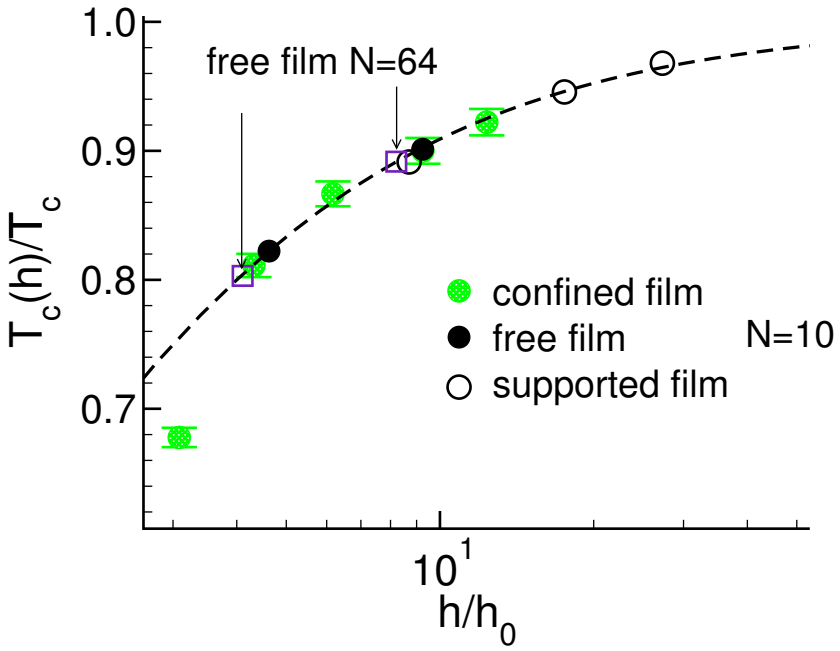

Figure 4: $T_{\rm c}(h)/T_{\rm c}$ ($T_{\rm c}$ = valeur en volume) en fonction de l'épaisseur redimensionnée h/h_0 pour un film supporté (cercles), un film libre (disques pleins) et des résultats de simulation pour un film confiné entre des parois lisses (modèle BE à $p = 1$) [35, 36] (cercles grisés). La ligne pointillée représente la courbe maîtresse $y = 1/(1 + x)$ avec $h_0 = 0.77$ pour le film supporté, $h_0 = 1.47$ pour le film libre et $h_0 = 1.64$ pour le film confiné.

ce seul résultat, il semble donc que le substrat pourrait être introduit dans le plan au centre d'un film libre sans entraîner de perturbations considérables de ses propriétés. Nos résultats concernant la dynamique résolue en couches indique cependant qu'une telle interprétation pourrait être trop simplifiée. Pour notre modèle, la présence du substrat entraîne une dynamique plus rapide, semblable à celle observée à l'interface libre.

En ce qui concerne la température de transition vitreuse mesurée dans nos simulations, l'influence exercée par les bords sur les propriétés (dynamiques) du système est un facteur clé (il est à noter que certains types de murs peuvent laisser la structure inchangée tout en affectant la dynamique : pour une discussion complète, cf. [19, 32]). Dans le cas de nos films-modèles, l'interface polymères–substrat comme l'interface polymères–vide contribuent à une mobilité accrue. Alors que cela peut être le cas en général pour l'interface avec le vide, ce n'est pas forcément vrai pour un liquide susceptible de former un verre en contact avec un substrat. Alors, la diminution de $T_{\rm g}$ dépend de l'interaction "particule–paroi". Ici, le terme "particule–paroi" possède un double sens. D'une part, il s'agit de l'attraction entre les particules et les parois. Une attraction suffisamment forte peut entraîner une augmentation de $T_{\rm g}$ [16, 17].

D'autre part, cela correspond à la topographie de la surface : même en l'absence d'une attraction préférentielle, la dynamique peut être fortement ralentie si les particules sont prisonnières dans des anfractuosités à la surface du substrat (voir par exemple [19, 33, 34]). Cet effect stérique peut également entraîner une augmentation de T_{g}.

En accord avec de récents résultats expérimentaux sur les films supportés de PS [9], nous avons observé que la surface libre donne lieu à une température de transition vitreuse locale qui décroît à l'approche de la surface. Mous avons montré que cette dépendence en la distance peut se comprendre d'après le comportement moyen du film, c'est-à-dire d'après la diminution de T_{g} quand l'épaisseur du film diminue. Ceci est bien décrit par une expression suggérée par Hermingaus et al. [4].

Solvant explicite

Nous avons étudié l'influence de la préparation du film sur sa structure finale. Une méthode couramment employée pour la préparation de couches ultra-minces est le procédé dit du spin coating. Ce procédé consiste à déposer une goutte de solution diluée de polymères (par exemple, du polystyrène en solution dans le toluène) sur une surface qui est ensuite mise en rotation rapide. L'étalement de la goutte sous l'influence des forces centrifuges et l'augmentation de la surface de contact qui en résulte conduisent à une évaporation initiale très rapide du solvant jusqu'à ce que le film vitrifie. Il reste alors une fraction volumique d'environ $\phi_{\mathrm{S}} = 20\%$ de solvant à l'intérieur du film. L'épaisseur du film peut être mesurée au cours du processus de spin coating à l'aide de l'ellipsométrie. On observe alors une décroissance exponentielle avec le temps, l'échelle de temps étant de l'ordre de la minute.

Des expériences [42–44] et des travaux théoriques [45] suggèrent que ce procédé pourrait piéger le film dans un état hors équilibre dont la nature n'est pas entièrement comprise. Les expérimentateurs rapportent des différences de comportement pour le démouillage ainsi qu'une dépendance en température du coefficient de dilatation thermique différente pour les films préparés par spin coating. Les tentatives de modéliser ce problème à l'aide de simulations numériques sont rares [46–48], et restreintes à l'étude de la dynamique de l'évaporation bien au dessus de la température de transition vitreuse.

Nous avons inclus une description explicite du solvant dans nos simulations afin de vérifier que le film se trouve piégé dans un état hors équilibre à cause de la transition vitreuse subie par le système de polymères. Afin d'obtenir une première estimation du type de comportement de phase auquel on peut s'attendre, nous avons utilisé le modèle Flory–Huggins pour les solutions de polymères. Les paramètres d'interaction sont choisis de manière à reproduire une solution polystyrène–toluène. Puisque la décroissance initiale de la concentration de solvant est très rapide, de même que la relaxation des polymères en solution, nous avons démarré nos simulations dans un état

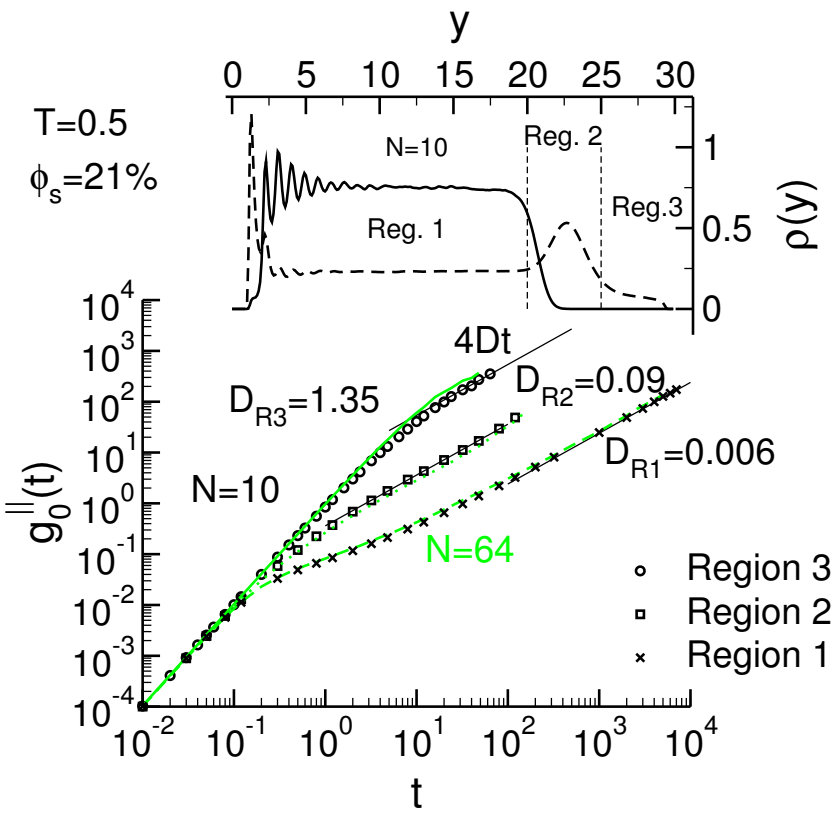

Figure 5: FIGURE PRINCIPALE : Déplacements carrés moyens des molécules de solvant dans les trois régions différentes détaillées dans l'encart. Les symboles correspondent à une longueur de chaîne $N = 10$ et les lignes grisées à $N = 64$. ENCART : Profils de densité pour solvant et polymères d'un film contenant $\phi_S = 21\%$ de solvant avec une longueur de chaîne $N = 10$ à $T = 0.5$. La ligne pointillée horizontale indique les limites des régions dans lesquelles les déplacements carrés moyens présentés dans la figure principale sont calculés.

de solution assez dense contenant une fraction volumique de solvant de $\phi_S = 21\%$. Nous avons caractérisé les propriétés initiales de la solution de polymères et discuté l'évaporation du solvant.

Le solvant est plus favorablement localisé aux interfaces entre le polymère et la paroi ou la surface libre. Nous observons une influence croissante de la concentration de solvant et de la proximité de l'interface sur la mobilité locale des monomères avec une baisse de la température. Le solvant se conduit comme un agent plastifiant qui accélère la relaxation du polymère. Par ailleurs, plus les monomères sont proches des interfaces, plus la dynamique est rapide. Ceci est visible sur la figure 5 où les déplacements carrés moyens du solvant sont présentés dans différentes régions du film comme il est indiqué dans l'encart. A la température de transition vitreuse, les valeurs des temps de relaxation locaux s'étendent sur trois ordres de grandeur en

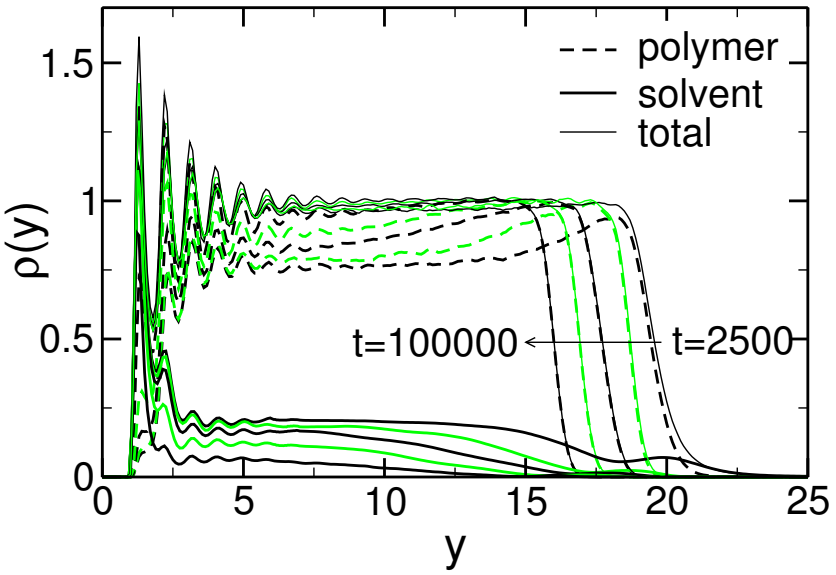

Figure 6: Profils de densité pour le polymére (pointillés), le solvant (ligne pleine épaisse) et l'ensemble (ligne pleine fine) lors de l'évaporation du solvant à $T = 0.5$ et pour $N = 64$, à des temps compris entre $t = 2500$ et $t = 100000$.

fonction de la composition et de la distance à la surface. Le processus d'évaporation s'en trouve fortement influencé.

Les profils de densité du solvant et du polymère alors que le solvant s'évapore à $T = 0.5$ sont présentés sur la figure 6. Au cours de l'évaporation, une couche riche en polymères se forme en surface. Dans la figure 7, l'épaisseur en fonction du temps est présentée à $T = 0.5$ et $T = 0.4$. A des températures bien au dessus de $T_{\rm g} = 0.4$ ($T = 0.5$), nous observons que l'épaisseur du film décroit comme la racine carrée du temps, ce qui est en accord avec un processus contrôlé par la diffusion jusqu'à ce que les effets de taille finie deviennent importants. Le solvant prisonnier entre le polymère et la paroi qui le supporte ne quitte le film que bien plus lentement. A haute température, l'évaporation complète du solvant est 10 fois plus lente pour un film supporté que dans le cas d'un film libre de la même épaisseur. Si l'évaporation se produit à $T_{\rm g}$, nous n'observons aucun régime dans lequel l'épaisseur se comporte en $\sqrt{t}$. Ceci est probablement dû à une forte dépendence des mobilités en composition et distance à la surface.

Conclusions

Nous avons utilisé des simulations de dynamique moléculaire pour étudier des films ultra-fins de polymères, supportés et libres, à l'aide d'un modèle coarse-grained qui retient uniquement les caractéristiques les plus importantes des polymères, c'est-à-

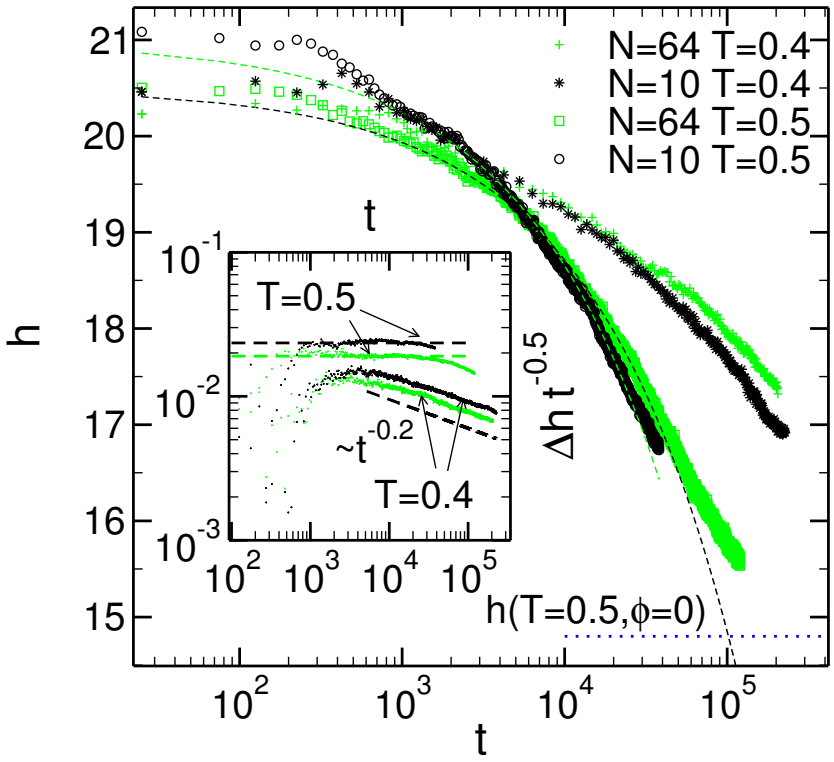

Figure 7: FIGURE PRINCIPALE : épaisseur du film $h(t)$ en fonction du logarithme du temps pour $N = 10$ à $T = 0.5$ (disques pleins) et $T = 0.4$ (étoiles pleines), ainsi que pour $N = 64$ à $T = 0.5$ (carrés gris) et $T = 0.4$ (croix grises). La ligne discontinue indique le résultat d'un fit selon l'équation (8.19) d'après lequel on obtient $\lambda(N = 10) = -0.022/2\sqrt{D_G}$ et $\lambda(N = 64) = -0.018/2\sqrt{D_G}$. ENCART : Données identiques ($N = 64$ (traits gris) $N = 10$ (traits pleins)) tracées sous la forme $[h(0) - h(t)]/\sqrt{t}$.

dire la connectivité de la chaîne, la répulsion à courte distance entre monomères, et leur attractivité à plus grande échelle qui assure l'intégrité du système en géométrie ouverte. Nous avons analysé la dynamique au sein du film, aussi bien en moyenne que par couches en fonction de la distance à la surface. Nous avons également déterminé la température de transition vitreuse $T_{\rm g}$ au cours de refroidissements. Il ressort de ces études que la dynamique est accélérée dans les couches minces par rapport à la situation du fondu en volume, et $T_{\rm g}$ diminue. Ces deux effets sont principalement dus à la surface libre du film. Ainsi, les films supportés relaxent moins rapidement que les films libres pour une épaisseur donnée.

Des films de polymères en solution ont également été étudiés en présence d'un solvant explicite. Nous nous sommes intéressés à la formation de films de polymères purs par évaporation du solvant; les résultats obtenus montrent que la dynamique est plus rapide et $T_{\rm g}$ plus basse en présence du solvant. Les temps de relaxation en fonction de la concentration de solvant s'étendent sur trois ordres de grandeur

à la transition vitreuse du polymère pur. La cinétique de l'évaporation s'en trouve fortement influencée. Alors que nous pouvons observer une diffusion fickienne à des températures supérieures à T_{g}, pour des températures plus basses, les déviations par rapport à ce comportement sont notables. A toutes températures, l'évaporation est plus rapide de plusieurs ordres de grandeur dans un film libre que dans un film supporté, ce qui est dû au piègeage des molécules de solvant entre le polymère et la paroi.

Chapter 1

Introduction

Polymer melts are bulk liquids consisting of macromolecules [49]. In the simplest case of linear homopolymers each macromolecule contains N monomeric repeat units of the same type, which are connected to form a chain. The chain length N may be large. A typical range in experiments is $10^3 \lesssim N \lesssim 10^5$. This implies that the average size of a polymer, measured e.g. by the radius of gyration R_{g} [50, 51], varies between $R_{\mathrm{g}} \sim 100$ Å and $R_{\mathrm{g}} \sim 1000$ Å. The size of a chain thus exceeds that of a monomer (~ 1 Å) by several orders of magnitude.

These different length scales are reflected in the particular features of a polymer melt. In the melt the monomers pack densely, leading to an amorphous short-range order on a local scale and to an overall low compressibility of the melt. Both features are characteristic of the liquid state. Qualitatively, the collective structure of the melt thus agrees with that of non-polymeric liquids. Additional features, however, occur if one considers the scale of a chain. A long polymer in a (three-dimensional) melt is not a compact, but a self-similar object [51–53]. It possesses a fractal 'open' structure which allows other chains to penetrate into the volume defined by its radius of gyration. On average, a polymer experiences $\sqrt{N}$ intermolecular contacts with other chains, a huge number in the large-N limit. This strong interpenetration of the chains has important consequences. For instance, intra-chain excluded volume interactions, which would swell the polymer in dilute solution, are screened by neighboring chains [50–52, 54–56]. A polymer in a melt thus behaves on large scales as if it were a random coil, implying that its radius of gyration scales with chain length like $R_{\mathrm{g}} \sim \sqrt{N}$. However it has been discovered recently that there are corrections to this so called ideality hypothesis [56]. Furthermore, the interpenetration of the chains creates a temporary network of topological constraints [50–52, 57]. These entanglements greatly slow down the chain dynamics and render the melt in general very viscous compared to low-molecular liquids.

Polymeric solids: crystallization and glass transition. Polymeric solids are either glassy or semicrystalline (figure 1.1) [60]. Semicrystalline polymers contain

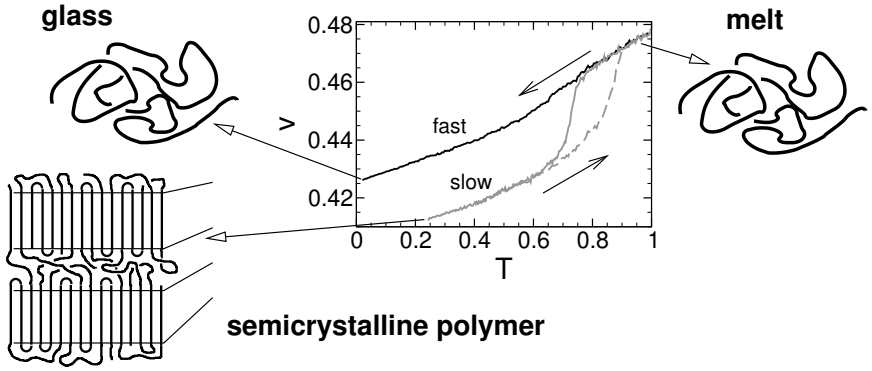

Figure 1.1: Volume per monomer v versus temperature T for a polymer melt which tends to crystallize. In the high-T liquid phase the chains have random-coil-like configurations and the structure of the melt is amorphous. The amorphous structure is preserved when the melt is cooled rapidly enough to avoid crystallization. Then, it undergoes a glass transition at $T_{\rm g}$. For slower cooling the melt transforms into a semicrystalline material at the crystallization temperature $T_{\rm crys}$. In the semicrystalline state sections of folded chains order in lamellar sheets that coexist with amorphous regions. On heating (dashed grey line) the crystal melts at $T_{\rm i} > T_{\rm crys}$. This hysteresis is characteristic of first-order phase transitions. The shown volume-temperature diagram is a result of molecular-dynamics simulations for a model of poly(vinyl alcohol) (courtesy of H. Meyer; see references [58, 59] for further details).

both amorphous and crystalline regions. The crystalline regions consist of lamellar sheets in which the polymers are folded back and forth so that sections of chains can align parallel to each other. The sheets twist and branch as they grow outward from a nucleus into spherulitic structures [60]. This hierarchy of morphological features, ranging from the lamellar ordering of the chains (~ 10 nm) to the macroscopic packing of the spherulites (100 μm and larger), reflects the complexity of the underlying crystallization process which is not yet fully understood [61–64].

The ability of crystal formation crucially depends on the microstructure of the chains. Only polymers with regular configurations, e.g. isotactic or syndiotactic orientations of the side-groups [51] or chains without side-groups, polyethylene being the prime example, can align parallel to each other so as to pack into crystalline lamellae. However, even in these favorable cases full crystallization is almost never achieved (see e.g. [62]).

Due to this intrinsic difficulty of crystal formation polymer melts are in general good glass formers [28, 29, 65]. Either they can be readily supercooled (figure 1.1) or, due to the irregular configuration of the chains, a crystalline phase does not exist at all. There are numerous examples for the latter case. They comprise homopolymers with an atactic orientation of (bulky) side-groups, e.g. atactic polystyrene, or random copolymers, such as *cis-trans* polybutadiene, in which monomers, having the same chemical composition, but different microstructure (*cis/trans* configuration of butadi-

ene), are randomly concatenated. These polymeric glass formers exhibit features that are also prevalent in other (intermediate and fragile) glass-forming liquids [28, 29]. For instance, as the melt is cooled from the liquid state toward the glass transition temperature $T_{\rm g}$, it displays a non-Arrhenius increase of all measured structural relaxation times. In proportion to this huge effect on the dynamics the amorphous structure of the melt only changes very little on cooling. This discrepancy poses a formidable scientific problem. Understanding its molecular origin represents an important issue in the research on the glass transition [29, 66–68].

A long-standing conjecture is that this non-Arrhenius increase of structural relaxation times upon approaching $T_{\rm g}$ is caused by the growth of a correlation length $\xi_{\rm g}$ with decreasing temperature. $\xi_{\rm g}$ is supposed to measure the average size of a cooperatively rearranging region (CRR), i.e. of a subensemble of particles which can rearrange into a new configuration independently of the other particles surrounding them [29].

The glass transition in confinement

An appealing approach to evidencing the existence of CRRs and estimating their size appears to lie in the study of the glass transition in spatial confinement. An increase of $\xi_{\rm g}$ should be truncated by the finite dimension of the confinement and this in turn should lower $T_{\rm g}$ [29].

Experiments [1–11], computer simulations [12–21], and theoretical approaches [22–27] have recently been used to explore the phenomenology and underlying mechanism of the glass transition in spatial confinement. Typically, these studies report deviations from bulk behavior if a glass former is confined to nanoscopic dimensions.

These experiments and computer simulations find shifts of $T_{\rm g}$ in confined glass-forming liquids and thin polymer films. But the shift can be upward and downward with respect to the bulk (see e.g. [2, 30, 31] for reviews; for recent theoretical approaches see e.g. [24, 25, 27]). This implies that, in addition to possible confinement effects, other factors are also important. One key factor should be the interaction of the liquid with the confining substrate (see e.g. [11]).

Simulations suggest that this liquid-substrate interaction consists of two contributions, an energetic and a steric one. For instance, strong liquid-substrate attractions can temporarily trap particles close to the confining walls and lead to slower dynamics than in the bulk [16, 17]. On the other hand, even without preferential attraction the dynamics may be slow if particles are caged in cavities of the substrate [19, 32–34]. In both cases, the slow particles at the walls partly slow down their neighbors which in turn obstruct the motion of their neighbors, and so on. This enables the wall-induced retardation to propagate into the core of the system. As a result, $T_{\rm g}$ can increase, particularly in strong confinement (narrow pores, ultra-thin films). Conversely, one expects non-attractive smooth walls to facilitate the motion of nearby particles and

thus to lead to a decrease of T_{g} [35, 36].

Computer simulations of model systems provide an example for the importance of these interfacial effects. For free-standing films, i.e. for systems with two liquid-vacuum interfaces, faster than bulk dynamics and, along with that, a depression of T_{g} is found [12, 16, 21, 38]. Furthermore, the simulations suggest that the dynamics of the confined liquid is very heterogeneous at low temperature T. Near the interface relaxation times are faster by orders of magnitude in comparison with those of the bulk. Below the bulk T_{g} one could interpret the presence of these more mobile monomers close to the surface as a molten layer on top of an already glassy polymer film. The thickness of the molten layer being dependent on temperature [5]. The fast relaxation continuously turns into bulk-like relaxation with increasing distance from the interface as already explained above. For all T this crossover remains continuous, but its range grows on cooling so that the surface-induced perturbations may propagate across the entire liquid at low T or for strong confinement (see [32] for a review) shifting T_{g}in parts of the film close to the surface or even the entire film if it is thin enough.

Most experimental approaches to the glass transition in restricted geometry have been concerned with the average response of the confined liquid. Notable exceptions are the recent work by Nugent et. al. [37] and by Ellison and Torkelson [9, 10]. Ellison et. al. employ a fluorescence/multilayer technique in which a thin fluorescent polystyrene (PS) layer is incorporated in an unlabeled PS film. This allows them to measure the local T_{g} at different positions in the film. They find a strong reduction of T_{g} at the free surface of the PS films and a continuous attenuation of the effect as the fluorescent layer is buried more and more deeply in the film. It was possible to measure a decrease of T_{g} in a labeled layer as far as 30 nm from the free surface. This distance exceeds by far the average estimated size of ξ_{g} of about 2-3 nm. Also recent computer simulation results point towards heterogeneous dynamics [17, 35, 38] and a continuous distribution of T_{g} in thin polymer films [15, 21].

Non-equilibrium nature of thin polymer films

A further point that has been raised repeatedly in connection with experimental studies on T_{g} in confinement is the sensitivity of the results to the exact experimental protocol applied to prepare and anneal thin polymer films [31, 42–45, 69]. It is argued that a thin polymer film whose thickness is smaller than the coil size of the bulk polymer is not an equilibrium structure. Experiments [42–44, 70, 71] and theoretical work [45] suggest that films prepared by spin-coating are trapped in an out-of-equilibrium state whose nature is not fully understood. Experiments report changes of the dewetting behavior [70, 71] and also a different temperature dependence of the thermal expansion coefficient of films prepared by spin-coating upon first heating after the film preparation [43, 72]. They find a decrease of film thickness upon

increasing temperature within a certain temperature interval.

The spin-coating process is a common method for the preparation of ultra-thin polymer films. In this procedure, a drop of a dilute polymer solution (for example polystyrene (PS) and toluene) is put onto a waver which is then spun very quickly (normally 1000-4000 rpm) [73, 74]. The spreading of the droplet due to the centrifugal forces and the accompanying increase of the surface lead to an ejection of excess material off the edge of the substrate and a very fast evaporation of the solvent. A PS film becomes glassy while there is still a volume fraction of about $\phi_{\mathrm{S}} = 14\%$ of the solvent (toluene) inside the film [75]. The final, slower thinning of the film is only due to solvent evaporation [76]. The remaining solvent is then evaporating out of an already glassy polymer matrix. This 'solvent quench' might trap the polymer coils in an out-of-equilibrium state as does a rapid temperature quench [43, 69]. The situation is complicated by the fact that some solvent might still be trapped in the film. The resulting film may contain so-called 'residual stresses' [44, 45, 71], because the chains below a critical solvent concentration are no longer mobile enough to relax their conformations to adapt to their changing environment as the solvent is lost. The final thickness of the film is dependent on parameters such as the initial viscosity of the solution, the spinning speed and the concentration of the solution [73, 74].

To allow a relaxation of these stresses, the films are usually annealed above the bulk T_{g}. The relaxation above T_{g} might include the loss of solvent still trapped in the film as well as the rearrangement of chains to minimize the energy, redistributing and changing the free volume available. Both processes result in changes of the film thickness. Strong interactions with the substrate can inhibit the reorientation of chains. In addition the films tend to break up and dewet at temperatures above T_{g}, limiting the amount of chain relaxation possible without destroying the film. There is no unambiguously defined procedure how to best relax chains in ultra-thin polymer films. Ideally, the film would be kept at an elevated temperature longer than the time it takes a polymer to displace over its size to allow a complete relaxation of the stresses. For the annealing of PS films at $T = 388\mathrm{K}$ for $12\mathrm{h}$ this condition is only met for molecular weights smaller than $M_{\mathrm{w}} < 850 \times 10^3 \mathrm{g/mol}$ [69, 77].

Keddie et. al. [42, 43] report measurements of the film thickness right after spin-coating and find an exponential decrease of film thickness, the time scale being of the order of minutes due to further solvent loss. There have been very few attempts to model this problem using computer simulations [46–48], all of which investigated the evaporation dynamics far above the glass transition temperature. One aim of this thesis is to make a first step to explore the phenomenon associated with solvent evaporation below T_{g}.

Simulations of free-standing and supported model polymer films

In this thesis we provide further evidence for the reduction of T_{g} in polymer films with a free surface and the scenario of a local glass transition temperature. We perform molecular-dynamics simulations of free-standing and supported films of non-entangled polymer chains using a simple coarse-grained bead-spring model for chains of length $N = 10$ and $N = 64$ monomers. In the supported films the substrate is modeled as a smooth attractive wall. Related previous work in the group [32, 35] was concerned with simulations of confined films at chain length $N = 10$.

For both film geometries we investigated the influence of confinement on static and dynamic properties of the melt on the local scale and determine the glass transition temperature T_{g}. The surface height fluctuations or capillary waves are investigated in detail as it has been suggested that a coupling of the viscous flow of the bulk to the capillary waves at the surface is responsible for the found T_{g} reductions [4]. In ultra-thin polymer films the thickness of the film can become comparable or even smaller than the equilibrium size of the polymer coil. Therefore perturbations of the chain conformations are expected in thin films. We assess the structure of the chains and its dependence on confinement by looking at the intra-chain structure factor and the layer-resolved R_{g} and R_{e}.

Simulations with explicit solvent

With the help of computer simulations we try to gain a better understanding of the spin-coating process. We include the solvent explicitly in our simulations and choose the interaction parameters to mimic the solution of polystyrene and toluene. A simulation of the entire experimental procedure starting from a dilute solution is certainly beyond the scope of this thesis. Since the initial decrease of the solvent concentration is very rapid and also the relaxation of the polymer in solution is very fast we only start our simulations for a rather dense polymer solution containing a volume fraction of solvent of $\phi_{\mathrm{S}} = 20\%$, initially at thermodynamic equilibrium. As it is known that in the final stages of the film preparation, when the solution reaches a very high viscosity and vitrifies, the decrease in film thickness is only due to solvent evaporation, a simulation only taking into account this final stage of the process could nevertheless be able to capture the creation of residual stresses and the trapping of the chains in an out-of-equilibrium state.

Therefore we limit our simulations to the evaporation of solvent from a dense solution at low temperature. The problem of drying and the evaporation of a liquid is omnipresent. The observed cases range from the drying of a coffee droplet, the drying of a paint to the formation of ultra-thin films and coatings by the evaporation of solvent. Our approach will treat this problem on the microscopic scale. Therefore we

cannot describe phenomena where large-scale inhomogeneities, i. e. larger than the size of our system of approximately $10\,\mathrm{nm}$, due to for example convection or intrinsic inhomogenties of the material are important. We will study the solvent evaporation at different temperatures and film geometries and compare the results to the predictions of simple theoretical approaches to solvent evaporation [78–83] based on diffusion equations. We will determine whether our systems show deviations from Fickian diffusion. Non-Fickian diffusion is often observed upon solvent penetration into a glassy polymer matrix in experiments [84–88]. Also in computer simulations non-Fickian diffusion has been recently observed by Janeva and coworkers [89], while a recent study on inter-diffusion of solvent into glassy polymer films by Grest and Tsige did not find any deviations from Fickian behavior [90]. Theoretical descriptions [91–95] of this so called anomalous or case-II diffusion are based on a high dynamic asymmetry between polymer and solvent in combination with a strong acceleration of the polymer dynamics in the presence of the solvent. While this phenomenon has been studied systematically in the literature, the inverse process of solvent evaporation from a glassy matrix, has to our knowledge, obtained much less attention. A notable exception is the recent work of Souche and Long who investigated solvent evaporation from a glassy polymer using a mesoscale model [95].

Outline of this thesis

First we will introduce the coarse-grained bead-spring model used in our simulations of thin polymer films in chapter 2. Details are given on how the films are set up and which algorithms are used to perform the MD simulations. In the following chapter 3 results on T_g in thin polymer films are presented. T_g is determined upon cooling the film with a constant rate while monitoring its thickness, a pseudo-thermodynamic approach often used in experiments. Subsequently we present a detailed analysis of the local structure of the films in comparison with the structure of the bulk in section 3.2.

Chapter 4 gives a detailed analysis of the dynamics of the films averaged over the whole system (section 4.1) as well as layer-resolved (section 4.3) as a function of the distance from the surface looking at the incoherent scattering function at the maximum of the static structure factor and the mean-square displacements. We extract the characteristic temperature T_c of mode coupling theory (MCT) from an analysis of relaxation times extracted from equilibrium simulations in section 4.2. In section 4.4 a comparison of our results of the thickness dependence of T_c and T_g to experimental results is presented. In connection with the functional dependence of T_g on film thickness suggested in reference [4] we will introduce a position dependent T_c in section 4.5. Finally an analysis of the non-Gaussian parameter is given in section 4.6.

The influence of capillary waves at the free surface on the structure and relaxation of the films is addressed in chapter 5. This is interesting in connection with

the found T_{g} reductions since it was suggested by Herminghaus [96] that a coupling of the bulk flow to the capillary wave fluctuations at the free surface gives rise to T_{g} reductions in thin polymer films. We first look at the static correlations of these fluctuations (section 5.1), followed by an analysis of the relaxation of these fluctuations in section 5.2.

As a complementary approach to analyze polymer dynamics, used in experiments employing dielectric spectroscopy, the dielectric relaxation spectra in our thin model polymer films are calculated in chapter 6. We determine the effect confinement has on the different relaxation modes of the film.

The last part of this work is dedicated to simulations with explicit solvent described in chapters 7 and 8. First the choice of the model parameters is explained in section 7.2. We study the equilibrium structures of our model of a polymer-solvent mixture based on toluene and polystyrene. We will present data on the local mobility of polymer and solvent as a function of composition in section 7.3 and on the static structure of the binary mixture in section 7.4. The evaporation of solvent is discussed in chapter 8. We will first present the simulation results in section 8.1 and a simple theory of evaporation in section 8.2 followed by a discussion of the results in comparison with theories of solvent evaporation in section 8.3.

Chapter 2

Model

There are several methods to simulate the behavior of a system [97, 98]. A choice has to be made according to the length scale to be probed, to capture the relevant phenomenon. In case we are interested in physical properties which involve several polymer chains—which amounts to thousands of atoms at least—, the method of choice would definitely not involve explicit electrons, nor should it consider the system as a continuous medium. In the former case one would have to cope with a lot of unnecessary information, while in the latter the relevant degrees of freedom would already be averaged out and therefore not accessible anymore.

Since we are interested in polymer melts and solutions, we need to adopt a method that allows to keep track of the behavior of the chains themselves, and therefore retain enough detail in the way they are modeled. The possibilities are numerous, depending on the degree of accuracy we require in the description of the chains. The more detailed scheme we can use consists in simulating the molecules by taking into account all the atoms of a chain [99, 100] ('atomistic model'). This scheme has the advantage that, doing so, we can hope to reproduce precisely the structure and dynamics of a specific polymer. Since we are more interested in the aspects of the behavior common to many polymers independent of chemical specificity, we adopt a more coarse grained model [101–103] where the atomistic degrees of freedom are not accounted for explicitly, but only implicitly through the choice of the effective potentials describing the interactions of the coarse-grained blobs. Such a coarse grained model which retains only the generic features of polymers, like chain connectivity and excluded volume interactions, allows to study the behavior of the system on larger time and length scales than an atomistic simulation [98].

2.1 Simulation model

We performed molecular dynamics (MD) simulations [104] of a generic bead-spring (BS) model [101] for a polymer melt. Non-bonded monomer-monomer interactions are given by a truncated and shifted Lennard-Jones (LJ) potential with cut-off radius

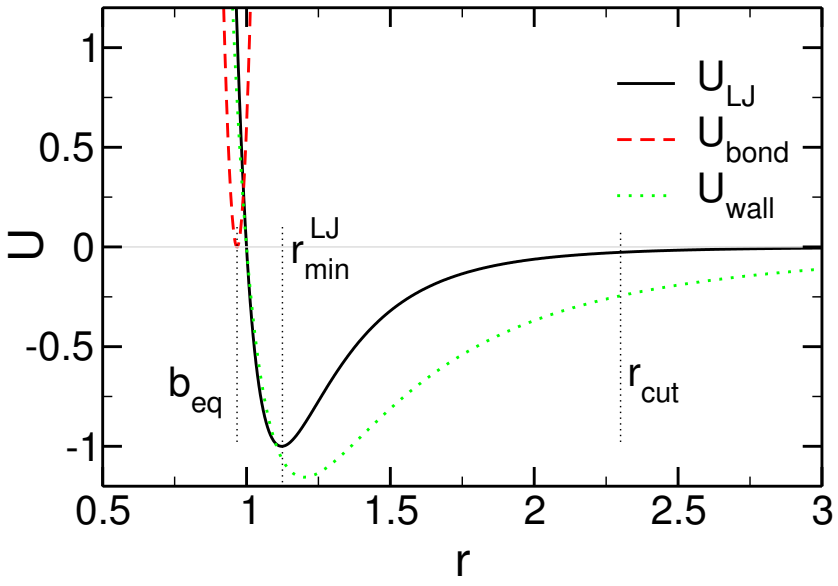

Figure 2.1: The Lennard-Jones potential $U_{\mathrm{LJ}}(r)$ (equation (2.1)), the harmonic bond potential $U_{\mathrm{bond}}(r)$ (equation (2.2)) and the potential to mimic the interaction with the substrate $U_{\mathrm{wall}}(r = y)$ (equation (2.3)) are shown.

$r_{\mathrm{c}} = 2.3 \simeq 2r_{\mathrm{min}}$ (r_{min} is the minimum of the LJ potential),

$$U_{\mathrm{LJ}}(r) = 4\epsilon \left[\left(\frac{\sigma}{r}\right)^{12} - \left(\frac{\sigma}{r}\right)^{6} \right] - U_{\mathrm{LJ}}(r_{\mathrm{c}}) \ , \quad r \leq r_{\mathrm{c}} \ . \tag{2.1}$$

For nearest neighbors along the chain the LJ interaction is not included. These monomers are connected to each other by a harmonic spring potential of equilibrium distance $b_{\mathrm{eq}} = 0.967\sigma$ and spring constant $k = 1111\ \epsilon/\sigma^2$,

$$U_{\mathrm{bond}}(r) = \frac{k}{2}(r - b_{\mathrm{eq}})^2 \ . \tag{2.2}$$

k is chosen large enough so that chains cannot cut through each other, which allows the formation of entanglements [50]. The potentials are displayed in figure 2.1.

In the following we will use LJ units. That is, $\epsilon = 1$, $\sigma = 1$, and mass $m = 1$. Then, temperature is measured in units of ϵ/k_{B} (Boltzmann constant $k_{\mathrm{B}} = 1$), and time in units of $\tau = (m\sigma^2/\epsilon)^{1/2}$.

In previous work [32], a slightly different bead spring model, the Bennemann (BE) model [105], was used. This model differs from the present one in the choice of the bond potential (BE model: superposition of FENE potential and nearest neighbor Lennard-Jones interaction [106]). In equation (2.2), we adapted the potential parameters so that static and dynamic properties of our BS model are identical or at least very similar to those found for the BE model. This will be shown in chapters 3.2.1 and 4.1.1.

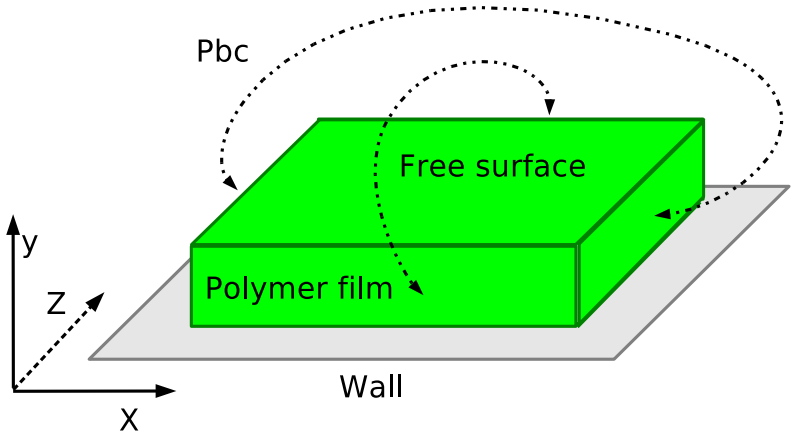

Figure 2.2: A schematic drawing of a supported polymer film.

The distance $r_{\min}$ of the LJ potential is incommensurate with b_{eq} of the bond potential. This implies that the bond potential locally distorts possible crystalline arrangements of the monomers (fcc or bcc), which the LJ potential alone would impose. Moreover, the polymer chains are very flexible because back-folding of adjacent bonds is only suppressed by the repulsive part of the LJ potential. These two features together effectively eliminate the risk of crystallization on cooling [32].

We mainly simulate chains consisting of $N = 10$, $N = 64$ and $N = 256$ monomers each. The chain length $N = 10$ has already been employed in the previous studies (see e.g. [32] for a review) and is below the estimated entanglement length of $N_{\text{e}} \approx 32$ [106, 107]. When employing the primitive path analysis a higher entanglement length is found $N_{\text{e}} \approx 64$ [108].

Modeling polymer films

With this model we simulate thin polymer films. Three film geometries are investigated: confined films, supported films with one polymer-substrate and one polymer-vacuum ("free") interface, and free-standing films with two polymer-vacuum interfaces. A schematic drawing of a supported film is shown in figure 2.2.

For supported and confined films we introduce a wall at $y = 0$ and in the latter case also at $y = h$ in the xz-plane of the simulation box. To model the monomer-wall interaction we use a (non-truncated) 9-3 LJ-potential

$$U_{\text{wall}}(y) = \epsilon_{\text{w}}\epsilon \left[\left(\frac{\sigma}{y}\right)^9 - \left(\frac{\sigma}{y}\right)^3 \right] \quad , \tag{2.3}$$

where y denotes the distance from the wall in the y-direction and ϵ_{w} is the potential strength. Equation (2.3) can be obtained, up to a prefactor for the term proportional to y^{-3}, by integrating the LJ-interaction between monomers and wall atoms over the half space $y < 0$ [109]. The wall potential is shown in figure 2.1.

With increasing ϵ_{w} the wall attracts the monomers more and more, and finally the polymers will wet the substrate. The wetting transition was investigated in reference [110]. It was found that a film at temperature $T = 1.68$ and pressure $p = 0$ wets the wall for $\epsilon_{\mathrm{w}} \gtrsim \epsilon_{\mathrm{w}}^{\mathrm{wet}} = 3.2$. Here, we chose a value in the vicinity of the wetting transition, $\epsilon_{\mathrm{w}} = 3$, for all temperatures studied ($T \in [0.1, 1]$). For this choice we did not observe any sign of dewetting.

2.2 Molecular dynamics simulations

Classical molecular dynamics (MD) simulations [97, 98] consist in solving Newton's equations of motion for a set of particles interacting via effective forces, in our case determined by the coarse grained model potentials defined above. The equations of motion have to be solved:

$$m_i \ddot{\mathbf{r}}_i = \mathbf{F}_i \ , \tag{2.4}$$

where m_i, $\mathbf{r}_i$ and $\mathbf{F}_i$ are respectively the mass and position of monomer i, and the force exerted on it. These equations have to be solved for all nN particles (n chains of N monomers) in our system. The force $\mathbf{F}_i$ derives from the potentials describing the interactions:

$$\mathbf{F}_i = -\frac{\partial U_{\mathrm{pot}}(\mathbf{r}_1, \ldots, \mathbf{r}_N)}{\partial \mathbf{r}_i} \ ; \tag{2.5}$$

and in our case of single particle and pairwise additive interactions,

$$U_{\mathrm{pot}} = \sum_{i=1}^{nN} U_{\mathrm{wall}}(y_i) + \sum_{i=1}^{nN} \sum_{j=i+1}^{nN} \left[U_{\mathrm{LJ}}(\mathbf{r}_{ij}) + U_{\mathrm{bond}}(\mathbf{r}_{ij}) \right] , \qquad \mathbf{r}_{ij} = \mathbf{r}_i - \mathbf{r}_j \ . \tag{2.6}$$

Using the MD simulation scheme, the positions and velocities of the nN particles in the system are calculated at all times, allowing to compute from there all the physical properties. These quantities are time-averaged in the course of the simulation, which corresponds to an ensemble average, if the ergodic principle holds [97, 98]. An MD simulation originally creates configurations in the microcanonical ensemble since the number of particles N remains unchanged, the volume V of the simulation box does not vary in time, and the equations of motion are known to conserve the total energy E. It is possible to add some other degrees of freedom to the system so as to run a simulation in other ensembles than NVE [97, 98]. This will be described in section 2.2.2.

2.2.1 Integration of the equations of motion

The method used to simulate the time evolution of the system consists in solving numerically the equations of motion (2.4). There are several algorithms to do so. All of them rely on the Taylor expansion of the expression of the positions at time $t+\Delta t$, Δt being a short time interval (called "time-step" in the following):

$$\mathbf{r}_i(t+\Delta t) = \mathbf{r}_i(t) + \Delta t \mathbf{v}_i(t) + \dots \ , \tag{2.7}$$

where $\mathbf{v}_i(t)$ is the velocity of particle i. Combining this with the equivalent expression for $\mathbf{r}_i(t-\Delta t)$, one arrives at the Verlet formulation for the resolution of equation. (2.4), which gives an estimate for $\mathbf{r}_i(t+\Delta t)$ and $\mathbf{v}_i(t)$ as a function of $\mathbf{r}_i(t)$, $\mathbf{r}_i(t-\Delta t)$, Δt and the forces $\mathbf{F}_i(t)$. This result achieves accuracy up to Δt^2 for velocities and Δt^4 for positions; though, this particular algorithm suffers from several inconveniences ($\mathbf{r}_i(t+\Delta t)$ and $\mathbf{v}_i(t+\Delta t)$ are not known at the same time, and other problems mentioned, for instance, in [97]).

***Velocity-Verlet* algorithm.** There exist other forms of the algorithm that tackle those problems, such as the so-called *velocity-Verlet* algorithm (this algorithm is implemented in the `md_spherical` program that we used for our simulations). The positions are updated using

$$\mathbf{r}_i(t+\Delta t) = \mathbf{r}_i(t) + \Delta t \mathbf{v}_i(t) + \frac{1}{2m_i}\mathbf{F}_i(t)\Delta t^2 \ . \tag{2.8}$$

By adding the equation

$$\mathbf{r}_i(t) = \mathbf{r}_i(t+\Delta t) - \Delta t \mathbf{v}_i(t+\Delta t) + \frac{1}{2m_i}\mathbf{F}_i(t+\Delta t)\Delta t^2 \tag{2.9}$$

one obtains the following expression which is used for the calculation of the velocities:

$$\mathbf{v}_i(t+\Delta t) = \mathbf{v}_i(t) + \frac{1}{2m_i}\Delta t\big(\mathbf{F}_i(t) + \mathbf{F}_i(t+\Delta t)\big) \ . \tag{2.10}$$

2.2.2 Different ensembles: NVE, NVT, NPT

By integrating Newton's equations of motion an MD simulation would explore the phase space of the microcanonical (NVE) ensemble provided that the algorithm is accurate enough (i.e. the time step small enough) to guarantee the conservation of the total energy. In practice integration errors can cause a drift of the energy. The Verlet algorithm has the advantages of conserving the phase space volume and being time-reversible. The fact that the algorithm is simplectic makes larger time steps admissible. Simulations of the NVT and NpT ensemble are often more desirable because they often represent an experimental situation better. A local thermostat can stabilize the integration scheme allowing for even larger time-steps [111].

NVT ensemble

The canonical ensemble models a subsystem in contact with a much larger system the so called heat bath. The two systems cannot exchange particles but energy can be transferred between them. Therefore the total energy is not conserved in the subsystem of interest. The heat bath is assumed to be so large as not to be affected by these energy transfers. At equilibrium the temperature T of the subsystem is equal to the one of the heat bath T_{ext}.

T is related to the kinetic energy via the equipartition theorem (we are considering instantaneous values of the different quantities here):

$$E_{\text{k}} = \sum_{i=1}^{nN} \frac{1}{2} m_i {\mathbf{v}_i}^2 \tag{2.11}$$

$$= \frac{3}{2} nN k_{\text{B}} T \ . \tag{2.12}$$

There are many different ways to include the effects of a heat bath on a system in a simulation. We will discuss here two different thermostating mechanisms used in our simulations.

Nose-Hoover thermostat. One way to control the temperature is by acting on the global kinetic energy of the system defined in equation (2.11). Nose and Hoover achieved this by deriving equations of motion

$$\dot{\mathbf{r}}_i = \frac{\mathbf{p}_i}{m_i} \tag{2.13}$$

$$\dot{\mathbf{p}}_i = \mathbf{F}_i - \xi \mathbf{p}_i \tag{2.14}$$

$$\dot{\xi} = \frac{1}{Q} \left(\sum \frac{\mathbf{p}_i^2}{m_i} - 3Nk_{\text{B}}T_{\text{ext}} \right) \tag{2.15}$$

using an extended Lagrangian [112–114]. A further degree of freedom ξ is introduced whose equation of motion is governed by the imbalance between the total instantaneous kinetic energy and the desired canonical average, i.e. the temperature T_{ext}.

Choice of the coupling strength. The strength of the coupling is determined by the fictitious mass parameter Q. The rate of change of ξ is proportional to the inverse of Q. For very small values of Q one is in the strong coupling limit. In this case ξ oscillates much faster than the energy fluctuations. As ξ enters directly the rate of change of the momenta, the kinetic energy will mainly follow large magnitude oscillations of ξ. The configurational part of the energy, however, will be decoupled from ξ which can make the thermostat very inefficient. On the other hand in the limit $Q \to \infty$, ξ is constant and Newton's equations (2.4) and a simulation in the NVE

ensemble are recovered. The thermostat is known to work well for a wide Q range between these two extremes. Noose [115] suggested to choose Q as

$$Q \sim \frac{6Nk_{\mathrm{B}}T}{\omega^2_{\mathrm{intrinsic}}} \sim 5 \,, \tag{2.16}$$

where $\omega_{\mathrm{intrinsic}}$ is a typical intrinsic oscillation frequency of the system. This allows an optimal coupling of the thermostat to the system.

Dissipative particle dynamics (DPD) thermostat. In many simulations of polymer melts, a Langevin thermostat is used [111, 116]. Another possibility to perform simulations at constant temperature using stochastic dynamics is the DPD thermostat. We do not perform dissipative particle dynamics but only use the thermostat in MD simulations [117] as described below. The DPD thermostat controls the temperature, as the Langevin thermostat, by the counter-balance between a friction force dissipating energy and a random force pumping energy into the system. These two forces are linked through the fluctuation-dissipation theorem. But as opposed to the Langevin thermostat the DPD thermostat allows to conserve the total momentum of the system and should therefore treat problems were fluxes and thus hydrodynamics are important more accurately.

The equations of motion of the particles including the thermostat are given by

$$\dot{\mathbf{r}}_i = \frac{\mathbf{p}_i}{m_i} \,, \tag{2.17}$$

$$\dot{\mathbf{p}}_i = \mathbf{F}_i + \mathbf{F}_i^D + \mathbf{F}_i^R \tag{2.18}$$

where $\mathbf{F}_i^D$ is the damping force and $\mathbf{F}_i^R$ is the random force, both acting on the particle i. $\mathbf{F}_i$ refers to the conservative force defined in equation (2.6). The DPD forces are given as sums over pairwise inter-particle forces according to

$$\mathbf{F}_i^D = \sum_{j \neq i} \mathbf{F}_{ij}^D, \qquad \mathbf{F}_i^R = \sum_{j \neq i} \mathbf{F}_{ij}^R \,. \tag{2.19}$$

All forces exerted on the particle by the thermostat are based on two-particle forces acting along the inter atomic axis $\mathbf{r}_{ij} = \mathbf{r}_i - \mathbf{r}_j$. This thermostat therefore conserves the total momentum. Since it only acts on the difference of the velocities, it does not extenuate hydrodynamic correlations. Following Warren et al [118] the inter-particle damping force is defined as

$$\mathbf{F}_{ij}^D = -\gamma w^D(r_{ij})(\hat{r}_{ij} \cdot \mathbf{v}_{ij})\hat{r}_{ij} \,, \tag{2.20}$$

where γ denotes the friction constant and $\mathbf{v}_{ij} = \mathbf{v}_i - \mathbf{v}_j$ is the relative velocity of particles i and j and $\hat{r}_{ij} = \mathbf{r}_{ij}/|r_{ij}|$. The corresponding random force is given by

$$\mathbf{F}_{ij}^R = \sigma w^R(r_{ij})\theta_{ij}\hat{r}_{ij} \,. \tag{2.21}$$

σ is the strength of the noise and θ_{ij} is a gaussian random variable with $\theta_{ij} = \theta_{ji}$ whose first and second moments are

$$\langle \theta_{ij}(t) \rangle = 0 \tag{2.22}$$

$$\langle \theta_{ij}(t)\theta_{kl}(t') \rangle = (\delta_{ik}\delta_{jl} + \delta_{il}\delta_{jk})\delta(t - t') \; . \tag{2.23}$$

Note that the DPD thermostat is not applied between particles bonded to each other and also not between the particles and the wall.

In our implementation a random number generator which provides uniformly distributed random numbers is used. In order to satisfy the fluctuation-dissipation theorem, the equations

$$\sigma^2 = 2k_{\mathrm{B}}T\gamma \tag{2.24}$$

and

$$\left(w^R(r)\right)^2 = w^D(r) \tag{2.25}$$

need to be fulfilled. The functional dependence of w_D can be chosen arbitrarily. Following Warren et. al. [118] we chose

$$w^D(r) = (1 - \frac{r}{r_{\mathrm{c}}}) \; , \quad r < r_{\mathrm{c}} \tag{2.26}$$

with a cut-off radius which is the same as the one used for the Lennard-Jones potential. Another possibility would be to choose $w^D(r) = 1$ for $r < r_c$.

When integrating the equations of motion (2.17) and (2.18) the dependence of the damping forces on the velocities can cause problems. Deviations from true equilibrium behavior have been encountered, including an unphysical systematic drift of the temperature [119–122]. In the velocity-Verlet scheme the forces at times t and $t + \Delta t$ are required to update the velocities since

$$\mathbf{v}_i(t + \Delta t) = \mathbf{v}_i(t) + \Delta t \frac{\mathbf{F}_i^{\mathrm{tot}}(t) + \mathbf{F}_i^{\mathrm{tot}}(t + \Delta t)}{2} \; , \tag{2.27}$$

where $\mathbf{F}_i^{\mathrm{tot}} = \mathbf{F}_i + \mathbf{F}_i^D + \mathbf{F}_i^R$. For the calculation of the force $\mathbf{F}_i^{\mathrm{tot}}(t + \Delta t)$ on the other hand $\mathbf{v}_i(t + \Delta t)$ must be known due to the velocity dependence of the damping force.

As a first approximation the velocities at time t only can be used to calculate the forces at times t and $t + \Delta t$ necessary for the updating of the velocities. This increases the error of the algorithm and leads to a slightly increased temperature in our systems. For the step size $\Delta t = 0.005$ used in these simulations the relative error $\Delta T/T = 0.1\%$, for a cut-off radius $r_{\mathrm{c}} = 2.3$. The error decreases with decreasing time step.

There have been different methods suggested to overcome these problems [120–122]. Corrections based on the inclusion of higher order terms were suggested by several authors [120, 121]. The Euler formula can be used to predict the velocities at time $t + \Delta t$,

$$\mathbf{v}_i^{\mathrm{e}}(t + \Delta t) = \mathbf{v}_i(t) + \Delta t \mathbf{F}_i^{\mathrm{tot}}(t) \; . \tag{2.28}$$

This allows to calculate an estimate for $\mathbf{F}_i^{\text{tot}}(t+\Delta t)$. The inclusion of this correction is sufficient to improve the accuracy and allow a propagation with a time step as large as $\Delta t = 0.01$ in our systems. An alternative, more rigorous approach, would be to determine the force and the velocity self consistently [119, 122]. But that requires a repeated calculation of the forces for each time step. Since for the time step applied in this calculation a satisfactory accuracy can be obtained without implementing this time consuming procedure it is not used.

We first investigated the dependence of the dynamics on the thermostats. We calculate the velocity auto-correlation function

$$Z(t-t') = \langle \mathbf{v}(t)\mathbf{v}(t')\rangle \ . \tag{2.29}$$

For the dense polymer melt under investigation this correlation develops a negative tail for large times, signifying the rattling motion of a particle in the cage formed by its surrounding particles. It is related to the mean square displacement of the monomers $g_0(t) = \langle |\mathbf{r}(t) - \mathbf{r}_0|^2\rangle$ by a Green-Kubo relation [123]

$$g_0(t) = \int_0^t dt' \int_0^t dt'' Z(t'-t'') \ . \tag{2.30}$$

The negative tail of the velocity autocorrelation function is reflected in a lowering of the diffusion coefficient $D = g_0(t)/6t$ or equivalently

$$D = \int_0^\infty dt Z(t) \ . \tag{2.31}$$

In a normal liquid the diffusion coefficient is inversely proportional to the viscosity.

It can be shown that the Nose-Hoover thermostat as well as the DPD thermostat allow to sample a canonical distribution [113, 118]. The Nose-Hoover scheme is also known to not alter the dynamics of the system in comparison to the dynamics in an NVE simulation [98]. We compared the dynamics of polymers in a confined film of thickness $h = 10$ at temperature $T = 1$ being thermostated by the Nose-Hoover thermostat and the DPD thermostat respectively via the velocity auto-correlation function. The area of the simulation box was chosen such that the average pressure was set to $p = 0$. The dependence of the DPD results on the friction parameter γ were explored.

In figure 2.3 the velocity auto-correlation functions are shown. For higher values of the friction parameter γ the velocities decorrelate faster. We find a decreasing diffusion constant with increasing friction parameter γ. In the following we will always use a value of $\gamma = 0.5$ which is large enough to efficiently thermostat the system and on the other hand is small enough to not significantly alter the dynamics of the monomers.

NpT ensemble

It is also possible to perform simulations in the isothermal-isobaric (NpT) ensemble. In this case, the volume of the simulation box has to fluctuate, allowing the pressure to

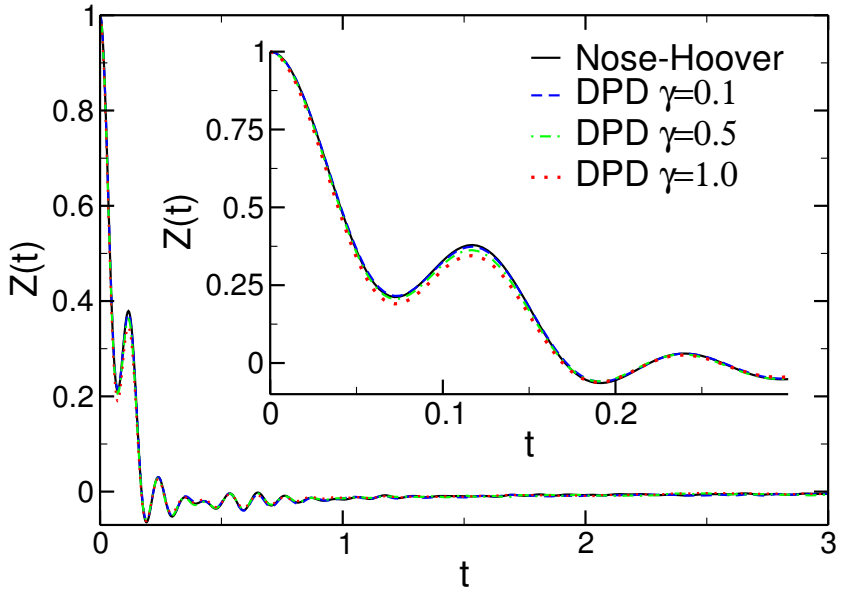

Figure 2.3: Velocity-autocorrelation functions for different values of the friction parameter γ at constant volume (The volume was set to the mean value obtained from a NpT simulations at $p = 0$) for a confined film with wall-to-wall distance $h = 10$ at $T = 1$ are compared to the result for the Nose-Hoover thermostat. The chain length was 10. The time step was $dt = 0.005$ in all cases.

remain constant. In an isotropic system the instantaneous pressure can be calculated as [97]

$$p(t) = \frac{1}{3V}\left(\sum_i m_i \mathbf{v}_i^2 + \sum_{i<j} \mathbf{r}_{ij} \cdot (\mathbf{F}_{ij} - \mathbf{R}_{\text{cm}})\right) . \tag{2.32}$$

Here, $V = B_x B_y B_z$ is the volume of the simulation box (B_x, B_y, B_z are the linear dimensions of the box in x, y, and z directions) and $\mathbf{F}_{ij}$ the force acting between particles i and j which are a distance $\mathbf{r}_{ij}$ apart from each other and $\mathbf{R}_{\text{cm}}$ is the system's center of mass. (It is subtracted to allow a correct sampling of the NpT ensemble using this expression for the instantaneous pressure in the equations of motion of the Andersen barostat [124] described in the following.) For anisotropic systems the total pressure is a tensor [125] given by

$$\hat{P} = \frac{1}{V}\left(\sum_i m_i \mathbf{v}_i \mathbf{v}_i^T + \sum_{i<j} \mathbf{r}_{ij} (\mathbf{F}_{ij} - \mathbf{R}_{\text{cm}})^T\right) . \tag{2.33}$$

The superscript T refers to the transposed vector. For a fluid at equilibrium that is confined in one direction (in our case the y direction) the off-diagonal components of $\hat{P}$ vanish, and the two diagonal components parallel to the wall are identical. For

films, there is thus only a normal component (cf. e.g. [104, 126])

$$P_{\mathrm{N}} = \frac{1}{V}\left[\sum_i \frac{p_{i,\perp}^2}{m_i} + \sum_i F_{i,\perp}(y_i - R_{\mathrm{cm},\perp})\right] , \tag{2.34}$$

and a parallel component

$$P_{\mathrm{T}} = \frac{1}{2V}\left[\sum_i \frac{\mathbf{p}_{i,||}^2}{m_i} + \sum_i \mathbf{F}_{i,||}\cdot(\mathbf{r}_{i,||} - \mathbf{R}_{\mathrm{cm},||})\right] . \tag{2.35}$$

Here, $\mathbf{p}_i = (\mathbf{p}_{i,||}, p_{i,\perp})$ is the momentum of particle i at position $\mathbf{r}_i = (\mathbf{r}_{i,||}, r_{i,\perp} = y)$, $\mathbf{F}_i = (\mathbf{F}_{i,||}, F_{i,\perp})$ is the total force acting on particle i, and $\mathbf{R}_{\mathrm{cm}} = (\mathbf{R}_{\mathrm{cm},||}, R_{\mathrm{cm},\perp})$ is the position of the system's center of mass.

We would like to use our bulk simulations to bench mark the results we obtain for the films. If a free surface is present and no external forces act on the monomers, the component of $\hat{P}$, the pressure tensor, perpendicular to the surface vanishes. The pressure becomes isotropic as we go further from the interface, so that $p = 0$ far from the interface. It is therefore natural to choose an NpT ensemble with $p = 0$ in the simulation of the bulk polymer and the confined films.

Berendsen barostat. A very simple approach to simulate at constant pressure in the bulk is the Berendson barostat [127]. With the Berendsen method, one defines a time constant τ_{P} which couples the system to an external piston through

$$\frac{\mathrm{d}p}{\mathrm{d}t} = \frac{P_{\text{ext}} - p}{\tau_{\mathrm{P}}} , \tag{2.36}$$

where P_{ext} is the target pressure; to satisfy such a requirement, it is then necessary to impose a new form for the equations of motion, and to modify the volume accordingly:

$$\dot{r}_i = v_i + \eta r_i \tag{2.37}$$

$$\dot{V} = 3\eta V . \tag{2.38}$$

The isothermal compressibility is defined by

$$\beta = -\frac{1}{V}\left(\frac{\mathrm{d}V}{\mathrm{d}p}\right)_T \tag{2.39}$$

and can be used to link η to the coupling constant τ_{P} [using eqs. (2.36) and (2.38)]:

$$\frac{\mathrm{d}p}{\mathrm{d}t} = -\frac{1}{\beta V}\frac{\mathrm{d}V}{\mathrm{d}t} \simeq \frac{\Delta p}{\Delta t} \tag{2.40}$$

$$\frac{P_{\text{ext}} - p}{\tau_{\mathrm{P}}} = -\frac{1}{\beta V} 3\eta V \tag{2.41}$$

$$\Rightarrow \eta = -\frac{\beta}{3\tau_{\mathrm{P}}}(P_{\text{ext}} - p) . \tag{2.42}$$

The differential equation (2.37) for r_i can be solved by scaling the positions by a factor

$$\mu = 1 - \frac{\beta \Delta t}{3\tau_{\mathrm{P}}}(P_{\mathrm{ext}} - p) \tag{2.43}$$

to first order in Δt. So that the system volume and coordinates are rescaled after each time step according to

$$\mathbf{r}_i' = \mu \mathbf{r}_i \tag{2.44}$$

and

$$B_x' = \mu B_x \quad B_y' = \mu B_y \quad B_z' = \mu B_z \; . \tag{2.45}$$

This coupling scheme will adapt the system volume such that the average pressure reaches the imposed value P_{ext}. The height of the fluctuations is proportional to the parameter μ and thus dependent on the ratio $\beta \delta t / \tau_{\mathrm{P}} = 0.0001$. The choice made here mirrors the small compressibility of the system keeping the amplitude of volume fluctuations low. The Berendsen barostat does not rigourously sample the isobaric-isothermal ensemble but provides a simple stable method to get the desired average system size.

The Berendson barostat needs to be modified for anisotropic systems. We choose to adjust the area that the film covers and impose the normal pressure P_{N}. The wall-to-wall distance is kept constant. The following coupling scheme was used to allow a simulation at constant normal pressure P_{N}.

$$x_i' = \mu x_i \quad z_i' = \mu z_i \tag{2.46}$$

$$B_x' = \mu B_x \quad B_z' = \mu B_z, \tag{2.47}$$

where $\mu = 1 - \frac{\beta \delta t}{3\tau_P}(P_{\mathrm{ext}} - P_{\mathrm{N}})$ is thus dependent on the normal component of the pressure tensor. This coupling scheme adjusts the area and gives the desired average pressure. This scheme does not rigourously sample the isobaric-isothermal ensemble which was already noted for the bulk system.

Andersen barostat. As in the case of the thermostat it is possible to realize states distributed according to the isothermal isobaric ensemble by the use of an extended Lagrangian [124, 128]. As a further degree of freedom, the volume is introduced. The system volume and its conjugate variable η are driven by the difference between the imposed pressure and the instantaneous pressure of the system. The resulting equations are the Hoover-Melchionna equations [124].

For a bulk system the barostat acts isotropically in all three directions such that the chosen external pressure P_{ext} is imposed. The equations governing the time evolution of the particles are given by

$$\dot{\mathbf{r}}_i = \frac{\mathbf{p}_i}{m_i} + \eta(\mathbf{p}_i - \mathbf{R}_{\text{cm}}) \tag{2.48}$$

$$\dot{\mathbf{p}}_i = \mathbf{F}_i - (\xi + \eta)\mathbf{p}_i \tag{2.49}$$

$$\dot{\xi} = \frac{1}{Q}\left(\sum \frac{\mathbf{p}_i^2}{m_i} - 3Nk_{\text{B}}T_{\text{ext}}\right) \tag{2.50}$$

$$\dot{\eta} = \frac{V}{M}\left(P(t) - P_{\text{ext}}\right) \tag{2.51}$$

$$\dot{V} = 3V\eta\,. \tag{2.52}$$

The position of the center of mass R_{cm} is subtracted to ensure that the isothermal isobaric ensemble is realized [124, 126]. The coupling parameter is the mass of the barostat M. It determines the frequency of the volume fluctuations, but not their amplitude as opposed to the Berendson barostat. In the case of $M \to \infty$ the Nose-Hoover equations and the canonical ensemble are recovered.

Choice of the mass parameter M. As opposed to the Nose-Hoover thermostat which performs well for a rather larger range of the coupling parameter Q, this barostat is more sensitive to the value of M. According to Anderson the time scale of the volume fluctuations should be comparable to the time it takes a sound wave to make at least one round trip in the simulation box. This time is sufficient for the system to respond to the volume changes [129]. Using this criterion an expression for the mass parameter can be found [126]

$$M \sim n_{\text{rt}}^2 3N \left(\frac{V^{1/3}}{\pi}\right)^2 \sim 10^6\,, \tag{2.53}$$

where n_{rt} refers to the number of round trips of a sound wave during a full period of volume fluctuations. Andersen suggested that $n_{\text{rt}} = 1$ but we use $n_{\text{rt}} = 10$ which gives the system more time to respond to volume fluctuations and increases the performance of the barostat [130].

Barostating a film. When applying this barostat to a film one is faced with the problem that there are different possibilities how to couple the barostat to the asymmetric simulation box. One can either vary the area of the film or its thickness to adjust the tangential or normal pressure respectively [126]. We adopt a solution where the normal pressure is kept constant and thus the wall-to-wall separation is allowed to vary.

The equations in this case read as follows:

$$\dot{\mathbf{r}}_{i,||} = \frac{\mathbf{p}_{i,||}}{m_i} \tag{2.54}$$

$$\dot{y}_i = \frac{p_{i,y}}{m_i} + \eta(y_i - R_{\text{cm,y}}) \tag{2.55}$$

$$\dot{\mathbf{p}}_{i,||} = \mathbf{F}_{i,||} - \xi \mathbf{p}_{i,||} \tag{2.56}$$

$$\dot{p}_{i,y} = F_{i,y} - (\eta + \xi) p_{i,y} \tag{2.57}$$

$$\dot{\xi} = \frac{1}{Q}\left(\sum \frac{\mathbf{p}_i^2}{m_i} - 3Nk_{\text{B}}T_{\text{ext}}\right) \tag{2.58}$$

$$\dot{\eta} = \frac{V}{M}\left(P_N(t) - P_{\text{ext}}\right) \tag{2.59}$$

$$\dot{B}_y = B_y \eta \,. \tag{2.60}$$

The normal pressure is calculated as indicated in equation (2.34). While the thermostat acts isotropically in all three directions, the variable η, conjugate to the separation of the walls B_y, acts only in the direction perpendicular to the wall. Equally only the wall-to-wall distance B_y is changing while the lateral box size is kept constant.

Fathollah Varnik [126, 130] chose in his simulations of confined films to vary the area of the film $A = B_x B_z$ and keep its thickness given by the wall-to-wall distance B_y fixed while still imposing the normal pressure of the system to be equal to $P_{\text{N}} = 1$. This corresponds to the coupling scheme we employed when using the Berendsen barostat for confined films. As P_{N} and A are not conjugate variables a slightly more complicated procedure has to be used to achieve a rigorous sampling of the desired ensemble within the frame work of the Andersen barostating scheme [126, 130].

DPD thermostat and Andersen barostat. A third approach we explored was to combine the Andersen barostat with the DPD-thermostat [131] to be able to simulate a system where hydrodynamic correlations are important. As one of the goals of this thesis is the simulation of the solvent evaporation from a thin polymer-solvent film, it is desirable to include hydrodynamic effects as accurately as possible. The equations of motion are given by:

$$\dot{\mathbf{r}}_{i,||} = \frac{\mathbf{p}_{i,||}}{m_i} \tag{2.61}$$

$$\dot{y}_i = \frac{p_{i,y}}{m_i} + \eta(y_i - R_{cm,y}) \tag{2.62}$$

$$\dot{\mathbf{p}}_{i,||} = \mathbf{F}_{i,||} + \mathbf{F}^D_{i,||} + \mathbf{F}^R_{i,||} \tag{2.63}$$

$$\dot{p}_{i,y} = F_{i,y} + F^D_{i,y} + F^R_{i,y} - \eta p_{i,y} \tag{2.64}$$

$$\dot{\eta} = \frac{V}{M}\left(P_N(t) - P_{ext}\right) \tag{2.65}$$

$$\dot{B}_y = B_y \eta \,. \tag{2.66}$$

The random $\mathbf{F}_i^R$ and friction $\mathbf{F}_i^D$ forces are still defined by equations (2.19). The coupling of the barostat to the wall-to-wall separation and the coordinates in the perpendicular direction remains unchanged. In the limit of an infinite mass of the barostat $M \to \infty$, the equations of motion using the DPD thermostat to sample the isothermal ensemble are recovered.

The volume undergoes long-range fluctuations in these cases whose frequency is dependent on the mass parameter M. These fluctuations can show undesired long-range correlations which decay very slowly in time. Therefore it can be useful to introduce a random force acting on the friction coefficient η in analogy with the Langevin thermostat. This method is called the Langevin piston method [128, 132]. The Andersen barostat and the Langevin Piston method in combination with the DPD thermostat have been studied in detail by Jacobsen [131].

The equation of motion of the friction coefficient η changes accordingly to

$$\dot{\eta} = \frac{V}{M}\left(P_N(t) - P_{\text{ext}}\right) - \gamma_p \eta + \sigma_p \theta_p \,, \tag{2.67}$$

where σ_p is the strength of the noise and θ_p is a gaussian random variable whose first and second moments are

$$\langle \theta_p(t) \rangle = 0 \tag{2.68}$$

$$\langle \theta_p(t)\theta_p(t') \rangle = \delta(t - t') \,. \tag{2.69}$$

In our implementation a random number generator which provides equally distributed random numbers is used. In order to obtain an isothermal- isobaric probability density equation

$$\sigma_p^2 = 2 k_{\text{B}} T \gamma_p M \tag{2.70}$$

needs to be fulfilled.

In figure 2.4 the volume of the box in a bulk simulation at $T = 1$ with 288 chains of 10 monomers at pressure $p = 0$ is shown. The DPD thermostat was used in all three cases. The Berendson barostat tends to underestimate the volume fluctuations considerably for the chosen value of the coupling strength. Probably it would be possible to improve its performance by tuning the coupling parameter better. The volume and energy showed a gaussian distribution in all cases. For the Berendson barostat the half width of these curves was much smaller than for the other barostats as the fluctuations were underestimated.

2.3 Simulation procedure

All simulations presented in the following chapters are performed under isothermal and isobaric conditions (NpT ensemble). To control temperature the DPD thermostat is used with coupling constant $\gamma = 0.5$ and a cutoff function $w(r_{ij}) = 1 - \frac{r_{ij}}{r_{\text{c}}}$

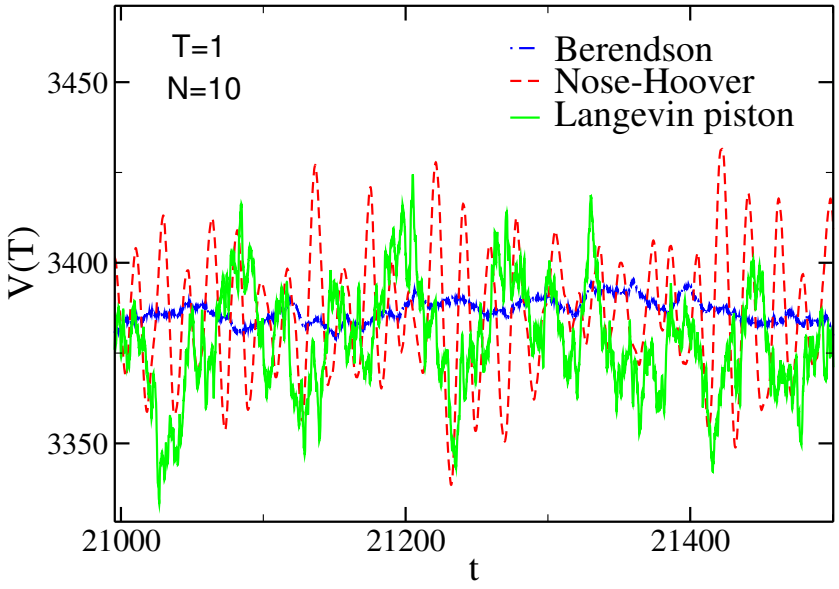

Figure 2.4: The time evolution of the volume of the box for the bulk system at $p = 0$ and $T = 1$ for different barostating methods. The chain length was 10.

employing the same cutoff $r_c = 2.3$ as the LJ-potential (see for further detail [117]). The pressure in the bulk system and the confined films is adjusted using the Andersen barostat [114, 131] described in the last section. No barostat is necessary in the case of the supported and free films.

To perform the simulations the program `md_spherical` developed by Hendrik Meyer was used. The DPD and Nose-Hoover thermostat as well as the Andersen barostat and the Langevin piston method were implemented as described in section 2.2.2. In addition the double bridging algorithm was included to allow a faster equilibration of systems containing longer chains. This will be described in section 2.4.

All simulations are carried out in 3 steps. First the initial configurations have to be set up from which the MD simulations can start. Then an equilibration run needs to be carried out, so that the system reaches its equilibrium properties and results are independent from the method initially chosen to prepare the system. Finally production runs are carried out to gather data which allows the calculation of diverse static and dynamic properties of the system.

Initial configuration. It is advantageous to try to provide a starting configuration that closely resembles an equilibrated, disordered system. This can be achieved using a Monte-Carlo algorithm that will efficiently decorrelate an artificial configuration so as to let it mimic the properties of the system in questions at thermodynamic equilibrium as is best possible. For instance in our simulation program, an algorithm pre-

pares a random-walk-like configuration for each chain, with bond lengths and bond angles distributed according to distributions determined by the potentials constraining them. As we did not impose a bending potential the angles are chosen randomly. Then the chains' centers of mass are moved using a Monte-Carlo method to distribute the monomers as uniformly as possible. In the initial set up of the film configurations we introduce walls at $y = 0$ and $y = B_y$. Reflecting boundary conditions are used at the walls, meaning that chains that would penetrated the wall are folded back into the film. In this way we can create start configuration for films confined between two walls.

Up to this point, the chains are treated as ideal, i. e. no excluded volume is taken into account. The simulation is then started with an intermolecular potential that is multiplied by a factor increasing steadily in time, from 0 to 1, in order to allow the overlaps of different particles to relax. The time scale upon which the intermolecular potential is switched on is important. The faster it is done the larger are the distortions of the chain conformations induced by this procedure. A slow push-off provides less deformed chain conformations and is therefore preferable [133]. The initial velocities are picked up at random from a Maxwell-Boltzmann distribution, corresponding to the desired temperature, as expected in the NVT ensemble.

Set up of films. The different film geometries are prepared in two steps. The initial configurations of the confined films are equilibrated in an NpT simulation at $T = 1$ and $p = 0$. (Note that the profile of the normal pressure must be constant across the film due to mechanical stability [134].) The thermodynamic variable conjugate to P_{N}, the wall-to-wall distance (B_y), thus fluctuates in the simulation, while the area A ($= B_x B_z$) of the simulation box is kept constant and chosen equal for all films studied. Periodic boundary conditions are applied in the parallel xz-directions.

In a second step the equilibrated configuration of the confined film is used to create films with one or two free surfaces. The wall potential at $y = B_y$ and in the latter case also at $y = 0$ is switched off and the resulting films are equilibrated at $T = 1$. It is not necessary to employ a barostat to maintain $p = 0$ because the system has free interfaces.

For the chain length $N = 10$ we prepared supported and free-standing films containing $n = 288$ and $n = 576$ chains (lateral system size of $B_x = B_z = 20.21$). This gives rise to an initial film thickness of $h = 8.4$ and $h = 16.6$ at $T = 1$ for both film geometries. Furthermore, a supported film of $n = 864$ chains was set up with an initial thickness of $h = 24.9$ at $T = 1$. For the chain length $N = 64$ supported and free-standing films were set up containing $n = 48$ and $n = 96$ chains each. The lateral system size was in this case $B_x = B_z = 20.9$ and the initial film thickness at $T = 1$ was found to be $h = 8.2$ and $h = 16.3$.

Equilibration. These initial configurations were cooled to low T in the following way. We first performed cooling runs in which the temperature is continuously

decreased from $T = 1$ to $T = 0.1$ with a finite rate of $\Gamma_T = 2 \times 10^{-5}$ via the cooling schedule $T(t) = 1 - \Gamma_T t$. The configurations obtained on cooling were then used as starting points for isothermal runs. For $N = 10$ they were equilibrated until the monomer mean-square displacement $g_0(t)$ exceeded the mean-square end-to-end distance of a chain, i.e., $g_0(t) > R_e^2$. Subsequent production runs were of a maximum length of 150000 for $T \gtrsim T_c$, where T_c is the characteristic temperature of Mode coupling theory. No isothermal runs were carried out below T_c. For $N = 64$ the double-bridging algorithm which will be introduced in the following section was used to equilibrate the systems. The isothermal runs of maximal length 200000 were not long enough to reach $g_0(t) > R_e^2$. Also in this case no isothermal runs were carried out below T_c. At the high temperature $T = 1$ we also set up films of thickness $h = 4$ and $h = 17$ for chains of length $N = 256$. They were equilibrated at this high temperature by isothermal runs of length 500000 and also by long bridging runs. No isothermal runs below $T = 1$ were carried out.

2.4 Double-bridging algorithm

To thoroughly equilibrate a system in MD simulations, i.e. to erase all memory of the initial configuration, it is necessary to propagate the system as long as its largest relaxation time. This time corresponds to the relaxation of the end-to-end vector of a chain i, $\mathbf{R}_e^i = \mathbf{r}_i^1 - \mathbf{r}_i^N$. As this time grows very fast with increasing chain length it becomes impossible to equilibrate a system of long chains on all length scales in an MD simulation.

In order to achieve a faster equilibration of the systems we implement the double bridging algorithm following [133, 135]. Applying Monte Carlo moves, changing the chain connectivity every $N_{\text{bridge}} = 2$ MD-steps in a way such that the sample remains monodisperse, allows to improve the statistical accuracy for static observables such as the radius of gyration. The applied changes in connectivity are illustrated in figure 2.5. Here a schematic drawing of a chain before and after the bridge move is shown. A move is carried out as will be described in the following paragraph.

At each move a certain fraction of all monomers $N_B = 0.05Nn$ are chosen at random. For a selected monomer i, we determine the number k_{bridge} of possible bridge partners by checking how many of its non-bonded neighbors are within $a_{\text{cut}} = 0.1$ of the equilibrium bond length $b_{\text{eq}} = 0.967$, so that $(r_{i,j} - b_{\text{eq}})^2 < a_{\text{cut}}^2$ and $(r_{l,k} - b_{\text{eq}})^2 < a_{\text{cut}}^2$, where $l = i \pm 1$ and $k = j \pm 1$ refer to the neighbors of particle i and j with which the bonds are cleaved. The move is only suggested if the chain indices of k and j allow to preserve monodispersity

$$\text{mod}(j, N) = \text{mod}(i, N) \pm 1 \quad \text{or} \quad \text{mod}(j, N) = N - \text{mod}(i, N) \pm 1 \tag{2.71}$$

$$\text{mod}(k, N) = \text{mod}(l, N) \pm 1 \quad \text{or} \quad \text{mod}(k, N) = N - \text{mod}(l, N) \pm 1. \tag{2.72}$$

One of these pairs of bridge partners, j and k, is chosen at random.

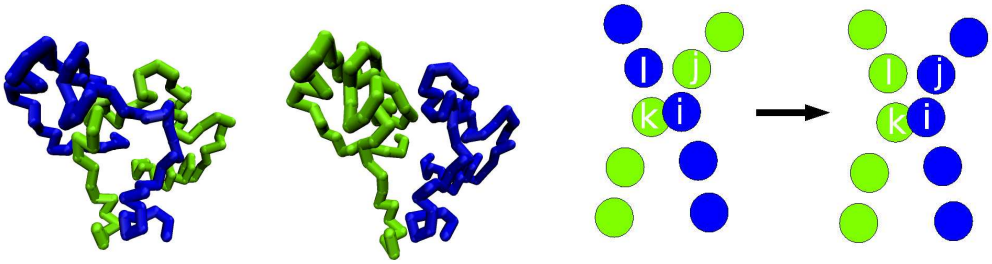

Figure 2.5: UPPER PANEL: Snapshot of a chain before and after a bridge move. LOWER PANEL: Schematic drawing of the chain before and after the bridge move.

The change in energy due to the move is calculated by

$$\Delta E = U_{\mathrm{LJ}}(r_{i,j}) + U_{\mathrm{bond}}(r_{i,l}) + U_{\mathrm{bond}}(r_{j,k}) + U_{\mathrm{LJ}}(r_{i,k}) \\ - U_{\mathrm{LJ}}(r_{i,l}) - U_{\mathrm{bond}}(r_{i,j}) - U_{\mathrm{LJ}}(r_{j,k}) - U_{\mathrm{bond}}(r_{k,l}) \ . \quad (2.73)$$

Here one has to pay attention that the cleaved bonds fulfill as well the criterion $(r_{i,l} - b_{\mathrm{eq}})^2 < a_{\mathrm{cut}}^2$ and $(r_{j,k} - b_{\mathrm{eq}})^2 < a_{\mathrm{cut}}^2$. Otherwise the inverse move is not possible and to maintain detailed balance the move has to be rejected. The number of possible bridge moves for the chosen bridge partner j after the exchange of the bonds k_{return} needs to be determined to fulfill detailed balance. The end monomers and its nearest neighbors are excluded from bridge moves. The probability to carry out a move is then found as

$$P = \min\left(\mathrm{e}^{\frac{\Delta E}{k_{\mathrm{B}}T}} \frac{k_{\mathrm{bridge}}}{k_{\mathrm{return}}}, 1\right) \ . \quad (2.74)$$

We tested this algorithm in the bulk as well as for films with the parameters $N_B = 0.05Nn$, $a_{\mathrm{cut}} = 0.1$ and an attempted double-bridging move every $N_{\mathrm{bridge}} = 2$ MD-steps, as stated above. N_B should not become too large because otherwise a lot of the performed moves are reversed upon the next attempt. A small value of N_{bridge} also increases the number of reversed moves as the configurations do not change significantly between successive series of moves, on the other hand the number of attempted moves per τ increases which in turn also leads to an increase of the accepted moves per τ. a_{cut} should be on the order of the normal bond-fluctuations since a move which suggested an energetically very unfavorable conformation is very unlikely to be accepted.

The amount of successful attempts decreases strongly with temperature as

$$m_{\mathrm{ac}}(T)/\tau = A\,\mathrm{e}^{\frac{-E_{\mathrm{a}}}{k_{\mathrm{B}}T}} \ , \quad (2.75)$$

where $E_{\mathrm{a}} = 2.43$ is independent of the system's geometry, while A is higher in the bulk ($A = 8.8$) than in the film ($A = 6.79$). As the density is the same this

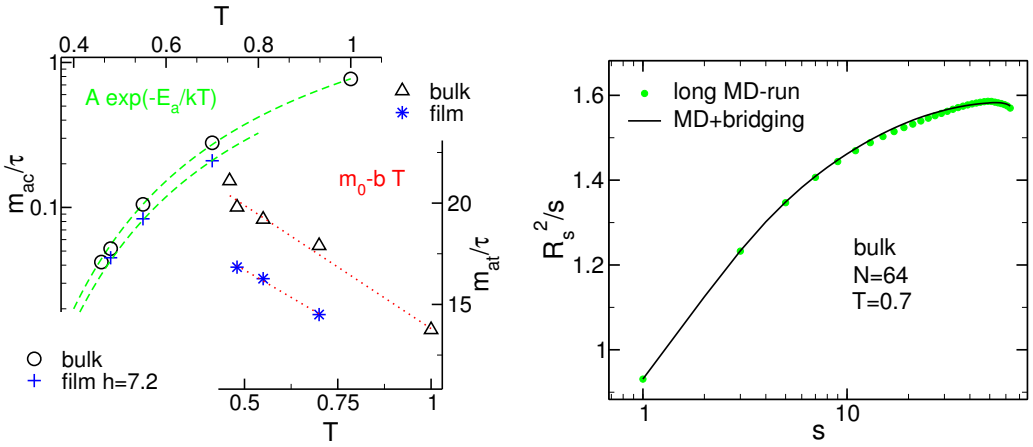

Figure 2.6: LEFT PANEL: The acceptance rate as a function of temperature is shown on the left ordinate. On the right axis the attempt rate as a function of temperature is displayed. The circles and triangles refer to the bulk system of chain length $N = 64$ while the stars and crosses refer to a thin film of thickness $h \sim 7$ of chains of length $N = 64$. Both systems contained $n = 48$ chains. RIGHT PANEL: R_s^2/s as a function of a is shown for a long MD run (circles) and a much shorter run using the bridge algorithm (line) at $T = 0.7$ for chains of length $N = 64$ in the bulk.

might be due to a difference in the number of entanglements in the bulk and the films because the number of attempted bridge moves increases with the number of inter-chain contacts. There is also the possibility of a chain bridging with itself. Indeed we do find an increase in the self bridges for the film in comparison with the bulk, but it is not strong enough to make up for the decrease in inter-chain bridge moves.

The number of attempted moves increases with decreasing temperature as the density gets higher

$$m_{\rm at}(T)/\tau = m_0 - bT \;, \tag{2.76}$$

where $m_0 = 26.6$ and $b = 12.97$ for the bulk. The values in the film are again by a factor of 1.3 lower. Fits of the above equations to the simulation results for a bulk system and a film are shown in figure 2.6.

In order to test that the algorithm works correctly and allows to sample the chain conformations efficiently we look at the intra-chain distance function of a chain R_s^2/s. We thus consider a set of n chains of N monomers each, whose positions are denoted by

$$\mathbf{r}_i^a \;, \quad (a = 1, \ldots, N; \quad i = 1, \ldots, n) \tag{2.77}$$

meaning that the different chains are indexed by i, j, ... and the monomers by a, b, ... R_s^2/s which describes the mean-square distance of two monomers which have $s - 1$ monomers in-between them is defined as

$$R_s^2/s = \langle \mathbf{R}_s^2 \rangle / s = \frac{1}{s}\frac{1}{n}\sum_{i=1}^{n} \frac{1}{N-s} \sum_{a=1}^{N-s} \left\langle |\mathbf{r}_i^a - \mathbf{r}_i^{a+s}|^2 \right\rangle \;. \tag{2.78}$$

For long chains it is found that $R_{\mathrm{s}}^2/s = C_\infty b_{\mathrm{eq}}^2$, where C_∞ is Flory's characteristic ratio [51].

For chains of $N = 64$ it takes 150000τ to fully equilibrate the system at $T = 0.7$. Using the bridge algorithm the system is considered as equilibrated after each monomer has bridged at least once. So the average time for equilibration is found to be $Nn/m_{\mathrm{ac}}\ \tau \sim 15000\tau$ as $m_{\mathrm{ac}} = 0.27$ and $nN = 3072$ for a bulk system of $n = 48$ chains of length $N = 64$ at $T = 0.7$. This is much faster than for a normal MD simulation. As can be seen in figure 2.6 the results obtained for the mean-square distance of monomers as a function of their distance along the chain are the same. Unfortunately the performance of the algorithm decreases considerably due to the very low acceptance rates at lower temperatures. Therefore the double bridging scheme, at least in its present implementation, is not of much help for the equilibration of the system close to T_{c}.

Chapter 3

Static structure

Experiments find a decrease of the glass transition temperature (T_{g}) for thin supported polymer films of thickness below $h < 100\mathrm{nm}$ if the interactions between polymer and substrate are weak. The magnitude of the decrease with decreasing thickness depends on the specific polymer. For polystyrene reductions as large as $40\mathrm{K}$ were found for films of thickness $h \simeq 15\mathrm{nm}$ (see e. g. for reviews [31, 69]). Experimentally T_{g} is often determined using ellipsometry which allows to monitor the changes of film thickness with decreasing temperature as the sample is cooled. Because this is a non-equilibrium procedure the results are found to be dependent on the cooling rate. We will also measure T_{g} by determining the film thickness on cooling in section 3.1.

The decrease of T_{g} found in thin polymer films with a free surface was linked to a higher mobility of the monomers in the vicinity of the free interface in experiments [5, 9, 10] and computer simulations [12, 16, 21, 38]. In the framework of mode coupling theory (MCT) the local density correlations have a large influence on the dynamics of the system. Small changes in the structure can in the vicinity of T_{c}, the characteristic temperature of MCT, entail large differences in the dynamics [67, 136]. We study therefore the local packing of the monomers by looking at the total structure factor as a function of the distance from the surface and compare the results to the structure found in the bulk in section 3.2. A similar simulation study by Fathollah Varnik concerned with films confined between smooth repulsive walls found that the encountered T_{c} reductions could be linked to a suppression of the first maximum of the static structure factor, indicating smaller local packing constraints [32, 35].

Additionally in ultra-thin polymer films the thickness of the film can become comparable or even smaller than the equilibrium size of the polymer coil. Therefore perturbations of the chain conformations are expected in thin films. We asses the structure of the chains and its dependence on confinement by looking at the intra-chain structure factor and the layer-resolved R_{g} and R_{e} in section 3.3.

3.1 Glass transition temperature

We begin our analysis by a discussion of the glass transition temperature T_{g} in our thin model polymer films. To determine T_{g} we monitor the film thickness h on cooling, and identify T_{g} with the temperature where the slope of h changes. Such a "pseudothermodynamic" approach [31] is commonly employed in experiments.

3.1.1 Definition of the film thickness

The density profile can be determined numerically

$$\rho(y) = \frac{1}{A} \left\langle \sum_{i=1}^{nN} \delta\left(y - y_i\right) \right\rangle \ , \tag{3.1}$$

where A is the area of the simulation box.

The film thickness can be derived from the monomer density profile defined by equation 3.1 via the method of the Gibbs dividing surface (GDS) [123]. First, the mean density of the film $\bar{\rho}$ is calculated by averaging $\rho(y)$ over an interval of width $\Delta y = 3\sigma$ in the center y_{c} of the film

$$\bar{\rho} = \frac{1}{\Delta y} \int_{y_{\mathrm{c}}-\Delta y/2}^{y_{\mathrm{c}}+\Delta y/2} \mathrm{d}y \ \rho(y) \ . \tag{3.2}$$

The position of the left (y_{-}^{G}) and the right (y_{+}^{G}) GDS is found by

$$y_{\pm}^{\mathrm{G}} = y_{\mathrm{c}} + \frac{1}{\bar{\rho}} \int_{y_{\mathrm{c}}}^{\pm\infty} \mathrm{d}y \ \rho(y) \ , \tag{3.3}$$

from which we obtain h as $h = y_{+}^{\mathrm{G}} - y_{-}^{\mathrm{G}}$. The result weakly depends on the choice for Δy, especially for thin supported films at low T where density oscillations propagate far into the core of the system (cf. figure 3.1).

Figure 3.1 shows equilibrated density profiles of a supported and a free-standing film at $T = 1$ and $T = 0.44$. The vertical dashed lines indicate the position of the GDSs at $T = 1$. At this temperature the GDSs coincide for both films and the average density $\bar{\rho}$ in the middle of the film is very close to the bulk density ρ_{bulk} at the same p and T. Because the density increases on cooling, h decreases. This decrease is probably too strong in our simulations, since the system can only adapt the volume in one direction (the y-direction; we keep A fixed). Figure 3.1 also shows that the density profile is qualitatively different at the free and supported surfaces. Close to the wall, $\rho(y)$ displays density oscillations which are typical of liquids in contact with an impenetrable smooth substrate (see e.g. [32]), while at the free surface the density smoothly goes to zero. On cooling the oscillations become more pronounced and the width of the vacuum-polymer interface decreases. Nevertheless, even at $T = 0.44$ the difference in h between the two film geometries remains small (cf. table A.1).

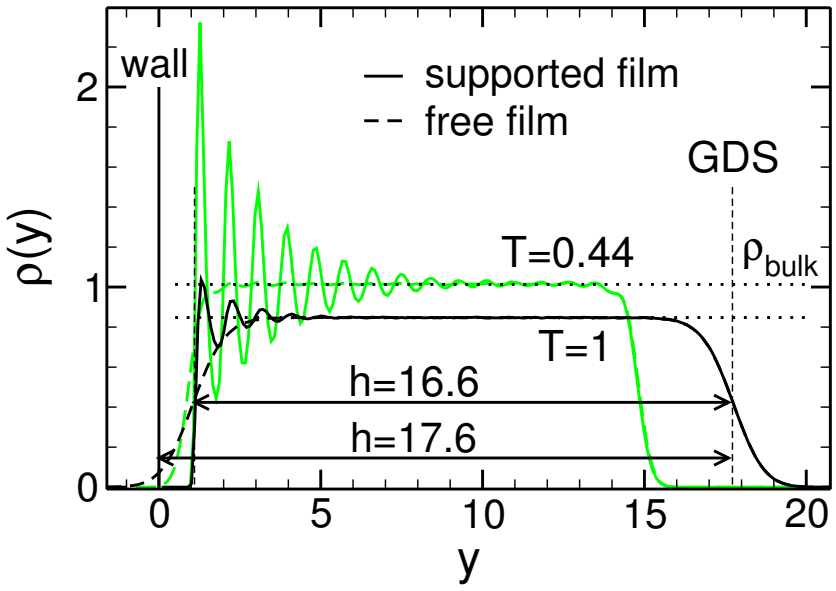

Figure 3.1: Density profiles $\rho(y)$ for a supported film (full lines) and a free-standing film (dashed lines) at $T = 1$ and $T = 0.44$. Both systems contain $n = 576$ chains. The solid vertical line, labeled "wall", shows the position of the wall in the simulation of the supported film. The vertical dashed lines indicate the positions of the GDSs. Since the left GDS y_-^{G} of the supported film is at a distance of about 1 from the wall, the definition $h = y_+^{\mathrm{G}} - y_-^{\mathrm{G}}$ results in a lower value for h than the definition $h = y_+^{\mathrm{G}}-$ (wall position), e.g. $h = 16.6$ instead of $h = 17.6$ at $T = 1$. We always use the former definition $h = y_+^{\mathrm{G}} - y_-^{\mathrm{G}}$ in the following. The horizontal dotted lines correspond to the average bulk density at $T = 1$ and $T = 0.44$ ($\rho_{\mathrm{bulk}}(T = 1) = 0.85$ and $\rho_{\mathrm{bulk}}(T = 0.44) = 1.013$).

3.1.2 Thickness dependence of T_{g}

A common approach to determine T_{g} is to monitor $h(T)$ as the film is continuously cooled with a constant rate Γ_T. Since this is not an equilibrium procedure, the result will depend on Γ_T. Figure 3.2 provides an example. It depicts the temperature dependence of h, of the thermal expansion coefficient

$$\alpha_p = \frac{1}{h}\frac{\partial h}{\partial T} \,, \tag{3.4}$$

and of its derivative $\alpha_p' = \partial\alpha_p/\partial T$, obtained from cooling runs with $\Gamma_T = 2 \times 10^{-5}$. The liquid and the glassy states have different thermal expansion coefficients which are constant over a wide temperature range. $h(T)$ gradually changes slope upon crossing T_{g}. Following previous experimental and computational studies we first determine T_{g} as the intersection point of linear extrapolations from the liquid and glass sides. As has been pointed out before (see e.g. [17]), the result of this procedure depends on the interval chosen for the fit. We only used a relatively small T interval

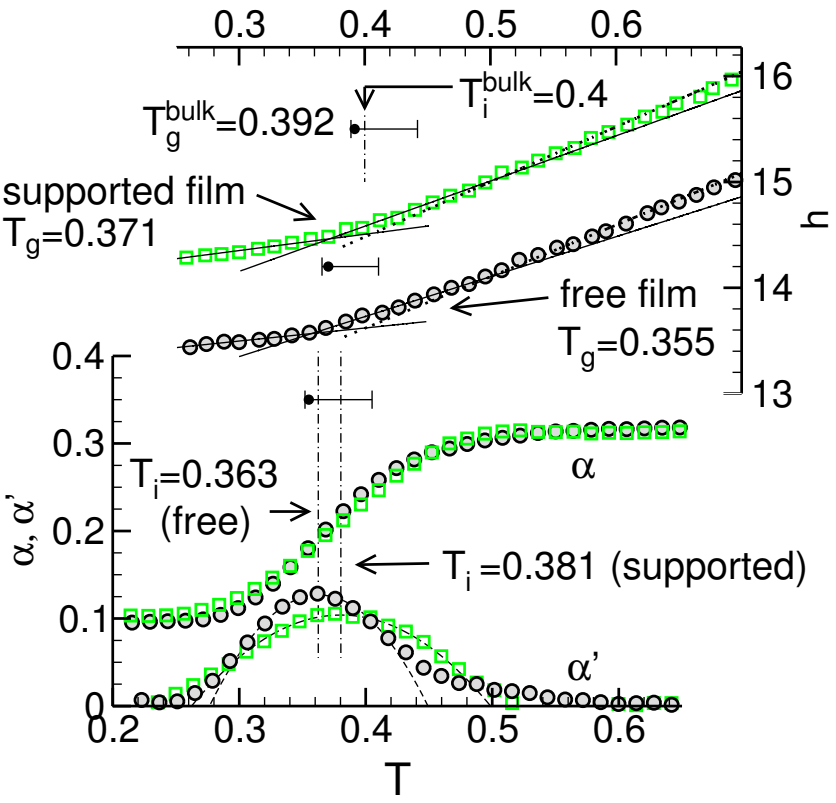

Figure 3.2: Results from continuous cooling runs with rate $\Gamma_T = 2 \times 10^{-5}$ for a supported (squares) and a free-standing film (circles) of $h \simeq 15$. The figure shows the film thickness $h(T)$ (RIGHT ORDINATE), the thermal expansion coefficient $\alpha(T)$ and its first derivative $\alpha'(T) = \partial\alpha/\partial T$ (LEFT ORDINATE). The thickness of the supported film is shifted upward by 1 and α' was divided by 10 for clarity. The solid lines represent tangents fitted to the low-T and high-T branches of $h(T)$ in order to determine T_g via the intersection of these lines. For the high-T branch, only temperatures close to the transition to the glassy phase were used in the fit. The resulting T_g values (cf. table A.1) are indicated by filled circles. If the tangent in the liquid phase was fitted to the whole high-T branch shown in the figure (dotted line), a larger value for T_g would be obtained (intersection of the dotted line with the solid line for low T). We indicate this uncertainty due to the choice of the fit interval at high T by a horizontal error bar associated with the filled circles. The dashed lines show parabola fits to α' in order to determine its maximum. This maximum occurs at T_i (vertical dash-dotted lines: $T_\mathrm{i} = 0.363$ free-standing film, $T_\mathrm{i} = 0.381$ supported film; cf. table A.1). For the bulk, T_g, its systematic error due to choice of the high-T fit interval, and T_i are also indicated for comparison.

above T_g, since in experimental studies the range of temperatures explored above T_g is much smaller than in our simulations. This analysis results in a systematically lower value of T_g than had we used the whole T range available. The systematic error due to this arbitrary choice is rather large. However, this error does not affect the

qualitative dependence of $T_{\rm g}(h)$ on h so long as the same interval at high-T is chosen for all films and the bulk.

As a less ambiguous definition of $T_{\rm g}$ which does not hinge on hidden fit parameters, such as the T interval, we suggest to identify $T_{\rm g}$ with the inflection point $T_{\rm i}$ of α_p, i.e., with the maximum of α_p'. We determine this maximum by fitting a parabola to $\alpha_p' \propto -(T - T_{\rm i})^2$ for T near $T_{\rm i}$. This procedure requires the calculation of the second derivative $d^2 \ln(h)/dT^2$ which is only possible after considerable smoothing of the data for both h and α_p. We carried out running averages over T intervals as large as $\Delta T = 0.08$. Nevertheless we did not find a systematic dependence of $T_{\rm i}$ on ΔT. The results for $T_{\rm i}$ are higher than those for $T_{\rm g}$ but within the error bars of the systematic error.

Qualitatively, $T_{\rm g}$ and $T_{\rm i}$ show the same trends (cf. table A.1). The glass transition is depressed with respect to the bulk. The thinner the films, the lower $T_{\rm g}$ or $T_{\rm i}$. Moreover, we find the depression of $T_{\rm g}$ to be larger for free-standing films than for supported films of the same thickness.

3.1.3 Chain length dependence of $T_{\rm g}$

As most experiments are done with polymers of much higher molecular weight than the chains we used in our simulation, it is interesting to see how the found results depend on chain length although, of course, the window of N we can cover is much smaller than in experiments. Chains of $N = 64$, are too short to show the dynamic signatures of long chains such as reptation - the entanglement length for this model was estimated to be $N = 32$,- but their characteristic size is already considerably larger than for $N = 10$ ($R_{\rm e}(N = 10) \simeq 3.5$ versus $R_{\rm e}(N = 64) \simeq 10$). Therefore the chain configurations are influenced more strongly by the confinement. To see whether this has an effect on the thermodynamic properties of the film we compare the results for $T_{\rm g}$ and $T_{\rm i}$ in the last sections to the ones found for $N = 64$.

In figure 3.3 the volume per monomer $V(T)/nN$ is shown as a function of temperature for bulk systems of chains of $N = 10$ and $N = 64$ monomers. The longer chains have a higher density and thus a lower volume per monomer. The thermal expansion coefficient α_p, defined in equation (3.4), in the liquid state is smaller, while the one in the glassy state seems to be rather independent of chain length. We find an increase of $T_{\rm g}$ and $T_{\rm i}$ with increasing chain length. This increase of $T_{\rm g}$ towards an asymptotic limit with chain length has also been observed experimentally [137, 138].

Figure 3.3 also displays the volume per monomer $V(T)/nN = h(T)A/nN$ found in free standing films of different thickness for both chain lengths. As for $N = 10$ we find a decrease of $T_{\rm g}$ and $T_{\rm i}$ with decreasing film thickness for the free-standing films of $N = 64$. The decrease is more pronounced in comparison with the shorter chains, so that free standing films of thickness $h \simeq 7$ have the same $T_{\rm g}$ within the error bars for both chain length. As for the bulk systems the thermal expansion coefficient in the liquid state is smaller for the longer chains while the one in the glassy state

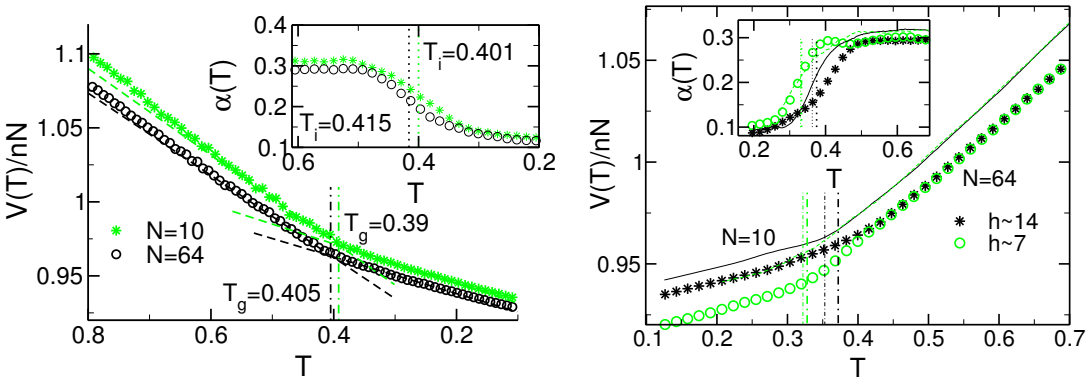

Figure 3.3: LEFT PANEL: The Volume per particle is shown as a function of temperature for a cooling rate of $\Gamma_T = 2 \times 10^{-5}$ for $N = 10$ (stars) and $N = 64$ (circles) for a bulk system at $p = 0$. The vertical lines indicate the values of $T_{\rm g}$ extracted from the data. In the inset the thermal expansion coefficient for $N = 64$ (circles) is compared to the one for $N = 10$ (stars). The vertical lines indicated the values of $T_{\rm i}$ extracted from the data. RIGHT PANEL: The volume per particle is shown as a function of temperature for a cooling rate of $\Gamma_T = 2 \times 10^{-5}$ for $N = 10$ (thin lines) and $N = 64$ (symbols) for free standing films of $h \simeq 7$ (grey symbols and lines) and $h \simeq 14$ (black symbols and lines). The vertical lines indicate the values of $T_{\rm g}$ extracted from the data. In the inset the thermal expansion coefficient is plotted. The symbols and lines are attributed as for the main plot. The vertical lines indicated the values of $T_{\rm i}$ extracted from the data.

is approximately equal to the one found for $N = 10$. The thicker film of chains $N = 64$ shows a larger broadening of the transition region than the thinner film or the films containing chains of $N = 10$. In the bulk system we did not see a significant broadening of the transition with increasing chain length. A summary of the different $T_{\rm g}$ values etc. can be found in table A.2.

3.1.4 Cooling rate dependence of $T_{\rm g}$

The transition from the liquid to the amorphous solid state can be described as the falling out of equilibrium of the system, because the relaxation times of the system exceed the time scale of the experiment. Thus the resulting glass is not in thermal equilibrium and it can therefore be expected that the properties of the glass will depend on the production history of the system, as, e. g., the cooling rate with which the sample was cooled. This has been observed in various experiments probing the density of the glass and $T_{\rm g}$ as a function of the cooling rate (see e. g. [139]) as well as in computer simulations [140, 141]. $T_{\rm g}$ is usually found to decrease with decreasing cooling rate. Experimentally this dependence is found to be logarithmic in the cooling rate. Therefore a large window of cooling rates has to be sampled to evidence this phenomenon.

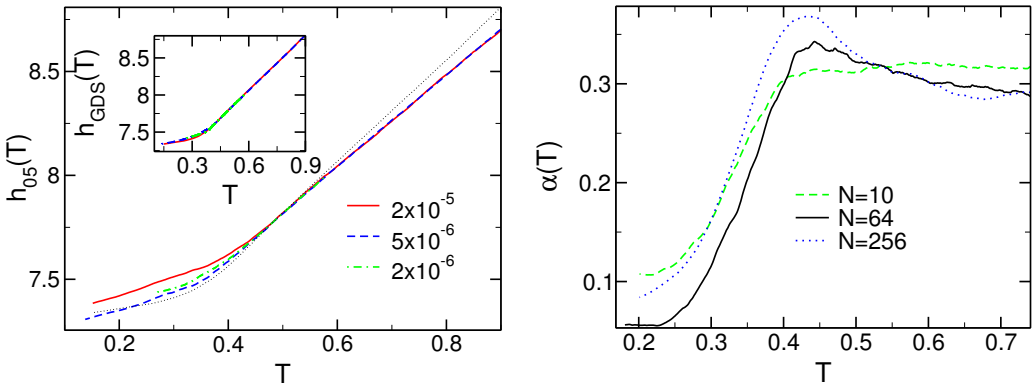

Figure 3.4: LEFT PANEL: The position of the surface as a function of the temperature is shown for 3 different cooling rates $\Gamma_T = 2\times10^{-6}$ (dash-dotted line), $\Gamma_T = 5\times10^{-6}$ (dashed line) and $\Gamma_T = 2\times10^{-5}$ (full line). The method used to determine the position of the interface was the criterion $\rho(y = h_{05}) = 0.5$ as described in the text. Also indicated is the result for the position of the interface using the method of the GDS (thin dotted line) described in section 3.1.1 ($\Gamma_T = 2\times10^{-5}$). INSET: The inset shows the position of the surface according to the GDS method as a function of temperature for 3 different cooling rates $\Gamma_T = 2\times10^{-6}$ (dash-dotted line), $\Gamma_T = 5\times10^{-6}$ (dashed line) and $\Gamma_T = 2\times10^{-5}$ (full line). The chain length was $N = 64$ in all cases. RIGHT PANEL: The thermal expansion coefficient for a cooling rate of $\Gamma_T = 2\times10^{-5}$ is shown for chains of length $N = 256$ and film thickness $h \simeq 5$ (dotted line), $N = 64$ (full line) and $N = 10$ (dashed line). The thermal expansion coefficient was calculated from the results of the film thickness obtained from the method of the GDS.

We did not find a pronounced dependence on the cooling rate for the system investigated which should not be expected as we only varied the cooling rate by a factor of 10. The most significant change we encountered for a rather thin supported film of chains of length $N = 64$. This dependence might be due to the inaccuracy of the determination of the film thickness as it becomes more and more difficult to unambiguously determine the overall density of the film because of very pronounced layering effects which propagate through the whole film (see section 3.1.1). As the density profile in the simulation is not a step profile there is always a certain ambiguity where to place the interface exactly. Therefore the method of choice can change the values one obtains for the thickness systematically. This error is on the order of the interfacial width $\Delta \simeq 1$. It will have a larger influence on the overall h of the film, the thinner the film is, so that the relative error increases with decreasing film thickness. For our thinnest films the thickness $h \simeq 7$ and the error is $\Delta/h \simeq 15\%$.

Therefore we employed two different approaches for determining the thickness of the films. The first one was based on the method of the GDS as described in section 3.1.1 while the other was a much simpler approach for which it was not necessary to know the momentary overall density. We simply chose the interface to be at the point where the density reached the value $\rho(y = h_{05}) = 0.5$. This choice of course

is rather arbitrary and changes the curves one obtains for the dependence of the film thickness on temperature considerably. This can be seen in the left panel of figure 3.4 (compare the thin line (GDS method) and the thick lines). While one does not detect a cooling rate dependence using the method of the Gibbs dividing surface, a clear trend can be seen using the simpler approach. This means that the average density and the film thickness depend on the cooling rate. These two effects seem to counteract when determining the film thickness with the GDS method resulting in almost no dependence on the cooling rate.

In figure 3.4 the thermal expansion coefficient is also shown. No matter how one determines the film thickness one always finds an increase of the thermal expansion coefficient with decreasing temperature before the system undergoes the glass transition. This overshoot increases with increasing chain length. It is not yet present for the short chains $N = 10$. For thicker films and free-standing films we did not encounter this phenomenon. Probably it is related to layering effects at the wall. This makes it difficult to determine the glass transition temperature in very thin supported films. Therefore we do not report a value of T_g for the thinnest supported film at chain length $N = 64$.

3.2 Static structure factors

Since we are interested in the glass transition in these thin films which is a local phenomenon, an analysis of the structure of the melt on this length scale might give important insight into the reasons for the found T_g reductions. Although T_g was determined by a non-equilibrium procedure, the equilibrium structure of the liquid slightly above T_g could still provide some understanding of the observed changes in T_g in thin films. In this section, we will therefore be mainly concerned with equilibrium properties. For our simulations this limits the temperature regime to $T > T_\mathrm{c}(h)$, $T_\mathrm{c}(h)$ being the critical temperature of mode-coupling theory (MCT) [67] for a film of thickness h. A detailed discussion how $T_\mathrm{c}(h)$ is determined will be given in section 4.2.

Density fluctuations for the wave vector $\mathbf{q}$ can be measured by static structure factors [123]. For a polymeric liquid it is natural to distinguish between the structure factor of a chain and of the melt. To introduce these quantities we consider a system containing n monodisperse chains of length N in a volume V. The chain density ρ_cm and the monomer density ρ are then given by

$$\rho_\mathrm{cm} = \frac{n}{V}, \quad \rho = \frac{nN}{V}. \tag{3.5}$$

We write the static structure factor of the melt $S(q)$ as a sum of an intrachain and an interchain part:

$$S(q) = w(q) + \rho h(q) \qquad (q = |\mathbf{q}|)\ . \tag{3.6}$$

The intrachain part is given by

$$w(q) = \frac{1}{nN}\Big\langle \sum_{i=1}^{n}\sum_{a,b=1}^{N} \exp\big[-\mathrm{i}\mathbf{q}\cdot(\mathbf{r}_i^a - \mathbf{r}_i^b)\big]\Big\rangle\,, \tag{3.7}$$

and the interchain part by

$$\rho h(q) = \frac{1}{nN}\Big\langle \sum_{i\neq j}^{n}\sum_{a,b=1}^{N} \exp\big[-\mathrm{i}\mathbf{q}\cdot(\mathbf{r}_i^a - \mathbf{r}_j^b)\big]\Big\rangle\,. \tag{3.8}$$

In these equations $\mathbf{r}_i^a$ is the position of the ath monomer in the ith chain. $h(q)$ is the Fourier transform of the intermolecular pair-correlation function [123].

3.2.1 Bulk

We begin our discussion with the bulk system at $p = 0$ which will serve as an important reference point for the analysis of the statics in the films. Figure 3.5 compares $S(q)$ and $w(q)$ for the BS model at $p = 0$ to the results for the BE model at $p = 1$ (see section 2.1 for details on the different models). The temperature interval extends from the "normal" liquid state of the melt to temperatures in the supercooled state slightly above the critical temperature T_c of mode-coupling theory in both systems. The results of both models agree very well with each other if one shifts the temperature axes to make up for the difference in T_c. The critical temperature $T_\mathrm{c} \simeq 0.45$, deduced from an extensive analysis of the dynamics of the BE model (see e.g. [32] for a review) is about $\Delta T \simeq 0.045$ higher than T_c for our model which was determined as $T_\mathrm{c} \simeq 0.405$ (see section 4.2). The fingerprint of this difference in T_c reappears in the static structure of the melt: $S(q)$ at $T = 0.46$ for the BE model overlaps almost completely with the $S(q)$ at $T = 0.42$ for the BS model.

We observe that $w(q)$ of the BS and BE models agree quantitatively with one another. Apparently, the different bond potentials do not affect the intrachain structure factor. Furthermore, the dependence of $w(q)$ on T is negligible. This demonstrates that the chains preserve a random-coil-like conformation upon cooling. There is no discernable trend of incipient crystallization. The same applies to the collective structure factor. $S(q)$ exhibits features characteristic of a dense disordered system. The structure factor is small at low q, reflecting the small compressibility of the melt. Then, it increases with increasing q toward a maximum, the 'amorphous halo', before it converges to 1 in an oscillatory manner as $q \to \infty$. As $w(q)$ is (almost) independent of T, modifications of $S(q)$ with decreasing T must be caused by changes in the intermolecular packing. The fact that the position q^* of the amorphous halo and its amplitude $S(q^*)$ grow on cooling indicates that the packing of the monomers on a local scale becomes tighter as a consequence of the increase of density with decreasing T.

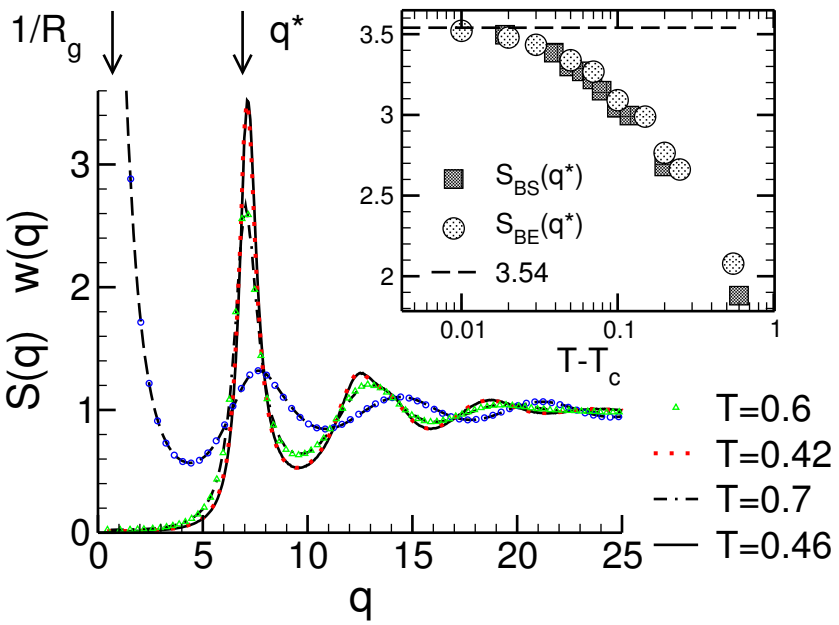

Figure 3.5: MAIN FIGURE: Static structure factor $S(q)$ of the melt (equation (3.6)) and intrachain structure factor $w(q)$ (equation (3.7)) versus the modulus of the wave vector $\mathbf{q}$ for the BE model ($T = 0.7$ and $T = 0.46$; $p = 1$; $N = 10$) and the BS model ($T = 0.6$ and $T = 0.42$; $p = 0$; $N = 10$). Since $w(q)$ is (almost) independent of T, it is depicted only for $T = T_c + 0.01$ (BE model: dashed line, BS model: circles). The arrows indicate the q-value corresponding to the radius of gyration ($R_g \simeq 1.45$) and the position of the amorphous halo, q^*, at $T = 1$. q^* slightly increases on cooling: $q^*(T = 1) \simeq 6.9$ and $q^*(T = 0.46) \simeq 7.15$. INSET: Amplitude of the amorphous halo $S(q^*)$ versus $T - T_c$ (BE model: $T_c(p = 1) = 0.45$; BS model: $T_c(p = 0)$=0.405). The dashed horizontal line at 3.54 indicates the Hansen-Verlet freezing criterion for the glass transition of hard spheres [142]. ($S(q^*)$ and q^* are expected to increase slightly with chain length N; see e.g. [143]).

Following reference [144] we may interpret this observation in terms of an empirical freezing criterion, the Hansen-Verlet criterion [145]. According to this criterion a liquid solidifies as soon as $S(q^*)$ surmounts a critical value. For crystallization this threshold is $S(q^*) \approx 2.85$. For the glass transition of hard sphere mixtures described within the framework of ideal MCT [67] the Hansen-Verlet criterion was suggested to be $S(q^*) \simeq 3.54$ [142].

We can compare this prediction with our results. The inset of figure 3.5 demonstrates for the BS and BE models that $S(q^*)$ approaches 3.54 on cooling toward T_c. The close agreement between the hard-sphere system and the present simulation results suggests that the modification of the local structure in the melt—and the attendant slowing down of the dynamics—is mainly driven by packing constraints resulting from the repulsive interactions between the monomers.

In this respect, our polymer melt behaves similarly to a soft-sphere system. For

such a system it is known that the only relevant parameter needed to fully specify its thermodynamic state is $\Gamma = \rho_{\mathrm{m}}(T_{\mathrm{c}})T^{-1/4}$ if the repulsive interaction scales as $\sim r^{-12}$ [123]. For the BE model we determined $\Gamma_{\mathrm{c}} = \rho_{\mathrm{c}}{T_{\mathrm{c}}}^{-1/4} = \rho_{\mathrm{m}}(T_{\mathrm{c}}){T_{\mathrm{c}}}^{-1/4}$ for different pressures ($p = 0.5, 1, 2$) [146] and found that Γ_{c} is constant to a good approximation ($\Gamma_{\mathrm{c}} = 1.27 \pm 0.02$). Here, we confirm this finding also for the BS model. We obtain $\Gamma_{\mathrm{c}} \simeq 1.28$ for $T_{\mathrm{c}} \simeq 0.405$ and $\rho_{\mathrm{c}} \simeq 1.024$ at $p = 0$. The observation that Γ_{c} is a pertinent parameter was also made in simulations of other glass-forming systems [147, 148] and in experiments [149].

3.2.2 Films

Since the results for the bulk suggest in accordance with MCT that the glass transition is driven by packing constraints of the monomers and short range order which is reflected in the amplitude of the structure factor's amorphous halo we also try to apply the Hansen-Verlet criterion $S(q^*) = 3.54$ to find an estimate of the transition temperature for supported and free films.

We look at $S(q)$ averaged over the whole film as well as in layers close to the surface. For thin films the structure factor is determined within planes parallel to the surface as

$$S(q, y) = \frac{1}{n_l} \left\langle \sum_{i,j}^{nN} \mathrm{e}^{-\mathrm{i}\mathbf{q}\cdot(\mathbf{s}_i - \mathbf{s}_j)} \, \delta\left(y - y_i\right) \delta\left(y - y_j\right) \right\rangle , \tag{3.9}$$

where n_l is the total number of monomers in the slab for which $S(q)$ is calculated. The typical width of the slab is $\Delta y = 2$.

Figure 3.6 shows that $S(q)$ depends on the distance from the interface and thus on the film thickness. The first peak of $S(q)$ is lower for the structure factors averaged over the whole films than the bulk value. In the middle of the films the behavior is bulk-like while at the surfaces the first peak is shifted to lower q and $S(q^*)$ is considerably smaller. As has been pointed out [35] this resembles the behavior of the bulk at higher temperature. Since the influence of the surfaces is felt more strongly in thinner films, their averaged structure factors exhibit a weaker first maximum than the thicker films irrespective of film geometry. The compressibility of the films reflected by the low-q behavior of the structure factor is larger at the supported surface than the bulk value. The presence of capillary waves at the free surfaces causes the structure factor to increase at small q as $S(q) \propto q^{-2}$ as predicted by Jäckle [150]. The capillary waves at the free surface and their influence on the structure and relaxation of the films will be discussed in chapter 5

The suppression of the first peak is comparable at $T = 0.44$ for the supported surface and the free surface as can be seen in figure 3.6. Both layers were not chosen to be of the same thickness but to contain the same number of monomers. As a consequence the height of the first peak of the structure factor averaged over the

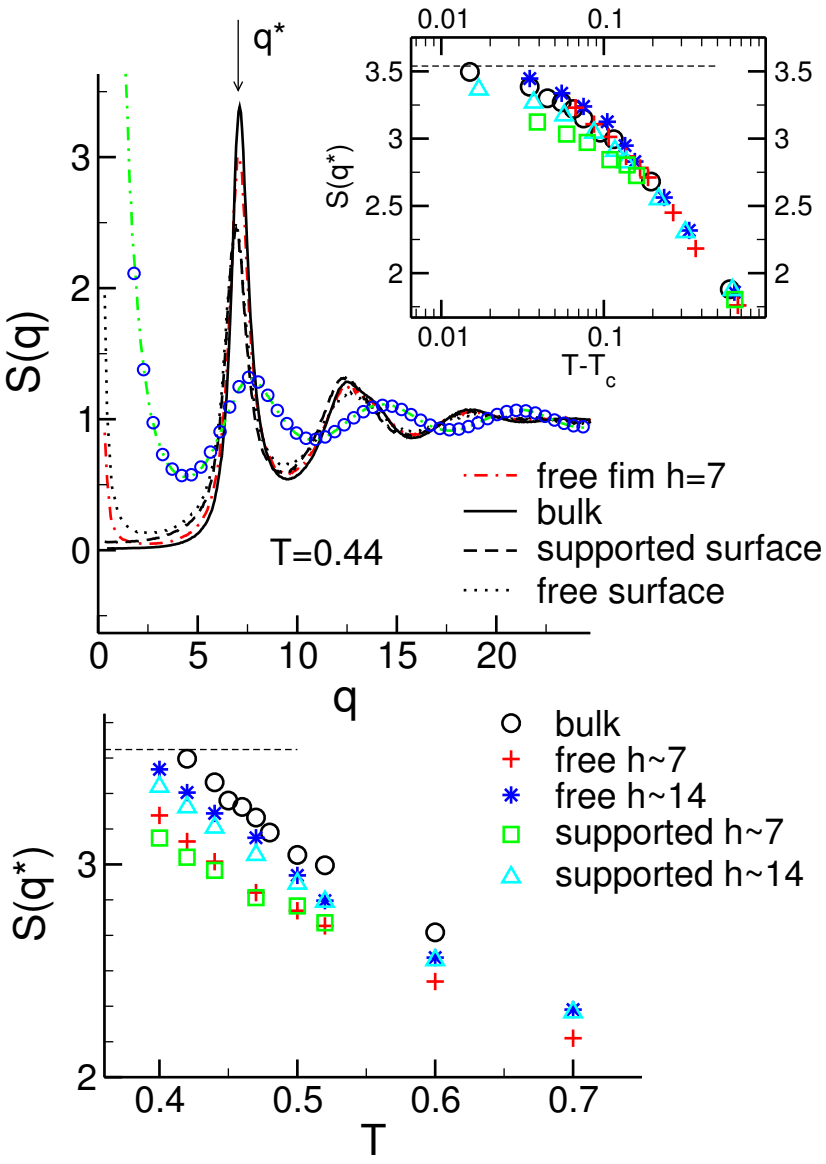

Figure 3.6: MAIN FIGURE: Two dimensional structure factor averaged over a free film with $h = 7$ (dash-dotted line) at $T = 0.44$ for chains of $N = 10$ monomers at $p = 0$. The structure factor in the middle of the films (full line) at the supported surface (dashed line) and at the free surface (dotted line) given by equation (3.9). All bins contained $n = 300$ monomers. The chain length was $N = 10$. INSET: Amplitude of the amorphous halo $S(q^*)$ versus the $T_c(h)$ for the bulk (circles) and supported films with $h \simeq 7$ (rectangles) and $h \simeq 14$ (triangles) and free standing films (crosses: $h \simeq 7$ and stars: $h \simeq 14$). The dashed horizontal line at 3.54 indicates the Hansen-Verlet freezing criterion for the glass transition of hard spheres [142]. LOWER PANEL:The lower panel shows the same plot as a function of T.

whole film is not strongly dependent on the film geometry but only on film thickness. At even lower temperatures the suppression of the amplitude of the amorphous halo is larger for the supported films than for the free standing films of similar thickness.

Varnik et al [32, 151] found in the vicinity of purely repulsive walls the first peak of the structure factor and thus the local order in the packing of the monomers to be less pronounced. They linked this decrease in constraints of the monomers to the faster relaxation of the monomers they found in their system. In the film the cage cannot tighten as quickly as in bulk which leads to an acceleration of the dynamics. This could in turn be an explanation for the found T_{g} reductions. We also see a decrease in $S(q^*)$ with decreasing film thickness.

The amplitudes of $S(q^*)$ for the different films and the bulk do not superimpose upon shifting the temperature axis by $T = T_{\mathrm{c}}(h)$ (How T_{c} is determined will be described in section 4.2 in chapter 4.). It would be possible to obtain good agreement of $S(q^*)$ by shifting the temperature axis by T^*. The temperature decreases with decreasing h is in qualitative agreement with the results found for T_{c} (see section 4.2) and T_{g} (section 3.1), but the suppression of T^* is larger for supported films than for free standing films in contrast to the analysis of T_{g} and T_{c}. The Hansen-Verlet criterion which worked well for the bulk cannot be applied to the films successfully. We thus conclude that the packing of the monomers as measured by the amplitude of the amorphous halo cannot alone account for the reduction of T_{g} and T_{c} found in our systems.

Longer chain length $N = 64$. So far the discussion was concerned with chains of length $N = 10$. The dependence of the total structure factor $S(q)$ and the intra-chain structure factor $w(q)$ on chain length is explored in figure 3.7. The dependence of the total structure factor on chain length is rather weak. The local packing of the monomers is not strongly effected by N. We observe the same trends as for the shorter chains. The first peak of the structure factor is lower in the films than in the bulk and the properties of the free surface are reflected in the divergence of $S(q)$ for small q. As the surface tension is slightly higher for the longer chains this effect is a bit weaker for the longer chains. A more detailed discussion of the influence of capillary waves at the free surface on the relaxation in the films is given in chapter 5.

The intra-chain structure changes as the chain-length is increased. But the chain-structure at $N = 64$ is not strongly effected by confinement on the local scale as $w(q)$ for bulk and film of the same chain length agree well as can be seen in figure 3.7. The influence of the confinement on the chain conformation for $N = 64$ on larger scales can be explored in more detailed by an analysis of the end-to-end distance, the radius of gyration and more generally of the gyration tensor performed in the next section.

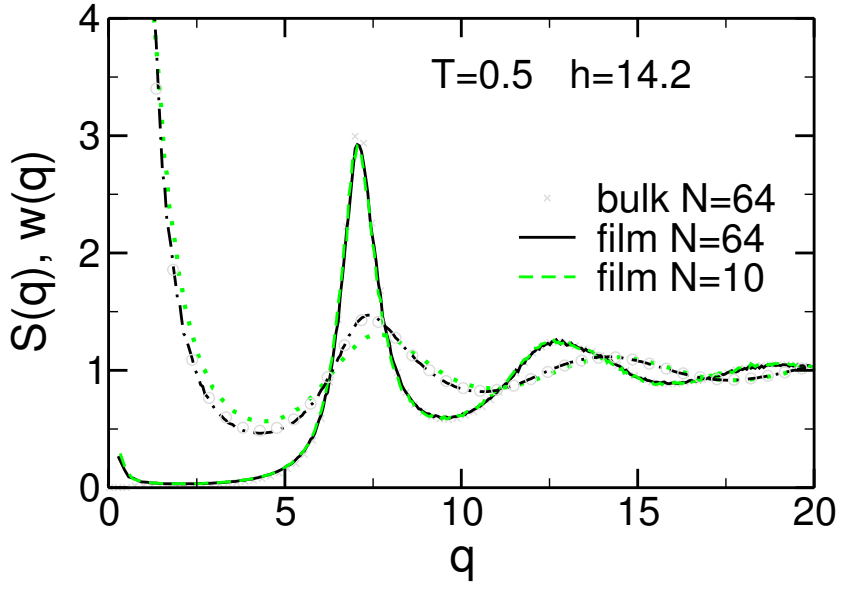

Figure 3.7: Two dimensional total structure factor averaged over a supported film containing $n = 96$ chains of chain length $N = 64$ (black line) and $N = 10$ (grey dashed line) with $h \simeq 14$ at $T = 0.5$ at $p = 0$. Also indicated is the total structure factor of a bulk system of chains of 64 monomers (crosses). Also indicated is the intra-chain structure factor $w(q)$ for these systems. For chains of $N = 64$ monomers in the bulk (circles) and the supported films (dash-dotted line) and a supported film of chains of length $N = 10$ (grey dotted line).

3.3 Radius of gyration $R_{\rm g}$ and end-to-end distance $R_{\rm e}$

End-to-end distance. In order to characterize the size of one chain, one can use the end-to-end vector $R_{\rm e}$ that is defined by

$$R_{\rm e}^2 = \langle \mathbf{R}_{\rm e}^2 \rangle = \left\langle \left(\sum_{a=1}^{N-1} \mathbf{b}_i^a \right)^2 \right\rangle_i = \sum_{a,b=1}^{N-1} \left\langle \mathbf{b}_i^a \cdot \mathbf{b}_i^b \right\rangle_i \ , \tag{3.10}$$

where $\langle \ldots \rangle_i$ denotes an average over all chains i $(= 1, \ldots, n)$ [51].

Radius of gyration. The radius of gyration $R_{\rm g}$ is also frequently used:

$$R_{\rm g}^2 = \frac{1}{N} \sum_{a=1}^{N} \left\langle \left(\mathbf{r}_i^a - \mathbf{R}_{\rm cm}^i \right)^2 \right\rangle_i = \frac{1}{2N^2} \sum_{a,b=1}^{N} \left\langle \left(\mathbf{r}_i^a - \mathbf{r}_i^b \right)^2 \right\rangle_i \ . \tag{3.11}$$

$\mathbf{R}_{\rm cm}^i = \frac{1}{N} \sum_{a=1}^{N} \mathbf{r}_i^a$ refers to the position of the center of mass of chain i. For an ideal chain, one expects the following property:

$$R_{\rm g}^2 = \frac{1}{6} R_{\rm e}^2 = \frac{1}{6} N \ell^2 \tag{3.12}$$

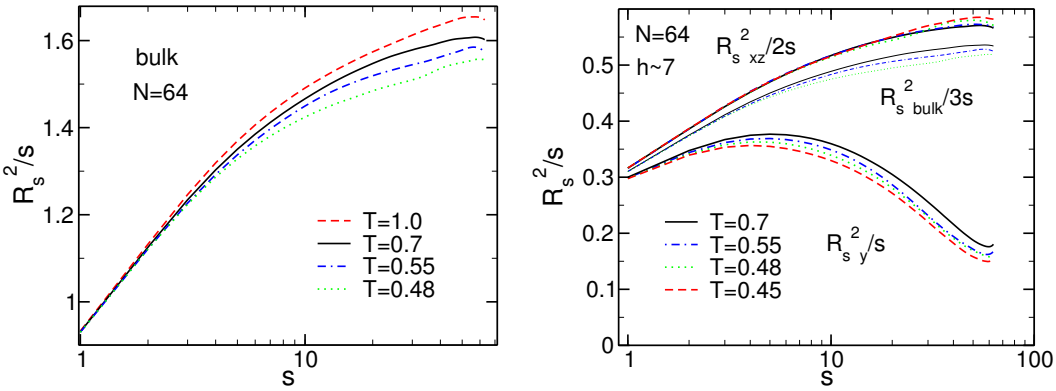

Figure 3.8: LEFT PANEL: R_s^2/s as a function of n is shown for a $T = 1$ (dashed line), $T = 0.7$ (full line), $T = 0.55$ (dash-dotted line) and $T = 0.48$ (dotted line) for chains of length $N = 64$ in the bulk. The results were obtained by combining the MD simulations with the bridge algorithm as described in section 2.4. RIGHT PANEL: $R_{s\,xz}^2/2s$ and $R_{s\,y}^2/s$ as a function of n are shown for a $T = 0.45$ (dashed line), $T = 0.7$ (full line), $T = 0.55$ (dash-dotted line) and $T = 0.48$ (dotted line) for chains of length $N = 64$ in a supported film of thickness $h \simeq 7$. Also indicated (thin lines) is $R_s^2/3s$ calculated in the bulk.

which defines the statistical segment ℓ. To get a better idea of the over-all structure of a chain also the intra-chain distance function as defined in equation (2.78) in section 2.4 is calculated.

In figure 3.8 the mean-square intra-chain distance is shown for a bulk system at different temperatures. While the qualitative behavior does not change upon cooling, i.e. there is no sign of crystallization, one can see clearly that the chains in the bulk system are shrinking as the system becomes cooler. This effect should be due to the densification of the system. Nevertheless the overall change of R_g and R_e remains small ($R_g^2(T = 1) = 16.99$ and $R_g^2(T = 0.48) = 16.03$). The chains have the property of an ideal random walk given by equation (3.12) within the accuracy of our calculations at all temperatures.

In the films we in addition look at the intra-chain distance function split into the directions parallel $R_{s\,xz}^2/2s$ and perpendicular $R_{s\,y}^2/s$ to the surface defined as

$$R_{s\,xz}^2/2s = \frac{1}{2s}\sum_{i=1}^{n}\frac{1}{n}\sum_{a=1}^{N-s}\frac{1}{N-s}\left\langle (x_i^a - x_i^{a+s})^2 + (z_i^a - z_i^{a+s})^2\right\rangle \tag{3.13}$$

and

$$R_{s\,y}^2/s = \frac{1}{s}\sum_{i=1}^{n}\frac{1}{n}\sum_{a=1}^{N-s}\frac{1}{N-s}\left\langle (y_i^a - y_i^{a+s})^2\right\rangle \ . \tag{3.14}$$

These quantities are compared to the bulk results in figure 3.8. The chain is compressed on all length scales in the y-direction. The larger the distance of the monomers the stronger the effect of the confinement is felt. This effect grows with lowering

the temperature probably because the film thickness decreases with decreasing temperature. The extensions of the chains in the parallel direction are larger than in the bulk system. The stretching increases slightly as the temperature decreases but the effect of temperature seems to be rather small.

In the films we find that the overall R_{g} decreases with decreasing film thickness as the confinement effect becomes stronger, i.e. the compression in the y-direction has a stronger impact on the overall structure than the stretching in the parallel direction. The radius of gyration decreases from $R_{\mathrm{g}}^2 = 16.29$ in the bulk to $R_{\mathrm{g}}^2 = 14.58$ in a thin film of thickness $h = 7.2$ at $T = 0.7$. The relation between the radius of gyration and the end-to-end distance given by equation (3.12) is violated in the films. For a film of $h = 7.2$ we find for example $R_{\mathrm{g}}^2 = \frac{1}{5.68} R_{\mathrm{e}}^2$ at $T = 0.7$. To understand this difference better we calculate a layer-resolved radius of gyration and end-to-end distance by considering only chains whose center of mass is in a certain distance y from the wall.

Layer-resolved R_{e} and R_{g}. As the dimensions of the film become comparable to the size of the polymer coil the Gaussian statistics of the chains in the melt are perturbed due to the confinement.

The layer-resolved radius of gyration is defined as

$$\begin{aligned} R^2_{\mathrm{g\,xz}}(y) &= \left\langle \frac{1}{2n(y)N} \sum_{i=1}^{n} \sum_{a=1}^{N} \left[\left(x_i^a - R^i_{\mathrm{cm\,x}}\right)^2 + \left(z_i^a - R^i_{\mathrm{cm\,z}}\right)^2 \right] \delta\left(y - R^i_{\mathrm{cm\,y}}\right) \right\rangle \\ R^2_{\mathrm{g\,y}}(y) &= \left\langle \frac{1}{n(y)N} \sum_{i=1}^{n} \sum_{a=1}^{N} \left[\left(y_i^a - R^i_{\mathrm{cm\,y}}\right)^2 \right] \delta\left(y - R^i_{\mathrm{cm\,y}}\right) \right\rangle , \end{aligned} \tag{3.15}$$

where $n(y)$ is the number of chains whose center of mass is at distance y from the wall. Analogously the layer-resolved end-to-end distance as

$$\begin{aligned} R^2_{\mathrm{e\,xz}}(y) &= \left\langle \frac{1}{2n(y)} \sum_{i=1}^{n} \left[\left(x_i^1 - x_i^N\right)^2 + \left(z_i^1 - z_i^N\right)^2 \right] \delta\left(y - R^i_{\mathrm{cm\,y}}\right) \right\rangle \\ R^2_{\mathrm{e\,y}}(y) &= \left\langle \frac{1}{n(y)} \sum_{i=1}^{n} \left[\left(y_i^1 - y_i^N\right)^2 \right] \delta\left(y - R^i_{\mathrm{cm\,y}}\right) \right\rangle . \end{aligned} \tag{3.16}$$

We also determine the density profile of the chain's center of mass

$$\rho_{\mathrm{cm}}(y) = \frac{1}{A} \left\langle \sum_{i=1}^{n} \delta(y - R^i_{\mathrm{cm}\ y}) \right\rangle . \tag{3.17}$$

In figure 3.9 the results of this analysis are shown. The confinement on the one hand, constrains the chain in the y-direction where also the ratio between R_{e}^2 and R_{g}^2 deviates from the prediction for Gaussian chains. The chains are the stronger deformed, the closer they are to the surfaces. There is no pronounced difference of

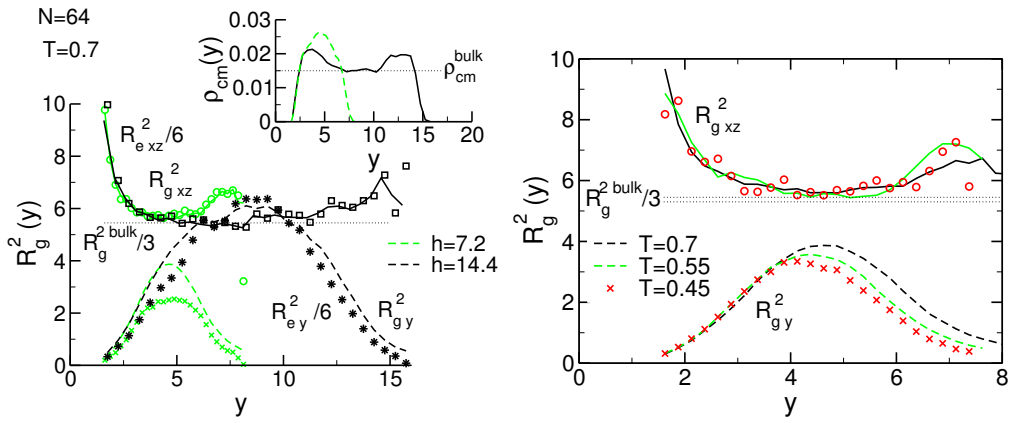

Figure 3.9: LEFT PANEL: The layer-resolved radius of gyration (lines) and end-to-end distance divided by 6 (symbols) in the parallel and the perpendicular direction as indicated in the film are shown for a supported film of thickness $h = 7.2$ (grey) and $h = 14.4$ (black) are shown for chains of length $N = 64$ at $T = 0.7$. The horizontal line indicates the $R_g^2/3 = 5.45$ of the bulk system at the same conditions. The inset shows the density profile of the chains center of mass in both films. RIGHT PANEL: The layer-resolved radius of gyration is shown in the parallel and the perpendicular direction as indicated in the graph for $T = 0.7$ (black lines), $T = 0.55$ (gray lines) and $T = 0.45$ (symbols) for a supported film ($h = 7.2$) of chains of length $N = 64$. The horizontal lines indicate $R_g^2/3$ of the bulk system at $T = 0.7$ and $T = 0.45$.

the extension of the chains in the perpendicular direction between the free and the supported surface. The end-to-end distance is stronger affected by the confinement than the radius of gyration. In the parallel direction, on the other hand, the chains have the same dimension as in bulk in the center of the film. When approaching the surface the chains are stretched in comparison to the bulk system. This effect is stronger at the supporting surface. Nevertheless they still have the property of Gaussian chains as far as the ratio of R_g and R_e is concerned.

In the films of thickness $h = 14.4$ the chains have bulk dimensions in the center of the film within the accuracy of our calculations. The density profile changes qualitatively between the two film thicknesses. While the thinner film only has the highest density of chains in the center of the film the thicker films shows two peaks in the density at a distance of about 3 from the surface. The density is constant in the center of the film. The deviations from the bulk values at a given distance form the surface does not increase upon stronger confinement. A chain at a given instant in time is on average not a spherical object but can be described by an ellipsoid. In bulk simulations of our model we find the ratio of the axis of the ellipsoid to be $12.2 : 2.7 : 1$ for $N = 64$. The confinement leads to a preferential orientation of these ellipsoids with the shortest axis perpendicular to the wall. This was also described in detail in a review by Mischler [152].

Upon cooling one finds a stronger decrease of R_g and R_e in the films than for

the bulk. As can be seen in figure 3.9 this is mainly due to the decrease of the film thickness and the therefore stronger confinement of the chains in the y direction and not due to a homogeneous shrinkage of the chains . The layer-resolved values of R_{g} are not accurate enough to see the rather small effect of temperature on the overall extensions of the chains we encountered in the bulk systems. Overall the change in structure of the chains remains small. Note that temperature effects are small because the model is completely flexible. Models with rigidity should exhibit a more pronounced T-dependence.

3.4 Summary

T_{g} was determined upon cooling the bulk system as well as the thin model polymer films at a constant rate for chains of length $N = 10$ and $N = 64$. The glass transition temperature was suppressed in the films in comparison with the bulk. The decrease becomes more pronounced with decreasing film thickness. At a given film thickness the decrease in T_{g} is stronger for free-standing films than for supported films. For chains of length $N = 64$ the relative decrease of T_{g} was stronger than for chains of length $N = 10$.

We investigated the local packing of the monomers in the film in comparison with the bulk using the total static structure factor. The first maximum of the static structure factor is smaller in free-standing and supported films at a given temperature in comparison with the bulk. The weaker packing constraints with decreasing film thickness could give rise to faster dynamics in the films. This in turn could be an explanation for the observed T_{g} reductions. Such an argumentation along the lines of mode-coupling theory was also used in previous studies on confined films to explain the reduction of T_{c}, the critical temperature of MCT, with decreasing film thickness [32, 151]. Nevertheless the suppression of the first maximum of the static structure factor is comparable in supported and free-standing films and can therefore not explain the differences in T_{g} between the two film geometries.

The conformations of the chains are perturbed by the confinement. We find a decrease of the radius of gyration and the end-to-end distance in the perpendicular direction and an increase in the plane of the film. The effect is strongest at the surfaces and decreases towards the film center where the chains have bulk like dimensions if the film is thick enough.

Chapter 4

Dynamic properties

In this chapter we would like to see whether the structural differences we found between bulk and film entail also differences in the dynamics. These dynamic differences could be linked to the observed changes in T_{g}. First we present an analysis of the dynamics in the bulk system which is going to serve as a benchmark for the further analysis. Then we are going to look at the dynamics of the confined systems averaged over the whole film via the mean-square displacements and the incoherent-scattering function. We also perform a layer-resolved analysis of the dynamics to show the spatial inhomogeneity of the relaxation. The film analysis will allow us to present a formula for the thickness dependence of T_{c} and to suggest a position dependent T_{c} to explain the found profiles of the relaxation times. Eventually we will look at the non-Gaussian parameter α_2 in the bulk and the films.

4.1 Average dynamic properties

Mode-coupling theory (MCT) [67, 136] predicts that structural relaxation times of a (bulk) glass-forming system diverge when T approaches a critical temperature T_{c} from above. To extract such relaxation times we determine the mean-square displacement (MSD) of the innermost monomer

$$g_1(t) = \left\langle \left[\mathbf{r}^{\parallel}_{N/2}(t) - \mathbf{r}^{\parallel}_{N/2}(0) \right]^2 \right\rangle. \tag{4.1}$$

and the incoherent intermediate scattering function at the maximum q^* of the static structure factor $S(q)$

$$\phi^{\mathrm{s}\parallel}_{q^*}(t) = \frac{1}{nN} \left\langle \sum_{i=1}^{nN} \exp\left(-\mathrm{i}\mathbf{q}^{*\parallel} \cdot [\mathbf{r}_i^{\parallel}(t) - \mathbf{r}_i^{\parallel}(0)] \right) \right\rangle . \tag{4.2}$$

Here, $\mathbf{r}_i^{\parallel}(t)$ is the position, parallel to the wall, of monomer i at time t, and both $g_1^{\parallel}(t)$ and $\phi^{\mathrm{s}\parallel}_{q^*}(t)$ are averaged over all monomers in the film. We only consider displace-

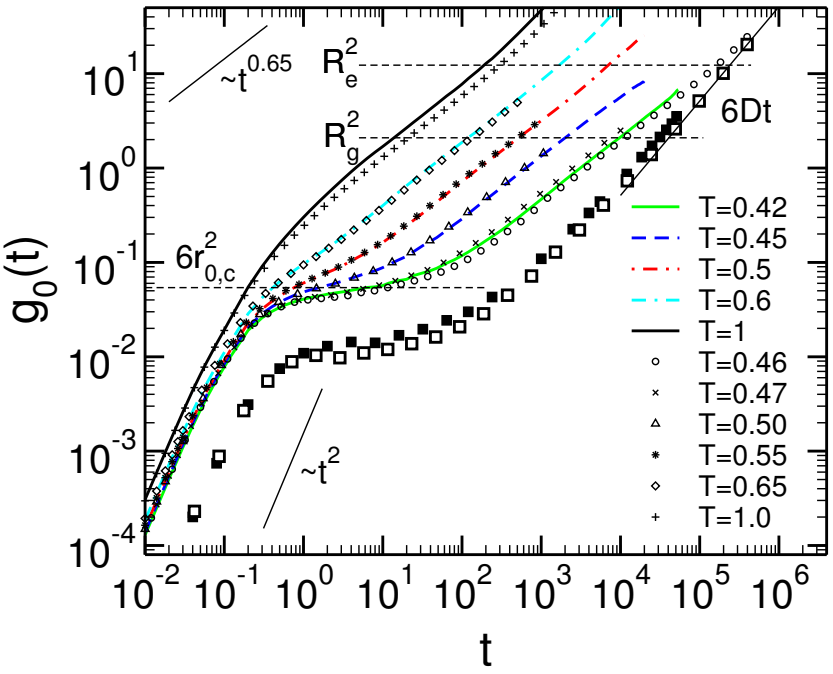

Figure 4.1: Log-log plot of the MSD of all monomers $g_0(t)$ for $N = 10$ at $p = 0$ and $T = 1$, $T = 0.6$, $T = 0.5$, $T = 0.45$ and $T = 0.42$ for the BS model (lines) and at $p = 1$ and $T = 1$, $T = 0.65$, $T = 0.55$, $T = 0.5$, $T = 0.47$ and $T = 0.46$ for the BE model (symbols). The open squares indicate the MSD $g_3(t)$ of the chain's center of mass at $T = 0.46$ in the BE model and the filled squares show $g_3(t)$ at $T = 0.42$ in the BS model. The dashed horizontal lines represent the radius of gyration $R_g^2 \simeq 2.09$, the end-to-end distance $R_e^2 \simeq 12.3$, and the plateau value $6r_{0,c}^2 = 0.054$ (the latter value is obtained from an MCT analysis of the BE model [32]). The solid lines indicate early-time ballistic motion ($\sim t^2$), sub-diffusive motion due to chain connectivity ($\sim t^{0.63}$), and final diffusion at late times ($= 6Dt$, D being the diffusion coefficient).

ments and scattering vectors within the plane of the film, since motion in perpendicular direction is constrained by film thickness.

To further explore the correspondence between the BE and BS models for the bulk system established in section 3.2.1, we also compare the MSDs of all monomers

$$g_0(t) = \frac{1}{nN} \sum_{i=1}^{nN} \left\langle |\mathbf{r}_i(t) - \mathbf{r}_i(0)|^2 \right\rangle \ , \tag{4.3}$$

and of the chain's center of mass (CM)

$$g_3(t) = \frac{1}{n} \sum_{i=1}^{n} \left\langle |\mathbf{R}_{\text{cm}}^i(t) - \mathbf{R}_{\text{cm}}^i(0)|^2 \right\rangle \ , \tag{4.4}$$

where $\mathbf{R}_{\text{cm}}^i(t)$ is the position of the center of mass of the ith chain at time t.

In the films it can often be useful to distinguish between the MSD in the directions parallel to the wall

$$g_0^{\parallel}(t) = \frac{1}{nN} \sum_{i=1}^{nN} \left\langle |\mathbf{r}_i^{\parallel}(t) - \mathbf{r}_i^{\parallel}(0)|^2 \right\rangle \ , \tag{4.5}$$

and the MSD perpendicular to the wall

$$g_0^{\perp}(t) = \frac{1}{nN} \sum_{i=1}^{nN} \left\langle |\mathbf{r}_i^{\perp}(t) - \mathbf{r}_i^{\perp}(0)|^2 \right\rangle \ . \tag{4.6}$$

4.1.1 Bulk

Figure 4.1 shows $g_0(t)$ and $g_3(t)$ for the BE and the BS model at different temperatures ranging from the liquid regime to the supercooled state close to $T_{\rm c}$. For short times the motion is ballistic and $g_0(t) \propto g_3(t) \sim t^2$. For longer times and low T, a plateau regime emerges which becomes more and more pronounced as temperature decreases. The plateau implies that the monomers remain temporarily trapped in the cage formed by their nearest neighbors. When they escape from their cages the monomers enter a sub-diffusive regime ($g_0(t) \propto t^{0.63}$) due to connectivity. This sub-diffusive regime does not exist for the MSD of the CM, which continuously crosses over to the final diffusion directly after the plateau regime. At very large t the chains and monomers move diffusively $g_0(t) = g_3(t) = 6Dt$ with the same diffusion constant D.

As for $S(q)$ we find good agreement for the MSDs at the same distance from $T_{\rm c}$, especially at low T. This agreement, between the two models under different external conditions ($p = 0$ for the BS model and $p = 1$ for the BE model) for both static and dynamic quantities, upon shifting the temperature axis by $\Delta T_{\rm c} \simeq 0.045$ is an argument in favor of MCT which suggests that a strong coupling between local spatial correlations on the scale $1/q^*$ and the dynamics is responsible for the slowing down of the relaxation on cooling toward $T_{\rm c}$.

4.1.2 Film versus bulk dynamics: qualitative features

Figure 4.2 compares $g_1^{\parallel}(t)$ and $\phi_{q^*}^{\rm s\parallel}(t)$ obtained for supported and free-standing films at $T = 0.44$ with the corresponding bulk results. Qualitatively, bulk and film display the same relaxation features. For $g_1^{\parallel}(t)$ for instance we find the following behavior: At short times the motion is ballistic ($g_1^{\parallel}(t) \sim t^2$). For longer times, the monomer displacement slows down, particularly in the bulk where a plateau regime emerges. The plateau implies that the monomers remain temporarily trapped in the "cage" formed by their neighbors. When they escape from their cage the motion becomes sub-diffusive due to chain connectivity ($g_1^{\parallel}(t) \propto t^{0.63}$). This sub-diffusive

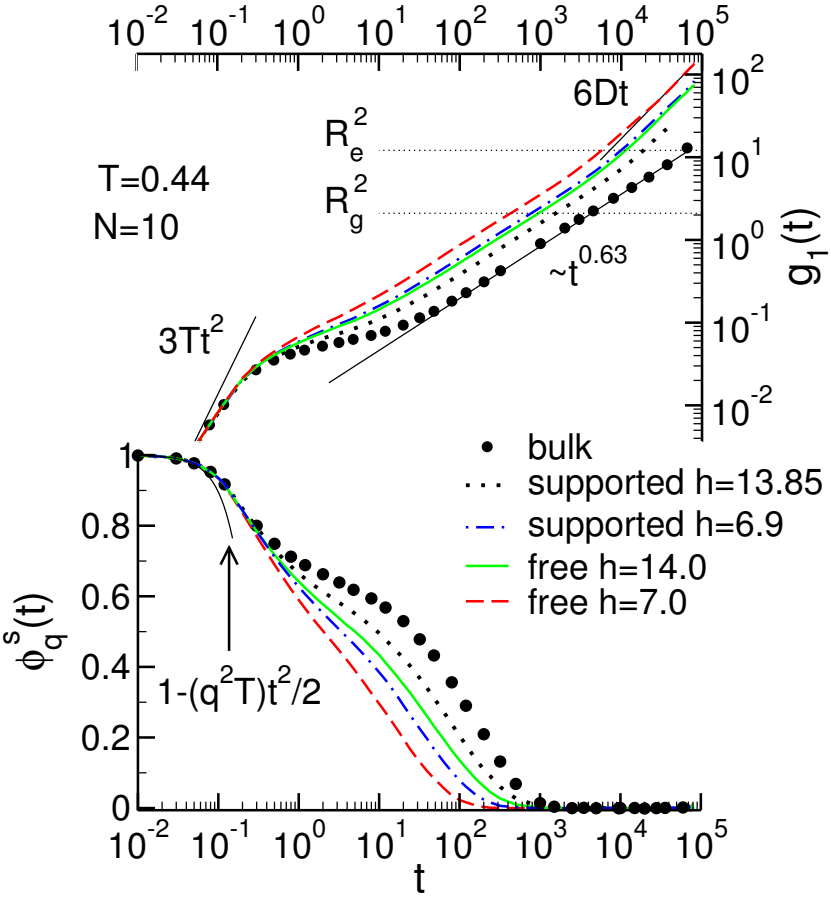

Figure 4.2: MSD of the innermost monomer ($g_1(t)$) and incoherent intermediate scattering function ($\phi_q^{\mathrm{s}}(t)$) at $T = 0.44$. RIGHT ORDINATE: Log-log plot of $g_1(t)$ versus t; the MSDs are measured in direction parallel to the wall and multiplied by $3/2$ to account for the difference in the number of directions compared to the bulk. The dotted horizontal lines represent the bulk radius of gyration $R_{\mathrm{g}}^2 \simeq 2.09$ and bulk end-to-end distance $R_{\mathrm{e}}^2 \simeq 12.3$. The ballistic ($\sim t^2$), sub-diffusive ($\sim t^{0.63}$), and diffusive regimes ($\sim t$) are indicated (D is the diffusion coefficient of a chain). LEFT ORDINATE: Incoherent intermediate scattering function $\phi_q^{\mathrm{s}}(t)$ at $q = 6.9$ ($\approx q^* =$ maximum of the static structure factor $S(q)$). The ballistic regime ($\sim t^2$) is also indicated.

motion crosses over to diffusive behavior, $g_1^{\parallel}(t) \sim t$, if the MSD exceeds the average chain size.

Compared to the bulk, figure 4.2 shows that the film dynamics is faster and caging is less pronounced. It appears as if the films would correspond to a bulk melt at a higher temperature than $T = 0.44$. This conclusion was also drawn in our previous studies of polymer films confined between two smooth walls [32, 35]. But here the films have free surfaces, and the number of free surfaces seems to have a large influence on the relaxation. We find e.g. that the dynamics of a free-standing film of the

thickness h and a supported film of the thickness $h/2$ are very similar (cf. $h \simeq 7.5$ for the supported film and $h \simeq 15$ for the free-standing film in figure 4.2).

This finding qualitatively agrees with experimental results on the depression of T_g for supported and free-standing polystyrene (PS) films [4, 40, 41]. These experiments suggest that T_g of a free-standing film of thickness h agrees, within the error bars, with the T_g of a supported film of thickness $h/2$. It appears as if the substrate could be introduced in the midplane of the free-standing film with negligible perturbation of its properties. While there may be concerns about the generality of this result, it still suggests that the T_g reduction of PS films should be related to the presence of the free surface which possibly allows for an enhanced mobility of the monomers. We will show in section 4.3 that monomers at the free surface are indeed more mobile than those in the center of the film.

4.2 Relaxation times and T_c

Following reference [35] we introduce two relaxation times τ_1 and τ_{q^*} which are obtained from $g_1^{\parallel}(t)$ and $\phi_{q^*}^{s\parallel}(t)$ by

$$g_1^{\parallel}(t = \tau_1) = 1 \tag{4.7}$$

and

$$\phi_{q^*}^{s\parallel}(t = \tau_{q^*}) = 0.3\,. \tag{4.8}$$

These times correspond to the α-relaxation regime. For τ_1 we can quickly see this by the following argument. τ_1 is the time it takes a monomer to cover the distance of its own size. This is only possible after the monomer manages to leave the cage of its nearest neighbors (cf. figure 4.2 and figure 4.1). This time thus belongs to the final structural (α-) relaxation.

In analogy to the prediction of ideal MCT for the bulk [136] we attempted to fit the relaxation time for quantity A by a power law of the form

$$\tau_A(T, h) \propto \left(\frac{1}{T - T_c(h)}\right)^{\gamma_A(h)}\,. \tag{4.9}$$

Here, we assume that the critical temperature $T_c(h)$ only depends on film thickness and geometry, whereas the exponent $\gamma_A(h)$ may additionally change with the quantity under consideration (for further discussion of this assumption see [32]). We find that equation (4.9) is only applicable in a limited T interval above T_c. For large $T - T_c$ and very close to T_c equation (4.9) is expected to break down (see e.g. [32]). In the first case the asymptotic formula (4.9) is not valid yet, whereas for T very close to T_c decay processes which are not included in the ideal MCT allow the system to relax after a large but finite time. The choice of the interval for which the MCT-like prediction (4.9) may be expected to hold cannot be made unambiguously; this introduces an uncertainty in the determination of T_c.

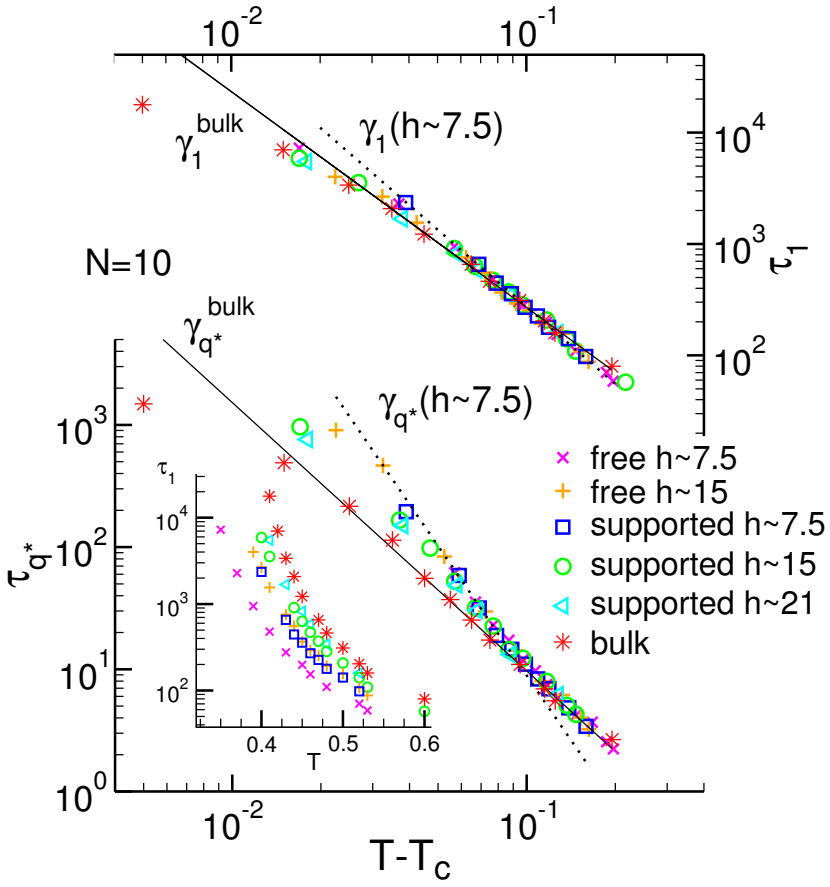

Figure 4.3: MAIN FIGURE: Relaxation times τ_1 and τ_{q*}, defined in equations (4.7) and (4.8), versus $T-T_c(h)$. Results for all studied systems are shown: free-standing films [$h \simeq 7.5$ ($\times$) and $h \simeq 15$ ($+$)], supported films [$h \simeq 7.5$ (open squares), $h \simeq 15$ (open circles), and $h \simeq 21$ (open triangles)], and the bulk (stars). The values of $T_c(h)$ and $\gamma_A(h)$, obtained by fits to equation (4.9), are compiled in table A.1. The fit curves for the bulk and the supported film with $h \simeq 7.5$ chains (corresponding to $h = 7.5$) are shown for τ_1 and τ_{q*} (they are labeled by the exponent $\gamma_A(h)$). INSET: The inset depicts τ_1 as a function of the absolute temperature T.

4.2.1 Chain length $N = 10$

Figure 4.3 displays τ_1 and τ_{q^*} as a function of $T - T_c(h)$, while the inset depicts a plot of τ_1 versus T. When the relaxation times are plotted versus $T - T_c(h)$, film and bulk data agree well with each other for intermediate distances from T_c. The films, however, show a larger exponent γ_A. Following MCT [67, 136] this should imply a larger stretching of the α-relaxation when passing from bulk to films. A glance at figure 4.5 reveals that this interpretation is in qualitative agreement with the simulation data.

While the value of γ_A depends on the quantity from which it is extracted (we find

$\gamma_1 < \gamma_{q^*}$; cf. table A.1), the fit results for T_c are independent of A. All films have a T_c which is lower than the bulk value $T_c = 0.405$. The films with two free surfaces show a larger decrease of T_c for a given film thickness. Furthermore, we find that a free-standing film of thickness h and a supported film of thickness $h/2$ have very similar relaxation times and T_c values (compare open squares and pluses in the inset of figure 4.3). This suggests again that the influence of the supported surface on the dynamics is weaker than that of the free surface.

We find the same trends for T_c and T_g with respect to their dependence on film thickness and geometry. While $T_g < T_c$, the fit results for T_c coincide within the error bars with T_i (cf. table A.1). Experimentally, one often observes that $T_c/T_g \simeq 1.2$ [153]. We rather find that $T_c/T_g \simeq 1.03$ or even $T_c/T_g \simeq 1$, if T_i is identified with T_g. The difference between T_c and T_g is thus much smaller than in experiments. The difficulty to distinguish T_c and T_g is due to the very high cooling rate used in the nonequilibrium simulations of section 3.1.

4.2.2 Chain length $N = 64$

For the longer chains $N = 64$ we performed the same analysis. This provides a hint at the chain length dependence T_c. As for the results on T_g we find the same trends as for the short chains. T_c in the bulk increases from $T_c(N = 10) = 0.405$ to $T_c(N = 64) = 0.415$ for the longer chains. The relaxation times are slightly larger than for the longer chains but the qualitative behavior remains the same. The relaxation in the films is faster than the one in the bulk. Free-standing films and supported films of twice the thickness show similar relaxation behavior.

In figure 4.4 the relaxation time extracted from the mean-square displacement of the innermost monomer is shown as function of temperature as well as distance from the respective T_c. Again when plotted as a function of the distance from T_c the results collapse onto a master curve. Nevertheless the exponent $\gamma_A(h)$ increases with decreasing film thickness as we also observed for $N = 10$. The values $T_c(h)$ as well as the exponents $\gamma_A(h)$ are compiled in table A.2.

The decrease for a given film thickness h is larger for the longer chains $N = 64$ than for the shorter chains $N = 10$. We already observed a stronger influence of the confinement on T_g for the longer chains in section 3.1, where we determined the glass transition temperature upon cooling of the sample at a constant rate. Also for T_c we find that films of thickness $h \simeq 7$ have the same value of T_c independent of chain length which is due to the stronger decrease of T_g or T_c in films with longer chains which makes up for the initially higher value of T_c and T_g in the bulk.

4.2.3 Film versus bulk behavior: choosing T_c as a reference point

MCT suggests that T_c is an important reference temperature for the structural relaxation in the (moderately) supercooled state. It is therefore interesting to compare bulk

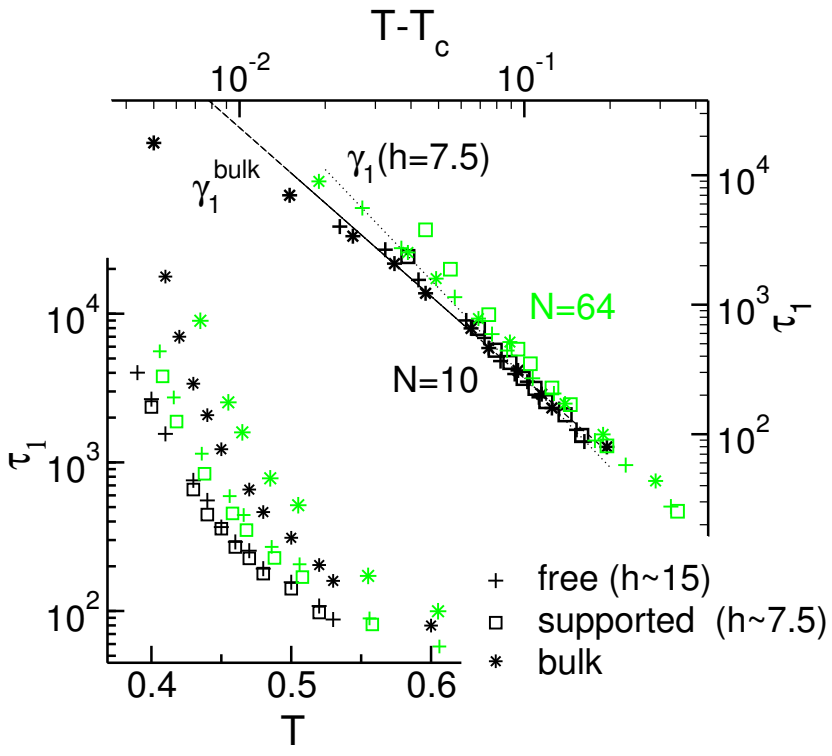

Figure 4.4: RIGHT AXIS: The relaxation times τ_1, defined in equations (4.7) and (4.8), versus $T - T_c(h)$. Results for $N = 10$ (black symbols) and $N = 64$ (grey symbols) are shown: free-standing film [$h \sim 15$ (+)], supported film [$h \sim 7.5$ (open squares)] and the bulk (stars). The values of $T_c(h)$ and $\gamma_A(h)$, obtained by fits to equation (4.9), are compiled in tables A.1 and A.2. The fit curves for the bulk and the supported film of $N = 10$ with $h \simeq 7.5$ are shown for τ_1 (they are labeled by the exponent $\gamma_A(h)$). LEFT AXIS: The relaxation times τ_1 as a function of the absolute temperature T are depicted.

and film dynamics for temperatures that are at the same distance ΔT_c ($= T - T_c$) to the respective T_c. Figure 4.5 shows such a comparison. For $\Delta T_c \simeq 0.05$ and $\simeq 0.03$, the figure depicts $g_1^{\parallel}(t)$ and $\phi_{q^*}^{s\parallel}(t)$ for two supported films of respective thickness $h \simeq 14$ and $h \simeq 21$, for a free-standing film with $h \simeq 14$, and for the bulk. T_c provides indeed an important reference point. For the same ΔT_c the main differences, observed in figure 4.2 when comparing bulk and film dynamics at the same T, are removed and finer details of the time evolution become apparent. For the incoherent scattering function we find good agreement between bulk and film in the plateau regime. In the α-regime, however, differences emerge and grow with time. The scattering functions of the films are more stretched, and the differences are larger for thinner films. For the MSDs, however, we find the opposite trend. Film and bulk dynamics agree fairly well for late times, while they differ in the plateau regime.

In reference [32] the same analysis as shown in figure 4.5 was performed for films

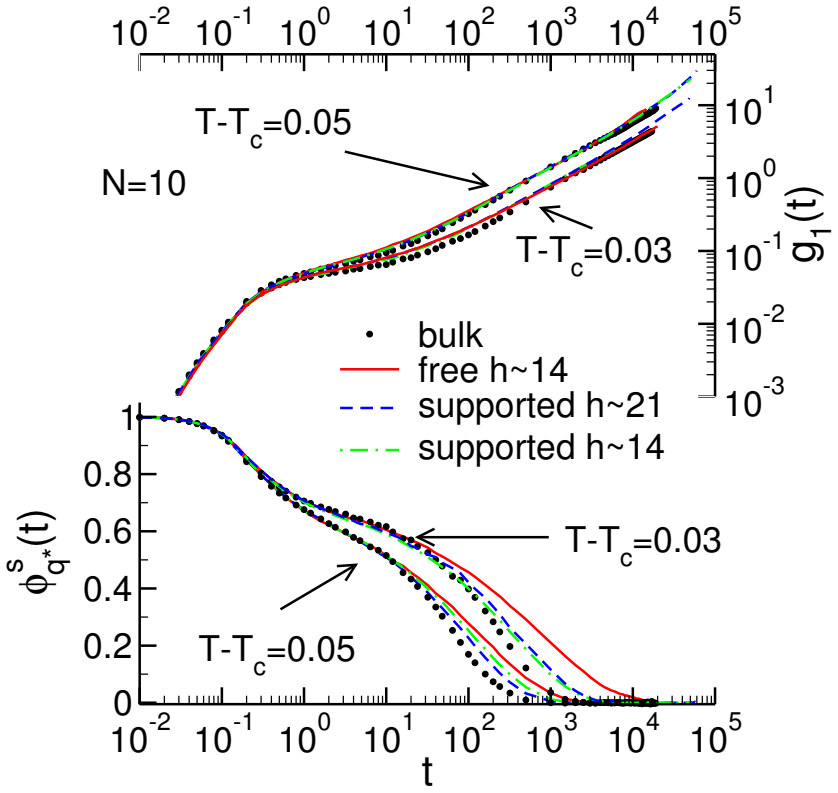

Figure 4.5: RIGHT ORDINATE: Log-log plot of $g_1(t)$ versus t; the MSDs are measured in the direction parallel to the wall in the films and multiplied by $3/2$. LEFT ORDINATE: Incoherent intermediate scattering function $\phi^s_q(t)$ at $q = 6.9$ (first maximum of $S(q)$). In all plots the temperatures for the films and the bulk are different, but the distance ΔT_c to the respective T_c is the same, i.e., $\Delta T_c \simeq 0.05$ and $\Delta T_c \simeq 0.03$. For the bulk (filled circles) the temperatures are $T = 0.455$ and $T = 0.435$, for the supported film with $h \simeq 21$ chains (dashed line) $T = 0.442$ and $T = 0.422$, for the supported film with $h \simeq 14$ chains (dash-dotted line) $T = 0.433$ and $T = 0.413$, and for the free-standing film with $\simeq 7$ chains (full line) $T = 0.415$ and $T = 0.395$.

confined between two smooth purely repulsive walls. There, it was also found that measuring T with respect to $T_c(h)$ is a viable approach to bring film and bulk results in close agreement with one another. But the details of this comparison appear to differ from the results presented in figure 4.5. Reference [32] reports good agreement, better than for $\phi^s_{q^*}(t)$, for the MSDs in the plateau regime, whereas deviations between bulk and film MSDs occur in the α-regime and grow with t (more precisely, the MSD of the bulk increases faster than that of the films).

This difference between the present findings and those of [32] can be explained by the fact that the quality of the superposition between bulk and film results is fairly sensitive to the precise value of T_c. A slight difference in $T_c(h)$ for the films due to a different choice of the temperature interval for the fits to equation (4.9) may affect

the time interval over which a good collapse of the data is observed. For instance, if we extended the fit interval to T closer to T_c, as done in [32], we could obtain lower values of $T_\mathrm{c}(h)$ (and along with that, larger values for γ_A). A lower value of $T_\mathrm{c}(h)$ would imply that a smaller temperature T must be used in order to preserve the same ΔT_c as in figure 4.5. Then, $g_1(t)$ of the bulk and the films would no longer coincide at late times (e.g. at $g_1(t = \tau_1) = 1$). By lowering $T_\mathrm{c}(h)$ by approximately $\Delta T = 0.007$ we could thus improve the superposition of $g_1(t)$ for the bulk and the films in the plateau regime, while, of course, the agreement of $\phi^\mathrm{s}_{q^*}(t)$ between the bulk and the films would deteriorate. This would allow us to reproduce the results of [32] very well. This shift of $T_\mathrm{c}(h)$ by ΔT is outside of the statistical error given in table A.1, but well within the much larger systematic error due to the choice of the T interval for the fit.

4.3 Layer-resolved dynamics

In order to pinpoint the origin of the faster dynamics in supported and free-standing films it is interesting to determine the y dependence of dynamic quantities. This will allow us to test the hypothesis that the surfaces have the main impact on the change of T_g in our films.

4.3.1 Layer-resolved analysis: definition and qualitative features

The mean-square displacement discussed in chapter 4.1.2 aggregates contributions from all (middle) monomers, irrespective of their position in the film. Further insight can be obtained by a layer-resolved analysis. When trying to perform such a layer-resolved analysis the question arises of how local time-displaced correlation functions should be defined [32]. Here, we introduce the y-dependent MSD $g_0^\parallel(t, y)$ of all monomers and the incoherent scattering function $\phi_q^{\mathrm{s}\,\parallel}(t, y)$. These quantities are defined in the following way:

$$g_0^\parallel(t, y) = \left\langle \frac{1}{n_t} \sum_i \prod_{t'=0}^{t} \delta\left[y - y_i\left(t'\right)\right] \left|\mathbf{r}_i^\parallel(t) - \mathbf{r}_i^\parallel(0)\right|^2 \right\rangle \tag{4.10}$$

and

$$\phi_q^{\mathrm{s}\,\parallel}(t, y) = \left\langle \frac{1}{n_t} \sum_i \prod_{t'=0}^{t} \delta\left[y - y_i\left(t'\right)\right] \mathrm{e}^{-\mathrm{i}\mathbf{q}\cdot\left[\mathbf{r}_i^\parallel(t) - \mathbf{r}_i^\parallel(0)\right]} \right\rangle . \tag{4.11}$$

These definitions only take into account the n_t monomers which are at all times $t' < t$ within the slab centered at y and of width $\Delta y = 2$. As before, we only consider the dynamics in the unconstrained directions parallel to the surface in order to allow for a

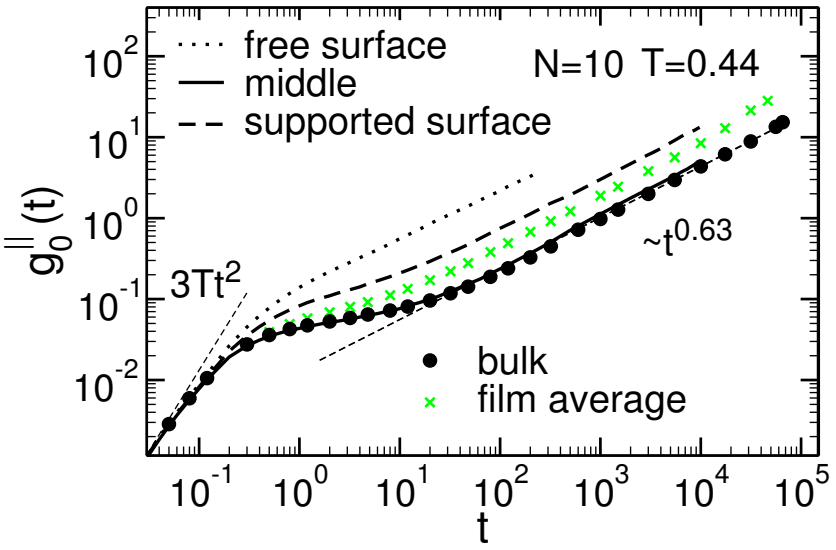

Figure 4.6: Monomer MSD $g_0(t)$ versus t at $T = 0.44$ for the bulk (filled circles) and a supported film of thickness $h = 13.85$ ($n = 576$ chains). The average over all monomers in the film, irrespective of their y position, is shown by crosses ($\times$). The full line indicates the layer-resolved MSD (cf. equation (4.10)) in the middle of the film; the dashed and dotted lines depict the layer-resolved MSD at the supported and free surfaces, respectively. Eventually, monomers will leave the layer to which they were initially assigned, which deteriorates the statistics. Thus, the curve corresponding to the free surface is shorter than the others. $g_0^{\parallel}(t)$ is multiplied by $3/2$ for all films to account for the difference in spatial directions with respect to the bulk. Early-time ballistic motion ($\sim t^2$) and sub-diffusive motion due to chain connectivity ($\sim t^{0.63}$) are also indicated.

comparison with the bulk. (4.10) averages over all monomers of a chain—instead of focusing only on the middle monomer as in (4.1)—because the layer-wise resolution of the dynamics is statistically very demanding.

Figure 4.6 compares the monomer MSDs of the bulk and a supported film of thickness $h = 13.85$. We see that the monomer motion close to the surfaces is faster than in the middle of the film, where $g_0^{\parallel}(t)$ is bulk-like. Furthermore, the motion at the free surface is faster than at the supported one. We may thus expect that the acceleration of the monomer dynamics is more pronounced in thinner films (due to the stronger overall influence of the interfaces) and in free-standing films (due to two free surfaces).

Figure 4.7 depicts $g_0(t, y)$ for a free-standing film of thickness $h = 14$ at $T = 0.44$ ($T_c(h) = 0.365$). The figure reveals a pronounced dependence of the monomer dynamics on the distance from the free surface. While $g_0(t, y)$ displays a two-step relaxation—characteristic of the cold melt close to T_c—in the center, this feature is gradually lost on approaching the surface, and is absent at the surface. Similar results are found in other simulations [12, 14, 16, 21]; our findings also agree qualitatively

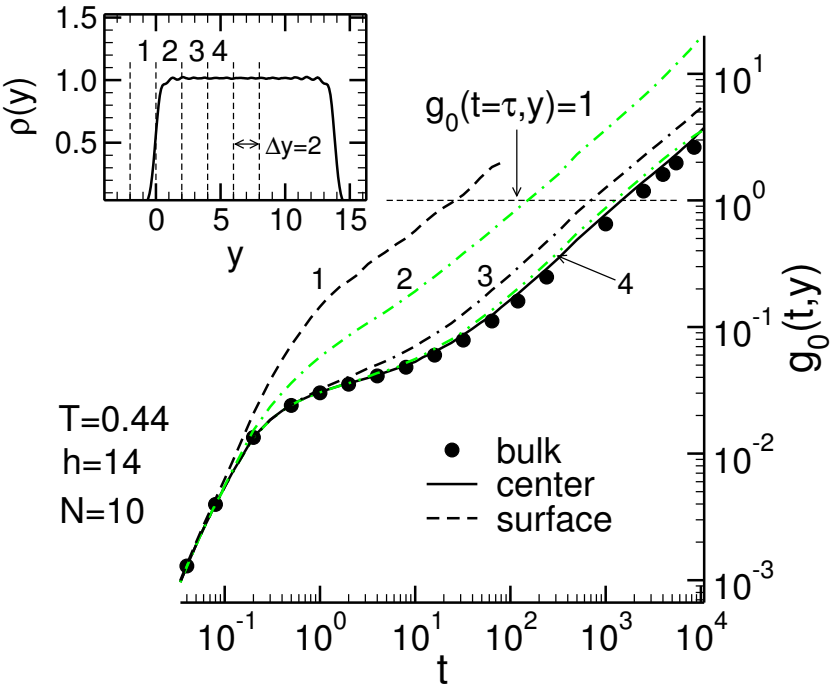

Figure 4.7: MAIN FIGURE: Layer-resolved MSD $g_0(t,y)$ at $T = 0.44$ for a free-standing film of thickness $h = 14$. y denotes the distance from the Gibbs's dividing surface (situated at $y = 0$). Only displacements parallel to the wall are considered for the films (lines); the bulk data (•) are multiplied by $2/3$ to put them on the same scale as the film data . $g_0(t,y)$ is obtained as an average over all monomers of a chain which remain for all times shown in a layer of width $\Delta y = 2$ that is centered at y (equation (4.10)). Eventually, monomers will leave the layer in which they were initially. This gives rise to a loss of statistical accuracy at long t; the data are thus sometimes truncated at late times where large statistical noise occurred. The dashed horizontal line indicates the definition of the local relaxation time $\tau(y,T)$ ((4.12)). INSET: Corresponding monomer density profile $\rho(y)$ versus y. The layers for which $g_0(t,y)$ is shown in the main figure are labeled by numbers (1, 2, 3, 4).

with the results of fluorescence [9] and NMR experiments [5].

It is tempting to try to correlate the layer dependence of $g_0(t,y)$ to the monomer density profile $\rho(y)$ (cf inset of figure 4.7). Since the average monomer density decreases on approaching the free surface, this could give rise to faster relaxation. However, while the low density is certainly an important factor for the fast dynamics in the surface layer (layer '1'), figure 4.7 suggests that a one-one correspondence between $\rho(y)$ and $g_0(t,y)$ is too simplified. For instance, the density of layers '2' and '3' is already bulk-like, whereas the corresponding $g_0(t,y)$ is larger than the bulk MSD. Apparently, surface effects penetrate into the film more deeply for the monomer MSD than for the monomer density (see [32] for a fuller discussion).

Figure 4.8 displays the layer-resolved incoherent intermediate scattering func-

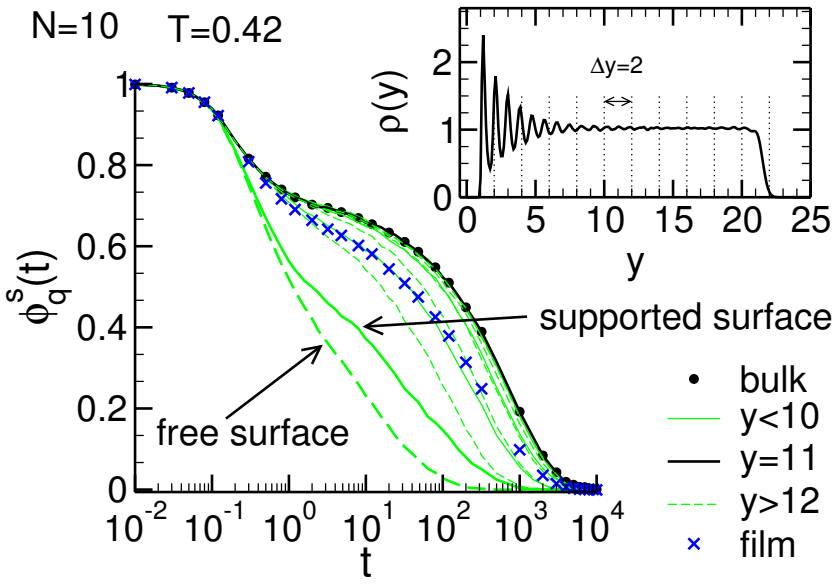

Figure 4.8: MAIN FIGURE: Layer-resolved incoherent scattering function $\phi_q^{s\parallel}(t,y)$ at $q = 6.9$ ($\approx$ maximum of $S(q)$) at $T = 0.42$ for a supported film of thickness $h = 20.3$. y denotes the distance from the wall. Only q vectors parallel to the wall are considered for the films while the bulk data (•) are averaged over 3 spatial directions. $\phi_q^{s\parallel}(t,y)$ is obtained as an average over all monomers which remain for all times in a layer of width $\Delta y = 2$ which is centered at y (cf. equation (4.11)). The average behavior of the film (average over all layers) is indicated by crosses ($\times$). The dashed lines show $\phi_q^{s\parallel}(t,y)$ in layers situated between the free surface and the film center ($y > 12$), the thick line presents the results for the middle of the film ($y = 11$), and the thin gray lines show $\phi_q^{s\parallel}(t,y)$ for layers located between the supported surface and the film center ($y < 10$). INSET: Monomer density profile $\rho(y)$ versus y for a supported film of $h = 20.3$ at $T = 0.42$. The layers for which $\phi_q^{s\parallel}(t,y)$ is shown in the main figure are indicated.

tion $\phi_{q^*}^{s\parallel}(t,y)$ for a supported film of $h = 20.3$ at $T = 0.42$. The data presented in figure 4.8 confirm a result that one might have expected from the discussion of figures 4.6 and figure 4.7. The monomer mobility decreases as we go from the supporting wall toward the center of the film and increases again as we cross the middle and approach the free surface. While there is a clear two-step relaxation—characteristic of the cold melt close to T_c—in the center, this feature is gradually lost on approaching the surfaces and is completely absent at the free surface. Seemingly, the forces acting on monomers at the surfaces (monomer-wall and monomer-monomer interactions) are very different from those in the bulk-like center of the film, and this leads, in the present case, to faster relaxation.

The accelerated dynamics at the surface (the "boundary condition") described above seems to fuel—in the present case of smooth attractive walls and free surfaces—a form of continuous tempering which induces the observed decrease of T_c (or

T_g) of the film: "Fast" monomers at the surface transfer part of their higher mobility to monomers in the adjacent layer, which in turn partly excite a high monomer mobility in the next deeper layer, and so on until the surface-induced stimulus is damped, and bulk behavior is recovered. This gradual damping should allow one to extract a length scale ξ characterizing the penetration of the surface effects into the inner part of the film.

4.3.2 An attempt to quantify the penetration depth of the surface effects

An approach for determining ξ was suggested in references [19, 20, 33, 154]; it utilizes a local relaxation time as an intermediate step. Following reference [32] we introduce such a relaxation time by

$$g_0^{\parallel}(t = \tau(y, T), y) = 1 \; . \tag{4.12}$$

Thus, $\tau(y, T)$ is the time it takes a monomer to move across its own size parallel to the wall in a layer at distance y from the wall.

Figure 4.9 depicts the results of this analysis for a supported film of $n = 864$ chains at various temperatures. Not unexpectedly, we find that surface effects are small for high T. At $T = 1$, for example, $\tau(y)$ is independent of y in a large portion of the film. The corresponding constant value of $\tau(y)$ agrees with the relaxation time τ obtained by applying equation (4.12) to the bulk data for $g_0(t)$. Upon cooling, however, surface effects become pronounced. They penetrate more and more into the film, the region of constant relaxation time shrinks, and it should finally disappear when the perturbations emanating from both surfaces, overlap in the center of the film. Figure 4.9 shows that this problem occurs already at $T = 0.44$ for all films—free and supported ones—if the system contains less than $n = 864$ chains. Such finite-thickness effects seriously interfere with the desired determination of ξ and should be avoided. For $n = 864$, the thickest supported film studied here, they become prominent if $T \lesssim 0.41$. We thus restricted the analysis to $T \geq 0.42$.

In the following we want to extract a length scale from the range over which $\tau(y)$ deviates near the surfaces from bulk behavior. When addressing this issue one is faced with the problem that there appears to be no theoretical concept to guide the analysis. One thus has to resort to an empirical parametrization of the data. Depending on the quantity under consideration different parameterizations have been proposed (see e.g. [19, 20, 33, 154]).

Simulations of a confined binary LJ-liquid [19, 33] suggest the ansatz

$$\ln\left(\frac{\tau(y,T)}{\tau(T)}\right) = -A(T)\exp\left(-\frac{y}{\xi(T)}\right) \tag{4.13}$$

to model the y-dependence of some local relaxation time, such as $\tau(y, T)$. Equation (4.13) introduces the length scale $\xi(T)$ to quantify the range of the deviations

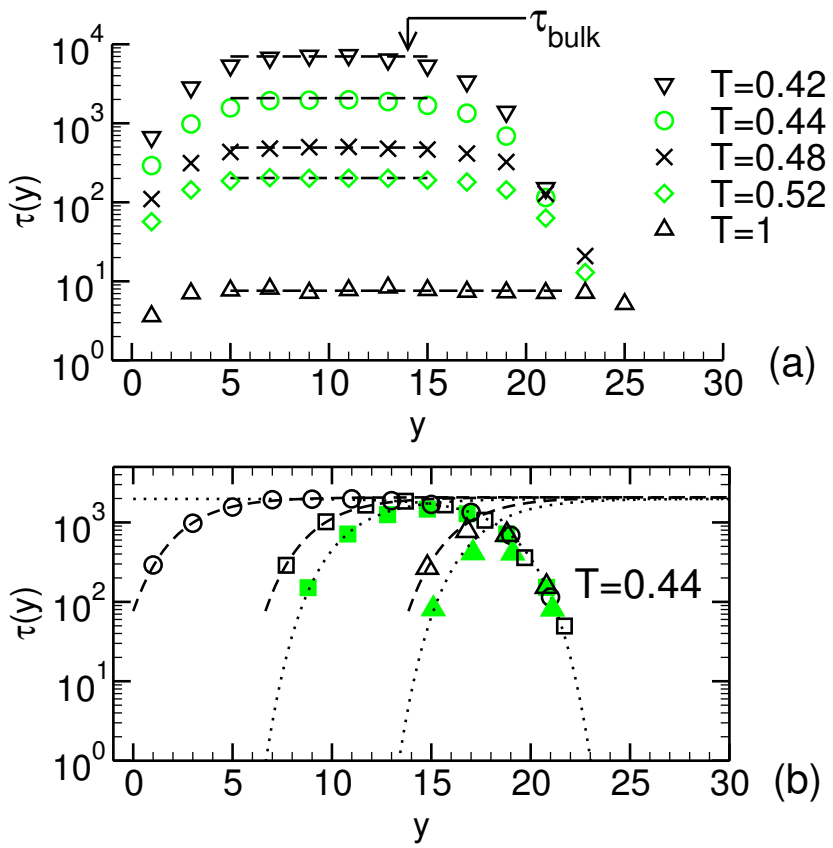

Figure 4.9: UPPER PANEL: Layer-resolved relaxation time $\tau(y,T)$ for various T versus distance y from the wall for a supported film containing $n = 864$ chains. y is defined as the distance of the center of a layer from the wall. The thickness of a layer is $\Delta y = 2$. $\tau(y,T)$ is computed from $g_0^{\parallel}(t,y)$ via equation (4.12). In this analysis, only those monomers were considered that remained in the layer at y for all times (equation 4.10). LOWER PANEL: $\tau(y,T)$ at $T = 0.44$ for free-standing films of $h = 7$ (filled triangles) and $h = 14$ (filled squares) and supported films of $h = 6.9$ (open triangles), $h = 13.85$ (open squares), and $h = 20.5$ (open circles) (cf. table A.1). The films are shifted in y direction so that the free surfaces coincide for all film thicknesses. The dashed lines indicate a fit to equation (4.13) for the supported surface and the dotted lines for the free surface.

of $\tau(y,T)$ from the bulk value $\tau(T)$. The fact that this ansatz provides an accurate description of various local relaxation times in previous studies, not only for smooth walls [32], but also for rough amorphous walls [19, 33], prompted us to apply equation (4.13) to our simulation results for $\tau(y,T)$. In addition to $\xi(T)$, $A(T)$ is a further adjustable parameter which was found previously [19, 32, 33] to depend only weakly on temperature.

Figure 4.9 illustrates that the y dependence of the relaxation times can indeed be well described by equation (4.13). The temperature dependence of the fit parameters,

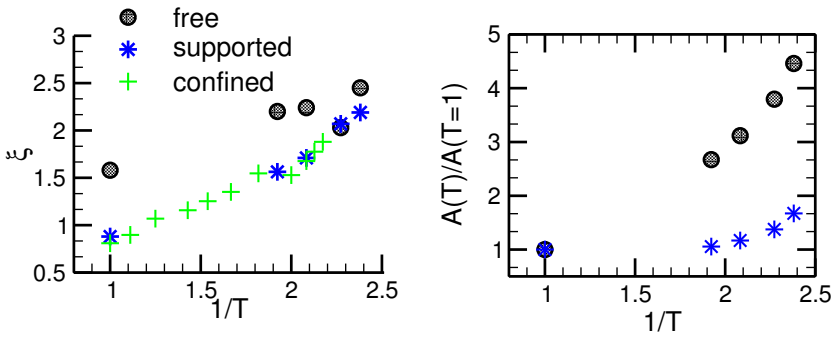

Figure 4.10: LEFT PANEL: Penetration depth ξ versus T. ξ is obtained from a fit of equation (4.13) to the $\tau(y,T)$ data shown in figure 4.9. Also reproduced are the results of reference [32] for a polymer film confined between two purely repulsive walls (crosses; the model of reference [32] is slightly different from that studied in the present work (BE model, cf. section 2.1), and the pressure was $p = 1$ instead of $p = 0$ employed here). RIGHT PANEL: Temperature dependence of $A(T)/A(T = 1)$, the prefactor in equation (4.13) normalized to one at $T = 1$. $A(T = 1) = 2.03$ at the free surface and $A(T = 1) = 2.19$ at the supported surface.

ξ and A, is depicted in figure 4.10. For the supported surface we find that $\xi(T)$ slightly increases on cooling and that this increase closely agrees with that obtained previously for confined films [32]. However, the numerical value of $\xi(T)$ remains small for all T studied ($\xi(T) \sim 1 \mathrel{\widehat{=}}$ monomer diameter). For the free surface, we also find an increase of $\xi(T)$. However, it is weaker than that obtained at the supported surface, although visual inspection of figure 4.9 would suggest the penetration depth of the perturbation of the dynamics to be of comparable range for both the free and supported surfaces. Apparently, the increase of the second fitting parameter $A(T)$ interferes with that of ξ (cf. figure 4.10). Due to this interdependence of ξ and A, it appears fair to say that, while equation (4.13) allows to parameterize the data, it does not provide an unambiguous interpretation of ξ as a length scale measuring the penetration depth of the surface-induced deviation of the dynamics from bulk behavior.

4.4 Thickness dependence of T_c

In references [4, 5] Herminghaus et al. suggested a formula for the thickness dependence of T_g

$$T_g(h) = \frac{T_g}{1 + h_0/h} \,. \tag{4.14}$$

Here T_g denotes the bulk glass transition temperature and h_0 is a characteristic length scale. Equation (4.14) is obtained from the assumption that the relaxation in a film close to T_g is mainly due to a coupling of the viscoelastic bulk to capillary waves at

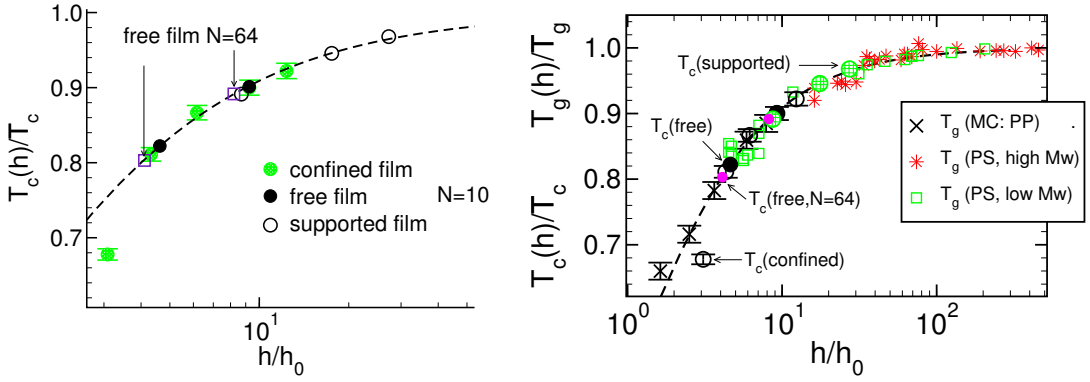

Figure 4.11: LEFT PANEL: $T_c(h)/T_c$ (T_c = bulk value) versus rescaled height h/h_0 for supported films (open circles), free-standing films (full circles), and MD results for a polymer film confined between two smooth repulsive walls (BE model at $p = 1$) [35, 36] (shaded circles). The dashed line indicates the master curve $y = 1/(1 + x)$ with $h_0 = 0.77$ for the supported films, $h_0 = 1.47$ for the free-standing films, and $h_0 = 1.64$ for the confined films. RIGHT PANEL: same scaling plot for $T_c(h)$ and $T_g(h)$. The results for $T_c(h)$ are reproduced from the left figure. They are compared to the glass transition temperatures $T_g(h)$ of three studies: (i) Monte Carlo simulations of a lattice model for free-standing atactic polypropylene (PP) films [12] (crosses; $N = 50$; $T_g = 391$ K, $h_0 = 6.1$ Å; 9.95 Å $\leq h/2 \leq 48.1$ Å). Both T_g and h_0 are results of a fit to equation (4.14). (ii) Experiments of supported atactic polystyrene (PS) films (spin cast from toluene solution onto silicon wafers) [4] (open squares; $N \simeq 20$; $T_g = 327$ K = bulk T_g for $N = 20$, $h_0 = 8.2$ Å; 38.5 Å $\leq h \leq 1678$ Å). (iii) Experiments of supported, high-molecular weight PS films [1] (stars; $N \simeq 29000$; $T_g = 375$ K, $h_0 = 6.8$ Å [155]; 110 Å $\leq h \leq 3100$ Å). The data of references [4, 12] are reproduced with permission. The high-molecular weight PS data are reproduced from reference [2]. The dashed line indicates equation (4.14).

the free surface. The analysis of this model determines the parameter h_0 as $h_0 = \gamma/E$ where E is Young's modulus of the film and γ the surface tension at the free surface. Equation (4.14) allows to parameterize the h dependence of T_g fairly well, for both experimental (see e.g. [4, 8, 155]) and simulation results (see inset of figure 4.11).

We want to apply equation (4.14) to our simulation data and use the critical temperatures $T_c(h)$ for this analysis. Since the bulk T_c is known, the only open parameter is h_0. We deduce h_0 by inversion of equation (4.14), i.e., by $h_0 = h\,(T_c/T_c(h) - 1)$ with the choice $h = h(T_g)$. (The difference in film thickness between T_g and T_c is negligible because both temperatures are fairly close to each other.)

The results of this analysis are included in table A.1 for $N = 10$ and in table A.2 for $N = 64$. Two conclusions may be drawn: (i) The h_0 values obtained from different thicknesses of the same film geometry (supported or free-standing) are almost constant, although the agreement is better for the free-standing films. (ii) The h_0 value for the free-standing film is almost twice as large as that for the supported film. This corroborates our previous conclusion that a free-standing film of thickness h

(roughly) corresponds to a supported film of thickness $h/2$. Both findings are in accordance with experimental results (see e.g. [5, 40, 156]). We find an increase of h_0 with increasing chain length. However, from the experimental results—cf. figure 4.11—one should expect h_0 to decrease with increasing N. We found the opposite trend.

In figure 4.11 we show $T_c(h)/T_c$ for all films as a function of the rescaled height h/h_0, using $h_0 = 1.47$ for the free-standing films and $h_0 = 0.77$, the average of the h_0 values quoted in table A.1, for the supported films. With a surface tension at the free surface of $\gamma = 1.55$ this would suggest an elastic modulus of approximately $E \sim 1$. This value is not unreasonable [15].

Figure 4.11 also includes the data from references [35, 36] obtained from MD simulations of polymer films confined between purely repulsive, flat walls at $p = 1$ employing a slightly different bead-spring model (BE model, see section 2.1). Here the good agreement with equation (4.14) is surprising, since capillary waves should be suppressed by the solid interface. In references [32, 35, 36] the depression of T_c for the confined films was attributed to the weaker packing of the monomers (i.e., smaller $S(q^*)$) compared to the bulk. This raises doubts that the mechanism which led Herminghaus et al. to suggest equation (4.14) is alone responsible for the found T_c (or T_g) reductions (for further discussion of references [4, 5] and other theoretical approaches see e.g. [32]).

4.5 Position-dependent T_c

In the following we want to once again focus on the penetration depth of the surface effects for the dynamics at a free surface and explore its T dependence further. To this end, we use again the local relaxation time defined in equation (4.12). $\tau(y, T)$ measures the time it takes a monomer to move across its own size parallel to the wall, provided the monomer is in a layer at distance y from the wall.

Figure 4.12 shows the results of this analysis for a free-standing film $h \sim 14$ at various temperatures. Not unexpectedly, we find that $\tau(y, T)$ is small at the free surface and increases towards the bulk value with increasing y. Upon cooling, wall effects penetrate further and further into the film. In section 4.3.2 we tried, as was done in previous work on confined films [32], to extract a growing length scale from the range over which $\tau(y, T)$ deviates near the interface from bulk behavior. The analysis used an empirical formula suggested in [19]. We found that a drawback of this approach was that it was not always possible to unambiguously identify a growing length scale because other fit parameters could also increase (strongly) on cooling (see section 4.3.2 and [38]). Therefore, we suggest a different approach here which does not introduce a length scale, but associates a different critical temperature $T_c(y)$ with each layer at distance y from the interface.

Our approach is based on two assumptions. First, we presume that the average

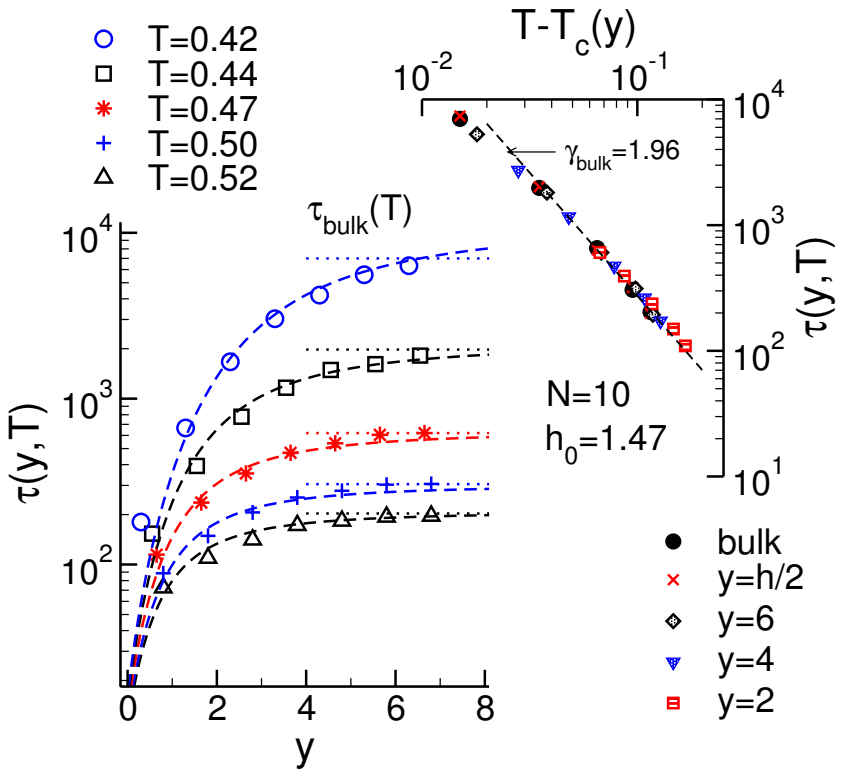

Figure 4.12: LEFT ORDINATE: Layer-resolved relaxation time $\tau(y,T)$ for $N = 10$ and various T versus distance y from the Gibbs dividing surface (GDS) for a free-standing film with $h \sim 14$. y is defined as the distance of the center of a layer from the GDS. The thickness of a layer is $\Delta y = 1$. $\tau(y,T)$ is defined by (4.12). The dotted horizontal lines indicate the bulk value $\tau_{\rm bulk}(T)$. The dashed lines represent (4.17) where $T_c(y)$ is computed from (4.16). RIGHT ORDINATE: $\tau(y,T)$ as a function of the reduced temperature $T - T_c(y)$ in different layers of the films. The dashed line indicates (4.17). The bulk results are also included.

$T_c(h)$ of the film can be written as an arithmetic mean of $T_c(y)$. That is,

$$T_c(h) = \frac{2}{h}\int_0^{h/2} {\rm d}y\, T_c(y). \tag{4.15}$$

Here we integrate from the position of the free surface (i.e. of the Gibbs dividing surface) to $h/2$ because a free-standing film is symmetric about its center. Using then (4.14) one can determine $T_c(y)$ by differentiation. This gives

$$T_c(y) = \frac{T_c(1+\frac{h_0}{y})}{(1+\frac{h_0}{2y})^2}. \tag{4.16}$$

The second hypothesis is that the sole effect of the surface is to shift T_c—from the bulk value to $T_c(y)$. We thus postulate that the position and temperature dependent

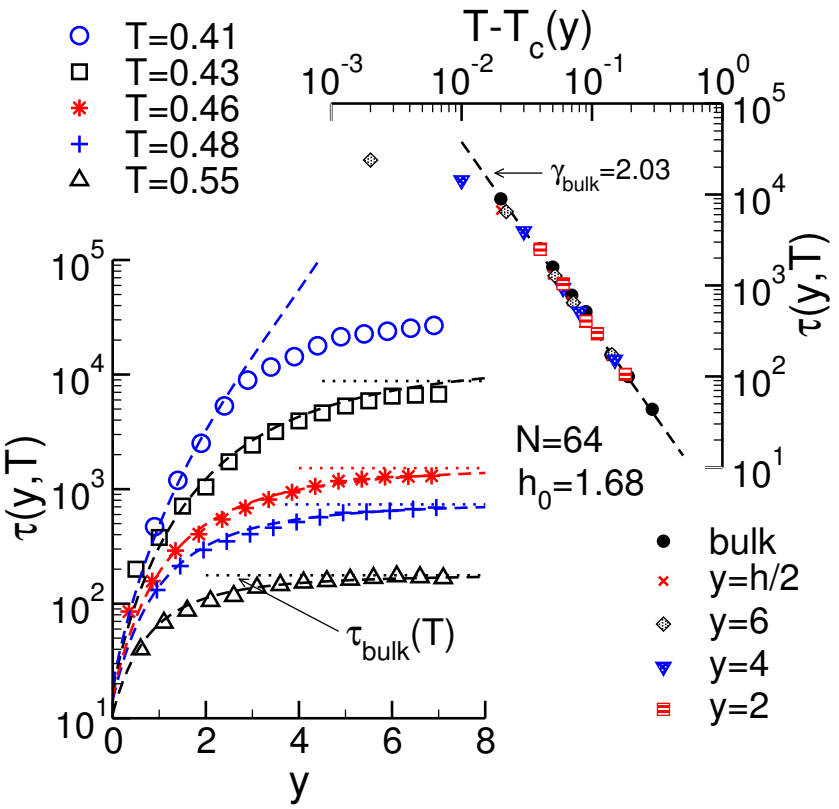

Figure 4.13: LEFT ORDINATE: Layer-resolved relaxation time $\tau(y,T)$ for $N = 64$ and various T versus distance y from the Gibbs dividing surface (GDS) for a free-standing film with $h \sim 15$. y is defined as the distance of the center of a layer from the GDS. The thickness of a layer is $\Delta y = 1$. $\tau(y,T)$ is defined by (4.12). The dotted horizontal lines indicate the bulk value $\tau_{\rm bulk}(T)$. The dashed lines represent (4.17) where $T_{\rm c}(y)$ is computed from (4.16). RIGHT ORDINATE: $\tau(y,T)$ as a function of the reduced temperature $T - T_{\rm c}(y)$ in different layers of the films. The dashed line indicates (4.17). The bulk results are also included.

relaxation time $\tau(y,T)$ can be expressed as

$$\tau(y,T) = \frac{a_{\rm bulk}}{(T - T_{\rm c}(y))^{\gamma_{\rm bulk}}}. \tag{4.17}$$

For $N = 10$ all parameters of equations (4.16) and (4.17) are known from the analysis performed in the previous sections (see also [38]), so that $h_0 = 1.47$; $T_{\rm c} = 0.405$, $a_{\rm bulk} = 3.01$ and $\gamma_{\rm bulk} = 1.96$ can be used to evaluate equation (4.17) and allow for a direct comparison between the prediction and simulation. Figure 4.12 depicts the results of this comparison. For all T shown the y-dependence of $\tau(y,T)$ is very well described by (4.17). Only if the distance from the surface becomes comparable to the thickness of the layer the MSDs are calculated in deviations arise. This is the case here for $y \leq 1$. Additionally, it can be seen from the inset that the slowing

down within the different layers of the film is indeed bulk-like upon replacing the bulk T_c by $T_c(y)$. This supports our initial assumption, (4.15).

The results presented in figure 4.12 are not an exception. To demonstrate that, we extended our analysis to longer chains, $N = 64$. For $N = 64$ we obtained $h_0 = 1.68;\ T_c = 0.415,\ a_{\rm bulk} = 3.3$ and $\gamma_{\rm bulk} = 2.03$. As expected, T_c is (slightly) larger than for $N = 10$ ($T_c = 0.405$). Figure 4.13 shows that we can again describe $\tau(y, T)$ by (4.17) over the whole y and T range, except for the lowest temperature $T = 0.41$. Contrary to the analysis for $N = 10$, this temperature is below the bulk critical temperature $T_c = 0.415$. Close to T_c the MCT approximation for the relaxation time breaks down (see e.g. [32] for a detailed discussion of this point) and thus also equation (4.17) cannot be expected to reproduce the simulation data.

4.6 Non-Gaussian parameter

The parameter α_2 quantifies the deviation of the distribution of the mean-square-displacements from a Gaussian distribution. Here we investigate the deviations of the MSD of all monomers $g_0(t)$, defined in equation (4.3) from a Gaussian distribution of displacements. In three dimensions the non-Gaussian parameter is defined as

$$\alpha_2(t) = \frac{3\langle|\mathbf{r}_i(t) - \mathbf{r}_i(0)|^4\rangle}{5g_0(t)^2} - 1\ . \tag{4.18}$$

If the probability P to have a displacement of r at time t is given by a Gaussian distribution

$$P(r) = (\pi\sigma^2)^{-3/2}\exp(-\frac{r(t)^2}{\sigma(t)^2})\ , \tag{4.19}$$

the second moment m_2 and fourth moment m_4 of this Gaussian distribution are given by

$$m_2 = \int_0^\infty 4\pi r^2 dr r^2 P(r) = \sigma/3 \tag{4.20}$$

and

$$m_4 = \int_0^\infty 4\pi r^2 dr r^4 P(r) = \sigma^2/15\ . \tag{4.21}$$

It follows directly that $m_4/m_2^2 = 5/3$ and $\alpha_2 = 0$.

Upon the assumption of a Gaussian distribution of the displacements the incoherent scattering function defined in equation (4.2) can by approximated by

$$\phi_q^{\rm G}(t) = {\rm e}^{-\frac{1}{6}q^2 g_0(t)}\ . \tag{4.22}$$

Non-Gaussian displacements can result in slower relaxation than expected from equation (4.22). A first correction is given by introducing α_2 [123]

$$\phi_q^{\rm Gc}(t) = \phi_q^{\rm G}(t)\left(1 + \frac{1}{2}\left[\frac{q^2 g_0(t)}{6}\right]^2 \alpha_2(t)\right)\ . \tag{4.23}$$

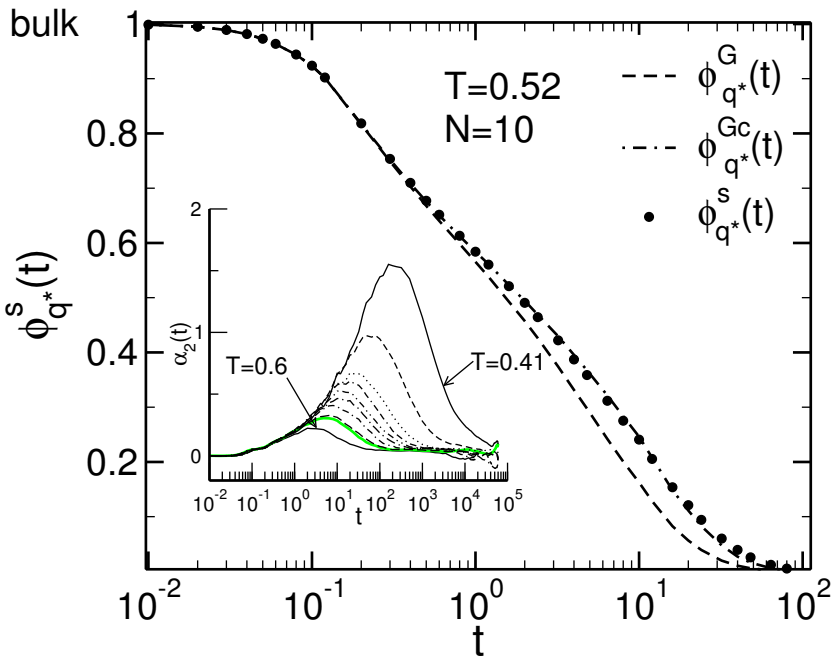

Figure 4.14: MAIN FIGURE: Incoherent scattering function at wave vector $q = 7$ and $T = 0.52$ for the bulk. The dashed line corresponds to the Gaussian approximation (equation (4.22) while the dash-dotted line includes the first correction (equation (4.23); the bin width was $\Delta q = 0.1$. INSET: shows the non-Gaussian parameter α_2 at temperatures $T = 0.6$, $T = 0.53$, $T = 0.52$, $T = 0.5$, $T = 0.48$, $T = 0.47$, $T = 0.46$, $T = 0.45$, $T = 0.43$, and $T = 0.41$

4.6.1 Bulk

In figure 4.14 the incoherent scattering function of the bulk melt at $T = 0.52$ and $p = 0$ is displayed. In addition the Gaussian approximation is indicated. Already at this relatively high temperature $(T - T_c \simeq 0.1)$ the system relaxes more slowly than expected from equation (4.22). The inclusion of the first correction as given in equation (4.23) allows to represent the incoherent scattering function quite well.

The inset shows α_2 for different temperatures. At very small times the displacement of the monomers is proportional to their velocities which are spread in a Gaussian distribution, the Maxwell distribution. At very large times the motion is diffusive and this by definition is a Gaussian process. Thus α_2 is zero for very large and very small times. At intermediate times deviations from Gaussian behavior occur. The non-Gaussian parameter exhibits a small step at $t \sim 0.1$ due to the inter-particle forces followed by a strong increase towards a maximum as the effects of caging become apparent and a plateau as the monomers move sub-diffusively which might be due to the weak interactions of the chains centers of mass. For a more detailed description see [157].

As the system is cooled the peak of the non-Gaussian parameter increases and is

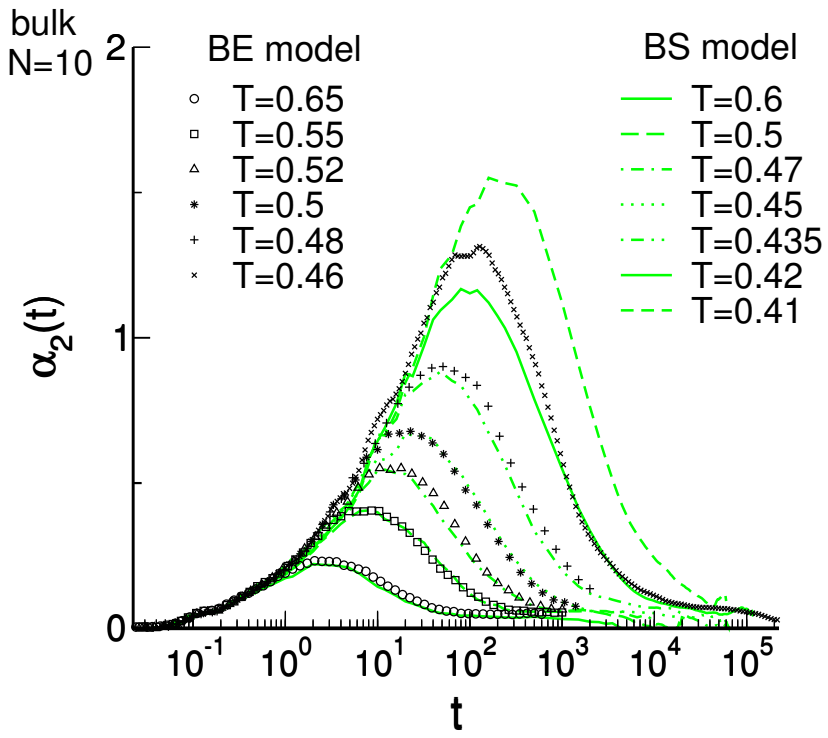

Figure 4.15: We show the non-Gaussian parameter α_2 at temperatures $T = 0.6$, $T = 0.5$, $T = 0.47$, $T = 0.45$, $T = 0.435$, $T = 0.42$, and $T = 0.41$ for the BS model (see section 2.1) at $p = 0$ and at temperatures $T = 0.65$, $T = 0.55$, $T = 0.52$, $T = 0.5$, $T = 0.48$, and $T = 0.46$ for the BE model at $p = 1$ (data from reference [157]).

shifted to larger times as more and more particles need to move cooperatively to leave their cage. The height of the following plateau remains unaltered as temperatures changes.

In reference [157] the BE model at $p = 1$ introduced in section 2.1 was used to calculate the non-Gaussian parameter and investigate the dynamics of the particles. As we already have done for the static properties in section 3.2.1 and the MSDs in section 4.1.1 we now want to also compare our results at $p = 0$ using the BS model (see section 2.1) for $\alpha_2(t)$ at the same distance from T_c to the results obtained in [157]. The difference in T_c between the two models at $p = 1$ and $p = 0$ respectively was determined to be $\Delta T_c \simeq 0.045$ (see section 3.2.1 and 4.1.1).

Figure 4.15 shows the results of this comparison at different temperatures reaching from the liquid state down into the super-cooled regime close to T_c. α_2 in the two different systems agrees quantitatively if one accounts for the difference in T_c at all temperatures but for the lowest temperatures. For most of the curves shown $\Delta T = 0.05$ while $\Delta T_c \simeq 0.045$. Because the dynamics become very sensitive to small changes in temperature, deviations occur due to small mismatches in ΔT_c be-

tween the two systems. At the lowest temperature displayed this effect can be seen clearly. The good agreement of the two models is another hint that the same mechanism is responsible for the slowing down of the dynamics in our system as in the extensively studied BE model.

4.6.2 Films

The Gaussian approximation and the first correction are dependent on the dimensionality of the system. Therefore one obtains for displacements within the plane of the film

$$\phi_q^{\mathrm{G}\parallel}(t) = \mathrm{e}^{-\frac{1}{4}q^2 g_0^{\parallel}(t)} \tag{4.24}$$

and

$$\phi_q^{\mathrm{Gc}\parallel}(t) = \phi_g^{\mathrm{G}\parallel}(t) \left(1 + \frac{1}{2} \left[\frac{q^2 g_0^{\parallel}(t)}{4} \right]^2 \alpha_2^{\parallel}(t) \right) \tag{4.25}$$

with

$$\alpha_2^{\parallel}(t) = \frac{\langle |\mathbf{r}_i^{\parallel}(t) - \mathbf{r}_i^{\parallel}(0)|^4 \rangle}{2 g_0^{\parallel}(t)^2} - 1 \,, \tag{4.26}$$

where $g_0^{\parallel}(t)$, given in equation (4.5), is the MSD of all monomers in the plane of the film. We also calculate the non-Gaussian parameter in layers centered at y as was done for the MSDs and the incoherent scattering function in section 4.3.1.

$$\alpha_2^{\parallel}(t,y) = \frac{1}{2 g_0^2(y,t)} \left\langle \frac{1}{n_t} \sum_i \prod_{t'=0}^{t} \delta\left[y - y_i\left(t'\right) \right] |\mathbf{r}_i^{\parallel}(t) - \mathbf{r}_i^{\parallel}(0)|^4 \right\rangle - 1 \,, \tag{4.27}$$

where $g_0(y,t)$ is the layer-resolved MSD of all monomers defined in equation (4.10).

In figure 4.16 the non-Gaussian parameter $\alpha_2^{\parallel}$ is compared for the bulk to the one averaged over the whole film for supported and free standing films of different thickness at $p = 0$ and $T = 0.52$. This is about $\Delta T = 0.1$ above the critical temperature of the bulk. As for the bulk at very small times $\alpha_2^{\parallel} = 0$ in the films. Then $\alpha_2^{\parallel}$ increases towards a maximum and decays to zero for very large times. The bulk exhibits the smallest maximum at the largest time. The maxima shift to shorter times the smaller the film thickness. The height of the maxima is slightly larger for thicker films and the decay time is longer. The films have an additional source of dynamic heterogeneity, since the beads at the surface move faster than the ones in the middle which is responsible for the increase in $\alpha_2^{\parallel}(t)$ as we will show in the following.

Also indicated in the left panel of figure 4.16 is the layer-resolved $\alpha_2^{\parallel}(y,t)$ calculated in layers at the center, at the supported and at the free surface of the films of width $\Delta y = 1$. The results in the center of the film agree well with the bulk data while the ones at the surfaces show a lower maximum at a shorter time. This is in agreement

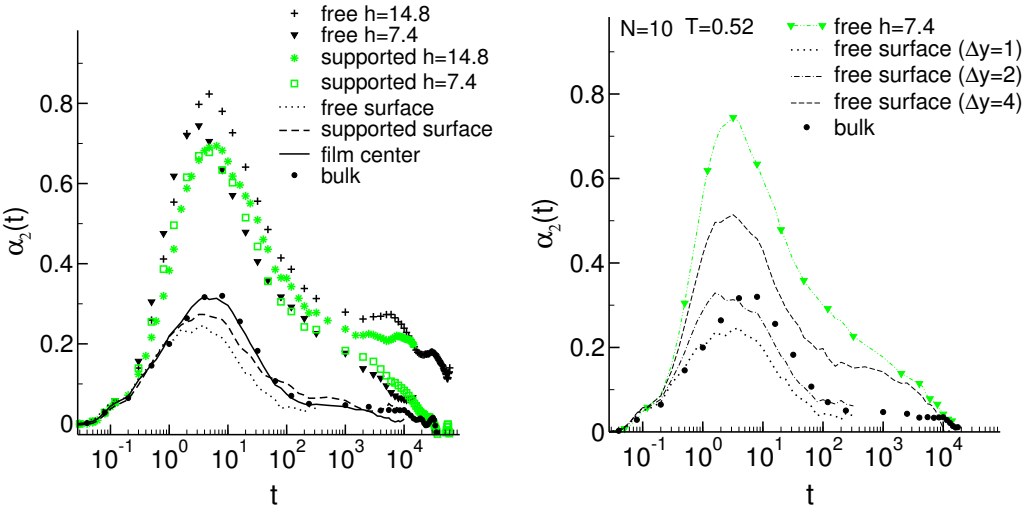

Figure 4.16: LEFT PANEL: The non-Gaussian parameter α_2, calculated for the MSDs in the parallel direction is compared between the bulk (circles) and supported films of $h = 7.4$ (squares) and $h = 14.8$ (stars) and free-standing films of $h = 7.4$ (triangles) and $h = 14.8$ (+) at $T = 0.52$ and $N = 10$. Also indicated is α_2 calculated for the layer resolved MSDs in a slab of thickness $\Delta y = 1$ at the supported surface (dashed line), in the center (full line) and at the free surface (dotted line). RIGHT PANEL: The non-Gaussian parameter α_2, calculated for the MSDs in parallel direction, is compared between the bulk (circles) and a free standing film of $h = 7.4$ (triangles) at $T = 0.52$ and $N = 10$. Also indicated is α_2 calculated for the layer-resolved MSDs in a slab of thickness $\Delta y = 1$ (dotted line), $\Delta y = 2$ (dash-dotted line) and $\Delta y = 4$ (dashed line) centered at the free surface.

with our previous observation that T_c is lower at the surfaces. Only if one looks at the overall non-Gaussian parameter of the films the peak is much higher than the bulk value. This stems from the heterogeneities of the dynamics between different layers, which is illustrated in the right panel of figure 4.16. The height of the maximum of $\alpha_2^{\parallel}(y,t)$ centered at the free surface of a free-standing film is strongly dependent on the width of the slab for which the coefficient is calculated. The wider the slab, the larger is the difference in the relaxation times of the beads because of their different distance from the surface. As a consequence the peak of $\alpha_2^{\parallel}(t)$ grows with growing slab width Δy.

The non-Gaussian parameter in the perpendicular direction is given as

$$\alpha_2^{\perp}(t) = \frac{\langle |\mathbf{r}_i^{\perp}(t) - \mathbf{r}_i^{\perp}(0)|^4 \rangle}{3 g_0^{\perp}(t)^2} - 1 \,, \tag{4.28}$$

where $g_0^{\perp}(t)$ defined in equation (4.6) is the MSD of all beads in the direction perpendicular to the wall. It does not decay to zero for large times due to the confinement. Since at large times the initial and final positions decorrelate, the probability to have

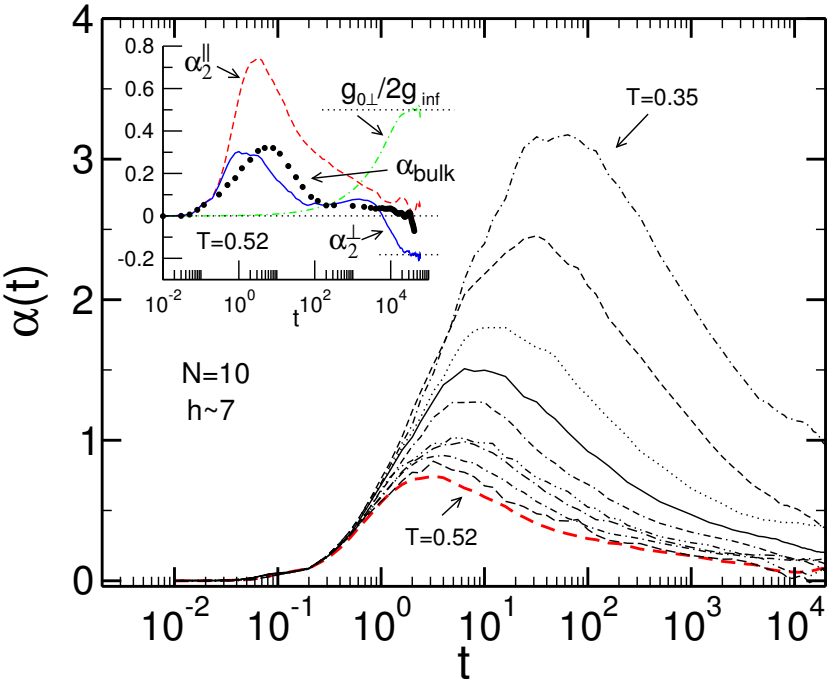

Figure 4.17: MAIN FIGURE:The non-Gaussian parameter in the parallel direction $\alpha_2^{\parallel}$ for a free standing film containing 288 polymers at $T = 0.52$, $T = 0.5$, $T = 0.48$, $T = 0.47$, $T = 0.46$, $T = 0.45$, $T = 0.43$, $T = 0.41$, $T = 0.38$ and $T = 0.35$. The thickness at $T = 0.52$ was $h = 8$. INSET: shows $\alpha_2^{\parallel}$ (dashed line), $\alpha_2^{\perp}$ (full line), α_2^{bulk} (full circles) and $g_0^{\perp}(t)/2g_0^{\perp}(\infty)$ (dash-dotted line). The horizontal lines indicate the asymptotic values.

a displacement y is proportional to the average density at the initial point y_i and final point $y_f = y_i \pm y$ so that $P(y) \propto \int dy_i \rho(y_i)\rho(y_i + y)$. For a free standing film the density is quite well approximated by a rectangular distribution $\rho(y) = \rho_0$ for $0 < y < h$ and zero elsewhere. In this case

$$\alpha_2^{\perp}(t \to \infty) = -0.2\,. \tag{4.29}$$

The exact limiting value found in the simulations is dependent on the exact features of the density profile. For the MSD in the perpendicular direction it is found that

$$g_0^{\perp}(\infty) = \frac{\int_0^{\infty} \mathrm{d}y' \int_0^{\infty} \mathrm{d}y \rho(y')\rho(y)(y - y')^2}{\left(\int_0^{\infty} \mathrm{d}y \rho(y)\right)^2}\,, \tag{4.30}$$

and the non-Gaussian parameter saturates at

$$\alpha_2^{\perp}(\infty) = \frac{1}{3}\frac{\int_0^{\infty} \mathrm{d}y' \int_0^{\infty} \mathrm{d}y \rho(y')\rho(y)(y - y')^4}{\left(\int_0^{\infty} \mathrm{d}y \rho(y)\right)^2 g_0^{\perp}(\infty)^2} - 1\,. \tag{4.31}$$

In figure 4.17 the non-Gaussian parameter $\alpha_2^{\parallel}$ for $T = 0.52$ to $T = 0.35$ is displayed for a free standing film of thickness $h = 8$. For small times the behavior is very similar to the one of the bulk but the increase towards the peak begins earlier and the maximum is higher. Also the decrease is much slower and no pronounced plateau can be seen. Only for the highest temperature, $\alpha_2^{\parallel}$ decays to zero.

The inset shows the dynamics in the direction perpendicular to the film. It can take much longer than the relaxation time of a chain to reach a regime where the conditions leading to equation (4.29) are full-filled. Only then each monomer has visited the whole film and all monomers move diffusively with the same effective diffusion constant. Thus the decay of the non-Gaussian parameter is coupled to the dynamics of the system in the perpendicular direction. This is also the reason why the decay is faster for thinner films because it takes a shorter time to reach the asymptotic condition in the perpendicular direction. The non-Gaussian parameter $\alpha_2^{\perp}$ saturates at a value close to -0.2 as explained above.

Therefore the assumption made in the previous section on the position dependence of T_{c} that the slowing down is bulk like but for the shift in T_{c} is in agreement with the fact that we could show that the non-Gaussian parameter is larger in the films only due to the dynamic differences between the layers and not due to a growing dynamic heterogeneity at a given distance from the wall.

4.7 Summary

When a supported or free-standing polymer film is confined to nanoscopic dimensions its glass transition temperature can be depressed relative to the bulk value [30, 31] in experiments. We extended the simulations of Fathollah Varnik on confined films [32, 35] to supported and free-standing films. For the studied polymer films we clearly find by a layer-resolved analysis (section 4.3.1) that monomers at the free and solid interfaces are faster than those in the center of the film, and that the monomers at the free surface are faster than those at the solid interface. These highly mobile monomers appear to transfer part of their mobility to the next deeper layer, which in turn can accelerate the next layer, and so on until the effect is damped out if the film is thick enough. The dynamics of the monomers in the film center is then bulk-like. This also leads to faster dynamics on average (section 4.1) in the thin films in comparison with the bulk. At the same thickness the relaxation is faster in free standing than in supported films. These trends are reflected in the decrease of T_{c} determined in section 4.2 and T_{g} (see section 3.1) with decreasing film thickness. At a given film thickness T_{c} and T_{g} are lower in a free-standing film than in a supported film. These results were published in reference [38].

We also find that the first maximum of the static structure factor $S(q)$ is smaller in the films than in the bulk when the same temperatures are compared (see section 3.2). By contrast, the intrachain structure factor remains essentially unchanged. This

implies that the confinement alters the intermolecular packing. The dynamic differences could therefore be explained along the lines of MCT by the difference in static structure of the bulk and the films. The "cage" around a monomer cannot "tighten" so quickly on cooling, as it is possible in the bulk. Since this effect becomes more pronounced with decreasing h, and the tightening of the cage appears to be the main factor triggering the slow relaxation in the supercooled bulk melt, we believe that this perturbation of the liquid structure is for our model an important reason why the dynamics is faster in the films than in the bulk as was also suggested by the simulations on confined films by Varnik et al. [32, 35]. Nevertheless it is not possible to explain the differences in relaxation time between supported and free standing films within this picture as the reduction of the first peak of the static structure factor is comparable in both film geometries at a given film thickness.

It appears natural to assume—and also other simulations [12, 14, 16, 21] suggest—that monomers in contact with the free surface are less constrained and thus more mobile than in the bulk. Faster dynamics at the free surface were also observed using atomistic MD simulation of thin films of polypropylene [12] as well as in simulations employing more coarse-grained models [14, 16, 21] similar to the one employed in this study. An investigation of the local mechanical properties of the films by de Pablo and coworkers [15, 16] as well as an analysis of the segmental mobility carried out very recently by Morita et al. [21] find evidence for a lower T_{g} at the surface.

One may thus hypothesize that the observed T_{g} reductions are caused by a liquid-like surface layer [1]. There is experimental evidence supporting this idea. For instance, NMR experiments by Herminghaus et al. suggest that there is a well-defined molten layer at the surface of a thin film of nonentangled polystyrene (PS) chains [5]. Similar results are also obtained for highly entangled PS chains by Ellison and Torkelson [9]. By means of a fluorescence/multilayer technique they conclude that there is a continuous reduction of T_{g} on approaching the free surface.

In section 4.5 we provide further evidence for these experimental observations by molecular dynamics simulations of a bead-spring model. We studied nonentangled ($N = 10$) and slightly entangled ($N = 64$) chains in a temperature regime above the critical temperature T_{c} of mode-coupling theory. For both chain lengths we find that the film dynamics is spatially heterogeneous. Monomers at the free surface relax faster than they would in the bulk at the same temperature T. The relaxation transitions from enhanced to bulk dynamics with increasing distance y from the surface. For all T the crossover to bulk dynamics remains smooth, but its range grows on cooling. This gradient in the relaxation dynamics may be associated with a gradient of critical temperatures $T_{\mathrm{c}}(y)$. Here $T_{\mathrm{c}}(y)$ is not a fit parameter; its distance dependence can be derived from two ingredients. First, we assume that $T_{\mathrm{c}}(h)$—the global T_{c} for a film of thickness h—is the arithmetic mean of $T_{\mathrm{c}}(y)$. Second, we use the result that the depression of $T_{\mathrm{c}}(h)$ with decreasing h, found in our simulations, can be well described by equation (4.14), an expression suggested in reference [4] for the reduction of T_{g} in supported PS films.

The so-obtained local $T_c(y)$ appears to be an important reference point for the layer-resolved dynamics in our model. When plotting $\tau(y, T)$, the local relaxation time, versus the reduced temperature $T - T_c(y)$ we find a master curve for all layers which coincides with the increase of the bulk relaxation time on cooling toward the bulk T_c (see figures 4.12 and 4.13). Individual layers thus behave as if they were a bulk system with reduced critical temperature. This suggests that the different T dependence of the bulk and film-averaged relaxation times—see figure 4.2—is probably due to 'dynamic heterogeneities' between the layers and not due to a growing heterogeneity within a given layer relative to the bulk. An assumption which is further supported by the analysis of the non-Gaussian parameter in the bulk and the films in section 4.6. Our results further suggest that the heterogeneity between the layers increases upon cooling because layers close to the film center experience a stronger slowing down than surface layers which are still quite far from their respective $T_c(y)$. These results were published in reference [39].

Chapter 5

Capillary waves

It was suggested that capillary waves at the free surface couple to the viscous flow of the bulk allowing a faster relaxation of the chain segments [4, 5] on the local scale, thus decreasing T_{g}. We found a decrease of T_{g} and T_{c} in our model polymer films and a decrease of the local packing constraints at the free surface as described in chapters 3 and 4. The question remains whether this effect is linked to capillary waves as suggested in reference [4]. Therefore in this chapter we would like to investigate the influence of capillary waves on the relaxation of the films in comparison with the bulk. We will first focus on the static correlations and then investigate the dynamics of the systems via the coherent scattering function and the dynamic structure factor.

While our study in section 3.2 was concerned with fluctuations at wavelengths of the order of $2\pi/\sigma$, where σ is the monomer diameter, and the properties of the chains in the melt, we now look at the long wavelength limit. This is often described by continuum theories. Here, we will compare the predictions of continuum theory to our simulation. In a film, density fluctuations at low q are dominated by capillary waves, i.e. fluctuations in the local film thickness. These fluctuations, as we will show, are a priori not limited in size. They are controlled by the surface tension and, in real experimental systems, the maximum length scale of the surface height fluctuations is limited by gravity or in thin films with strong substrate interactions by the so-called van der Waals cutoff related to the system's Hamaker constant [158]. As we did not include gravity in our model and the substrate interactions are weak they become as large as the lateral dimensions of the simulation box in our systems. These large spatial correlations entail long lived temporal correlations. A capillary wave is identified by its wave vector $\mathbf{q}$ and frequency $f = \omega_p + \mathrm{i}\Gamma_c$, where the real part reflects the propagation frequency and the imaginary part the damping. The wave can be either propagating or overdamped depending on $\mathbf{q}$, the surface tension γ, the viscosity η and the density ρ of the liquid [150, 159].

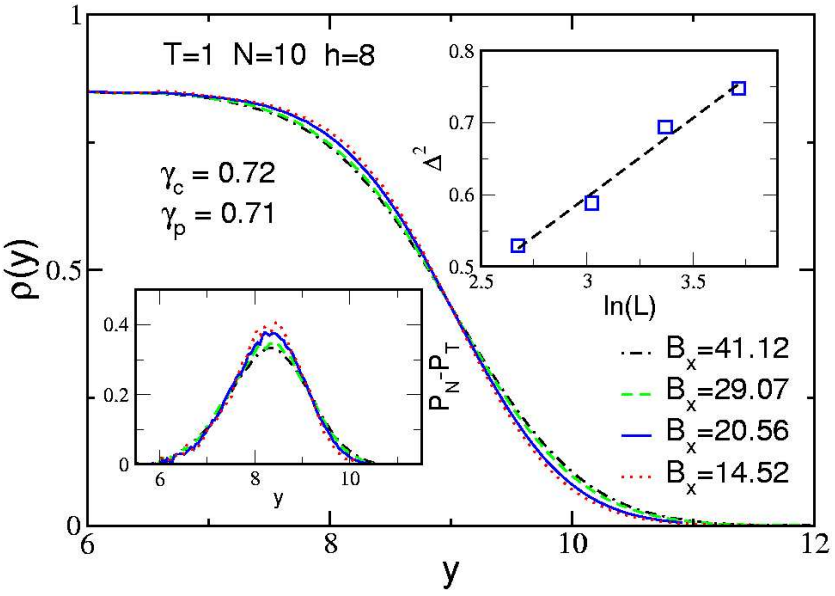

Figure 5.1: MAIN FIGURE: The density profile $\rho(y)$ of a supported film of thickness $h = 8$ at $T = 1$ is shown for different lateral system sizes [$B_x = 41.1245$ (dash-dotted line), $B_x = 29.0708$ (dashed line) , $B_x = 20.5622$ (full line) and $B_x = 14.5223$ (dotted line)]. INSETS:The right inset shows the width of the interface given by equation (5.8) as a function of the logarithm of the system size (rectangles) and a fit to equation (5.11) (dashed line). The left inset displays the y-resolved difference in normal and lateral pressure for different lateral system sizes. The same legends apply as for the main figure.

5.1 Statics

First we are interested in the influence of capillary waves on the static structure of the films. Here the relevant parameter is the surface tension.

5.1.1 Surface tension

The surface tension can be calculated from the difference of the normal and the tangential components of the pressure tensor defined in equation (2.33) as

$$\gamma_p = \int_{h/2}^{\infty} dy \, [P_N(y) - P_T(y)] \ . \tag{5.1}$$

Due to the mechanical stability of the film [125] the normal pressure has to be constant at $p = 0$ throughout the whole film while the tangential pressure can vary in the y-direction. Far from the surfaces the system assumes bulk-like behavior and the pressure is isotropic. In figure 5.1 the y-resolved difference in normal and tangential pressure at a free surface is shown for different lateral system sizes. The shape of the

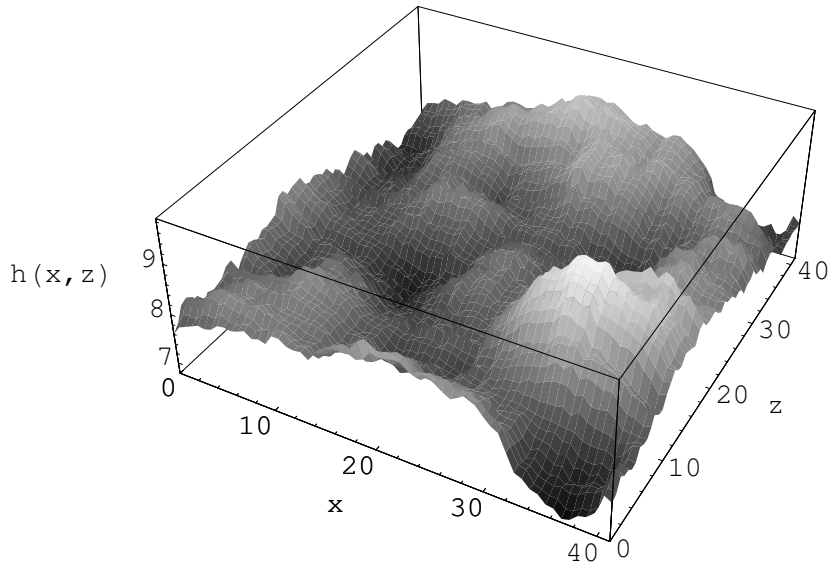

Figure 5.2: The local interface position h(x,z) for a film of average thickness $h = 8$. The lateral box size was 41.1245. In order to find the local position of the interface, averages over blocks of the size 6.85 were taken so that only the large scale fluctuations of the local interface position can be seen.

profile broadens as does the density profile with increasing lateral box size because larger and larger fluctuations of the interface position can be accommodated in the simulation box. But the surface tension given by equation (5.1) is $\gamma_p = 0.71$ within the error bars for all lateral box sizes investigated.

Alternatively, the surface tension can be calculated by analyzing the increasing broadening of the interface due to capillary waves with increasing lateral system size. This method was used to determine the surface tension of polymer mixtures by [160–162].

5.1.2 Capillary wave theory

The local position of the interface can be described by a function $h(x, z)$. Long-wavelength fluctuations of $h(x, z)$ lead to an increase of the interfacial area and thus they increase the free energy associated with the area. The capillary-wave Hamiltonian corresponding to this simple picture is given by

$$H_{\mathrm{CW}} = \frac{\gamma}{2} \int \mathrm{d}x\mathrm{d}z |\nabla h|^2 \, . \tag{5.2}$$

In Fourier space H_{CW} can be written as $\sum_q q^2 \frac{\gamma}{2} |\tilde{h}(\mathbf{q})|^2$ where $\tilde{h}(\mathbf{q})$ denotes the Fourier transform of the local interface position for the wave vector $\mathbf{q}$. From the equipartition theorem one can then deduce that

$$\langle |\tilde{h}(\mathbf{q})|^2 \rangle = \frac{T}{\gamma q^2} \, . \tag{5.3}$$

These assumptions result in a diverging mean-square displacement of the interface position

$$s^2 = \langle |h(x,z)|^2 \rangle \simeq \frac{T}{2\pi\gamma} \int dq \frac{1}{q} \, , \tag{5.4}$$

meaning, as already stated above, that fluctuations are not limited in size for a laterally infinite system. The amplitude of the fluctuations can be the larger, the larger their length scale is. It is necessary to introduce a lower cutoff $q_{\text{min}} = \frac{2\pi}{L}$ and an upper cutoff $q_{\text{max}} = \frac{2\pi}{B_0}$ of the wave vector yielding

$$s^2 = \frac{T}{2\pi\gamma} \ln \left(\frac{q_{\text{max}}}{q_{\text{min}}} \right) = \frac{T}{2\pi\gamma} \ln \left(\frac{L}{B_0} \right) \, . \tag{5.5}$$

In our simulations the fluctuations become as large as the lateral size of the box allows them to be. The largest length scale in our system is thus the lateral box size $B_x = B_z$ which naturally leads to the choice $L = B_x$. This only holds if the film thickness h is large in comparison with the surface height fluctuations at the q-vectors of interest. The smallest scale is related to the interfacial width of the so called intrinsic density profile which is in our case in the order of the monomer diameter, leading to $B_0 \sim 1$.

For the local interface position one finds a Gaussian height distribution

$$P_L(h) = \frac{1}{\sqrt{2\pi s^2}} e^{-h^2/2s^2} \tag{5.6}$$

The resulting interface is thus broadened due to capillary waves in addition to its intrinsic width Δ_0^2. This intrinsic width corresponds to an intrinsic interface profile. The apparent profile is assumed to be given by the convolution

$$\rho(y) = \int \mathrm{d}h \rho_{\text{int}}(y-h) P_L(h) \, . \tag{5.7}$$

The broadening of the interface due to capillary waves is simply added to the intrinsic broadening

$$\Delta^2 = \Delta_0^2 + \frac{T}{2\pi\gamma} \ln \left(\frac{L}{B_0} \right) \, , \tag{5.8}$$

in this approximation.

If one fits the density profile $\rho(y)$ defined in equation (3.1) to the function

$$\rho(y) = \frac{\bar{\rho}}{2} \left(1 - \text{erf} \left(\frac{\sqrt{\pi}\,(y-h)}{w_i} \right) \right) \, , \tag{5.9}$$

where h is the film thickness, $\bar{\rho}$ the average density of the film and w_i a fitting parameter related to the interfacial width through $\Delta^2 = \frac{w_i^2}{2\pi}$ [162]. erf(x) is the error function defined as

$$\text{erf}(x) = \frac{1}{\sqrt{2\pi}} \int_x^\infty \mathrm{d}u \, \mathrm{e}^{-\frac{u^2}{2}} \ . \tag{5.10}$$

By carrying out simulations at different lateral system sizes L the surface tension can be found by fitting the data to

$$\Delta^2 = a + b \ln(L) \, , \tag{5.11}$$

which gives $\gamma = \frac{T}{2\pi b}$. In figure 5.1 the density profile for different lateral system sizes L is shown. As expected from the theory sketched above, $\rho(y)$ broadens with increasing L. The surface tension $\gamma_\mathrm{c} = 0.72$ obtained by this approach and $\gamma_\mathrm{p} = 0.71$ calculated from the difference in lateral and normal pressure agree well and is independent of the area of the film. The films in our study are also thick enough for the surface tension and the surface height fluctuations to be independent of film thickness.

5.1.3 Low-q limit of the static structure factor

The fluctuations of the interface position due to capillary waves should also be reflected in the static structure factor $S(q)$ defined in equation (3.6) at small q. For $q < 1$ we expect

$$S(q) \propto \frac{T}{\gamma} \frac{1}{q^2} \, , \tag{5.12}$$

because at large length scales the dominant fluctuations are the ones due to capillary waves so that they should give a large contribution to $S(q)$.

In figure 5.3 we look at the structure factor at small q in layers in the middle and close to the surface of the film as well as in the bulk. All layers had a width of $\Delta y = 2$. In a bulk liquid $S(q = 0) = \beta \rho T$, where β is the isothermal compressibility of the system. Indeed we also find a constant value at small q in the middle of the film as well as at the supported surface. Indicating a higher compressibility of the system the plateau value is larger than in the bulk at the supporting wall as well as in the center of the film.

At the free surface we observe a completely different behavior. The structure factor shows a divergence following a power law as predicted by theory. Nevertheless, also the oscillations due to the packing of the monomers at larger q are still visible. The behavior at small q is independent of the system size which is as an indication that the periodic boundary conditions do not interfere with the longest wavelength capillary waves present so that an accurate description of the dynamics is possible down to wavelengths $q = \frac{2\pi}{L}$.

Following an analysis of the shape and width of the interfacial profile in a homopolymer blend in references [160, 161], we calculate the local interface position

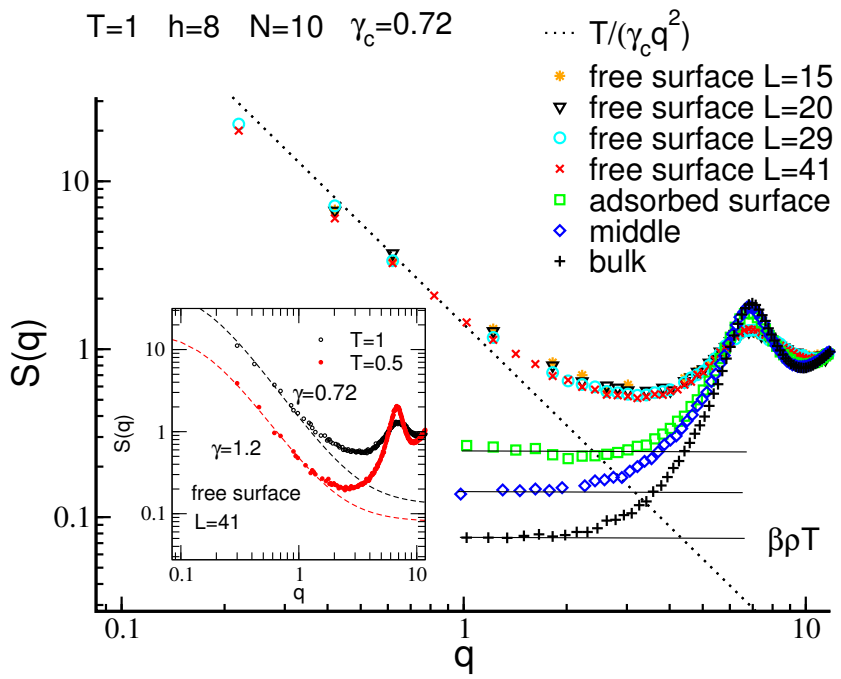

Figure 5.3: MAIN FIGURE: The layer-resolved structure factor in a slab of width $\Delta y = 2$ centered at the free surface of a supported film ($h = 8$, $N = 10$ and $T = 1$) for different lateral system sizes $L = 41.1245$ (crosses), $L = 29.0708$ (circles), $L = 20.5665$ (triangles) and $L = 12.5223$ (stars) is shown. Also indicated are the structure factor of the bulk melt (pluses), the layer-resolved structure factor found in the center of a supported film of thickness $h = 8$ with lateral box size $L = 20.5665$ (diamonds), and the layer resolved structure factor calculated at the supported surface of a film of thickness $h = 8$ with lateral box size $L = 20.5665$ (squares). The dotted line indicates the prediction of capillary wave theory for $S(q)$ given in equation (5.12). INSET: The inset compares the layer-resolved structure factor in a slab of width $\Delta y = 2$ centered at the free surface of a supported film ($h = 8$, $N = 10$) at $T = 1$ (open symbols) and $T = 0.5$ (full symbols). The lateral system size was $L = 20.5665$.

$h(x, z)$ on different length scales. We determine the local interface position $h(x, z)$ within slabs of different sizes. With the method of the GDS described earlier, one finds that $\bar{\rho} = \frac{N}{V} = \frac{N}{B_x B_z h}$. If the density is known, one can determine the height as $h = \frac{N}{B_x B_z \bar{\rho}}$. Under the assumption that density fluctuations are negligible on the scale of the slab size, i.e. the average density in the slab is assumed to be $\bar{\rho}$, the local interface position $h(x, z)$ can be calculated counting the particles $N_p(x, z)$ within a slab of area $L_x^B L_z^B$ centered at x and z by $h(x, z) = \frac{N_p(x,z) B_x B_y}{N L_x^B L_z^B} h$. We always chose the slab to be quadratic with $L_x^B = L_z^B = L_{\mathrm{CG}}$. This procedure averages out fluctuations on length scales smaller than the slab size L_{CG}. Thus it becomes now the natural upper cut-off for the fluctuation spectrum $B_0 = L_{\mathrm{CG}}$.

In figure 5.2 the local position of the interface is displayed for a supported film

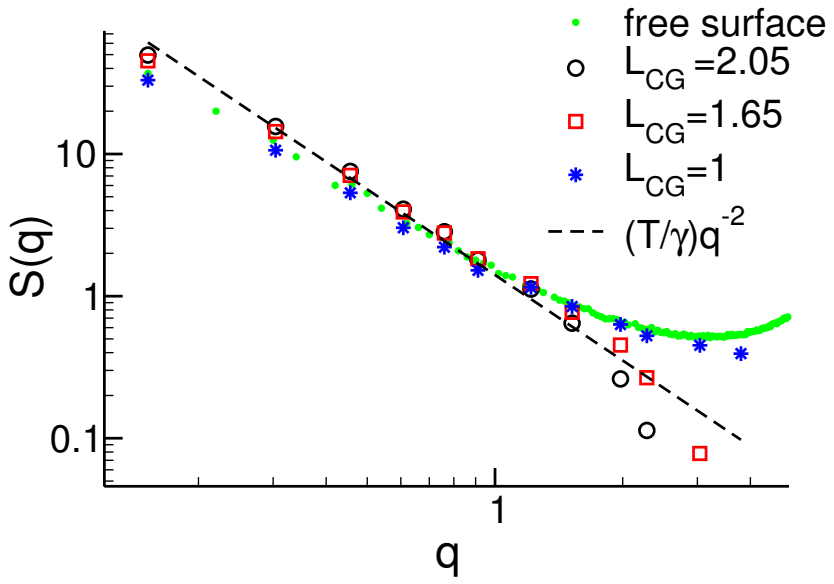

Figure 5.4: The spectrum of the surface height fluctuations calculated using different slab sizes ($L_{\mathrm{CG}} = 2.05$ circles,$L_{\mathrm{CG}} = 1.65$ squares and $L_{\mathrm{CG}} = 1$ stars) is shown. Also indicated are the static structure factor in the surface layer of the film (filled circles) and a fit to equation (5.12) (dashed line). The calculations were done for a supported film of $h = 8$ at $T = 1$ and a lateral box size $B_x = 41.1245$.

of average film thickness $h = 8$. For the calculation a very large size of the slabs was chosen $L_{\mathrm{CG}} = 6.85$ which averages out all fluctuations but the largest scale fluctuations present in the box resulting in a locally smooth surface. The smaller L_{CG} the rougher the resulting surface becomes as smaller and smaller fluctuations are picked up. The amplitude of the fluctuations is of the order of 2 monomer diameters, which is still considerably smaller than the overall thickness of the film.

In figure 5.4 the spectrum of the surface height fluctuations $\langle|\tilde{h}(\mathbf{q})|^2\rangle$ for different slab sizes L_{CG} is shown. At low wave lengths the results agree well with the theoretical predictions independent of slab size. If q becomes comparable to $2\pi/L_{\mathrm{CG}}$, a suppression of the fluctuations for $L_{\mathrm{CG}} = 2.05$ (circles) with respect to the theoretical prediction is seen, as expected. For the smallest value of L_{CG} which is comparable to the monomer diameter, on the other hand, an enhancement at higher q values becomes visible. As in this case there are only a few monomers in the slab, it becomes questionable whether the assumption of constant density used to derive the interface position is still valid. The result resembles the static structure factor just measured within the surface layer of the film.

Since the structure factor is normalized by the number of monomers which is proportional to the system volume while the effect of the capillary waves only increases with the surface area, we make the following ansatz for the overall structure factor

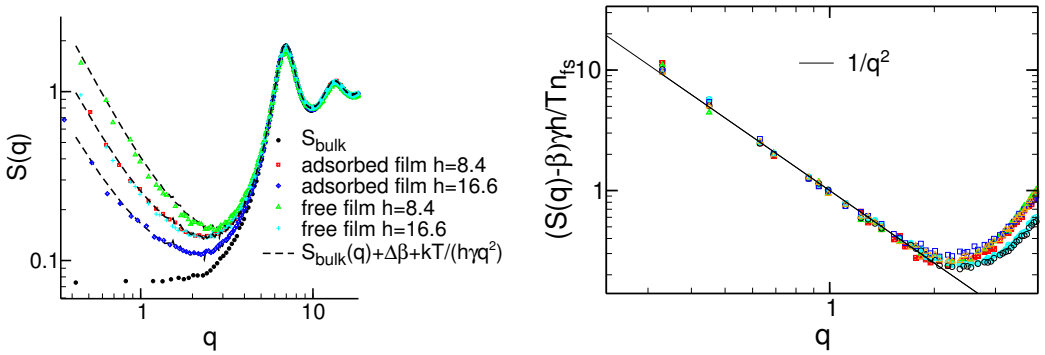

Figure 5.5: LEFT PANEL:The structure factor at $T = 1$ averaged over the whole film [supported film h=8.4 (filled squares), h=16.6 (filled diamonds), free film h=8.4 (triangles) and h=16.6 (pluses); the filled circles indicate the bulk] is displayed. The dashes lines show the approximation according to equations (5.13) and (5.14). Only q-vectors within the plane parallel to the surface are considered. RIGHT PANEL: Re-scaled structure factor $\frac{(S(q)-\beta)\gamma h(T)}{Tn_f}$ averaged over the whole film: supported film $n = 288$ (squares), free film $n = 288$ (circles) and $n = 576$ (triangles) at $T = 0.44$ (filled symbols) and $T = 0.52$ (open symbols). The black line indicates q^{-2}. Only q-vectors within the plane parallel to the surface are considered.

$S(q)$ of a supported thin film

$$S_{\text{sup}}(q) = S_{\text{bulk}}(q) + \frac{T}{\gamma h q^2} + \Delta\beta_{\text{T}} \, , \tag{5.13}$$

and $S(q)$ of a free film

$$S_{\text{free}}(q) = S_{\text{bulk}}(q) + \frac{2T}{\gamma h q^2} + \Delta\beta_{\text{T}} \, , \tag{5.14}$$

since there are two surfaces. h is the thickness of the film and the constant $\Delta\beta_{\text{T}}$ takes into account the difference in overall compressibility between the thin film and the bulk. As can be seen in figure 5.5 this works nicely for all film thicknesses displayed. The free film and the supported film of half the thickness agree very well at small q giving a further indication that the finite thickness of the films does not interfere with the surface height fluctuations.

We further test this assumption for lower temperatures by re-scaling the structure factor at low q with $\frac{(S(q)-\beta_{\text{T}})\gamma h(T)}{Tn_{\text{f}}}$ with n_{f} being the number of free surfaces and β_{T} a constant related to the compressibility. In figure 5.5 the re-scaled structure factor for different film geometries and temperatures is shown. The curves indeed collapse on a curve proportional to $1/q^2$ at low q although there is a large scatter.

5.2 Dynamic structure factors

It is now interesting to also investigate the influence of the capillary waves on the coherent scattering function given by

$$F(q,t) = \frac{1}{nN} \sum_{i=1}^{nN} \sum_{j=1}^{nN} \mathrm{e}^{-\mathrm{i}\mathbf{q}\cdot[\mathbf{r}_i(0)-\mathbf{r}_j(t)]} \ . \tag{5.15}$$

and its Fourier transform the dynamic structure factor $S(q,\omega)$

$$S(q,\omega) = \frac{1}{2\pi} \int_{-\infty}^{\infty} \mathrm{d}t \; e^{\mathrm{i}\omega t} F(q,t) \ . \tag{5.16}$$

5.2.1 Bulk relaxation in the hydrodynamic limit

We start by looking at the hydrodynamic limit i.e. at small q-vectors and large times of these functions in the bulk liquid. From the solution of the linearized Navier-Stokes equations one obtains for density fluctuations of wave vector q [123]:

$$\rho_q(t) = \rho_q(0) \left[\frac{\gamma_H - 1}{\gamma_H} \exp(-D_T q^2 t) + \frac{1}{\gamma_H} \exp(-\Gamma q^2 t) \cos(c_s q t) \right] \tag{5.17}$$

Here, $D_T = \frac{\lambda}{c_P \rho}$, where c_p is the isobaric specific heat capacity and λ the thermal conductivity, and $\Gamma = \frac{1}{2}\left[\frac{\lambda}{c_V \rho}\frac{\gamma_H - 1}{\gamma_H} + \frac{4/3\eta+\zeta}{\rho}\right]$, where c_V is the specific heat capacity at constant volume, $\gamma_H = \frac{c_P}{c_V}$, η is the shear-viscosity and ζ is the bulk viscosity. From the Fourier transform of the density by definition $F(q,t)$ can be calculated as

$$F(q,t) = \frac{1}{nN} \left\langle \rho_q(t) \rho_{-q}(0) \right\rangle \ , \tag{5.18}$$

yielding

$$F(q,t) = S(q) \left[\frac{\gamma_H - 1}{\gamma_H} \exp(-D_T q^2 t) + \frac{1}{\gamma_H} \exp(-\Gamma q^2 t) \cos(c_s q t) \right] \ . \tag{5.19}$$

$F(q,t)$ can be split into two parts one corresponding to a so-called thermal mode which describes entropy fluctuations decaying exponentially and a propagating mode representing sound waves damped in the viscous fluid [123]. Continuum theory thus predicts $S(q,\omega)$ to be given by

$$\begin{aligned} S(q,\omega) \ &= \ \frac{1}{2\pi} S(q) \left[\frac{\gamma_H - 1}{\gamma_H} \frac{2 D_T q^2}{\omega^2 + \left(D_T q^2\right)^2} + \right. \\ &\left. \frac{1}{\gamma_H} \left(\frac{\Gamma q^2}{(\omega - c_s q)^2 + \left(\Gamma q^2\right)^2} + \frac{\Gamma q^2}{(\omega + c_s q)^2 + \left(\Gamma q^2\right)^2} \right) \right] . \end{aligned} \tag{5.20}$$

It is possible to independently determine all parameters needed to evaluate $F(q,t)$ and $S(q,\omega)$ for our model system. The thermal conductivity λ, the shear viscosity η and the bulk viscosity ζ can be derived from Green-Kubo relations (all numbers refer to $N = 10$, $T = 1$ and $p = 0$ in a bulk system). The thermal conductivity can be evaluated as

$$\lambda = \frac{1}{3VT^2} \int_0^\infty dt \, \langle \, \mathbf{J}(t) \cdot \mathbf{J}(0) \rangle \simeq 4.9 \, , \tag{5.21}$$

where $\mathbf{J}(t)$ is the energy current in the system given by

$$J^\alpha(t) = \sum_i \frac{1}{2} \left[\mathbf{v}_i^\alpha \mathbf{v}_i^2 + \mathbf{v}_i^\alpha \sum_{j \neq i} U_{\text{pot}}(r_{i,j}) + \mathbf{v}_i \cdot \mathbf{r}_i \sum_{j \neq i} \mathbf{F}_{i,j}^\alpha \right] \, . \tag{5.22}$$

The viscosities can be found via the auto-correlation functions of the stress tensor calculated as

$$\sigma^{\alpha\beta} = \sum_i \left(\frac{1}{2} \sum_{j \neq i} \mathbf{F}_{i,j}^\alpha \mathbf{r}_i^\beta + \mathbf{v}_i^\alpha \mathbf{v}_i^\beta \right) \, . \tag{5.23}$$

The shear viscosity is given by

$$\eta = \frac{1}{VT} \int \mathrm{d}t \, \langle \sigma^{\alpha\beta}(t) \sigma^{\alpha\beta}(0) \rangle \simeq 9.3 \, . \tag{5.24}$$

The sum of the bulk and the shear viscosity can then be determined using

$$\frac{4}{3}\eta + \zeta = \frac{1}{VT} \int_0^\infty \langle \mathrm{d}t \, (\sigma^{\alpha\alpha}(t) - pV)(\sigma^{\alpha\alpha}(0) - pV) \rangle \simeq 21.5 \, . \tag{5.25}$$

The precision of the evaluation of these integrals is limited due to the long tail that especially the stress auto-correlation function exhibits. This problem is much smaller for the auto-correlation function of the energy current which decays much faster.

The isobaric and isochoric specific heat capacities can be determined at $p = 0$ by an analysis of the equilibrium fluctuations of the total energy E of the system in an NpT/NVT simulation with

$$c_V = \frac{\langle \delta E^2 \rangle_{NVT}}{(nN)T^2} \simeq 2.7 \, , \tag{5.26}$$

$$c_p = \frac{\langle \delta (E + pV)^2 \rangle_{NpT}}{(nN)T^2} \simeq 3.8 \, , \tag{5.27}$$

and thus estimates for $\gamma_H \simeq 1.4$, $\Gamma \simeq 14.5$ and $D_T \simeq 1.5$ can be found at $T = 1$ and $p = 0$ in the bulk. Due to the box size $B_x = 15$ the smallest q-vector which can be considered is $q_{\min} = \frac{2\pi}{B_x} = 0.42$.

In figure 5.6 the coherent scattering functions of the bulk at $T = 1$ and $p = 0$ is shown. The oscillations are due to propagating acoustic waves. Using equation (5.19)

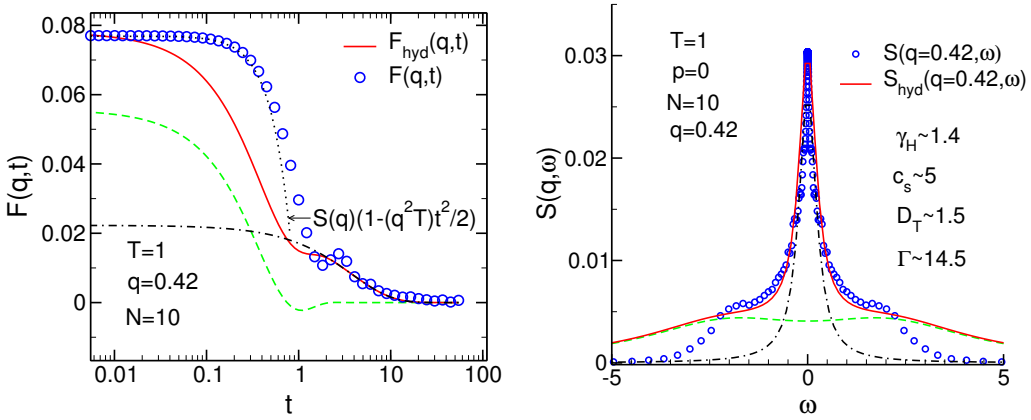

Figure 5.6: LEFT PANEL: Coherent scattering function at $q = 0.42$ of the bulk at $T = 1$ and $p = 0$. The system contained $n = 288$ chains of $N = 10$ monomers (circles). The thick lines indicate $F(q,t)$ given by equation (5.19) in the hydrodynamic limit using values of the constants extracted from the simulation ($\gamma_H = 1.4$, $\Gamma = 14.5$, $c_S = 5$ and $D_T = 1.5$). The dashed line and the dashed dotted line show the thermal and the viscous contribution to the dissipation. RIGHT PANEL: The dynamic structure factor of the bulk at $T = 1$ and $p = 0$ is shown (blue circles). Also indicated are the hydrodynamic limit for $S(q,\omega)$ which was calculated using the values for the various coefficients which were determined independently $\gamma_H = 1.4$, $\Gamma = 14.5$, $c_S = 5$ and $D_T = 1.5$ (dotted line). The partial contribution are indicated by the dash-dotted line and the dashed line.

and the constants extracted from simulations as described above, we can compare our results to the prediction for $F(q,t)$ at small wave vectors and large times. We indicate the total coherent scattering function in the hydrodynamic limit as well as the thermal mode and the propagating mode. At large times the agreement between theoretic prediction and the simulation results is much better than at short times were considerable deviations can be observed. The relaxation time predicted by the hydrodynamic theory is faster than the relaxation of the particles due to ballistic motion given as $S(q)(1-(q^2T)t^2/2)$. It would be necessary to go to smaller q-vectors ($q < 0.1$), which shifts the relaxation dynamics to larger times in comparison to which $S(q)(1-(q^2T)t^2/2)$ will be fast, to obtain a better agreement with the prediction given in equation (5.19).

In order to allow for a comparison with equation (5.20) we carried out a Fourier transformation of $F(q,t)$ to determine $S(q,\omega)$. The Fourier transform is carried out with a simple trapezoidal Filon algorithm [163] on a logarithmic grid in the time as well as in the frequency domain. This allows a much more efficient calculation of the Fourier transform for slowly varying functions than a fast Fourier transform (FFT). The results are shown in figure 5.6. The numerically calculated dynamic structure factor deviates considerably from the hydrodynamic limit at large ω which could already be expected from the results for $F(q,t)$. The deviations are the largest for

large frequencies corresponding to short times. If we attempt a fit to equation (5.20) we obtain a better agreement between theory and our results but at intermediate q the deviation are still large. Also the values for the parameters derived from the fit do not correspond very well to the estimates determined earlier. Especially Γ is underestimated by a factor of 3. Also in the time domain the agreement is improved at short times while at large times the agreement is not as good which is in contradiction with the expected range of validity of the theory. Therefore the fit does not provide reliable results as our simulations are not carried out at small enough q vectors.

5.2.2 Relaxation of surface height fluctuations

In the films the situation is different. Here the long-range (spatially as well as temporally) fluctuations of the interface position should dominate the relaxation at small q-vectors. The spectrum due to capillary waves was investigated in detail by [150] using linear response theory. The Hamiltonian of the system in the presence of an external perturbation is given by

$$H = H_0 + H_{\mathrm{e}}(t) \; , \tag{5.28}$$

where H_0 characterizes the unperturbed system. Following Jäckle [150, 164] the Hamiltonian for the external perturbation is chosen as

$$H_e(t) = -\int\int dA \; P_y(\mathbf{r},t)h(\mathbf{r}) = -\sum_{\mathbf{q}} \tilde{P}_y(-\mathbf{q},t)\tilde{h}(\mathbf{q}) \; , \tag{5.29}$$

where $P_y(\mathbf{r},t)$ is a time and position dependent force field acting on the liquid surface. It is defined as

$$P_y(r,t) = \frac{1}{\sqrt{A}} \sum_{\mathbf{q}} \tilde{P}_y(\mathbf{q},t) \exp(\mathrm{i}\mathbf{q}\cdot\mathbf{r}) \; , \tag{5.30}$$

where the Fourier components are given as $\tilde{P}_y(\mathbf{q},t) = P_{y,0}\exp(-\mathrm{i}\omega t)$. The vector $\mathbf{q}$ lies within the xz-plane. The changes in the interface position h introduced by this force field can be calculated in the regime of linear response as

$$\tilde{h}(q,t) = P_{y,0}\exp(-\mathrm{i}\omega t)\chi(q,\omega) \; , \tag{5.31}$$

where $\chi(q,\omega)$ is the dynamic susceptibility.

Through the fluctuation-dissipation theorem [123] the imaginary part of the dynamical susceptibility $\chi''(q,\omega)$ is related to the auto-correlation function of the surface height fluctuations $C(q,t) = \langle\tilde{h}(\mathbf{q},t)\tilde{h}(-\mathbf{q},0)\rangle$

$$C(q,\omega) = \frac{k_{\mathrm{B}}T}{\pi\omega}\chi''(q,\omega) \tag{5.32}$$

$$= \frac{1}{2\pi}\int dt \; \exp(i\omega t)C(q,t) \; . \tag{5.33}$$

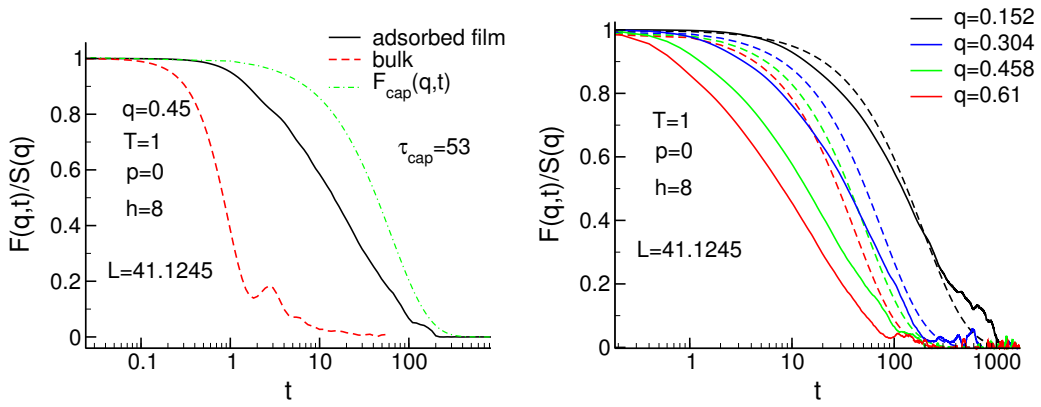

Figure 5.7: LEFT PANEL: The coherent scattering function normalized to 1 of a supported film of thickness $h = 8$ (full line) and the bulk (dashed line) at approximately the same $q = 0.45$ and at $T = 1$. The dash-dotted line indicates the single exponential decay predicted by capillary wave theory. RIGHT PANEL: The coherent scattering function normalized to 1 in an adsorbed film of $h = 8$ at $T = 1$ for various q-vectors (full lines). Also indicated are the approximations of capillary wave theory in the limit of an overdamped system (dashed lines).

Therefore by determining $\chi''(q,\omega)$ one can predict the relaxation behavior of the system. By solving the linearized Navier-Stokes equations which govern the hydrodynamics of an incompressible liquid of density ρ, Jäckle [150] obtained a rather complicated expression for $\chi(q,\omega)$ as a function of the density of the liquid, the surface tension, the depth and the viscosity. In the limiting cases of a dense, highly viscous liquid ($\eta > 1$ and $\rho \simeq 1$) the capillary modes at the surfaces should be strongly overdamped. In this case it can be shown [150, 159] that $C(q,\omega)$ is given by a Lorentzian function

$$C(q,\omega) = \frac{2k_{\mathrm{B}}T}{\gamma q^2}\frac{\Delta\omega^2}{\omega^2+\Delta\omega^2} \tag{5.34}$$

with line width $\Delta\omega = 1/\tau_{\mathrm{cap}}$. In our case of a dense, viscous polymer liquid we should be in this regime of overdamped capillary waves. Here, in the time domain the decay of the fluctuations should be described by a single exponential function with relaxation time

$$\tau_{\mathrm{cap}} = \frac{2\eta}{\gamma q}\frac{\cosh^2(qh)+(qh)^2}{\sinh(qh)\cosh(qh)-qh}. \tag{5.35}$$

This has been verified for various film thicknesses and temperatures experimentally by neutron scattering in reference [159].

First we look at the coherent scattering function of the films at a similar q vector as the bulk. This is shown in the left panel of figure 5.7. Although the correlations in the film 'live' longer than in the bulk, the decay is not exponential and the relaxation time is smaller than suggested by the theory. In the case of the films, due to the smaller extension in y-direction, it is easier to go to smaller wave vectors. The largest

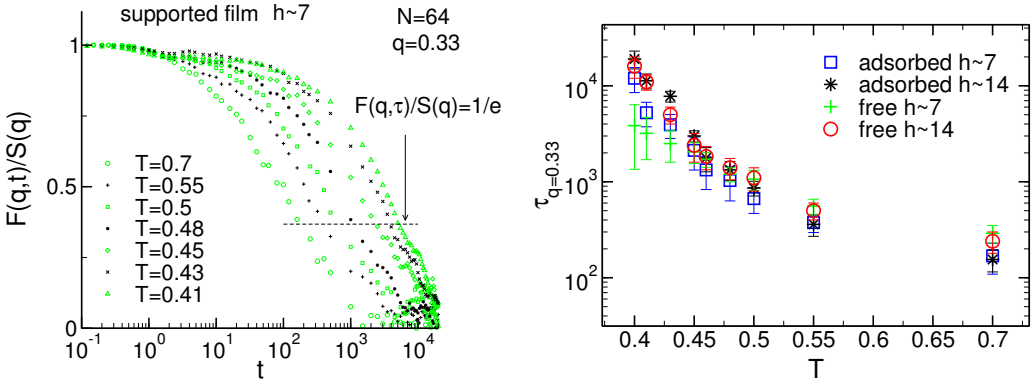

Figure 5.8: LEFT PANEL: The coherent scattering function at $q = 0.33$ normalized to 1 of a supported film of thickness $h \simeq 7$ at $T = 0.7$, $T = 0.55$, $T = 0.48$, $T = 0.45$,$T = 0.43$, and $T = 0.41$. The dashed line indicates the criterion $F(q, \tau_{\text{q=0.33}})/S(q) = 1/\,\text{e}$ used to extract the relaxation time. RIGHT PANEL: The relaxation time $\tau_{\text{q=0.33}}$ for a supported and free standing films as a function of temperature.

lateral box size investigated is $B_{xz} = 41.1245$; this allows us to look at wave vectors as small as $q = 0.152$.

In figure 5.7 (right) it can be seen that for this q-vector the agreement with the prediction form theory is much better although the decay is still not perfectly exponential. This is probably due to the fact that q is still too large, with an additional complication in the films. Since we do not separate the spectrum of the surface waves form the response of the rest of the film (bulk system), we get a contribution from both. The bulk contribution is proportional to the system volume and also the value of the static structure factor $S(q) = \rho T \beta_T$ for small q, where β_T is the system's compressibility which is rather small (at $T = 1$ and $p = 0$ we find $\beta_T = 0.076$), while the capillary wave contribution is proportional to the area and also to $S(q) \simeq \frac{T}{\gamma h q^2} \simeq 6$ which at this $q = 0.152$ is much larger.

In figure 5.8 the normalized coherent scattering function for a supported film of thickness $h \simeq 7$ is shown as a function of temperature. The dependence of the amplitude on film geometry and thickness was discussed in section 5.1. The relaxation of the capillary wave fluctuations becomes slower with decreasing temperature. We use the criterion

$$F(q, \tau_{\text{q=0.33}})/S(q) = 1/\,\text{e} \tag{5.36}$$

to extract a relaxation time to compare the decay times of the fluctuations at different temperature in different film geometries.

Equation (5.35) suggests that at a given temperature and q-vector the relaxation is slower in thinner films than in thicker films provided that the surface tension and the viscosity are independent of film thickness. In the limit $\lim_{h\to\infty} \tau_{\text{cap}} = \frac{2\eta}{\gamma q}$ is found. A film thickness of $h \simeq 14$ is already close to this asymptotic value for the q vectors investigated here. For films of thickness $h \simeq 7$ the relaxation is predicted

to be by a factor of 1.4 slower than at $h \simeq 14$ for $q = 0.33$. However it is unclear insofar this equation can be applied since we observed considerable deviations from the predictions of capillary wave theory at this q vector. Although the decay of the incoherent scattering function is dominated by the effects of capillary wave fluctuations at $q = 0.33$, the purely exponential decay with a relaxation time τ_{cap} could not be observed.

When comparing the relaxation times of the capillary wave fluctuations at a high temperature $T = 0.7$, the relaxation in thinner films is indeed slower than for thicker films at the same geometry. Nevertheless the differences in relaxation times are very small in comparison with the error bars, which makes a reliable comparison difficult. As $F(q,t)$ is a collective system property very long runs are necessary to obtain sufficiently good statistics to obtain reliable results.

Upon lowering the temperature this trend is reversed and at $T = 0.41$ which is close to the bulk T_{g} for $N = 64$ the relaxation in thinner films is faster than in thicker films. At a given film thickness the relaxation in free-standing films is faster than the one in supported films. This is the same dependence of relaxation times on film thickness and geometry as was observed for the local relaxation times extracted from the incoherent scattering function and the MSD. As the surface tension at the free surface changes only by a factor of 2 in the temperature interval investigated and is rather independent of film thickness and geometry this difference can only be explained if one assumes that the viscosity in the thinner films is lower than in the thicker films.

5.3 Summary

We find a divergence of the total structure factor at small q as $S(q) \propto q^{-2}$ in free standing and supported films as predicted by capillary wave theory. The effect of the capillary wave fluctuations on the total structure factor increases with decreasing film thickness and is stronger at a given film thickness in free-standing than in supported films due to the presence of two free surfaces.

The relaxation of the films is slower and qualitatively different than in the bulk at small q-vectors due to the presence of capillary waves. At high temperature the relaxation of the capillary wave fluctuations is faster in thicker films than in thinner films in agreement with capillary wave theory. At low temperatures however the relaxation is faster in thinner films which could be an indication that the viscosity in the films is lower than in the bulk and that the viscosity decreases with decreasing film thickness.

In the last chapter we showed that equation (4.14) introduced by [4] allows to parameterize the dependence of the local dynamics in the films very well. However, the theoretical basis remains unclear. The authors suggested a coupling of the capillary waves at the surface to the viscous flow in the bulk accelerating the dynamics. We

could show in section 5.2 that the relaxation in the low q limit is slower in the films than in the bulk because the capillary wave fluctuations are long lived. On the other hand we find the local relaxation to be faster in the films than in the bulk. Because the local relaxation times grow rapidly as the film approaches its glass transition, also the relaxation time of the capillary wave fluctuations related to the system's viscosity increase. Apparently the faster local dynamics encountered in the last chapter go along with a decrease in the film's viscosity in comparison with the bulk at low temperatures. This shows that the dynamics in our films is influenced on all scales by the confinement.

Whether the capillary wave fluctuations are the reason for the differences in the slowing down of the dynamics on the local scale between bulk and film could not be determined. Simulations on confined films which suppress these fluctuations find also a decrease of T_{c} which could be well described by equation (4.14) [32]. As in this case capillary wave fluctuations are strongly suppressed by the confining walls, other factors as the change in the local order induced by the confinement have a predominant influence on the system's dynamics.

Chapter 6

Dielectric relaxation

Broadband dielectric spectroscopy is a common experimental technique to study the conformation, the structure and the dynamics of polymers [165]. The sample is subjected to an ac electrical field and the response is measured in form of a frequency dependent complex dielectric permittivity. This allows to follow the different relaxation processes of polymeric systems. Using this method one can evidence modes which can have very different characteristic relaxation times as the frequency window these experiments can cover today is very large. The typical relaxation processes one encounters are the β relaxation corresponding to motion of side chains, the α relaxation linked to the structural relaxation of the monomers and the normal mode relaxation due to the reorientation dynamics of the whole chain [166]. The broad frequency range accessible also allows to follow the α relaxation dynamics during its many decade change from T_{g}, deep into the liquid state [167, 168].

Recently this technique was used to probe the dynamics of the normal mode of polymers in thin film geometry [169–173]. The experiments found evidence for an additional relaxation mode due to the confinement in these so-called type A-polymers. The additional mode is situated between the segmental mode and the normal mode. Its relaxation time decreases with decreasing films thickness while its dielectric strength increases with decreasing film thickness. Kremer and coworkers assigned this mode to the relaxation of terminal subchains. Due to the strong adsorption of monomers at the wall chain segments at the interface are immobilized. As more than one monomer of a chain can be immobilized at the surface large parts of the chain can become dielectrically inactive. Simulations of ideal random walks were monomers at the wall were pinned down support this explanation [174]. However a thickness dependent relaxation time of this confinement induced mode could only be observed in the simulations if monomers were only immobilized at one interface. This could be explained by the asymmetric preparation of the films.

We attempt to calculate the dielectric spectra of our model polymer films and compare it to the bulk spectrum to see how the film geometry alters the relaxation in our systems. By dielectric spectroscopy, dynamic processes can be detected that in-

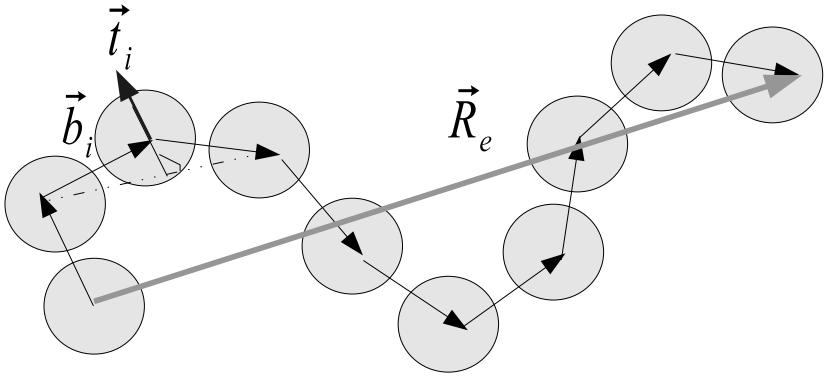

Figure 6.1: Schematic drawing of the dipoles on a chain.

volve the reorientation of dipolar entities or the displacement of charged entities. The results are usually reported as spectra of the real and imaginary part of the complex dielectric permittivity [165]. In order to calculate such spectra in our simulation we need to attach dipolar units to our bead-spring chains. How this can be achieved was reported in reference [175] and will be described in section 6.1. We will calculate the auto-correlation function of the polarization of the system and use the fluctuation dissipation theorem to obtain the permittivity measured in experiments. We will discuss the auto-correlation function in the bulk and the film in section 6.2. In section 6.3 the calculation of the dielectric loss spectra is explained. Finally results on the segmental mode and the normal mode relaxation in our systems are presented in section 6.3.1 and 6.3.2.

6.1 Definition of the system's polarization

Following a previous study [175] employing a similar model to analyze the dynamic properties of short chains in the bulk, we introduce two local dipole moments. One is oriented parallel to the chain back bone and therefore proportional to the bond-vector,

$$\mathbf{b}_j^a = \frac{1}{b_{\text{eq}}} \left(\mathbf{r}_j^a - \mathbf{r}_j^{a+1} \right) \ . \tag{6.1}$$

The other dipole is attached locally perpendicular to the chain backbone in the direction of

$$\mathbf{t}_j^a = (-1)^j \left(\mathbf{b}_j^{a-1} - \mathbf{b}_j^a \right) \ . \tag{6.2}$$

The total polarization in the system is then given by

$$\begin{aligned}\mathbf{P}(t) &= \mathbf{P}_{\text{seg}}(t) + \mathbf{P}_{\text{N}}(t) \\ &= \sum_{j=1}^{n} \mathbf{P}_j(t) = \sum_{j=1}^{n} \left(\mu_{\text{seg}} \mathbf{T}_j + \mu_{\text{N}} \mathbf{R}_{\text{e}}^j\right) \ , \end{aligned} \tag{6.3}$$

where

$$\mathbf{T}_j = \sum_{a=2}^{N-1} \mathbf{t}_j^a \tag{6.4}$$

and the end-to-end vector

$$\mathbf{R}_e^j = \sum_{a=1}^{N-1} \mathbf{b}_j^a \ . \tag{6.5}$$

μ_{seg} and μ_{N} account for the strength of the local dipole moments parallel and perpendicular to the chain back bone. They can be chosen arbitrarily to match a certain polymer. Following [175] we set $\mu_{\text{seg}} = 1.5$ and $\mu_{\text{N}} = 1$. This ratio corresponds to the one found for cis-polyisoprene. The choice of non-zero dipole moments parallel as well as perpendicular to the bond vectors corresponds to so called type A-polymers [166]. These polymers allow to follow the segmental motion or α-relaxation of the system via decorrelation of $\mathbf{P}_{\text{seg}}(t)$ as well as the relaxation of the whole chain via $\mathbf{P}_{\mathbf{N}}(t)$. This second process corresponds to the reorientation of the end-to-end vector $\mathbf{R}_{\mathbf{e}}$ of a chain and is also referred to as normal mode. Its characteristic time is dependent on chain length.

6.2 Auto-correlation functions of the polarization

The dynamics of the system can be investigated via the auto-correlation function of the total polarization vector.

$$C(t) = \frac{\langle \mathbf{P}(t) \cdot \mathbf{P}(0) \rangle}{\langle \mathbf{P}(0) \cdot \mathbf{P}(0) \rangle} \tag{6.6}$$

We expect there to be two distinct relaxation processes. One related to a reordering of the chain segments

$$C_{\text{seg}}(t) = \frac{\langle \mathbf{P}_{\text{seg}}(t) \cdot \mathbf{P}_{\text{seg}}(0) \rangle}{\langle \mathbf{P}_{\text{seg}}(0) \cdot \mathbf{P}_{\text{seg}}(0) \rangle} \ , \tag{6.7}$$

and a second one corresponding to the reorientation of the whole chain

$$C_{\text{N}}(t) = \frac{\langle \mathbf{P}_{\text{N}}(t) \cdot \mathbf{P}_{\text{N}}(0) \rangle}{\langle \mathbf{P}_{\text{N}}(0) \cdot \mathbf{P}_{\text{N}}(0) \rangle} \ . \tag{6.8}$$

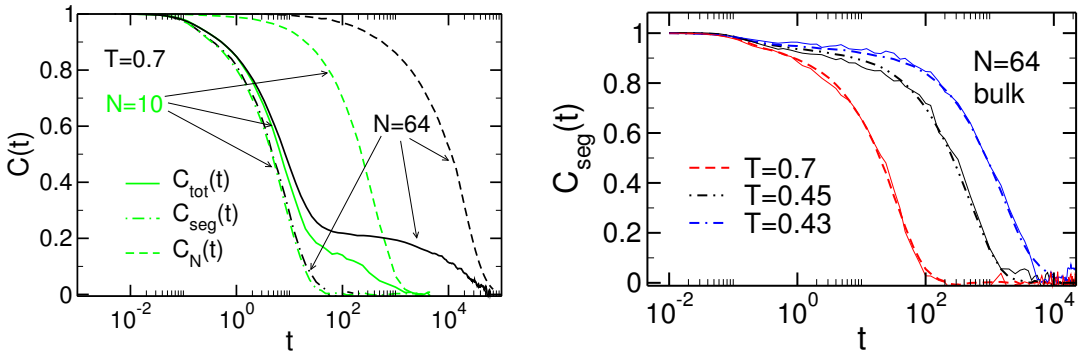

Figure 6.2: LEFT PANEL: The auto-correlation function (full line) given by equation 6.6 of a bulk system for $N = 10$ (black lines) and $N = 64$ (gray lines) at $T = 0.7$ is shown. Additionally the segmental (dash-dotted line) and the normal (dashed line) auto-correlation functions are shown. RIGHT PANEL: The auto-correlation function $C_{\rm seg}(t)$ for $T = 0.7$, $T = 0.45$, $T = 0.43$ of a bulk system at $p = 0$ with chains of length $N = 64$ are shown from left to right. The thin solid lines correspond to $C_{\rm seg}(t)$ while the thick lines are calculated from $C^{SC}_{\rm seg}(t)$.

If the chain length N is very large the time scales of these two modes are very different and therefore they decouple completely so that the total correlation function can be described as a sum of two distinct auto-correlation functions

$$C(t) = aC_{\rm seg}(t) + bC_{\rm N}(t) \; . \tag{6.9}$$

6.2.1 Bulk

In figure 6.2 the total correlation function as well as the separate components are shown for a bulk system at a temperature well above the glass transition for two different chain length. In both cases one can clearly observe a two step behavior in $C(t)$ corresponding to the segmental relaxation and the reorientation of $\mathbf{R_e}$. With increasing chain length, $\mathbf{R_e}$ relaxes more slowly while the α-relaxation is almost unaffected, and the two step behavior becomes more pronounced. While for shorter chains the approximation given by equation (6.9) does not hold entirely due to the coupling of the two relaxation processes, they are well separated for the larger chain length and $C(t)$ can be described well by this factorization.

We make a further approximation by

$$C^{\rm SC}(t) = \frac{1}{n}\sum_{j=1}^{n} C_j(t) = \frac{1}{n}\sum_{j=1}^{n} \frac{\langle \mathbf{P_j}(t)\cdot\mathbf{P_j}(0)\rangle}{\langle \mathbf{P_j}(0)\cdot\mathbf{P_j}(0)\rangle} \tag{6.10}$$

which assumes that there is no correlation between the polarization of the different chains i. e. $\langle \mathbf{P_j}(\mathbf{0})\cdot\mathbf{P_i}(\mathbf{0})\rangle = 0$ for $i \neq j$. While this certainly holds for the orientation of $\mathbf{R_{e,j}}$, there might be correlations between segments of different chains

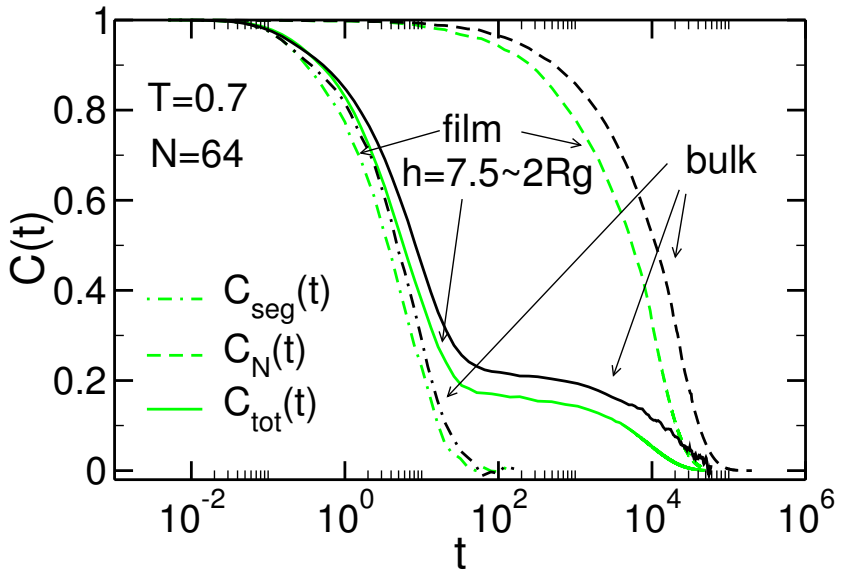

Figure 6.3: The auto-correlation function $C(t)$ is shown for a supported film of thickness $h = 7.5$ (grey lines) at $T = 0.7$ and the bulk (black lines) (chain length $N = 64$). Also indicated is the decomposition in segmental (dash-dotted lines) and normal (dashed lines) component given by equation (6.6).

due to local packing order. We test the validity of this assumption by looking at the auto-correlation function C_{seg} in comparison with C_{seg}^{SC} for a bulk system at different temperatures in figure 6.2. Although there are slight differences which might be due to insufficient statistics for $C_{\text{seg}}(t)$ the global features of the curves are unaffected. Therefore in the rest of this chapter we will only present data for $C_{\text{seg}}^{\text{SC}}$ and drop the super-script SC.

6.2.2 Films

To see the influence of the confinement we compare the relaxation in a supported thin film at high temperature to the properties of the bulk under the same conditions in figure 6.3. We find that the α-relaxation at this elevated temperature is rather unperturbed by the confinement although there can already be seen a slight acceleration of the dynamics in comparison to the bulk which becomes more pronounced as the systems are cooled. $\mathbf{R_e}$ on the other hand reorients much faster in the film than in the bulk.

The radius of gyration R_g of the chains in the film of thickness $h = 7.5$ is $R_g = 3.7 \sim \frac{h}{2}$. The film thickness is so small in comparison with the size of a molecule that the end-to-end distance of the polymers in the y-direction is less than the one within the plane of the film, which is still bulk like. This is schematically illustrated in figure 6.4. For the end-to-end distance of the chains in the film R_e^{film} in

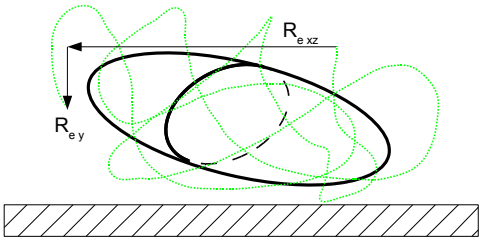

Figure 6.4: Schematic drawing of a chain confined in a film. Indicated are the gyration ellipsoid and the end-to-end distance.

comparison to the one of the bulk R_e^{bulk} one thus finds $R_e^{\text{bulk}} \simeq \frac{3}{2} R_{e\ \text{xz}} > R_e^{\text{film}} > 3R_{e\ \text{y}}$ (see equation (3.16) and figure 3.9 in section 3.3 for more details). In other words the momentary gyration ellipsoid tends to orient with its shortest axis perpendicular to the plane of the film. Since the relative amplitude of the normal mode is proportional to the expectation value of the end-to-end distance (the expectation value of $\langle T \rangle$ defined in equation (6.4) is not affected by the confinement within the accuracy of our calculation) the films show a lower plateau in the correlation function. This can be seen clearly for the total correlation function in the film and the bulk in figure 6.3.

6.3 Dielectric loss spectra

Through the dissipation fluctuation theorem it is possible to calculate the dielectric loss spectrum via a Fourier transform of the auto-correlation function

$$\frac{\epsilon(\omega) - \epsilon_\infty}{\Delta\epsilon} = -F\left[\frac{\partial}{\partial t} C(t)\right] , \tag{6.11}$$

where $\Delta\epsilon$ is the relaxation strength and ϵ_∞ the dielectric constant of the medium [123, 175].

The Fourier transform is carried out with a simple trapezoidal Filon algorithm [163] on a logarithmic grid in the time as well as in the frequency domain. This allows a much more efficient calculation of the Fourier transform for slowly varying functions than a fast Fourier transform (FFT).

In figure 6.5 the dielectric loss spectra of bulk systems with different chain lengths are compared. While for the shorter chain length the peak corresponding to the normal mode and the peak characteristic of the α-relaxation overlap considerably, so that the normal process can only be seen as a wing of the segmental relaxation peak, the two peaks are well separated at the larger chain length and the overlap of the two processes is rather small. As already stated above the normal mode exhibits a strong

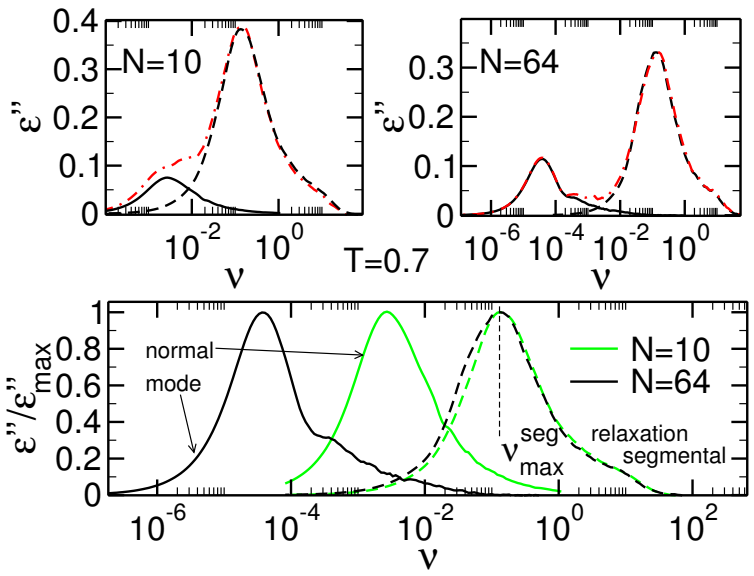

Figure 6.5: UPPER LEFT PANEL: The dielectric loss spectrum for chains of length $N = 10$ at $T = 0.7$ and $p = 0$ in the bulk is shown. The full line indicates the normal mode, the dashed line the segmental relaxation and the dash dotted line the total spectrum. UPPER RIGHT PANEL: The dielectric loss spectrum for chains of length $N = 64$ at $T = 0.7$ and $p = 0$ in the bulk is shown. The full line indicates the normal mode, the dashed line the segmental relaxation and the dash dotted line the total spectrum. LOWER PANEL: The renormalized peaks of the segmental and the normal mode at $T = 0.7$ and $p = 0$ in the bulk for $N = 10$ and $N = 64$ are shown.

dependence on chain length, while the local segmental relaxation is not strongly affected by the chain length.

6.3.1 Temperature dependence of the segmental mode relaxation

In figure 6.6 we look at $C_{\text{seg}}(t)$ and the corresponding dielectric loss-spectrum as a function of temperature. As the system is cooled the relaxation times grow and the cooperative α-relaxation process separates from the partial relaxation due to microscopic degrees of freedom. The strong increase of relaxation times as the system approaches the glass transition has already been observed in the last chapter when analyzing $\tau_1(T)$ extracted from the MSD of the inner monomers in section 4.2. We used a power-law diverging at T_{c} inspired by MCT to describe the slowing down of the dynamics as T_{c} is approached. There are other formulas which allow to describe these deviations from Arrhenius behavior common to glass-forming polymeric liquids equally well (see e. g. [28, 29] for a summary).

One of the most commonly used parameterizations is the so called Vogel, Fulcher,

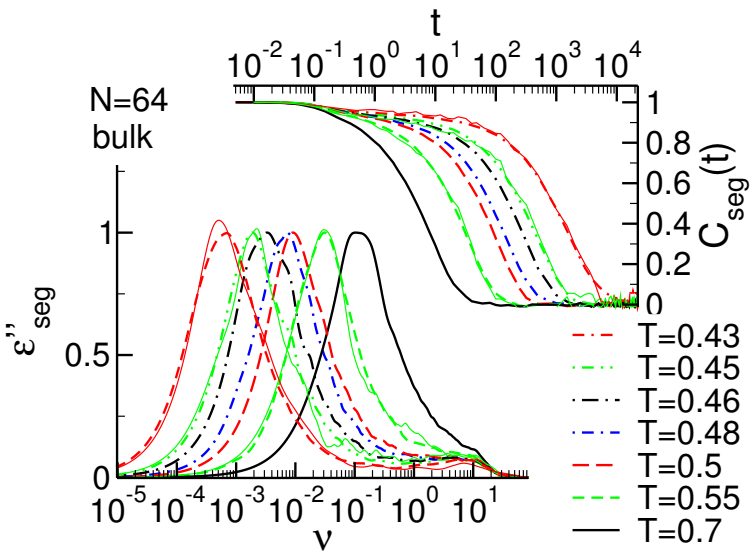

Figure 6.6: LEFT PANEL: The dielectric loss spectra $\epsilon''_{\rm seg}$ for $T = 0.7$, $T = 0.55$, $T = 0.5$, $T = 0.48$, $T = 0.46$, $T = 0.45$, $T = 0.43$ of a bulk system at $p = 0$ with chains of length $N = 64$ are shown from right to left. The thin solid lines correspond to the Fourier transform of $C_{\rm seg}(t)$ while the thick lines are calculated from $C^{SC}_{\rm seg}(t)$. The curves are normalized such that $\epsilon''_{\rm seg}(\nu_{\rm max}) = 1$. RIGHT PANEL: The autocorrelation function $C_{\rm seg}(t)$ for $T = 0.7$, $T = 0.55$, $T = 0.5$, $T = 0.48$, $T = 0.46$, $T = 0.45$, $T = 0.43$ of a bulk system at $p = 0$ with chains of length $N = 64$ are shown from left to right. The thin solid lines correspond to $C_{\rm seg}(t)$ while the thick lines are calculated from $C^{SC}_{\rm seg}(t)$.

Tammann (VFT) equation [176]

$$\nu_{\rm max}(T) \propto \exp\left(-\frac{DT_0}{T - T_0}\right) . \tag{6.12}$$

This equation implies the existence of a non-zero T_0 at which relaxation times diverge. In experiments T_0 is found to be lower than $T_{\rm g}$. Angell determined that this temperature is very close to the independently evaluated Kauzmann temperature $T_{\rm K}$ [177] at which the configurational entropy vanishes for many substances [28]. The MCT prediction of a power law divergence and the VFT equation both allow a fit of the relaxation times within the 4 decades accessible in our simulations.

The frequency $\nu_{\rm max}$ at the maximum of the dielectric loss spectrum is shown as a function of temperature in figure 6.7. The dependence can be fitted well with a VFT law for the films as well as the bulk system at both chain lengths. The temperature T_0 is lower in the films ($T_0^{N=64} = 0.293$, $T_0^{N=10} = 0.286$) than in the bulk system ($T_0^{N=64} = 0.327$, $T_0^{N=10} = 0.31$) and longer chains have a slightly higher T_0 for the same geometry. These trends are in agreement with the ones found for $T_{\rm g}$ and $T_{\rm c}$ earlier. The parameter $D \sim 2.5$ for all systems which shows that our model polymer

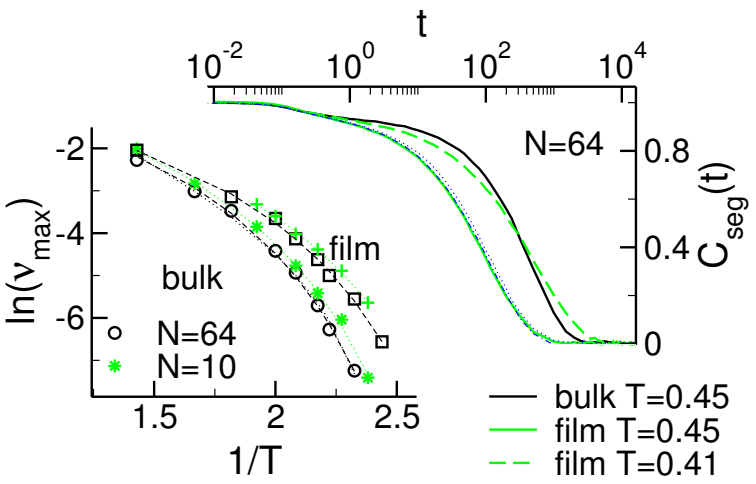

Figure 6.7: LEFT ORDINATE: An Arrhenius plot of the peak frequency of $\epsilon''_{\rm seg}$ is given for a bulk system of chains $N = 10$ (stars), a bulk system of chains $N = 64$ (circles), a film of thickness $h \sim 7$ (thickness changes as a function of T) of chains $N = 10$ (pluses) and a film of thickness $h \sim 7$ (thickness changes as a function of T) of chains $N = 64$ (squares). The dashed and dotted lines indicate a fit to equation (6.12). RIGHT ORDINATE: The auto-correlation functions of the segmental mode at $T = 0.45$ in the bulk system for chains of $N = 64$ (thick black line), at $T = 0.45$ (thick gray line) and at $T = 0.41$ (dashed gray line) in a film of $h = 7.5$ of chains of length 64 are shown. The thin lines indicate the auto-correlation functions of the segmental mode calculated only parallel (dashed) and only perpendicular (dotted) to the plane of the film.

is a rather fragile glass former.

The films exhibit globally the same behavior as the bulk system on approaching the glass transition but the onset of the strong slowing down is shifted to lower temperatures. This was already pointed out in other extensive MD-studies of the dynamics in thin films [32, 38]. If one compares data at the same relative distance form $T_{\rm c}$ as done in the right panel of figure 6.7 one finds that the large differences in relaxation time between the bulk and the film disappear but the film exhibits a stronger stretching of the correlation function as the bulk.

It is also interesting to look whether the confinement induces a different behavior parallel or perpendicular to the plane of the film. In order to study this dependence we introduce two additional correlation functions

$$C^{\perp}_{\rm seg}(t) = \frac{\langle \mathbf{P}^{\perp}_{\rm seg}(t) \cdot \mathbf{P}^{\perp}_{\rm seg}(0) \rangle}{\langle \mathbf{P}^{\perp}_{\rm seg}(0) \cdot \mathbf{P}^{\perp}_{\rm seg}(0) \rangle} \tag{6.13}$$

and

$$C^{\parallel}_{\rm seg}(t) = \frac{\langle \mathbf{P}^{\parallel}_{\rm seg}(t) \cdot \mathbf{P}^{\parallel}_{\rm seg}(0) \rangle}{\langle \mathbf{P}^{\parallel}_{\rm seg}(0) \cdot \mathbf{P}^{\parallel}_{\rm seg}(0) \rangle} \,, \tag{6.14}$$

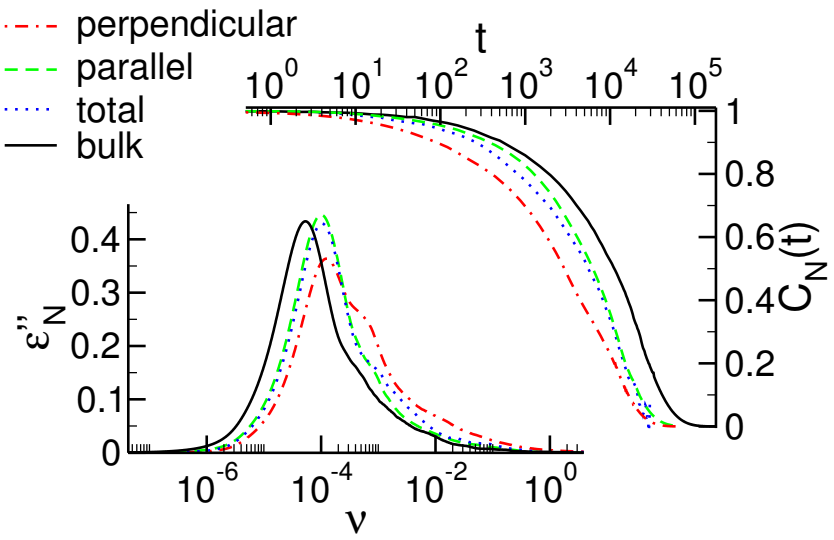

Figure 6.8: LEFT ORDINATE: The dielectric loss calculated from the total correlation function of the polarization (dotted line), the correlation function of the polarization within the plane of the film (dashed line), the correlation function of the polarization perpendicular to the plane of the film (dash-dotted line) and the correlation function of the bulk (full line). RIGHT ORDINATE: The total correlation function of the polarization (dotted line), the correlation function of the polarization within the plane of the film (dashed line), the correlation function of the polarization perpendicular to the plane of the film (dash-dotted line) and the correlation function of the bulk (full line). Only contribution from the dipole moment parallel to the chain backbone are shown. The film had a thickness of $h = 7.5$ and the chain length was $N = 64$. The temperature was $T = 0.7$.

where $\mathbf{P}^{\perp}_{\mathrm{seg}}(t)$ refers to the component of the segmental polarization perpendicular to the plane of the film and $\mathbf{P}^{\parallel}_{\mathrm{seg}}(t)$ to the component within the plane of the film. The result of this analysis is shown in figure 6.7. The confinement does not strongly bias the relaxation in the different directions. The segmental dynamics of the film are rather isotropic.

6.3.2 Normal mode relaxation

Now we apply the same analysis to the normal mode. It was suggested before [169–173] that type-A polymers exhibit upon confinement an additional relaxation mode whose relaxation time is dependent on film thickness. As it was related to chain segments being immobilized at the wall we do not expect to observe the same phenomenon in our simulations.

In complete analogy to the analysis of the segmental mode we define

$$C^{\perp}_{\mathrm{N}}(t) = \frac{\langle \mathbf{P}^{\perp}_{\mathrm{N}}(t) \cdot \mathbf{P}^{\perp}_{\mathrm{N}}(0) \rangle}{\langle \mathbf{P}^{\perp}_{\mathrm{N}}(0) \cdot \mathbf{P}^{\perp}_{\mathrm{N}}(0) \rangle} \tag{6.15}$$

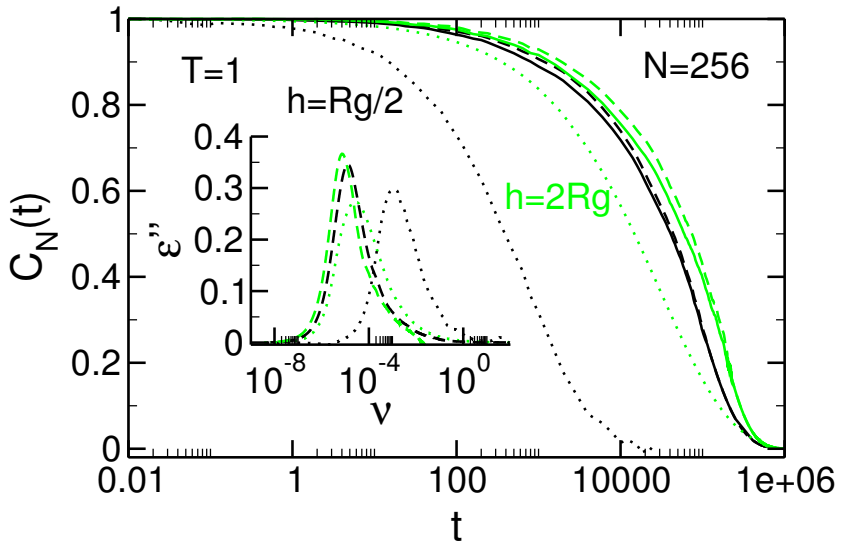

Figure 6.9: MAIN FIGURE: The correlation function of the polarization within the plane of the film (dashed line), the correlation function of the polarization perpendicular to the plane of the film (dotted line) and the total correlation function of the film (full line) are shown for $h = 17$ (gray lines) and $h = 4$ (black lines) and the chain length was $N = 256$. INSET: The dielectric loss calculated from the correlation functions. Colors as indicated above. Only contributions from the dipole moment parallel to the chain backbone are shown. The temperature was $T = 1$.

and

$$C_{\mathrm{N}}^{\parallel}(t) = \frac{\langle \mathbf{P}_{\mathrm{N}}^{\parallel}(t) \cdot \mathbf{P}_{\mathrm{N}}^{\parallel}(0) \rangle}{\langle \mathbf{P}_{\mathrm{N}}^{\parallel}(0) \cdot \mathbf{P}_{\mathrm{N}}^{\parallel}(0) \rangle} \,, \tag{6.16}$$

where $\mathbf{P}_{\mathrm{N}}^{\perp}(t)$ refers to the component of the normal polarization perpendicular to the plane of the film and $\mathbf{P}_{\mathrm{N}}^{\parallel}(t)$ to the component within the plane of the film.

In figure 6.8 the results of this analysis are shown. The relaxation of the normal mode is anisotropic in the films. The end-to-end distance in the y-direction reorients faster than the one within the plane of the film. Also the decay of R_{e} is more strongly stretched in the perpendicular direction than in the parallel direction. Partially this might be due to the fact that on average $R_{\mathrm{e}\,y}$ is smaller and a shorter vector can reorient faster. In the total normal mode relaxation of the film the relaxation in the y-direction does not play an important role since its amplitude is proportional to $R_{\mathrm{e}\,y}$ which is about 3-times smaller than $R_{e\,xz}$ whose dynamics dominates the total spectrum. It can be expected that for even longer chains/stronger confinement this effect becomes more pronounced and the time scales of the decorrelation of R_{e} in the two different directions could be well separated.

In figure 6.9 we extended our study to longer chains. In order to be able to equilibrate the chains the simulations were run at a higher temperature $T = 1$. Indeed in the thinnest film investigated the timescales of the relaxation of R_{e} in the normal

and the parallel direction are well separated. As expected this two step process is not visible in the total spectrum since the ratio $(R_{\mathrm{e}\,y}/R_{\mathrm{e}\,xz})^2 \sim 0.02$ is too small and the overall relaxation is dominated by the process within the plane of the film. We also observe that the assumption of the relaxation time of the end-to-end vector being only determined by its length does no longer hold in the plane of the film at these film thicknesses. The end-to end vector in the plane of the thinner film is larger than the one of the thicker film, nevertheless the decorrelation is faster in the thinner film.

6.4 Summary

We performed a complementary investigation of the dynamics in thin polymer films with a free surface in comparison with the bulk using the auto-correlation function of the system's polarization. Following Barbieri et al. [175] dipoles were attached to the chains parallel as well as perpendicular to the chain backbone allowing to follow the segmental relaxation and the relaxation of the whole chain. Via a Fourier transformation we calculated the dielectric loss spectrum.

We found that the segmental relaxation is isotropic in the films. The increase of the segmental relaxation times with decreasing temperature can be described well by a VFT law in the bulk as well as in the film. The temperature T_0 is found to be lower in the film than in the bulk which is in qualitative agreement with the trends observed for T_{g} and T_{c}.

The normal mode relaxation is anisotropic in thin films. It is faster in the perpendicular direction than in the parallel direction. The relaxation time of the mode in the perpendicular direction decreases with decreasing film thickness as the end-to-end vector in the perpendicular directions is diminished with decreasing film thickness but it is not independent of molecular weight within the range of chain length and film thickness investigated. The relaxation strength is found to be proportional to the end-to-end distance in the perpendicular direction $R_{\mathrm{e}\,y}$ which decreases with decreasing film thickness in comparison to the amplitude of the segmental mode. Within the regime of film thickness and chain-length investigated the normal mode within the plane is slightly accelerated in thinner films and its dielectric strength relative to the segmental mode increases as $R_{\mathrm{e}\,xz}$ increases with decreasing film thickness. However, for these effects to become significant, the film thickness must become smaller than the radius of gyration of the chains.

The explanation of the confinement induced mode observed in experiments [171–173] was based on a bimodal distribution in R_{e} due to chains that are not in contact with the immobilizing surface showing an almost bulk like distribution of the total R_{e} and chains that have segments arrested at one wall (the other wall was chosen to be purely reflecting) allowing only the shorter and film thickness dependent R_{e} of the terminal subchains to fluctuate [174]. The authors concluded that as the film becomes thinner there are more chains attached to the wall and therefore the confine-

ment induced mode grows in dielectric strength on the expense of the normal mode relaxation as there are less and less free chains. These results are in agreement with the experimental findings of [171–173].

In our system, however, we do not find a bimodal distribution of the total end-to-end distance in the films because also monomers at the supporting wall are highly mobile as we showed in chapter 4. If the total polarization is used to calculate the dielectric spectra we find a decrease of the normal mode in comparison with the segmental mode and a slight shift to higher frequencies.

Chapter 7

Simulations with explicit solvent

This and the following chapter deal with simulations of polymers in solution containing explicit solvent molecules. The aim of these simulations is to model the spin-coating process. Experiments and theoretical predictions suggest that films prepared in such a way are far from thermodynamic equilibrium. A strong dependence of the properties of these films on the annealing procedure after the preparation by spin-coating has been observed experimentally [31, 42–44, 69, 71]. An MD-simulation treating the entire process is certainly beyond the scope of current simulation capabilities because this would require the inclusion of a very high number of solvent particles to model the initially very dilute solution. Also the spinning of the waver is not compatible with the periodic boundary conditions of the simulation box requiring very large systems.

As the initial solvent loss is very rapid and the viscosity of the solution still low and therefore the chains can relax fast, it might be possible to capture the essential features of the process by starting the simulations from a rather dense solution at equilibrium. It is known [76] that at the last stages of the spin-coating process, the film thickness only decreases due to the evaporation of solvent from the at this point highly viscous solution which vitrifies while there is still a volume fraction of solvent of about $\phi_{\mathrm{S}} = 14\%$ inside the film [75]. Due to the vitrification of the polymer during solvent evaporation, the film might be trapped in an out-of-equilibrium state and residual stresses could be present.

Before we discuss the solvent evaporation in the next chapter, we assess the equilibrium structure of the chosen model in this chapter. To get a first idea of the type of phase behavior we can expect for a polymer solution we employ the Flory-Huggins model for polymer solutions described in section 7.1. The interaction parameters are chosen to mimic the solution of polystyrene and toluene as will be described in section 7.2. We start our simulations for a rather dense polymer solution containing a volume fraction of solvent of $\phi_{\mathrm{S}} = 21\%$. Ideally one should choose a temperature below T_{g} of the pure polymer but above the one of the solution used as a starting point, to observe a vitrification of the polymer upon solvent evaporation, while there is still

solvent trapped inside the film. Despite the fact that we only start from a dense solution it is still very challenging to run long enough simulations to be able to observe complete solvent evaporation at these low temperatures. This restricts the temperature interval accessible to our study. To cover the different temperature regimes we choose three different temperatures: $T = 0.5$ which is above T_{g} of the pure polymer, $T = 0.4 \simeq T_{\mathrm{g}}$ which is similar to T_{g} of the pure polymer and $T = 0.35$ which is below T_{g} of the pure polymer. The equilibrium properties of the polymer solution are described in section 7.3, where the dynamic characteristics of the solution are discussed and in section 7.4, where we investigate the static structure. In section 7.5 T_{g} at different solvent concentrations inside the film is determined.

7.1 Flory-Huggins model

In this model [51, 178] it is assumed that each monomer or solvent particle occupies a lattice site with coordination number z. To estimate the energy of mixing this theory randomly places monomers and solvent particles onto lattice sites, ignoring correlations. This means that all deviations from random placement due to the interactions between the particles are ignored. As the overall number of sites is constant the overall density is constant as well. The variable of interest is thus the volume fraction of polymer $\phi_{\mathrm{P}} = \phi$ or the volume fraction of solvent $\phi_{\mathrm{S}} = 1 - \phi_{\mathrm{P}} = 1 - \phi$. This follows from the incompressibility of the solution.

The entropy of mixing of a polymer solution is given by

$$\frac{S_{\mathrm{mix}}(\phi)}{k_B} = -k_B \left(\frac{\phi \ln \phi}{N} + (1-\phi)\ln(1-\phi) \right) . \tag{7.1}$$

The free energy of mixing can then be written as

$$\frac{\Delta F_{\mathrm{mix}}(\phi)}{k_B T} = \frac{\phi}{N} \ln \phi + (1-\phi)\ln(1-\phi) + \chi\phi(1-\phi), \tag{7.2}$$

where the Flory-Huggins parameter is defined to characterize the difference of interaction energies in the mixture as $\chi = e/k_B T$, by $e = z\left(u_{\mathrm{PS}} - \frac{u_{\mathrm{PP}}+u_{\mathrm{SS}}}{2}\right)$ we denote the average interaction energy per particle and by u_{ii} the energy gain per pair-interaction ($u_{\mathrm{ii}} < 0$). The topology of the phase diagram of the mixture is strongly dependent on the value of χ. For $\chi > 0$ the mixture is only stable within a certain composition range, where the entropy is sufficient to promote mixing, while for $\chi < 0$ solvent and polymer should mix at any composition.

7.2 Simulation model with explicit solvent

We will use the same coarse-grained bead-spring model as in the simulations of the pure polymer films to model the chains in solution. In addition we will add solvent

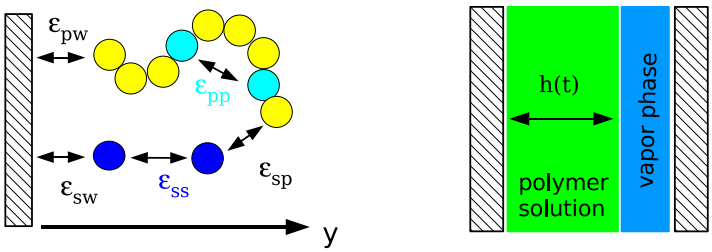

Figure 7.1: LEFT PANEL: Schematic drawing of polymer and solvent interactions in thin film geometry. RIGHT PANEL: Schematic drawing of the film geometry used to equilibrate the solution and its vapor.

particles, described by single coarse grained beads. The interactions will be chosen such as to model the solution of polystyrene and toluene. In figure 7.1 a schematic drawing of the interactions of polymer and solvent is shown.

7.2.1 Choice of the model parameters

Long and Lequeux provided a model for the thermodynamic equilibrium of a polymer melt above T_{g} [25]. They calculate the equilibrium density by balancing the van de Waals attractions between the monomers and the entropic repulsion. The theory suggests the following dependence of the density on temperature

$$\rho(T) = \frac{\rho_0}{2}\left(1+\sqrt{1-\frac{T}{T_{\mathrm{cr}}}}\right) \quad T_{\mathrm{g}} < T \ll T_{\mathrm{cr}}\,, \tag{7.3}$$

where T_{cr} is the hypothetical temperature at which air should be a good solvent for the polymer setting the energy scale and ρ_0 is the effective monomer density of the polymer melt at $T = 0$. For polystyrene they found the parameters to be $\rho_0 = 3.57 \times 10^{27}/\mathrm{m}^3$ and $T_{\mathrm{cr}} = 1225\mathrm{K} \simeq 3.3T_{\mathrm{g}}$. By adjusting the above density dependence to our LJ-model polymers we can deduce a mapping of our model to polystyrene. We obtain from a fit to equation (7.3) that $\rho_0 = 1.113/\sigma_{\mathrm{PP}}^3$ and $T_{\mathrm{cr}} = 1.32\epsilon_{\mathrm{PP}}/k_B$. In figure 7.2 it can be seen that equation (7.3) describes the temperature dependence of the density reasonably well in the interval $T_{\mathrm{g}} < T \ll T_{\mathrm{cr}}$. By comparing with the parameters of polystyrene this allows to conclude that $\epsilon_{\mathrm{PP}} = 1.3 \times 10^{-20}\mathrm{J}$ and $\sigma_{\mathrm{PP}} = 6.8 \times 10^{-10}\mathrm{m}$.

We also map the LJ monomer onto toluene to find the interaction parameters of the solvent. This is achieved by equating the critical point of toluene $T_{\mathrm{c}} = 591.8\mathrm{K}$, $p_{\mathrm{c}} = 4.11\mathrm{MPa}$ and $\rho_{\mathrm{c}} = 288\mathrm{kg}/\mathrm{m}^3$ [179] with the critical point of the LJ fluid found at $T_{\mathrm{c}} = 1.312\epsilon_{\mathrm{SS}}/k_B$, $\rho_{\mathrm{c}} = 0.316\sigma_{\mathrm{SS}}^3$ and $p_{\mathrm{c}} = 0.1279\epsilon/\sigma_{\mathrm{SS}}^3$ [123]. We obtain that

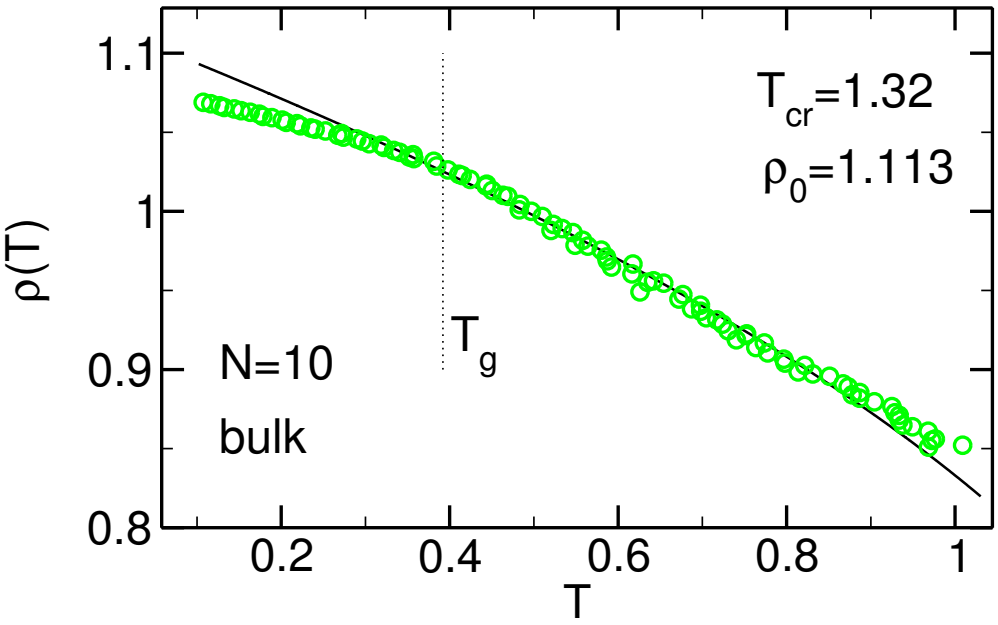

Figure 7.2: The density in a bulk polymer ($N = 10$) melt is shown as a function of temperature (circles). The black line indicates a fit to equation (7.3) with parameters as indicated in the plot and the text. The vertical line indicates the $T_{\rm g}$ in the bulk (see section 3.1).

$\epsilon_{\rm SS} = 6.23 \times 10^{-21}$J and $\sigma_{\rm SS} = 5.79 \times 10^{-10}$m. When comparing with the results for polystyrene we see that $\epsilon_{\rm PP} \simeq 2\epsilon_{\rm SS}$ and $\sigma_{\rm SS} \simeq \sigma_{\rm PP}$.

The molar masses of the monomer 'styrene' and the solvent are similar $\frac{m_{\rm S}}{m_T} \simeq 1.14$, so that we choose in our MD simulations $m_{\rm SS} = m_{\rm PP} = 1$. The interactions between solvent-solvent particles is chosen to be given by the Lennard-Jones potential defined in equation (2.1) with $\epsilon_{\rm SS} = 0.5$, while the monomer-monomer interaction is chosen as before $\epsilon_{\rm PP} = 1$. For the simulation of supported films we now also need to specify the interaction of the solvent with the wall $\epsilon_{\rm WS}$. We choose an attraction which is weaker than the polymer wall attraction $\epsilon_{\rm WP} = 3$ for the solvent wall interaction, so that $\epsilon_{\rm WS} = \epsilon_{\rm WP}\sqrt{\epsilon_{\rm PP}\epsilon_{\rm SS}} = 3/\sqrt{2}$, to avoid a very strong segregation of the solvent at the wall.

There are two additional parameters to determine, the interaction energy between polymer and solvent $\epsilon_{\rm PS}$ and the size between solvent and polymer $\sigma_{\rm PS}$. The solvent particles have the same size as the polymer particles, so that we chose $\sigma_{\rm SS} = \sigma_{\rm PP} = \sigma_{\rm PS} = 1$. According to the Lorentz-Berthelot mixing rules $\epsilon_{\rm SP} = \xi\sqrt{\epsilon_{\rm SS}\epsilon_{\rm PP}}$, with $\xi = 1$ [178, 180]. Here in order to promote mixing we chose $\xi = 1.1313$. If we denote by $\bar{u}_{\rm LJ}$ the average energy per pair interaction with a Lennard Jones potential and with $\bar{z}$ the average coordination number in our system we find $\chi = 0.05\bar{u}_{\rm LJ}\bar{z}/k_BT$ while in the case of the Lorentz-Berthelot mixing rules $\chi = -0.0429\bar{u}_{\rm LJ}\bar{z}/k_BT$. As $\bar{u}_{\rm LJ}$, the average energy per LJ interaction, is negative, for the choice of parameters

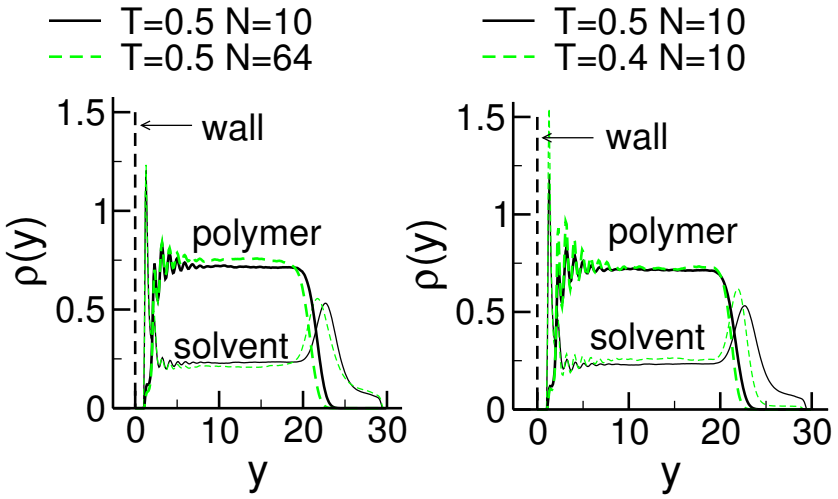

Figure 7.3: LEFT PANEL: The density profiles of the solvent (thin lines) and the polymer (thick lines) are shown at $T = 0.5$ for chains of length $N = 10$ (full black lines) and $N = 64$ (dashed grey lines). RIGHT PANEL: The density profiles of the solvent (thin lines) and the polymer (thick lines) are shown for at $T = 0.5$ (full black lines) and $T = 0.4$ (dashed grey lines) for chains of length $N = 10$.

used above, mixing is energetically favorable which would not be the case if we used the Lorentz-Berthelot mixing rule ($\xi = 1$). The exact numerical values of $\bar{u}_{\mathrm{LJ}}$ and $\bar{z}$ are dependent on solvent concentration and temperature. By integrating the radial distribution function up to the first minimum we obtain $\bar{z} \simeq 10$. We calculate the average interaction energy per particle $\bar{e}$ by integrating the Lennard-Jones potential weighed by the radial distribution function up to the first minimum of the latter and obtain $\bar{e} = \bar{u}_{\mathrm{LJ}}\bar{z} \simeq -6$. This gives an estimate of $\chi \simeq -0.3$.

7.2.2 System preparation

The system is equilibrated in an NVT simulation under constant vapor pressure. This is achieved by introducing a second wall at distance 30 or 40 (depending on solvent concentration as the films swell with increasing solvent concentration) allowing to form a solvent vapor phase in thermodynamic equilibrium with the solution as shown in the schematic drawing in figure 7.1. The potential at the upper wall is chosen to be purely repulsive

$$U_{\mathrm{upperwall}}(y) = \left(\frac{\sigma}{y}\right)^9 \quad , \tag{7.4}$$

for both species. The simulations contain $N_{\mathrm{tot}} = Nn + N_{\mathrm{S}}$ particles. The number of chains is kept fixed at $n = 96$ for chains of length $N = 64$ and $n = 576$ at chain length $N = 10$. We set up systems containing different numbers of solvent particles ($N_{\mathrm{S}} = 4608$, $N_{\mathrm{S}} = 3072$, $N_{\mathrm{S}} = 2304$, $N_{\mathrm{S}} = 1536$, $N_{\mathrm{S}} = 768$) at chain length

$N = 64$, while we only set up a system containing $N_S = 2880$ solvent particles at chain length $N = 10$.

In figure 7.3 density profiles for the solvent and the polymer are shown at solvent volume fraction in the center of the film of $\phi_S \simeq 21\%$ at $T = 0.5$. There is a strong accumulation of solvent at both surfaces. This leads to a reduction of the surface tension. The profiles are not strongly dependent on chain length. Nevertheless it can be seen that the solvent concentration in the center of the film decreases with increasing chain length at $T = 0.5$ ($N_S/N_{tot} = 1/3$ and $nN/N_{tot} = 2/3$ for both systems). The solvent density in the vapor phase decreases with decreasing temperature and the volume fraction of solvent in the film increases with decreasing temperature if the total number of particles is fixed. We will refer to the different systems not by the number of solvent particles in the system but by the volume fraction of solvent in the center of the film.

7.3 Dynamic properties of the binary mixture

The mobilities of polymer and solvent are expected to have a large influence on the evaporation process. We will look at the dependence of the monomer and solvent mobility on composition and position, i. e. distance from the interface, at different temperatures.

7.3.1 Mean-square displacements of polymer and solvent

We begin with an analysis of the dynamics of the solvent in the binary mixture by looking at the MSDs of the solvent molecules in the different regions of the film. This is shown in figure 7.4. The diffusion constants differ by a few orders of magnitude in the different regions of the film. While in the gas region (region 3) $g_0(t)$ crosses over directly from ballistic to diffusion dynamics, in the center of the film the MSD develops a slight plateau due to the onset of the cage effect. This is also the reason for the slow dynamics inside the film. The behavior in the solvent-rich transition region right at the film surface is also characterized by a direct cross over from ballistic motion to diffusion. Due to the higher density the 'mean free path', and thus the time window of ballistic motion, is much shorter than in the more dilute gas region.

The MSD of the polymer chains in presence of the solvent is accelerated. The solvent acts as a plasticizer speeding up the dynamics of the polymer at both chain lengths investigated $N = 10$ and $N = 64$. This is shown in figure 7.5. At short times the dynamics of the monomers is ballistic and independent of chain length or solvent concentration. The intermediate plateau due to the cage effect is reduced in the presence of the solvent. Here the curves for the two different chain lengths separate because they do not follow the same power-law in the sub-diffusive regime. This regime is characterized by chain connectivity. The Rouse theory [50] predicts

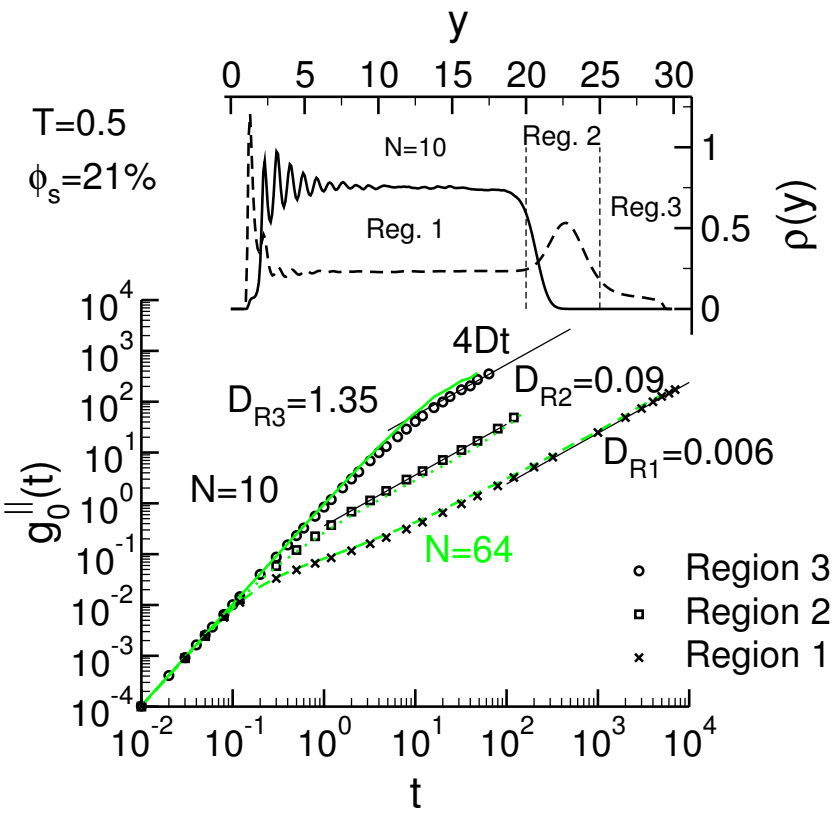

Figure 7.4: MAIN FIGURE: The MSD of the solvent molecules in 3 different regions of the film as indicated in the inset are shown. The symbols correspond to the chain length $N = 10$ and the gray lines indicate $N = 64$. INSET: The density profiles for solvent and polymer of a film containing $\phi_S = 21\%$ solvent with chain length $N = 10$ at $T = 0.5$ are shown. The horizontal dashed lines indicate the boundaries of the regions for which the MSDs in the main figure are calculated.

$g_0(t) \propto t^{0.5}$ whereas the exponent for $N = 10$ is found to be $g_0(t) \propto t^{0.63}$. The larger chain length $N = 64$ agrees better with the Rouse prediction. The shorter chains enter free diffusion sooner than the longer chains. In the diffusive regime the MSD increases linearly with time $g_0(t) \propto 4Dt$.

Figure 7.5 shows the dependence of the MSD of all monomers for $N = 64$ on temperature as well as solvent concentration. The acceleration due to the solvent becomes more pronounced at lower temperatures. This figure also indicates the MSD in layers situated in the center of the film as well as close to its surfaces calculated according to equation (4.10). As was observed in section 4.3 the dynamics at the surface is faster than in the center of the film. We found that further away from T_c the relative acceleration at the surface is weaker. In the solution the deviations are thus smaller than for the pure polymer films, because the presence of the solvent lowers the glass transition temperature.

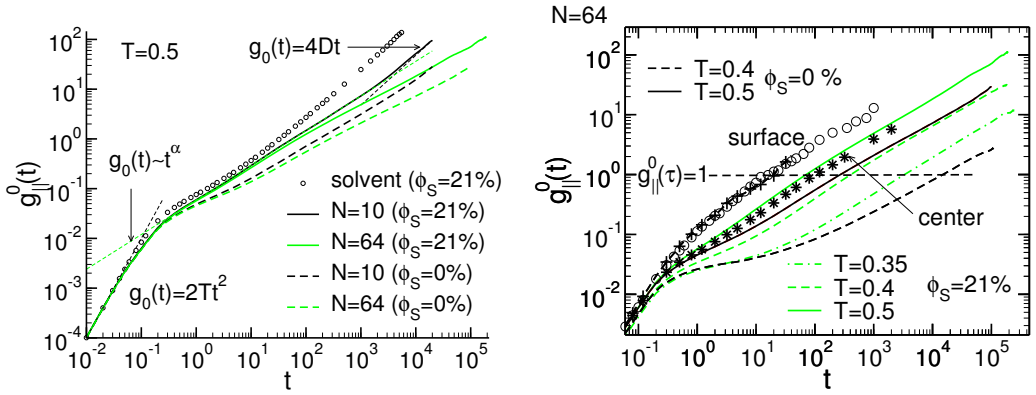

Figure 7.5: LEFT PANEL: The MSD of all monomers $g_0(t)$ for chains of length $N = 10$ (black lines) and $N = 64$ (gray lines) are shown for the pure polymer (dashed lines) and the mixture with $\phi_S = 21\%$ (full lines). The thin dashed lines indicate ballistic and diffusive motion respectively. The dotted lines indicates the sub-diffusive regime preceding the final free diffusion. The circles indicate the MSD of the solvent particles in solution. RIGHT PANEL: The MSDs of the monomers in a binary mixture averaged over the film (grey lines) are shown at $T = 0.5$, $T = 0.4$ and $T = 0.35$. The films contained a volume fraction $\phi_S = 21\%$ of solvent molecules in the center of the film. In addition at $T = 0.5$ the MSD of the monomers in the center, at the free surface (crosses) and at the supported surface (circles) are shown. The chain length is $N = 64$. Also indicated is $g_0(t)$ for the pure polymer at $T = 0.5$ and $T = 0.4$ (black lines). The horizontal line indicates the criterion used to extract the relaxation times $g_0(\tau) = 1$.

7.3.2 Layer-resolved relaxation times

We use again the definition of equation (4.12) to extract a local relaxation time to get an overview of the influence of composition as well as position on the relaxation in the film. We denote with $\tau_P(y, \phi_S)$ the time it takes a monomer to be displaced by its own diameter parallel to the walls in a film with a volume fraction ϕ_S of solvent in the center. Only monomers are taken into account which are within a slab of width $\Delta y = 2$ centered at distance y from the supporting wall placed at $y = 0$. $\tau_S(y, \phi_S)$ corresponds to the same time measured for a solvent particle in the same system.

Relaxation times above T_g ($T = 0.5$). The results of this analysis for solvent as well as polymer are shown in figure 7.6. The relaxation time of the polymer decreases at the surfaces and with increasing solvent concentration. The position of the free surface shifts to larger y at higher solvent concentration since the films are the thicker, the more solvent they contain. The solvent particles show the same behavior. The effect of the surfaces becomes weaker with increasing solvent concentration and the relaxation times increase with decreasing solvent concentration. The relaxation times of the solvent are about a factor of two lower than those of the polymer.

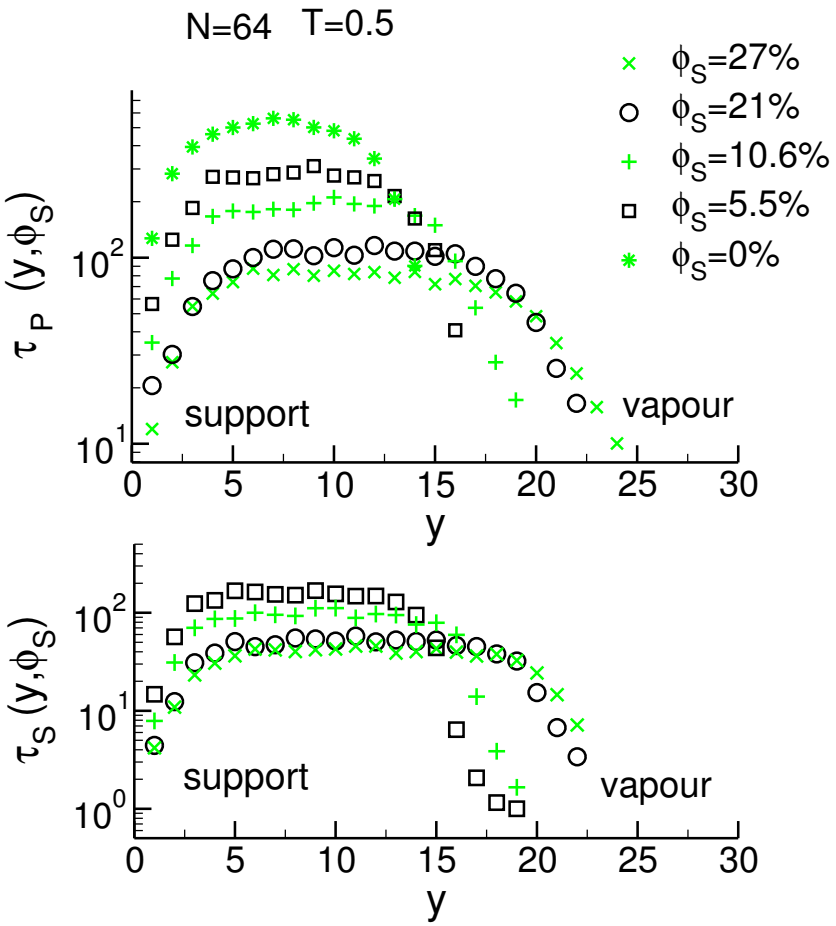

Figure 7.6: UPPER PANEL: The relaxation times for the polymer as a function of position for different compositions at $T = 0.5$ calculated according to equation (4.12). LOWER PANEL: The relaxation times for the solvent as a function of position for different compositions at $T = 0.5$ calculated according to equation (4.12) .

Relaxation at T_g ($T = 0.4$). Upon lowering the temperature to $T = 0.4$ the influence of the solvent concentration on the dynamics becomes stronger. In figure 7.7 the relaxation times of polymer and solvent are again shown as a function of the distance from the wall. As for the pure polymer films and the solution at higher temperature we find an increase of mobility at the surface. It is more pronounced than for $T = 0.5$. It can be seen in figure 7.7 that the relaxation times span more than 3 orders of magnitude as a function of position (distance from the surface) and composition. At $T = 0.5$ we found that the relaxation times of the solvent was by a factor of 2 faster than the one of the monomers independent of composition. At $T = 0.4$ this is no longer the case at low solvent concentrations. The relaxation times of the polymer and solvent become equal as the solvent concentration decreases and the system approaches its glass transition. $T = 0.4$ is approximately the glass transition temper-

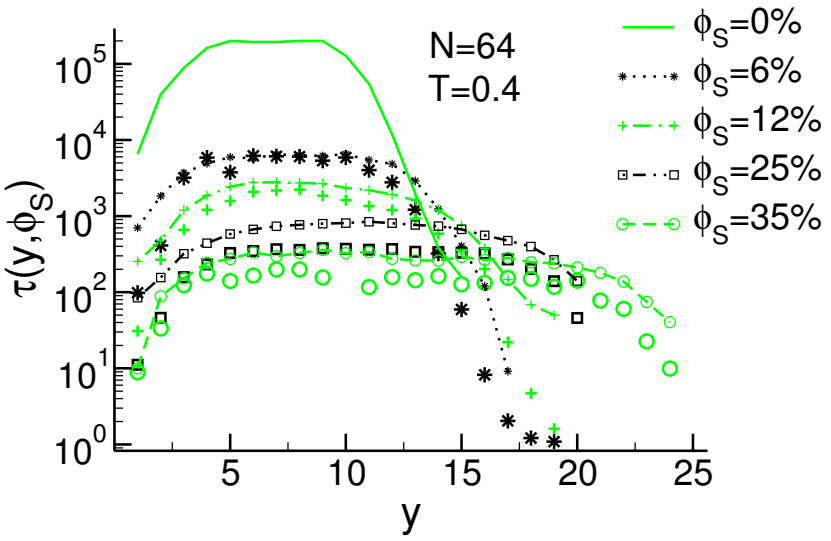

Figure 7.7: The relaxation times as a function of position for different compositions at $T = 0.4$ calculated according to equation (4.12) for the polymer (lines with symbols) and the solvent (symbols) are shown. The same symbols correspond to the same system. The chain length is $N = 64$.

ature of the pure polymer. This is a clear sign that the coupling of the dynamics of the two species becomes stronger as the system gets denser and the cage effect becomes more pronounced.

To allow for a better comparison of the relaxation times at different positions we rescale the y coordinate with the position of the right GDS (see section 3.1) at the given solvent concentration and temperature so that the polymer solvent vapor interface is always at $y/y_+^{\mathrm{G}} = 1$ and the relaxation times by the value they reach in the center of the film $\tau(y_c, \phi_{\mathrm{S}}) = \tau^c(\phi_{\mathrm{S}})$. The results of this comparison are shown in figure 7.8. It can be seen clearly that the acceleration emanating from the free surface reaches further into the film at lower temperature and lower solvent volume fraction ϕ_{S} both for the polymer and the solvent. The relative decrease of relaxation times at the free surface increases as well with decreasing temperature and solvent volume fraction. The relaxation of the pure polymer at $T = 0.4$ is thus by 3 orders of magnitude faster at the free surface than in the center of the film. In the lower panel it can also be seen that the relaxation time of the solvent in the gas phase in comparison to the one in the liquid phase decreases as the temperature decreases. The changes in relaxation time with temperature and composition at the supporting wall are smaller.

7.3.3 Composition dependence of the relaxation times

As the relaxation time of polymer and solvent are extracted from the MSDs of the solvent particles and the monomers in an equilibrium simulation they are related to

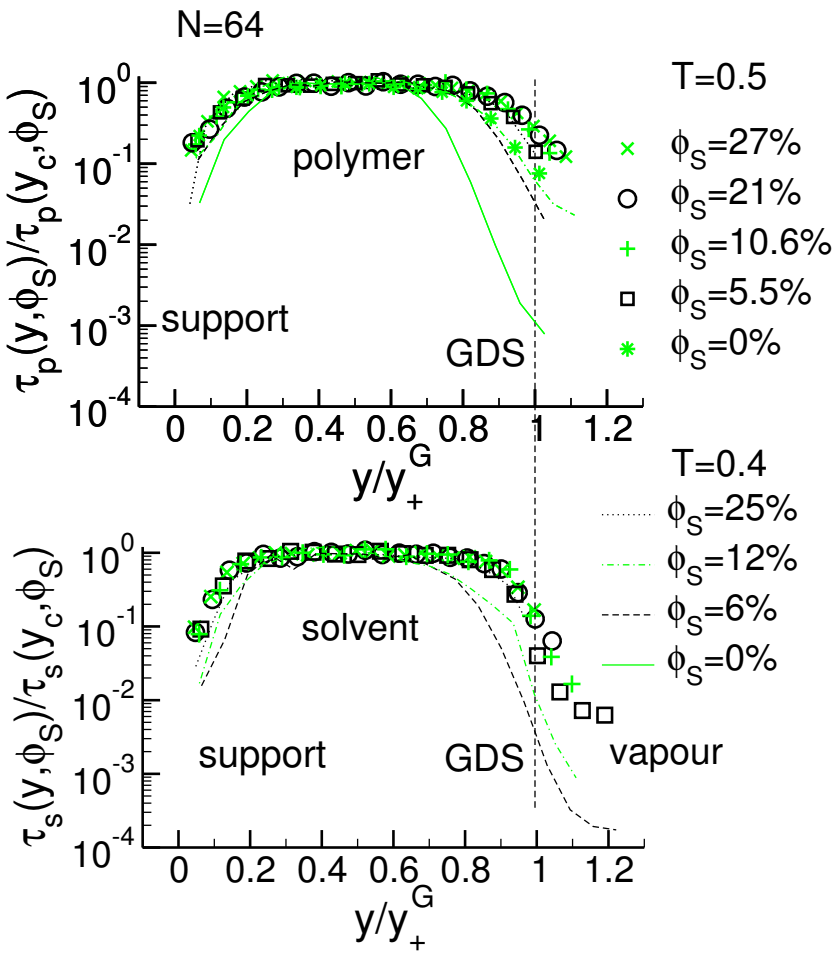

Figure 7.8: UPPER PANEL: The relaxation times as a function of position for different compositions at $T = 0.5$ calculated according to equation (4.12) for the polymer. LOWER PANEL: The relaxation times as a function of position for different compositions at $T = 0.5$ calculated according to equation (4.12) for the solvent. The y-coordinate is rescaled by the position of the right GDS y/y_+^{G} and the relaxation time by the value it reaches in the film center of the film denoted by y_{c} so that $\tau(y,\phi_{\mathrm{S}})/\tau(y_{\mathrm{c}},\phi_{\mathrm{S}})$. The vertical line indicates the position of the GDS.

the self-diffusion constants. There are many theories describing the self diffusion coefficient D_{self} of a polymer as a function of concentration in bulk polymer solutions (see for example [181] for a review). The appropriate model has to be chosen depending on the concentration of the solution and also its thermodynamic state. Polymer solutions close to their glass transition will behave differently than in the rubbery state. In rather concentrated polymer solutions far from the glass transition models taking into account the hydrodynamic interactions present in the system such as the friction between the monomers and the solvent are necessary to describe the findings correctly.

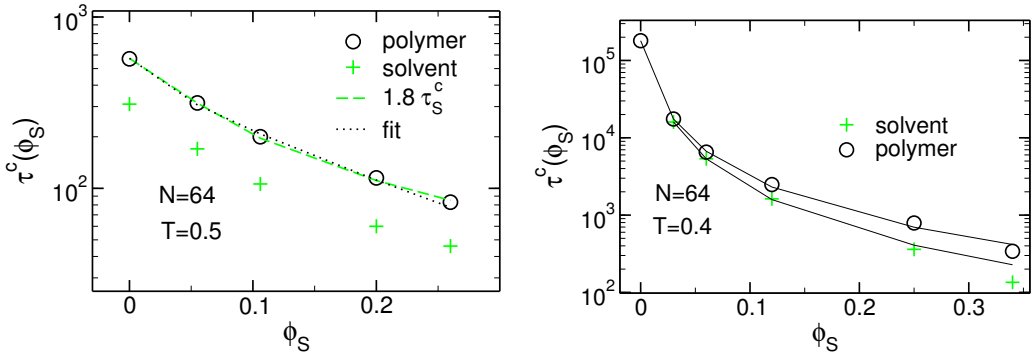

Figure 7.9: LEFT PANEL:The local relaxation times in the center of the film extracted according to equation (4.12) are plotted as a function of the volume fraction of solvent in the center of the film at $T = 0.5$. The chain length was $N = 64$. The dotted line indicates a fit to equation (7.6). RIGHT PANEL: The relaxation time of solvent and polymer in the center of the film as a function of the volume fraction of solvent ϕ_S in the center of the film at $T = 0.4$. The full lines indicate a fit to equation (7.7).

A theory by Phillies [182–184] is known to describe polymer self-diffusion in a wide range of concentrations successfully based on a stretched exponential law

$$D_{\text{self}} = D_0 \exp(-\alpha \phi_P^{\beta}) \, , \tag{7.5}$$

where α and β are scaling parameters. β is found to be dependent on molecular weight of the polymer. Experimentally, the exponent β ranges from 1 for low molecular weight 0.5 for very large molecular weight substances [182].

Indeed at $T = 0.5$ the dependence of the relaxation times of the polymer in the center of the film, which should best correspond to the ones of the bulk solution, on the volume fraction ϕ_S can be well parameterized by a stretched exponential function as follows

$$\tau(y_c, \phi_S) = \tau(y_c, 0) \exp\left[-(\phi_S/\phi_S^0)^{\beta}\right] \, , \tag{7.6}$$

where $\tau(y_c, 0) = 570$ corresponds to the relaxation time of the pure bulk polymer and y_c refers to the position of the film center which changes as a function of ϕ_S because the film is thicker at higher solvent concentrations. The fit parameters are found to be $\phi_S^0 = 0.105$ and $\beta = 0.75$. Also the relaxation times of the solvent can be described well by this law if one changes the prefactor $\tau(y_c, 0) = 320$ to account for faster movement of the solvent.

In the left panel of figure 7.9 the relaxation times of polymer and solvent in the center of the film at $T = 0.5$ are shown for films with different solvent volume fraction. The lines indicate a fit to equation (7.6). The relaxation times can be described well by the fit. It can be seen that the relaxation times of polymer and solvent are proportional to one another at all times, so that $\tau_P(y_c, \phi_S) = 1.8\tau_S(y_c, \phi_S)$.

At the lower temperature $T = 0.4$ this approach fails because it does not capture the very rapid increase of relaxation time with decreasing solvent concentration. As

we are faced with a non-Arrhenius increase of the relaxation time as the system approaches its glass transition at approximately $\phi_S \simeq 0$ because $T = 0.4 \simeq T_g$ is the glass transition temperature of the pure polymer film, we use a power law to model the increase in relaxation time as in section 4.2. The role of temperature is replaced by the volume fraction of solvent.

Both the relaxation time of the polymer and the one of the solvent in the center of the film at $T = 0.4$ can be fitted by

$$\tau(y_c, \phi_S) = \tau^c(\phi_S) = \frac{a}{(\phi_S - \phi_c)^\gamma} \,. \tag{7.7}$$

For the polymer we find $a = 67.8$ and $\gamma = 1.73$ while for the solvent we find $a = 29.0$ and $\gamma = 1.96$ with $\phi_c = -0.01$ in both cases. A negative volume fraction is not physical and due to the fact that the relaxation times remain finite at this temperature and do not diverge as suggested by the equation. The relaxation times of polymer and solvent at $T = 0.4$ are shown in the right panel of figure 7.9. In comparison with $T = 0.5$ where the relaxation times cover an order of magnitude within the composition window investigated, at $T = 0.4$ they already cover 3 orders of magnitude. If we return to figure 7.8 we see that the effect of composition and position on the relaxation times of polymer and solvent are comparable in magnitude at both temperatures.

7.4 Static structure in the presence of the solvent

First we will discuss the static structure factors of the binary mixture, then we will look at the layer-resolved radius of gyration.

7.4.1 Static structure factor

The layer-resolved partial structure factors are defined as

$$S_{SS}(q, y) = \frac{1}{n_S} \left\langle \sum_{i,j}^{N_S} e^{-i\mathbf{q}\cdot(\mathbf{r}_i - \mathbf{r}_j)} \delta(y - y_i)\, \delta(y - y_j) \right\rangle \,, \tag{7.8}$$

where n_S is the number of solvent particles in the layer and N_S the number of solvent particles in the system. Analogously the partial structure factor of the polymer is written as

$$S_{PP}(q, y) = \frac{1}{n_P} \left\langle \sum_{i,j}^{nN} e^{-i\mathbf{q}\cdot(\mathbf{r}_i - \mathbf{r}_j)} \delta(y - y_i)\, \delta(y - y_j) \right\rangle \,, \tag{7.9}$$

where n_P is the number of monomers in the layer and n the number of chains of N monomers.

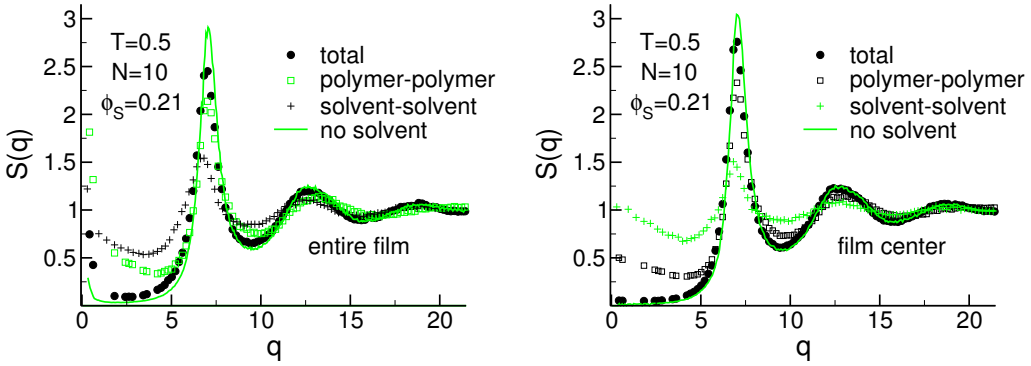

Figure 7.10: LEFT PANEL: The partial static structure factors $S_{\mathrm{SS}}(q)$ (+), $S_{\mathrm{PP}}(q)$ (squares) and the total structure factor (full symbols) averaged over the whole film are shown for chains of length $N = 10$ at $T = 0.5$. The solvent concentration in the center of the films was $\phi_{\mathrm{S}} = 21\%$. Also indicated is the structure factor of the pure polymer film (full line) containing the same number of chains. RIGHT PANEL: The partial static structure factors $S_{\mathrm{SS}}(q)$ (+), $S_{\mathrm{PP}}(q)$ (squares) and the total structure factor (full symbols) calculated in a slab of width $\Delta y = 2$ in the center of the film are shown for chains of length $N = 10$ at $T = 0.5$. The solvent concentration in the center of the films was $\phi_{\mathrm{S}} = 21\%$. Also indicated is the structure factor of the pure polymer film (full line) containing the same number of chains.

The total structure factor $S(q, y)$ is again calculated using equation (3.9) without making a distinction between solvent particles and monomers

$$S(q,y) = \frac{1}{n_{\mathrm{l}}} \left\langle \sum_{i,j}^{nN+N_{\mathrm{S}}} e^{-\mathrm{i}\mathbf{q}\cdot(\mathbf{r}_i - \mathbf{r}_j)} \delta\left(y - y_i\right) \delta\left(y - y_j\right) \right\rangle . \tag{7.10}$$

Here n_{l} thus indicates the total number of particles in a layer. The partial structure factor $S_{PS}(q)$ can then be defined as

$$S(q,y) = \phi_{\mathrm{S}}(y) S_{SS}(q,y) + \phi_{\mathrm{P}}(y) S_{PP}(q,y) + S_{PS}(q,y) . \tag{7.11}$$

In figure 7.10 the partial structure factors and the total structure factor are shown calculated in the center of the film and averaged over the whole film. The main difference between the two is found at small q where the total structure factor shows a divergence due to capillary waves (see section 5.1 for a more detailed discussion) at the free surface. Also the first maximum is slightly lower in the average structure factor in comparison to the one in the center. This is due to a less efficient packing of the monomers at the surface which we have already encountered in the pure polymer films (see section 3.2.2). The presence of the solvent lowers the surface tension which leads to a stronger increase of the structure factor at small q due to larger fluctuations of the local film thickness in comparison with the pure polymer film.

In addition it can be interesting to define the concentration structure factor [123, 185]. To measures the correlations in the deviations of the local volume fraction $\phi(\mathbf{r})$

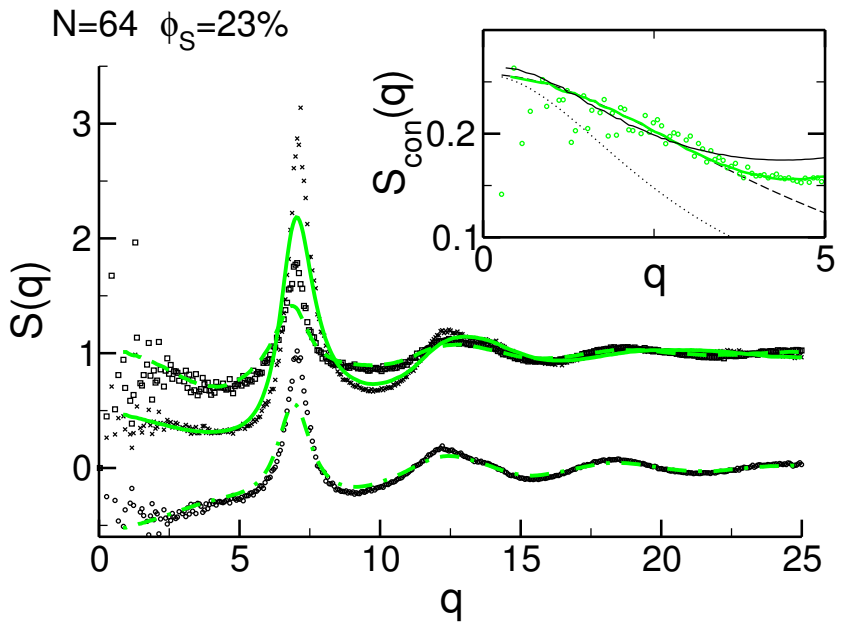

Figure 7.11: The partial static structure factors $S_{SS}(q)$ (dashed line), $S_{PP}(q)$ (full line) and $S_{PS}(q)$ (dash-dotted line) calculated in a slab of width $\Delta y = 2$ in the center of the film are shown for chains of length $N = 64$ at $T = 0.5$. The solvent concentration in the center of the films was $\phi_S = 23\%$. Also indicated are $S_{SS}(q)$ (circles), $S_{PP}(q)$ (rectangles) and $S_{PS}(q)$ (stars) for the same system at $T = 0.35$. INSET: The concentration structure factor (equation (7.12)) is shown at $T = 0.5$ (full grey line) and $T = 0.35$ (symbols) as well as the mean-field prediction in the small-q limit (dotted line), a best fit to equation (7.18) (dashed line) and the results obtained from equation (7.19) (thin black line).

from its average ϕ, we define the concentration density $\rho_{\text{con}} = [\rho_S(\mathbf{r})\phi_P - \rho_P(\mathbf{r})\phi_S]$, where ϕ_S and $\phi_P = 1 - \phi_S$ denote the average volume fractions of polymer and solvent in the film and $\rho_i(\mathbf{r})$ refers to the local density of solvent and polymer. The concentration structure factor is then defined as [123, 185]

$$S_{\text{con}}(q) = \frac{1}{N} \langle \rho_{\text{con}}(\mathbf{q}) \rho_{\text{con}}(-\mathbf{q}) \rangle \ . \tag{7.12}$$

The concentration structure factor can be expressed in terms of $S_{\text{SS}}(q)$, $S_{\text{PP}}(q)$, and $S(q)$ as

$$\begin{aligned} S_{\text{con}}(q) =& \phi_S^2 \phi_P S_{PP}(q) + \phi_P^2 \phi_S S_{SS}(q) - \phi_S \phi_P S_{PS}(q) \\ =& (\phi_S^2 \phi_P + \phi_P^2 \phi_S)(S_{SS}(q) + S_{PP}(q)) - \phi_S \phi_P S(q) \ . \end{aligned} \tag{7.13}$$

In the thermodynamic limit it can be found that [51]

$$\lim_{q \to 0} S_{\text{con}}(q) = k_B T \left(\frac{\partial^2 \Delta F_{\text{mix}}}{\partial \phi_S^2} \right)^{-1} \ , \tag{7.14}$$

which gives together with equation (7.2) the prediction of the Flory-Huggins theory for concentration fluctuations at vanishing wave vector

$$\frac{1}{S_{\text{con}}(0)} = \frac{1}{N\phi_{\text{P}}} + \frac{1}{1-\phi_{\text{P}}} - 2\chi \,. \tag{7.15}$$

This means that χ can be found by measuring $S_{\text{con}}(0)$. Using the random phase approximation this result can be extended to non-zero q using the form factor of an ideal chain $P(q,N)$ [51]

$$P(q,N) = \frac{2}{(q^2R_{\text{g}}^2)^2}\left(e^{-q^2R_{\text{g}}^2} - 1 + q^2R_{\text{g}}^2\right) \,. \tag{7.16}$$

By approximating $\frac{1}{P(q,N)} \simeq 1 + \frac{q^2Nb^2}{12}$ one finds that

$$\frac{1}{S_{\text{con}}(q)} = \frac{1}{S_{\text{con}}(0)} + \frac{q^2b^2}{12\phi_{\text{P}}(1-\phi_{\text{P}})} \,. \tag{7.17}$$

In the inset of figure 7.11 the comparison between $S_{\text{con}}(q)$ (symbols) and equation (7.17) (dotted line) is shown. They are not in good agreement. Equation (7.17) has a functional dependence according to

$$S_{\text{con}}(q) = \frac{S_{\text{con}}(0)}{1+(q\xi)^2} \tag{7.18}$$

and for $\xi = \xi_{\text{FH}} = \sqrt{\frac{b^2S(0)}{12\phi(1-\phi)}} = 0.335$ equation (7.17) is recovered. From a fit of equation (7.18) to $S_{\text{con}}(q)$ we obtain $\xi = 0.21$ (dashed line) and $S_{\text{con}}(0) = 0.255$. This value of ξ is not in agreement with the prediction $\xi_{\text{FH}} = 0.335$. The Flory-Huggins parameter is found using equation (7.15) $\chi = 0.22$. In comparison with $\chi = 0.05\bar{e}\bar{z} = -0.3$ this value is quite different. The obtained value for χ has a large error bar as the equation is very sensitive to the value of $S_{\text{con}}(0)$ which cannot be determined very accurately.

To improve the approximations made it is possible to use instead of the form factor of an ideal chain the intra-chain structure factor $w(q)$ determined in the simulations according to equation (3.7). Then still using the random phase approximation one gets

$$\frac{1}{S_{\text{con}}(q)} = \frac{1}{\phi w(q)} + \frac{1}{1-\phi} - 2\chi \,. \tag{7.19}$$

The agreement between this prediction (see thin black line and thick grey line in figure 7.11) and the measured curve is better but it does not resolve the differences found in the χ parameters, which is determined by $S_{\text{con}}(0)$ and this value does not change.

Also shown in figure 7.11 are the partial structure factors in the center of a supported film at $T = 0.5$ and $T = 0.35$ at a volume fraction of $\phi_{\text{S}} = 0.23\%$ in the

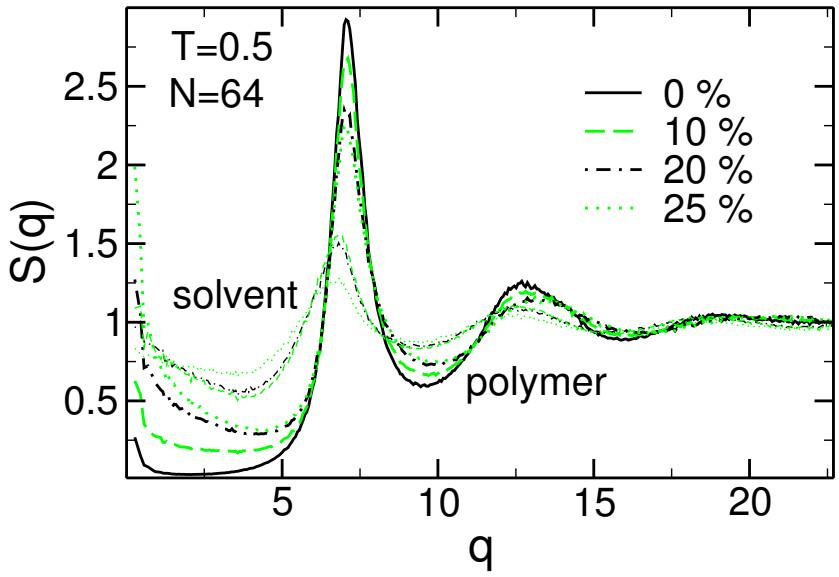

Figure 7.12: The partial static structure factors $S_{SS}(q)$ (thin lines), S_{PP} (thick lines) averaged over the whole film are shown for different solvent concentrations as indicated in the plot. Also shown is the structure factor of the pure polymer film (full black line) containing the same number of chains.

center of the film. Although we see an increase in the first peak of the partial structure factors upon lowering the temperature, the small-q dependence dominated by the concentration fluctuations is rather independent of temperature which shows clearly that we do not see any signs of demixing at lower temperatures. Also this should not be expected, since we chose the parameters in a way such that mixing is energetically favorable as described in section 7.2.

Figure 7.12 displays the composition dependence of the partial structure factors of solvent and polymer averaged over the whole film at $T = 0.5$. As stated above the surface tension is lowered with increasing solvent concentration which leads to a stronger increase of $S(q)$ at small q with increasing solvent concentration. The first peak of $S_{\mathrm{PP}}(q)$ decreases with increasing solvent concentration while the peak of $S_{\mathrm{SS}}(q)$ increases with increasing solvent concentration.

7.4.2 Layer resolved R_{g}

As the dimensions of the film become comparable to the size of the polymer coil the Gaussian statistics of the chains in the melt are perturbed due to the confinement as shown in section 3.3. In order to study this effect we look at the radius of gyration of

the chains introduced in section 3.3 given as

$$R_{\mathrm{g}}^2 = \frac{1}{N}\sum_{a=1}^{N}\left\langle \left(\mathbf{r}_i^a - \mathbf{R}_{\mathrm{cm}}^i\right)^2\right\rangle_i = \frac{1}{2N^2}\sum_{a,b=1}^{N}\left\langle \left(\mathbf{r}_i^a - \mathbf{r}_i^b\right)^2\right\rangle_i . \tag{7.20}$$

$\mathbf{R}_{\mathrm{cm}}^i = \frac{1}{N}\sum_{a=1}^{N}\mathbf{r}_i^a$ refers to the position of the center of mass of chain i. We also calculate a layer-resolved radius of gyration by considering only chains whose center of mass is in a certain distance y from the wall given by equation (3.15) here repeated for clarity

$$\begin{aligned} R_{\mathrm{g\,xz}}^2(y) &= \left\langle \frac{1}{2n(y)N}\sum_{i=1}^{n}\sum_{a=1}^{N}\left[\left(x_i^a - R_{\mathrm{cm\,x}}^i\right)^2 + \left(z_i^a - R_{\mathrm{cm\,z}}^i\right)^2\right]\delta\left(y - R_{\mathrm{cm\,y}}^i\right)\right\rangle \\ R_{\mathrm{g\,y}}^2(y) &= \left\langle \frac{1}{n(y)N}\sum_{i=1}^{n}\sum_{a=1}^{N}\left[\left(y_i^a - R_{\mathrm{cm\,y}}^i\right)^2\right]\delta\left(y - R_{\mathrm{cm\,y}}^i\right)\right\rangle , \end{aligned} \tag{7.21}$$

where $n(y)$ is the number of chains whose center of mass is at distance y from the wall.

In figure 7.13 the results of this analysis are shown for the pure polymer film and a film containing the same amount of polymer in solution with a volume fraction of $\phi_{\mathrm{S}} = 21\%$ of solvent. The chains in the center of the film have a radius of gyration very close to the bulk value of the pure polymer in the pure polymer film as well as in solution. The parallel component of R_{g}^2 increases as the film surface is approached while the perpendicular component decreases. Apart from the difference in film thickness there is no pronounced difference between the radius of gyration of the chains with or without solvent.

7.5 Glass transition temperature of the binary mixture

We saw in the last sections that the dynamics are accelerated in the presence of the solvent and also observed a decrease of the first maximum of the static structure factor in the presence of the solvent. Two factors which we linked in the previous chapters to a decrease in the glass transition temperature of the films.

We determine $T_{\mathrm{g}}(\phi_S)$ in the binary mixture as before upon cooling the solution at a constant rate and monitoring the film thickness as a function of temperature. We used a cooling rate of $\Gamma_T = 2 \times 10^{-5}$ as for most of the cooling runs for the pure polymer films described in section 3.1. The equilibrium concentration of solvent inside the polymer solution increases with decreasing temperature. Therefore the concentration of solvent inside the film did not stay constant upon cooling. But the amount of solvent initially in the vapor phase entering the film upon cooling remained

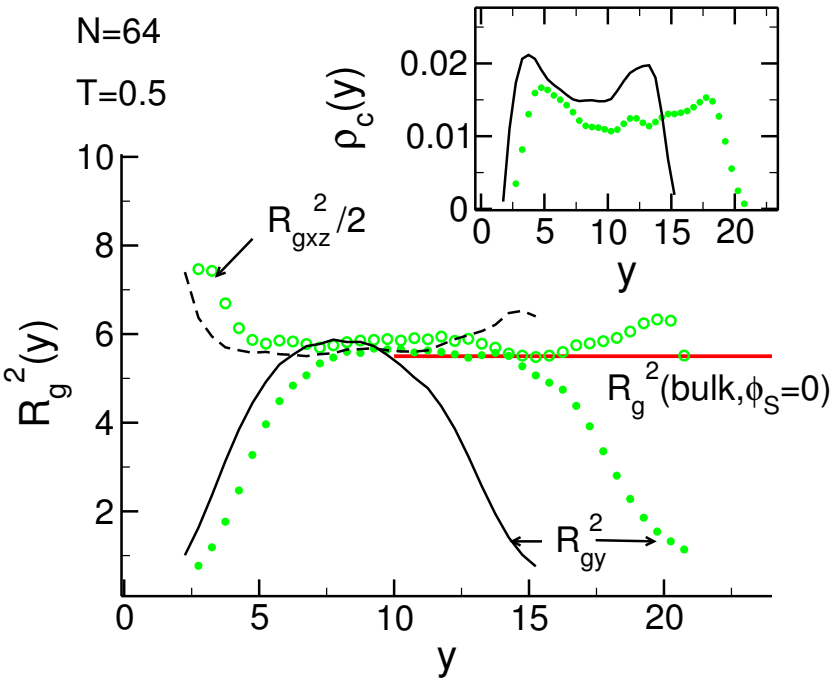

Figure 7.13: MAIN FIGURE: The square radius of gyration in the direction parallel and perpendicular to the plane of the film as a function of the distance of the chain's center of mass from the wall as introduced in equation (7.21). The symbols refer to a film containing a volume fraction of $\phi_S = 21\%$ of solvent in the center of the film while the lines indicate the results for the pure polymer film containing the same amount of chains. The open symbols and the dashed line show the parallel component of $R_g^2(y)$ and the full symbols and the full line show the perpendicular component. The horizontal line indicates $R_g^2/3$ of the pure bulk polymer. INSET: The density profile of the chains center of mass is shown for a film containing a volume fraction of $\phi_S = 21\%$ of solvent in the center of the film (symbols) and the pure polymer film (line).

small changing the solvent volume fraction ϕ_S by less than a percent, so that we only report the average solvent concentration.

In figure 7.14 the film thickness of the binary mixture at different concentrations is shown as a function of temperature. As expected from our previous results T_g decreases with increasing solvent concentration. The relative film thickness fluctuations increase with increasing solvent concentration especially at higher temperature which is due to a lower surface tension in the presence of the solvent. The thermal expansion coefficient increases slightly with increasing solvent concentration in both the liquid and the glassy state. At a solvent volume fraction of $\phi_S = 10\%$ the glass transition temperature is found to be $T = 0.35$ which is a moderate decrease in comparison with $T_g = 0.38$ for the pure polymer film. At a solvent concentration of $\phi_S = 25\%$ the decrease is much more pronounced.

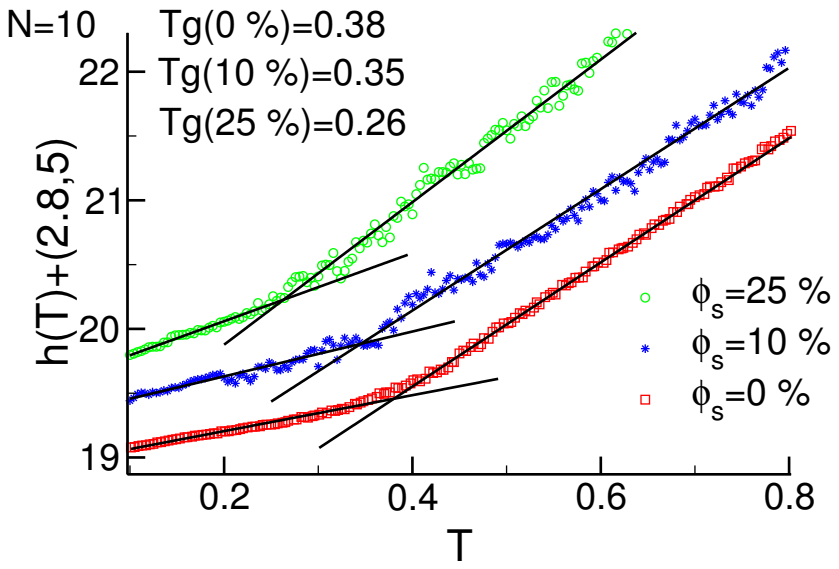

Figure 7.14: The film thickness as a function of temperature at different solvent concentrations as indicated is shown (symbols). The curves for $\phi_S = 10\%$ and $\phi_S = 0\%$ are shifted upwards by a constant value (2.8 and 5) for clarity. The black lines indicate fits to the liquid and the glassy branches of the curves. The values of T_g are found as indicated in the figure. The chain length is $N = 10$.

7.6 Summary

In this chapter we studied a dense polymer solution in two film geometries as for the pure polymer films, namely free-standing and supported films. The parameters were chosen such as to mimic the solution of polystyrene and toluene. The solvent is enriched between the polymer and the wall as well as at the free surface. The presence of the solvent reduces the glass transition temperature of the binary mixture. We find that the solvent also suppresses correlations in local density fluctuations as measured by the maximum of the static structure factor. The conformations of the chains in solution do not differ a lot from the conformations in the pure film at the studied concentrations. The chains are only very slightly swollen. The radius of gyration of the chains R_g in the parallel direction in the center of the pure polymer film and in the center of the polymer solution are close to the bulk value of R_g of the pure polymer.

An increasing sensitivity of the local mobility of the monomers on the solvent concentration and the proximity to the interface is observed with decreasing temperature. The solvent acts in our model solution as a plasticizer accelerating the relaxation of the polymer. A simulation study by Riggleman and coworkers with solvent molecules half the size of the monomers found an anti-plasticizing effect [14]. The closer the monomers are to the surface, the faster their dynamics. At T_g of the pure polymer the local relaxation times span three orders of magnitude as a function of

composition and distance from the surface for the solvent as well as for the polymer. The dynamics of solvent and polymer are strongly coupled at all times since polymer and solvent molecules have the same size and the overall density is very high at all temperatures ($\rho_{\text{tot}} \simeq 1$). This coupling increases with decreasing solvent concentration and decreasing temperature. Therefore in our model a movement of solvent molecules without a relaxation of the polymer on the local scale should not be possible.

Chapter 8

Solvent evaporation

The MD simulations of the solvent evaporation are carried out starting from an equilibrated configuration under constant vapor pressure as described in the last chapter with the solvent volume fraction in the center of the film around $\phi_{\mathrm{S}} = 20\%$. We remove the upper wall to create a vacuum above the film. Particles which travel further than 45σ from the supporting wall are not allowed to return. This is achieved by a very strongly attractive potential at the upper wall which traps the particles there. The evaporation runs are carried out for different temperatures $T = 0.5$, $T = 0.4$ and $T = 0.35$. One of the key features we want to capture with the simulations of the evaporation of solvent from our model polymer films is whether the vitrification upon solvent loss has an influence on the evaporation kinetics and the resulting structure. While at $T = 0.5$ the film is liquid at all times, $T = 0.4$ corresponds to T_{g} of the pure polymer film and at $T = 0.35$ the system undergoes the glass transition at a solvent volume fraction of about 10% as determined in the last section.

Mainly we are concerned with the evaporation of the solvent from supported films which contain always the same amount of polymer chains ($n = 96$ in the case of $N = 64$ and $n = 576$ for $N = 10$) as we have investigated the pure polymer films of these dimensions extensively. But we also carry out some evaporation runs for free-standing films. The preparation of the initial state was carried out by equilibration under constant vapor pressure analogously to the supported films. Then the walls were again moved at a distance of 45σ from the surfaces and a strongly attractive potential was switched on at both walls, not allowing particles having ventured a certain distance into the gas phase to return.

8.1 Simulation results

Snapshots of a supported film of chains of length $N = 64$ are shown as the solvent is evaporating in figure 8.1. Initially the surplus of solvent located at the free surface is evaporating fast. In the later stages of the evaporation the remaining solvent is mainly located between the polymer and the supporting wall. Only very few solvent

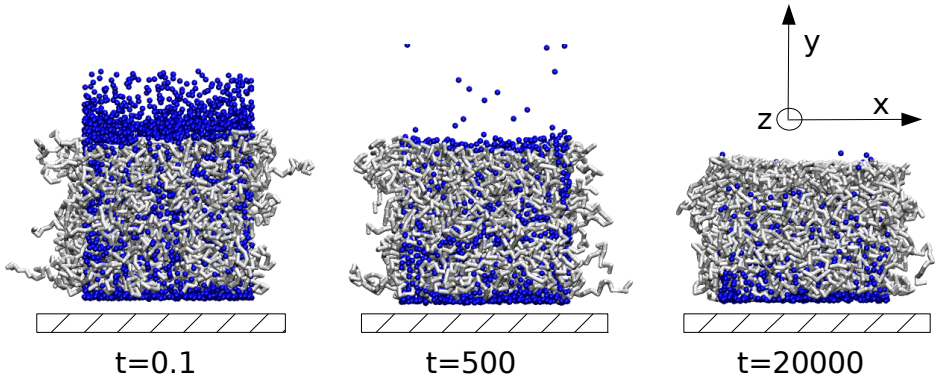

Figure 8.1: Snapshots of the film of polymer solution as the solvent is evaporating at $T = 0.5$ and $N = 64$. The solvent is indicated by dark spheres and the polymer by light lines. The horizontal rectangles indicate the supporting wall.

molecules manage to leave the film at a given time. Therefore the solvent vapor in the gas phase is so dilute that the solvent particles do not experience enough collisions to show diffusive behavior before they reach the adsorbing wall. The mean free path of the molecules is much larger than the distance between the surface and the wall, where the solvent particles are trapped. It should be expected that the simulation results are dependent on the position of the adsorbing wall. As we cannot place the wall far away enough for the particles to move diffusively, the exact position of the wall does not matter in our simulations as the particles fly into the boundary ballistically. Therefore the probability of solvent molecules returning into the liquid phase from the gas phase is very small once they detached from the surface.

In figure 8.2 the polymer as well as the solvent and the total density are shown as the solvent is evaporating from a supported film of chains with length $N = 64$ at $T = 0.5$. As could already be inferred from the snapshots, the solvent is depleted rather quickly close to the surface. The peak corresponding to the surplus of solvent decreases in height during the evaporation but it does not disappear. A deep minimum in the solvent density develops close to the surface. One could speculate that the solvent evaporation takes place in two stages. First the solvent molecules manage to leave the solution and are situated in the solvent rich layer at the surface from where they evaporate in a second step. The decrease in solvent density leads to an increase in polymer density close to the surface. A polymer rich crust forms there. Initially this peak in the polymer density is quite sharp but it broadens as the evaporation process continuous. The total density of the film varies only very weakly upon solvent loss.

Only in the later stages of the evaporation the accumulation of solvent at the supporting wall is depleted. In the final stages of the evaporation most of the solvent density is located at the adsorbing wall as was already suggested by the snapshots in

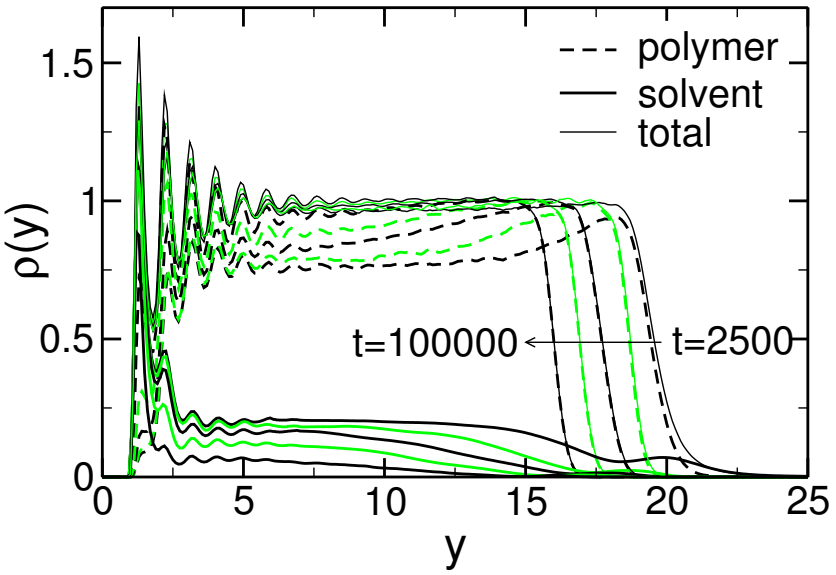

Figure 8.2: The density profile of polymer (dashed lines), solvent (thick full lines) and all particles (thin full lines) is shown as the solvent is evaporating from a supported film at $T = 0.5$ and $N = 64$ at times ranging from $t = 2500$ to $t = 100000$. The initial film was $h = 20.25$ and the film thickness of the corresponding pure polymer film at $T = 0.5$ is $h = 14.85$.

figure 8.1. As a consequence also the polymer density at the wall remains low and increases only in the final stages of the evaporation.

We also monitor the mobility of the solvent particles during evaporation as a function of position. In figure 8.3 the relaxation times determined as described in the section 7.3 from MSDs which were calculated in time intervals ranging from 20000τ to 100000τ during evaporation (as indicated in the legends) are shown. In doing so we average over a certain interval in the evaporation process. Initially the film thickness changes fast at larger times the change becomes slower. At $T = 0.5$ the decrease in film thickness in the chosen intervals is about $\Delta h \simeq 2$. At $T = 0.4$ the intervals are much smaller in comparison with the evaporation kinetics.

While at $T = 0.5$ the relaxation times change only very weakly with time and position the situation at $T = 0.4$ is entirely different. The relaxation times develop a maximum which does not correspond to the maximum of the polymer density but is shifted in wards by about 2σ. This maximum grows as the evaporation continues. At the free surfaces despite the high polymer concentration the dynamics are still fast but as we move away from the surface the system becomes more and more sensitive to the decrease in solvent density which leads to an increase of the relaxation time until it decreases once again as the supporting wall is approached.

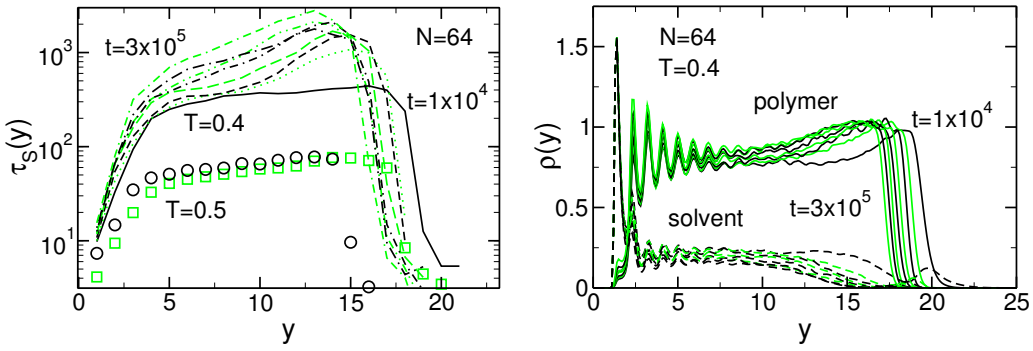

Figure 8.3: LEFT PANEL: The relaxation times of the solvent as a function of position calculated within the time intervals $[0 : 2 \times 10^4]$, $[2 \times 10^4 : 5 \times 10^4]$, $[5 \times 10^4 : 8 \times 10^4]$, $[8 \times 10^4 : 1.3 \times 10^5]$, $[1.3 \times 10^5 : 1.6 \times 10^5]$, $[1.6 \times 10^5 : 2.1 \times 10^5]$, $[2.1 \times 10^5 : 2.6 \times 10^5]$, $[2.6^5 : 3.6 \times 10^5]$ during the evaporation of the solvent at $T = 0.4$ (lines) and in the intervals $[0 : 2 \times 10^4]$ and $[2 \times 10^4 : 1.2 \times 10^5]$ at $T = 0.5$ (symbols) according to equation (4.12). RIGHT PANEL: The density profiles of polymer and solvent are shown averaged over the same time intervals as indicated for the relaxation time in the left panel. The chain length was $N = 64$ and the temperature $T = 0.4$.

8.2 Theories of diffusion and solvent evaporation

The first mathematical model describing the transport of particles was set up by Fick [186]. This simple diffusion model assumes that the flux **J** is proportional to the gradient in concentration c so that

$$\mathbf{J} = -D\nabla c \,, \tag{8.1}$$

where D, the diffusion constant, is the proportionality factor between the flux and the concentration gradient. Together with the continuity equation stating that no mass is lost

$$\frac{\partial c}{\partial t} + \nabla \cdot \mathbf{J} = 0 \tag{8.2}$$

this gives rise to Fick's law :

$$\frac{\partial c}{\partial t} = D\Delta c \,. \tag{8.3}$$

8.2.1 Mutual versus self diffusion

When describing the diffusion of particles in a binary mixture one has to distinguish between the self diffusion constants D_{self} and the intrinsic diffusion constant D_{int} of a given species [181]. There is also a so called mutual or collective diffusion constant D_{mut} which is common to both species [187]. Usually measured in simulation is the self diffusion constant D_{self} because it can be extracted either from the MSD of a given species or from its velocity auto-correlation function by an equilibrium simulation

at a given concentration. In an out of equilibrium situation, where a concentration gradient is present, the relevant diffusion constant is the intrinsic diffusion constant D_{int}. It takes into account the thermodynamic forces acting on the particles and is related to the self-diffusion constant via

$$D_{\text{int}} = D_{\text{self}}\phi\frac{\partial\mu}{\partial\phi} \ , \tag{8.4}$$

where ϕ is the volume fraction of the component and μ its chemical potential.

Finally the mutual diffusion constant D_{mut} describes the transport of two species A and B. As motion of either species leads to a change in concentration of both species a single diffusion constant D_{mut} describes the process. There have been proposed different relation between D_{self} and D_{mut}. One of the most widely used is the Darken equation [188]

$$D_{\text{mut}} = D_{\text{c}}\left(\frac{\partial\ln f}{\partial\ln\phi}\right) \ , \tag{8.5}$$

where f is the fugacity of the solvent in the polymer and D_{c} the so called corrected diffusivity. D_{c} can be extracted from a simulation at equilibrium as [187, 189]

$$D_{\text{c}} = \frac{1}{3N_{\text{tot}}\phi_{\text{P}}\phi_{\text{S}}}\int_0^\infty \mathrm{d}t\,\langle\mathbf{J}(t)\cdot\mathbf{J}(0)\rangle \ , \tag{8.6}$$

where $\mathbf{J}(t)$ is the interdiffusion current

$$\mathbf{J}(t) = \phi_{\text{S}}\sum_{i=1}^{Nn}\mathbf{v}_i(t) - \phi_{\text{P}}\sum_{i=1}^{N_{\text{s}}}\mathbf{v}_i(t) \ . \tag{8.7}$$

This Green-Kubo relation can also be evaluated in its corresponding Einstein form which is computationally more advantageous [187]

$$D_{\text{c}} = N_{\text{tot}}\phi_{\text{P}}\phi_{\text{S}}\lim_{t\to\infty}\frac{1}{6t}\left\langle\left|[\mathbf{R}^{\text{P}}_{\text{cm}}(0)-\mathbf{R}^{\text{S}}_{\text{cm}}(0)]-[\mathbf{R}^{\text{P}}_{\text{cm}}(t)-\mathbf{R}^{\text{S}}_{\text{cm}}(t)]\right|^2\right\rangle \ , \tag{8.8}$$

where $\mathbf{R}^{\text{P}}_{\text{cm}}$ and $\mathbf{R}^{\text{S}}_{\text{cm}}$ denote the position of the center of mass of polymer and solvent. While the self-diffusion constant is a single particle property the corrected diffusion constant is a collective property of the system.

Tsige and Grest [190] compared the values $D^{\text{S}}_{\text{self}}$ of the solvent, D_{c} and D_{mut} for a polymer solvent system using a similar coarse-grained polymer model at high temperature $T = 1$ and found $D_{\text{mut}} = D^{\text{S}}_{\text{self}}$ at very low solvent concentration as should be expected while D_{mut} was systematically smaller than D_{self} as the solvent concentration increased. Nevertheless the difference between the two remained small and both were of the same order of magnitude.

8.2.2 Fickian versus non-Fickian diffusion

In the case of solvent adsorption studies into a polymer network one finds two different types of diffusion, Fickian diffusion which is characterized by a diffusion distance proportional to the square root of time (Case-I) and non-Fickian diffusion [78]. If the polymer is in its rubbery state usually Fickian diffusion is observed upon solvent uptake while in glassy polymers non-Fickian diffusion namely, Case-II and anomalous diffusion, are often encountered as the solvent enters the glassy polymer. Non-Fickian diffusion is characterized by a deviation from the $\sqrt{t}$ scaling law predicted for Case-I diffusion. If the displacement of the front is linear in time it is classified as Case-II diffusion, the intermediate anomalous diffusion is characterized by exponents lying between $t^{0.5}$ and t^1.

Experimental studies reporting Case-II or anomalous diffusion in polymer/solvent systems upon solvent uptake are abundant [84–88]. Also a lot of theoretical models have been proposed to explain the phenomenon [91–94]. The most widely accepted model is the Thomas and Windle model for Case-II diffusion [91, 92] which was extended by [94]. It is based on the assumption of a strong disparity between the mobilities of the two pure species and the plasticizing effect, i. e. a strong enhancement of the dynamics of the slow species (glassy polymer) in presence of the fast species (solvent molecules). Upon plasticization of the slow polymer the solvent can enter quickly. A transient swelling regime obeying a $\sqrt{t}$ law followed by steady-state front motion, meaning a constant shape of the concentration profile together with a linearly moving front, is observed [86, 87]. Additionally, stresses between the swollen polymer solution and the glassy matrix can influence the process [191]. A mathematical model based on stresses induced in the glassy matrix during the process was proposed by Edwards [93].

In computer simulations non-Fickian diffusion has been observed by Janeva and coworkers [89] in a study of interdiffusion of Lennard-Jones spheres where the dynamical asymmetry was created by choosing different friction constants of the DPD thermostat for the two species. A large difference in the friction constants was necessary to observe deviations from Fickian diffusion in their system. A recent study on inter-diffusion of solvent into glassy polymer films by Grest and Tsige on the other hand did not find any deviations from Fickian behavior [90].

For the inverse process of solvent evaporation Fickian diffusion models where suggested by Vrentas [80] and Alsoy and Duda [82]. Recently Okuzono and Doi [192] proposed a model for the skin formation caused by solvent evaporation also based on Fickian diffusion equations. Computer simulations carried out for solvent evaporation from a polymer matrix far above the glass transition temperature of the matrix find Fickian behavior [46–48] as well. Souche and Long developed a mesoscale model [95] allowing to describe solvent evaporation from a glassy polymer. This model is also applicable to the swelling of glassy polymer films where anomalous or Case-II diffusion are observed.

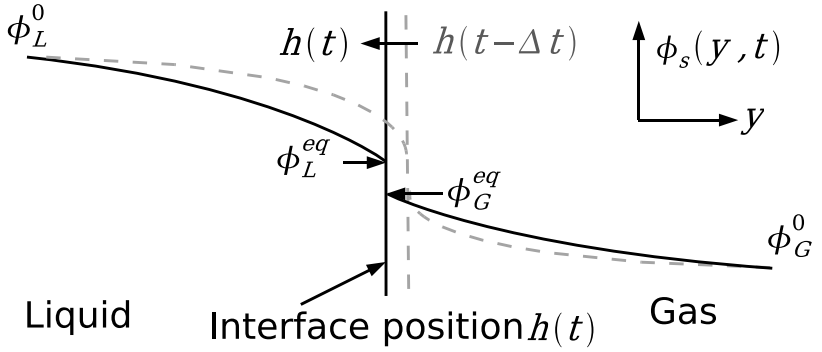

Figure 8.4: Schematic drawing of the density profiles of the solvent at the interface between the solution and the vapor upon solvent evaporation.

8.2.3 Moving boundary problem

Within the framework of Fickian diffusion a simple description of the problem is possible. It is assumed that the partial molar volumes of all components are independent of composition so that there is no volume change on mixing. This assumption leads to the conclusion that the gradient of the volume average velocity or flux is zero in both phases. Based on this result the volume average velocity becomes zero everywhere inside the polymer film because it is zero at the wall. In all phases it is a function of time only [78, 79, 81, 82].

This model is based on diffusion equations describing the concentration profiles of the solvent in the liquid and the gas phase. As the total fluid velocity is zero and there is no net flux, the purely diffusive dynamics inside the liquid film can be described by the following differential equation

$$\frac{\partial}{\partial t}\phi_L(y,t) = \frac{\partial}{\partial y}\left[D_L\left(\phi_L(y,t),y\right)\frac{\partial}{\partial y}\phi_L(y,t)\right], \tag{8.9}$$

where $D_L\left(\phi_L(y,t),y\right)$ is the diffusion coefficient in the binary mixture which is a priori, as we have seen in the last section, dependent on position and composition. $\phi_L(y,t)$ is the volume fraction of solvent in the mixture.

In the gas phase convection is possible and the flux of particles away from the interface has to be included to describe the evolution of the volume fraction of solvent in this phase:

$$\frac{\partial}{\partial t}\phi_G(y,t) = D_G\frac{\partial^2}{\partial y^2}\phi_G(y,t) + v_G(t)\frac{\partial}{\partial y}\phi_G(y,t)\,, \tag{8.10}$$

where D_G is the diffusion coefficient in the gas phase, $\phi_G(y,t)$ is the volume fraction of solvent in the gas and $v_G(t)$ is the average velocity of the particles in the gas phase.

These equations are subject to the following boundary conditions

$$\begin{aligned}
\phi_L(-\infty, t) &= \phi_L^0 && (8.11)\\
\phi_L(h(t), t) &= \phi_L^{\text{eq}} && (8.12)\\
\phi_L(y, t=0) &= \phi_L^0 && (8.13)\\
\phi_G(\infty, t) &= \phi_G^0 && (8.14)\\
\phi_G(h(t), t) &= \phi_G^{\text{eq}} && (8.15)\\
\phi_G(y, t=0) &= \phi_G^0\,, && (8.16)
\end{aligned}$$

where ϕ_L^0 is the initial volume fraction of solvent in the film and ϕ_G^0 the initial volume fraction of solvent in the atmosphere. We assume local equilibrium at the moving interface situated at position $y = h(t)$ so that $\phi_L^{\text{eq}} = K\phi_G^{\text{eq}}$, where K is the activity coefficient. The film is taken to be semi-infinite.

In addition at the interface the mass balance i.e. the fact that no material is lost provides another equation

$$(\phi_L^{eq} - \phi_G^{eq})\frac{dh}{dt} = D_G \left.\frac{\partial \phi_G}{\partial y}\right|_{y=h(t)} - v_G \phi_G^{eq} - D_L \left.\frac{\partial \phi_L}{\partial y}\right|_{y=h(t)} \tag{8.17}$$

determining the motion of the interface.

8.2.4 Analytical solution

To solve this moving boundary problem analytically we need to make a few further assumptions [81, 83]. The most restricting is certainly to set

$$D_L\left(\phi_L(y,t), y\right) = D_L \tag{8.18}$$

constant. Furthermore, motivated by the diffusion equation (8.9,8.10), we assume the interface to move as

$$h(t) = h(0) + 2\lambda\sqrt{D_G t}\,, \tag{8.19}$$

and then we perform a similarity transformation introducing the new variable

$$\eta = \frac{y - h(0)}{2\sqrt{D_G t}}\,. \tag{8.20}$$

As the interface is now immobilized at $\eta = \lambda$, this allows to rewrite the partial differential equation (8.9) with moving boundary conditions as an ordinary differential equation with stationary boundaries as follows

$$2\eta\frac{d}{d\eta}\phi_L(\eta) + \frac{D_L}{D_G}\frac{d^2}{d\eta^2}\phi_L(\eta) = 0, \tag{8.21}$$

with the boundary conditions

$$\phi_L(-\infty) = \phi_L^0 \tag{8.22}$$
$$\phi_L(\lambda) = \phi_L^{\text{eq}} . \tag{8.23}$$

The set of equations (8.21-8.23) can be solved analytically [81, 83]. The volume fraction of solvent in the film is dependent on position and time but can be expressed as a function of η only as follows:

$$\phi_L(\eta) = (\phi_L^0 - \phi_L^{eq}) \left[1 - \frac{1 + \text{erf}\left(\sqrt{D_L/D_G}\eta\right)}{1 + \text{erf}\left(\sqrt{D_L/D_G}\lambda\right)} \right] + \phi_L^{eq} , \tag{8.24}$$

where $\text{erf}(x)$ is the error function defined as

$$\text{erf}(x) = \frac{1}{\sqrt{2\pi}} \int_x^\infty \mathrm{d}u \, \mathrm{e}^{-\frac{u^2}{2}} . \tag{8.25}$$

If the diffusion constant was not constant, but a function of composition only, i. e. $D_L = D_L(\phi_L)$, it would still be possible to reduce the problem to a simple ordinary differential equation. In this case the differential equation would read

$$2\eta \frac{d}{d\eta}\phi_L(\eta) + \frac{d}{d\eta}\left[\frac{D_L(\phi_L)}{D_G} \frac{d}{d\eta}\phi_L(\eta) \right] = 0 , \tag{8.26}$$

which in general cannot be solved analytically anymore. But the solution would still be consistent with a decrease of the film thickness proportional to the square-root of time. Only the form of the profile as a function of η would change. This means that a different functional dependence of the thickness reduction requires an explicitly position dependent diffusion constant $D_L(\phi_L, y)$ within the framework of this diffusion theory.

8.3 Comparison of the simulation results with theory

Before comparing theory and simulation results we briefly comment on basic assumptions made by the theory:

- *The total density stays constant.* This is not perfectly fulfilled but the density varies very weakly from $\rho_t(\phi_S = 0.27) = 0.95$ to $\rho_t(\phi_S = 0) = 1.01$ and thus the net volume average velocity is zero within the accuracy of our simulation inside the film.

- *The diffusion constant is independent of position and composition.* This is not fulfilled as we have shown in the last section. It remains to be determined how this influences the results. As the dependence of the dynamics on composition and position will certainly become even stronger as we lower the temperature further this is an important point to investigate.

- *The system is semi-infinite.* This means that finite size effects as the solvent is completely depleted in the simulations are not accounted for by the theory.

Based on these assumptions the theory makes the following predictions we can compare to our simulation results:

- Equation (8.24) suggests a superposition of the density-profiles obtained by simulation at different times during the evaporation if plotted as a function of η and predicts also the functional form.

- The film thickness is predicted to decrease as the square-root of time according to equation (8.19).

8.3.1 Solvent evaporation from supported films

In figure 8.5 the film thickness as a function of time during the evaporation process is shown for two different temperatures $T = 0.5$ and $T = 0.4$ and chain length $N = 10$ and $N = 64$. The chain length slightly alters the results because also the local dynamics were weakly dependent on chain length. The qualitative features seem to remain unchanged but the process is slower for longer chains. The temperature has a much stronger influence on the evaporation kinetics. While for $T = 0.5$ we indeed find a regime at intermediate times where the film thickness decreases as $h(t) - h(0) \propto \sqrt{t}$, this is not the case at the lower temperature $T = 0.4$. This temperature is in the vicinity of the bulk T_g ($T_\mathrm{g}(N = 64) = 0.408$ and $T_\mathrm{g}(N = 10) = 0.392$) but it is above T_g of the pure polymer films ($T_\mathrm{g}(h, N = 10) = 0.371$ and $T_\mathrm{g}(h, N = 64) = 0.385$). The deviations from the theoretical prediction can be seen clearly in the inset of figure 8.5 where a decrease of the film thickness as the square root of time corresponds to a horizontal line. The exponent we find at $T = 0.4$ is smaller than 0.5 which is expected for Fickian diffusion.

At $T = 0.5$ the decrease of the film thickness is initially different than predicted by theory. This is probably due to the fast evaporation of the surplus of solvent at the surface (see figures 8.2 and 8.3) while the polymer film does not decrease in height. This leads to an increase in surface tension because the interfacial energy between polymer and vacuum is higher than the one between the binary mixture and its vapor. Therefore the polymer density profile narrows quickly in this stage of the evaporation.

At intermediate times $2500 < t < 50000$ we find a regime where the film thickness decreases as the square root of time as predicted for Fickian diffusion. This can also be seen in the inset of figure 8.5 where $\frac{h(0)-h(t)}{\sqrt{t}}$ is plotted as a function of time. In this plot this regime corresponds to a straight line at $-\lambda/2\sqrt{D_G}$. The difference in the parameter λ is rather small for the two chain length ($\lambda(N = 10) = -0.022/2\sqrt{D_G}$ and $\lambda(N = 64) = -0.018/2\sqrt{D_G}$). The diffusion constant of the solvent in the dilute gas phase is very large in the order of $D_G \simeq 10$ and of course independent of N.

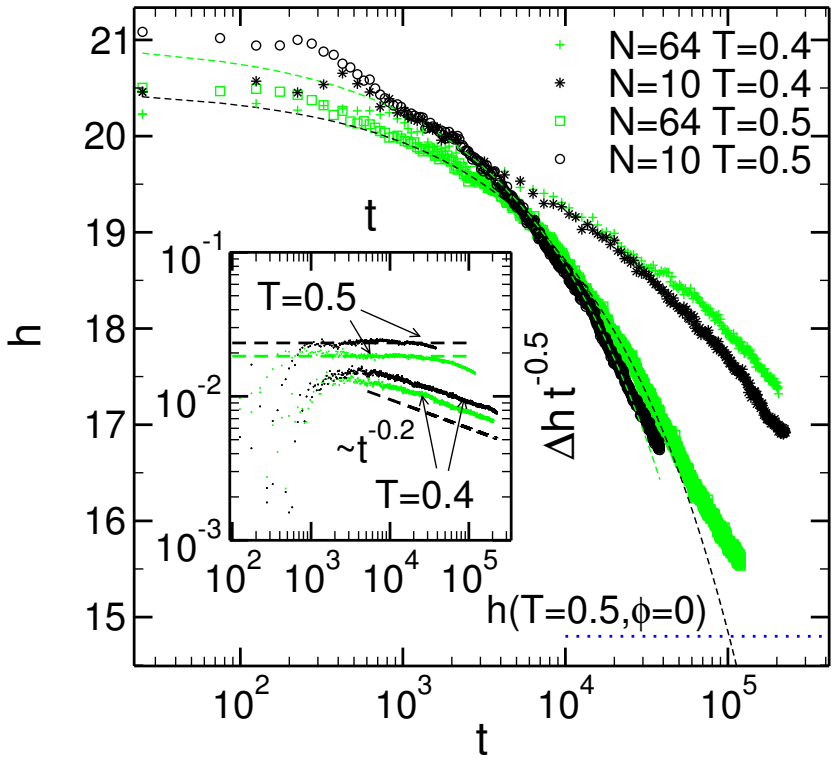

Figure 8.5: MAIN FIGURE: The film thickness $h(t)$ is shown as a function of logarithmic time for $N = 10$ at $T = 0.5$ (black circles) and $T = 0.4$ (black stars) and for $N = 64$ at $T = 0.5$ (grey squares) and $T = 0.4$ (grey crosses). The dashed lines indicate fits to equation (8.19) yielding $\lambda(N = 10) = -0.022/2\sqrt{D_G}$ and $\lambda(N = 64) = -0.018/2\sqrt{D_G}$. INSET: The inset shows the same data ($N = 64$ (grey lines) $N = 10$ (black lines)) replotted as $[h(0) - h(t)]/\sqrt{t}$.

In this regime ($2500 < t < 50000$) we attempt to describe the solvent density profile with equation (8.24). As can be seen in figure 8.6 for $N = 64$ at $T = 0.5$ this equation describes the density profile quite nicely. The fit gives an effective diffusion constant in the liquid of $D_L = 0.003$. This corresponds to an effective relaxation time of about

$$\tau_{\text{eff}} = \frac{1}{4D_L} = 83\,. \tag{8.27}$$

This value is reasonable in comparison with the relaxation times directly extracted from the MD-simulations shown in figure 7.6 in the last section. When comparing solvent evaporation and equilibrium simulations one has to bear in mind that the diffusion constant D_L is the mutual diffusion constant of the polymer and solvent mixture. As the volume is assumed to be constant neither species can move without the other and the transport is described by a single diffusion constant depending on the intrinsic diffusion constants of both polymer and solvent which take into account the gradient in chemical potential. The relaxation times extracted from the equilibrium simula-

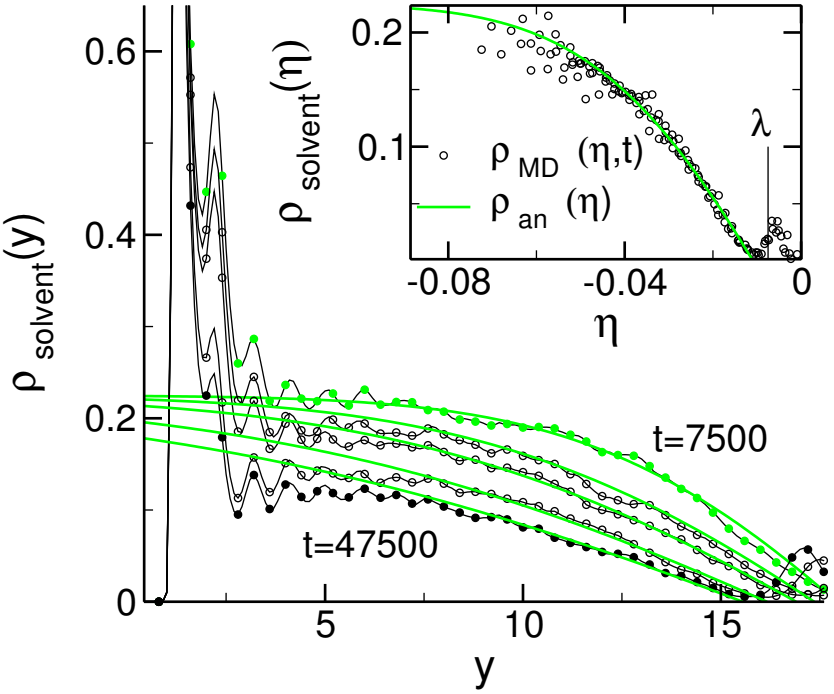

Figure 8.6: MAIN FIGURE: The density-profile of the solvent in the film as it is evaporating at $T = 0.5$ is shown every 10000τ starting from $t = 7500$ to $t = 47500$. The full lines indicate the theoretical prediction according to equation (8.24) and the connected circles the results of the MD simulations. INSET: The inset shows the same data as a function of the variable η defined in equation (8.20). The circles refer to the simulation data, the full line to the theoretical prediction.

tions on the other hand are related to the self-diffusion constant if the relation (8.27) holds. While this is not the case for the polymer due to the existence of the subdiffusive regime and might also not be the case for the solvent if the plateau due to the cage effect becomes very pronounced, it can still provide an estimate for the value of $D^{\mathrm{S}}_{\mathrm{self}}$ of the solvent. If we return to figure 8.3 we see that the relaxation times extracted from the simulations of the evaporation at $T = 0.5$ are almost constant in a wide range of positions and $\tau_S(y) \simeq \tau_{\mathrm{eff}}$ is approximately fulfilled.

8.3.2 Finite-size effects

To see how the finite size of the film affects the evaporation dynamics we look how the solvent concentration decreases in different parts of the film. In figure 8.7 the solvent density is shown at different times. We look at the height of the peak $\phi^P_{\mathrm{S}}(t)$ corresponding to the accumulation of solvent between the polymer and the wall and the mean solvent concentration $\phi^M_{\mathrm{S}}(t)$ in the region between $2 < y < 5$ as indicated in the figure.

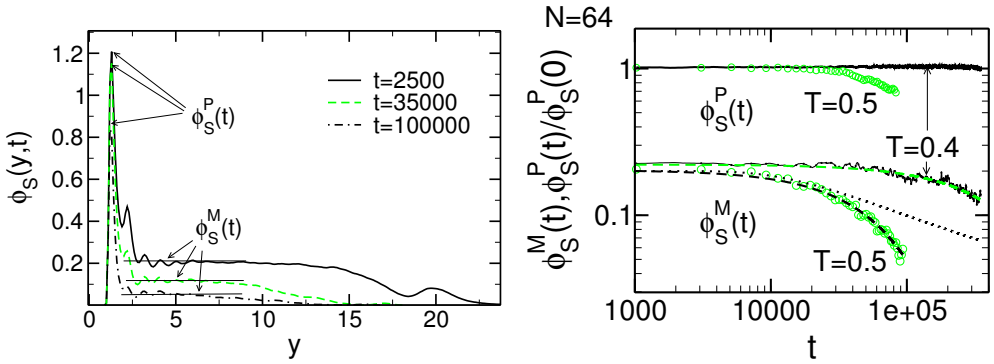

Figure 8.7: LEFT PANEL: The density of solvent at $T = 0.5$ in the film is shown at $\tau = 2500$, $\tau = 35000$ and $\tau = 100000$. The chain length was $N = 64$. The position of the maximum solvent density $\phi_S^P(t)$ and the mean solvent density $\phi_S^M(t)$ in the region $2 < y < 5$ are indicated. RIGHT PANEL: The position of the maximum solvent density $\phi_S^P(t)$ and the mean solvent density $\phi_S^M(t)$ in the region $2 < y < 5$ are plotted as a function of logarithmic time. The chain length was $N = 64$. The dashed line indicates a fit of the data to an exponential function while the dotted line shows the prediction of equation (8.28).

As the analytical theory outlined above predicts the solvent volume fraction to be given by equation (8.24), it follows directly that the concentration at a given position y as a function of time is given by

$$\phi_L(y,t) = (\phi_L^0 - \phi_L^{eq}) \left[1 - \frac{1 + \mathrm{erf}\left(\sqrt{D_L} \frac{y - h(0)}{2\sqrt{t}} \right)}{1 + \mathrm{erf}\left(\sqrt{D_L / D_G} \lambda \right)} \right] + \phi_L^{eq} \, . \tag{8.28}$$

Evaluated at $y = 3.5$ this gives an estimate for $\phi_S^M(t)$ indicated by the dotted line in figure 8.7.

In figure 8.7 $\phi_S^P(t)$ and $\phi_S^M(t)$ are plotted as a function of time. They show a quite different behavior. While $\phi_S^P(t)$ rests constant until $t \simeq 30000$ (this corresponds to the time where the film thickness $h(t)$ starts to deviate from equation (8.19) at $T = 0.5$), $\phi_S^M(t)$ seems to follow a simple exponential decay as

$$\phi_S^M(t) = \phi_S^M(0) \exp(-t/\tau_{\text{evap}}) \, . \tag{8.29}$$

The time constant τ_{evap} is found to be $\tau_{\text{evap}} = 66250$ at $T = 0.5$. The prediction of the analytical theory which does not account for the finite dimension of the film is in agreement with the simulation data for $t < 30000$.

It is also possible to fit $\phi_S^M(t)$ at $T = 0.4$ with a simple exponential but the time scale $\tau_{\text{evap}} = 420400$ is too large in comparison with the simulated time to judge the quality of the fit. The decrease of $\phi_S^M(t)$ reaches the value below which finite size effects become important only at the very end of the simulation for $t > 300000$. The

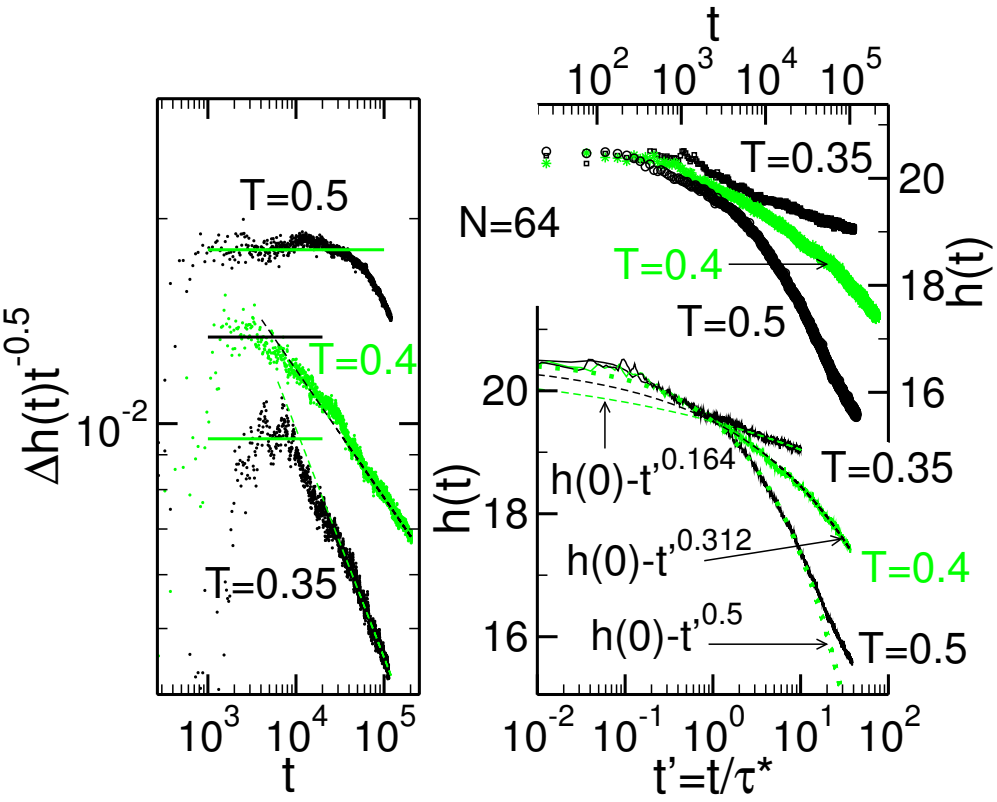

Figure 8.8: RIGHT PANEL: The film thickness h at temperatures $T = 0.5$, $T = 0.4$ and $T = 0.35$ is shown as a function of time (right ordinate) and as a function of rescaled time $t' = t/\tau^*$ (left ordinate) ($\tau^*(T = 0.5) = 3086$, $\tau^*(T = 0.4) = 5554$ and $\tau^*(T = 0.35) = 11100$). The curves are shifted vertically so that $h(0)$ is equal at all three temperatures. LEFT PANEL: The data is replotted as function of $[h(0)-h(t)]/\sqrt{t}$. The horizontal lines indicate the values of $\lambda/2\sqrt{D_G}$ at the respective temperatures. The dashed lines indicate

simulated time is also not long enough to see a decrease in $\phi_S^P(t)$ at $T = 0.4$ which stays constant through out the simulation. A finite size effect can therefore not explain the deviations from equation (8.19) at $T = 0.4$ which are observed for $t > 10000$.

8.3.3 Influence of temperature on the evaporation kinetics

We also look at the solvent evaporation for a supported film at $T = 0.35$, where the film undergoes the glass transition while there is still a volume fraction of about $\phi_S = 10\%$ inside the film (see figure 7.14). The results for all three temperatures for chain length $N = 64$ are summarized in figure 8.8. As should be expected the evaporation slows down with decreasing temperature. At $T = 0.35$ the amount of solvent evaporated within the simulated time is even smaller than at $T = 0.4$. Therefore also in this case we do not consider finite size effects to be important within the simulated

time interval. Only at $T = 0.5$ the simulations could be run long enough to come close to a complete evaporation of the solvent. But also in this case a small amount of solvent remained in the film mainly situated close to the supporting wall. The solvent trapped between the polymer and the support evaporates very slowly.

When the data for the film thickness $h(t)$ is plotted as a function of $[h(t) - h(0)]/\sqrt{t}$, it becomes apparent that at all T there is a regime at intermediate times which follows a decrease in film thickness according to $\sqrt{t}$ indicated by the horizontal lines in figure 8.8. While we showed in section 8.3.2 that at $T = 0.5$ the deviations encountered at large times are due to finite size effects this is not the case for $T = 0.4$ or for $T = 0.35$. At $T = 0.4$ as well as at $T = 0.35$ the time interval within which Fickian diffusion is observed is very small. While at $T = 0.4$ the subsequent regimes can be described by a power law where the thickness decreases as $h(0) - h(t) \propto t^{0.312}$ the exponent is even lower at $T = 0.35$ where the thickness at large times is described by $h(0) - h(t) \propto t^{0.164}$.

Upon these observations it is tempting to rescale the time axis by $t' = t/\tau^*$ ($\tau^*(T = 0.5) = 3086$, $\tau^*(T = 0.4) = 5554$ and $\tau^*(T = 0.35) = 11100$) which allows to bring the data for the decrease of film thickness at all three temperatures to superposition at early times as well as at intermediate times where $h(0) - h(t') = \sqrt{t'}$ is observed. At late times differences emerge as the power-law decrease in film thickness has different exponents $\kappa(T)$ at different temperatures. We find that

$$h(0) - h(t') = t'^{\kappa(T)} \tag{8.30}$$

as can be seen in the right panel of figure 8.8. While $\kappa(T = 0.5) = 0.5$ is valid until finite size effects become relevant, we find that $\kappa(T = 0.4) = 0.312$ and $\kappa(T = 0.35) = 0.164$ for large times, where finite size effects are not yet encountered because the simulations were not run long enough to include these. The pre-factor remains unaltered equal to 1 upon the change in exponent within the accuracy of our simulations.

8.3.4 Influence of film geometry on the evaporation kinetics

We also considered the solvent evaporation from free-standing films of similar thickness as the supported films. In figure 8.9 the evaporation of solvent from free-standing and supported films of similar initial solvent volume fraction and thickness is compared at $T = 0.4$ and $T = 0.5$. As the solvent is leaving through 2 surfaces the evaporation is by definition at least twice as fast in the free-standing films. Therefore we do not compare the decrease in total film thickness between the two geometries but we use the position of the right GDS y_+^{G} (see section 3.1) of the free-standing and supported films to monitor the evaporation process. Using this definition at small times the change in interface position is independent of film geometry within the accuracy of the simulations at $T = 0.5$ and $T = 0.4$. Finite size effects kick in much earlier for the free-standing films and the complete solvent evaporation is much faster

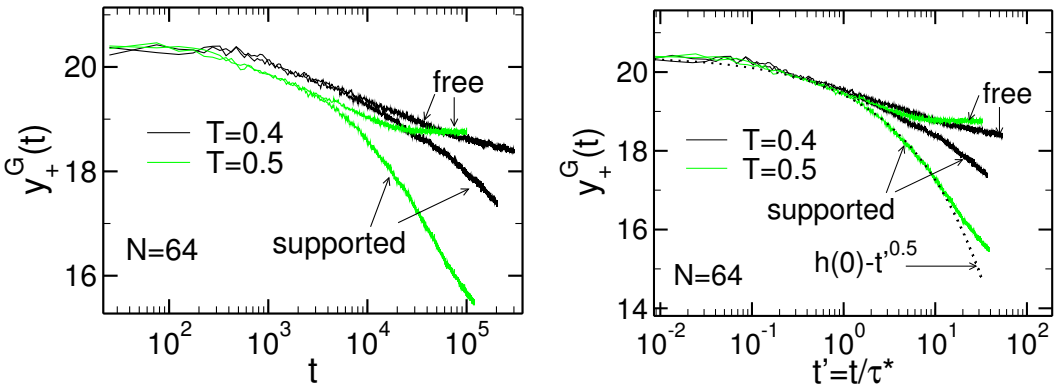

Figure 8.9: LEFT PANEL: The position of the right GDS (see section T_g) as a function of temperature upon solvent evaporation for supported ($h(0) = 19.2$ and $\phi_S = 21\%$ at $T = 0.5$; $h(0) = 19.6$ and $\phi_S = 25\%$ at $T = 0.4$) and free standing films ($h(0) = 18.2$ and $\phi_S = 19\%$ at $T = 0.5$; $h(0) = 18.1$ and $\phi_S = 23\%$ at $T = 0.4$) of similar initial solvent concentration and thickness. The curves are shifted as to coincide in the position of the right GDS y_+^G at $t = 0$. RIGHT PANEL: The same data replotted as a function of rescaled time $t' = t/\tau*$ ($\tau * (T = 0.5) = 3086$, $\tau * (T = 0.4) = 5554$ and $\tau * (T = 0.35) = 11100$).

than for the supported films of the same thickness. This disparity is on the one hand due to the fact that the film thickness per surface is twice as large for supported films and on the other hand caused by the very slow evaporation of solvent trapped between the polymer and the wall as the film dries completely.

Again by rescaling the time axis by $t' = t/\tau^*$ the data for all film geometries and temperatures collapse. While large differences arise between the data for $T = 0.4$ and $T = 0.5$ at later times in the supported films as discussed in the last section this is not the case for the free-standing films. Although there are differences for the two temperatures they are by far smaller than for the supported films and the regime where the film shrinks according to $h(0) - h(t) \propto \sqrt{t}$ is very short at both temperatures due to finite size effects. The differences arising are cut short by finite size effects altering the evaporation dynamics and thus the different power-law dependencies cannot be observed clearly for the free-standing films.

8.4 Numerical solution of the diffusion equation

An analytical solution for equation (8.9) can only be found if the system is semi-infinite and the diffusion constant is a constant while a numerical solution of the same problem does not have to resort to these restrictions. Our approach is similar to the one presented by [192] but we apply different boundary conditions which changes the evaporation kinetics. We implement a numerical solution of the evaporation problem based on equation (8.9). We only take into account the liquid phase explicitly. Mean-

ing that the condition of mass conservation at the interface at position $h(t)$ (8.17) has to be written differently. As we assume the total density to be constant we can express the volume fraction of polymer by $\phi_{\mathrm{P}}(y,t) = 1 - \phi_L(y,t)$. The polymers do not evaporate and their mass is conserved so that

$$\frac{d}{dt}\int_0^{h(t)} dy\,(1-\phi_L(y,t)) = 0\,, \tag{8.31}$$

or, in other words, the total amount of mass lost corresponds to the amount of solvent lost (i.e. there is no solvent returning to the liquid phase from the gas phase)

$$\frac{d}{dt}\int_0^{h(t)} dy = \frac{d}{dt}\int_0^{h(t)} dy\phi_L(y,t)\,. \tag{8.32}$$

The volume fraction of solvent at the interface is fixed assuming local equilibrium as for the theory presented before, while at the other end of the finite slab we now impose the gradient of the volume fraction as opposed to the volume fraction at infinity in an infinite slab as was considered by the analytical theory. The boundary conditions are thus chosen to be

$$\left.\frac{\partial\phi_L(y,t)}{\partial y}\right|_{y=0} = 0 \tag{8.33}$$

$$\phi_L(h(t),t) = \phi_L^{\mathrm{eq}}\,. \tag{8.34}$$

From these equation together with equation (8.9) one obtains the differential equation governing the evolution of the interface position

$$(1-\phi_L(h(t),t))\frac{dh(t)}{dt} = D(h(t),\phi_L(h(t),t))\left.\frac{\partial\phi_L(y,t)}{\partial y}\right|_{y=h(t)}\,. \tag{8.35}$$

As initial condition we chose again a rectangular profile so that

$$\phi_L(y,t=0) = \phi_L^0 \quad 0 < y < h(t)\,. \tag{8.36}$$

In order to be in agreement with the boundary condition (8.34) we set

$$\phi_L(h(0),t=0) = \phi_L^{eq}\,. \tag{8.37}$$

Equations (8.35-8.37) together with equation (8.9) form a set of coupled non linear differential equations that can be solved numerically for any functional dependence of the diffusion constant $D(y,\phi_L(y),t)$. The only further input parameters are ϕ_L^0, ϕ_L^{eq} and the initial film thickness $h(0) = h_0$.

8.4.1 Numerical implementation

To solve these equations numerically we perform the coordinate transformation

$$u = \frac{y}{h(t)} \tag{8.38}$$

which maps the film onto the interval [0:1] and thus immobilizes the moving boundary at $u = 1$. Equation (8.9) becomes in this new coordinate system

$$\frac{\partial \phi_L(u,t)}{\partial t} = \frac{1}{h(t)^2}\frac{\partial}{\partial u}\left[D(uh(t), \phi_L(u,t))\frac{\partial \phi_L(u,t)}{\partial u}\right] + \frac{u}{h(t)}\frac{dh}{dt}\frac{\partial \phi_L(u,t)}{\partial u} \ . \tag{8.39}$$

Following [193] we rewrite the above equation using the identities $\frac{\partial(\phi_L h)}{\partial t} = \phi_L \frac{dh}{dt} + h\frac{\partial \phi_L}{\partial t}$ and $\frac{\partial(\phi_L u)}{\partial u} = \phi_L + u\frac{\partial \phi_L}{\partial u}$ as

$$\frac{\partial(\phi_L h)}{\partial t} = \frac{dh}{dt}\frac{\partial(\phi_L u)}{\partial u} + \frac{1}{h}\frac{\partial}{\partial u}\left(D\frac{\partial \phi_L}{\partial u}\right) \ . \tag{8.40}$$

To discretize this differential equation the space coordinate u is given on an equidistant grid with step size $du = 1/(N-1)$ from $(u_0 = 0, ..., u_{N-1} = 1)$ and we use an equidistant time step dt so that $t^{j+1} = t^j + dt$. By integrating equation (8.40) over one space and one time step

$$\begin{aligned}\int_{u_{i-1/2}}^{u_{i+i/2}} \int_{t^j}^{t^{j+1}} dtdu \frac{\partial(\phi_L h)}{\partial t} = \\ \int_{u_{i-1/2}}^{u_{i+i/2}} \int_{t^j}^{t^{j+1}} dtdu \frac{\partial}{\partial u}\left[\frac{dh}{dt}\phi_L u + \frac{D}{h}\frac{\partial \phi_L}{\partial u}\right] \ ,\end{aligned} \tag{8.41}$$

where $u_{i\pm1/2}$ denotes the position midway between u_i and $u_{i\pm1}$ on obtains the following finite difference equation

$$\begin{aligned}(\phi_{L\ i}^{j+1} h^{j+1} - \phi_{L\ i}^{j} h^j)du = \\ \frac{dt}{h^{j+\sigma}}\left[D_{i+1/2}^{j+\sigma}\frac{\phi_{L\ i+1}^{j+\sigma} - \phi_{L\ i}^{j+\sigma}}{du} - D_{i-1/2}^{j+\sigma}\frac{\phi_{L\ i}^{j+\sigma} - \phi_{L\ i-1}^{j+\sigma}}{du}\right] \\ + (h^{j+1} - h^j)(\phi_{L\ i+1/2}^{j+\sigma} u_{i+1/2} - \phi_{L\ i-1/2}^{j+\sigma} u_{i-1/2}) \ ,\end{aligned} \tag{8.42}$$

where the superscript $j + \sigma$ represents the given quantity after a proportion σ of the time step has elapsed. This equation can be used to obtain the values of $\phi_{L\ i}^{j+1}$ for $i = 1, .., N-2$ if the future interface position h^{j+1} is known. In agreement with the boundary condition (8.37) we set $\phi_{L\ N-1}^{j+1} = \phi_L^{eq}$. If we discretize (8.33), this reads

$$(\phi_{L\ 0}^{j+1} h^{j+1} - \phi_{L\ 0}^{j} h^j)du/2 = \frac{dt}{h^{j+\sigma}} D_{1/2}^{j+\sigma}\frac{\phi_{L\ 1}^{j+\sigma} - \phi_{L\ 0}^{j+\sigma}}{du} + (h^{j+1} - h^j)\phi_{L\ 1/2}^{j+\sigma} du/2 \ . \tag{8.43}$$

Now we need to also find a finite difference representation for equation (8.35). This we do by applying the mass balance in its discretized form so that

$$(h^{j+1} - h^j) = h^{j+\sigma} du \sum_{i=0}^{N-1} \phi_{L\,i}^{j+\sigma} - h^j du \sum_{i=0}^{N-1} \phi_{L\,i}^{j} \tag{8.44}$$

This allows to determine h^{j+1} provided that $\phi_{L\,i}^{j+\sigma}$ and $h^{j+\sigma}$ are known.

This is only possible through an iterative procedure. So we proceed as follows to solve this system of coupled finite difference equations.

1. Initially we choose $\phi_{L\,i}^{j+\sigma}$=$\phi_{L\,i}^{j}$ and $h^{j+\sigma} = h^j$.
2. This allows to get a first result for h^{j+1} using equation (8.44).
3. Now we can update the estimate for $h^{j+\sigma}$.
4. Then we solve equation (8.42) to determine $\phi_{L\,i}^{j+1}$.
5. This gives updates for $\phi_{L\,i}^{j+\sigma}$.

Now we can return to the second point and recalculate the new interface position and also repeat the following steps until convergence is reached.

If we choose $\sigma = 1/2$ this implementation corresponds to the Crank-Nicolson scheme [194] which is accurate up to orders of dt^2 but is numerically less stable than the fully implicit procedure where $\sigma = 1$ which is only accurate up to order dt [195]. Stability is only guaranteed if $dt < du^2$ while the stability of the latter is not dependent on the size of dt. For the same reason of stability of the procedure we choose the so-called 'down wind' approximation and approximate $\phi_{Li+1/2} = \phi_{L\,i}$ and $\phi_{Li-1/2} = \phi_{L\,i-1}$ [79, 193].

8.4.2 Solvent evaporation at high temperature ($T = 0.5$)

We test our numerical implementation by comparing our results to the analytical solution outlined before and to an MD simulation of the evaporation of solvent from a free standing film of initial thickness $h = 18.2$ and a solvent volume fraction in the center of the film of $\phi_{\mathrm{S}} = 0.187$. As it is a good assumption that the boundary condition (8.33) is fulfilled in the center of the film, the numerical solution is only done for the half space $y > 0$. We set $\phi_L^{\mathrm{eq}} = 0$ assuming that the solvent concentration at the interface is very low and $h(0) = 8$ which is less than half of the film thickness in the MD simulation, as the film in the simulation is additionally swollen by the surplus of solvent at the surface and the thickness obtained from the density profile of the polymer is thus larger than would be found for a rectangular profile.

In figure 8.10 the results of this comparison are shown. The simulation data of the solvent density are well reproduced by the numerical solution of the diffusion

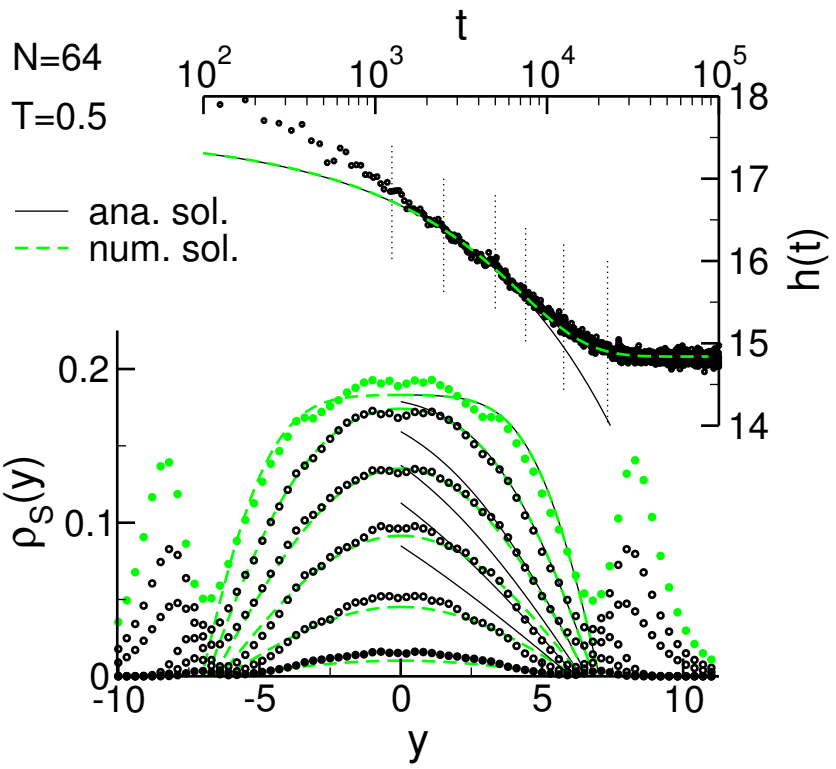

Figure 8.10: MAIN FIGURE: The density of solvent inside a free standing film during solvent evaporation at $t = 1250$, $t = 2500$, $t = 5000$, $t = 7500$, $t = 12500$ and $t = 22500$. The symbols refer to the MD data while the dashed lines indicate the numerical solution and the thin black lines the analytical solution of the problem. INSET: The film thickness as a function of time during evaporation is shown. The vertical dotted lines indicate the times for which the solvent profiles are shown in the main figure. The numerical and analytical solution are shifted vertically as to obtain best superposition with the MD data.

equation at all times. At this point we have not yet included the dependence of the diffusion constant on position or composition, but only the fact that the film has a finite size. We choose the value of the diffusion constant $D_L = 0.003$ extracted from the comparison with analytical theory. The composition dependence of the mobilities, we encountered in section 7.3 as well as the influence of the gradient of the chemical potential on the diffusion dynamics up to the fact that solvent and polymer have to move collectively to comply with the condition of constant density are buried within this diffusion constant. While it is not surprising that the composition dependence of D_L cannot be seen in the decrease of the film thickness, it could give rise to a different functional form of the density profiles. Apparently the above mentioned effects are not strong enough to considerably alter the profiles in comparison to the results obtained from the MD simulations. Initially also the analytical solution described in section 8.2.4 gives a good prediction of the results found in the MD simulation.

In the free-standing films as the solvent can leave through two surfaces the finite size effects kick in earlier than for the supported film of comparable thickness. The surplus of solvent at the surface is not accounted for by the theory. This effect only present in the MD simulations seems not to alter the evaporation kinetics noticeably but for the fact that the polymer film is initially thicker than anticipated by the theory.

8.4.3 Solvent evaporation at the glass transition temperature T_{g}

We also attempt a numerical solution of the diffusion equation to model the evaporation of the solvent at $T = 0.4$. At this temperature the analytical solution failed although there is still too much solvent inside the film for finite size effects to be relevant. The prediction that the interface position should decrease as the square root of time was not borne out (see figures 8.5 and 8.8). We try to improve the results by considering the position as well as the composition dependence of the diffusion constant. To this end, we have to parameterize the diffusion constant as a function of the distance from the interface and the volume fraction of solvent inside the film. The volume fraction of the polymer need not be considered as we assumed the overall density in the film to be constant.

We will use the local relaxation times extracted from the equilibrium simulations of the solvent polymer systems at different solvent concentrations described in section 7.3 to guide the model of the functional dependence on position and composition of the diffusion constant. We found that at $T = 0.4$ the relaxation times in the center of the film are well described by equation (7.7). We will thus use this formula for the composition dependence and add the position dependence by applying the phenomenological formula (equation 4.13) used to model the increase in mobility at the surface of the pure polymer films. To obtain the diffusion constant we assume that $D_{\mathrm{L}} = \frac{1}{4\tau(y,\phi_{\mathrm{S}})}$. Using these results $D_{\mathrm{L}}(y, \phi_{\mathrm{S}})$ is given as

$$D_L(y, \phi_{\mathrm{S}}) = \frac{(\phi_{\mathrm{S}} - \phi_{\mathrm{c}})^{\gamma}}{4a} \exp\left[A \exp\left(-\frac{y}{\xi}\right)\right] , \tag{8.45}$$

where we chose $\gamma = 2$, $\phi_{\mathrm{c}} = -0.01$ and $a = 30$ as determined in section 7.3. The further fit constants A and ξ are themselves dependent on composition but we do not account for that and choose an average value $A = 8$ and $\xi = 1.75$. As the interface changes upon evaporation one cannot hope to achieve more than a qualitative agreement from fits to equilibrium profiles anyway. In addition this description is lacking the influence of thermodynamic forces due to the gradients in the chemical potential. Also it does not consider correctly that polymer and solvent cannot move independently.

In figure 8.11 the results of the numerical solution using this time and explicitly position dependent diffusion constant $D_{\mathrm{L}}(y, \phi_{\mathrm{S}})$ are compared to the results for the evaporation of the solvent from a free-standing film of initial thickness $h = 18$ and

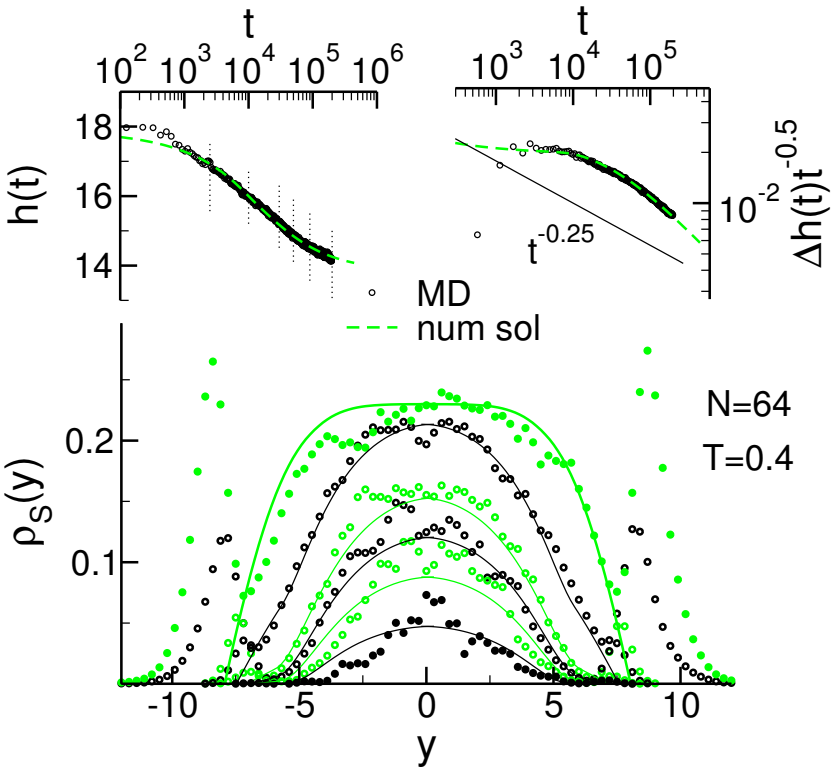

Figure 8.11: MAIN FIGURE: The density of solvent inside a free standing film during solvent evaporation at $t = 2500$, $t = 10000$, $t = 30000$, $t = 50000$, $t = 90000$ and $t = 300000$. The symbols refer to the MD data while the dashed lines indicate the numerical solution with the diffusion constant chosen according to equation (8.45). LEFT INSET: The film thickness as a function of time during evaporation is shown. The vertical dotted lines indicate the times for which the solvent profiles are shown in the main figure. The numerical solution are shifted vertically as to obtain best superposition with the MD data. RIGHT INSET The same data is presented as in the left inset replotted as $\frac{h(0)-h(t)}{\sqrt{t}}$. The thin black line indicates a slope of $\frac{h(0)-h(t)}{\sqrt{t}} \propto t^{-0.25}$.

initial solvent volume fraction $\phi_{\mathrm{S}} = 23\%$. Again the numerical solution is only computed for the half space $y > 0$, $\phi^{\mathrm{eq}} = 0$, and the initial thickness was less than half the initial thickness in the MD simulation, $h_0 = 8.7$. We can reproduce the deviations from the prediction that the thickness should decrease as the square-root of time and describe the thickness dependence encountered in the MD simulation correctly. The density profiles of the solvent are quite well approximated but at late times slight deviations arise and the time scale upon which the evaporation takes place is well predicted which is quite surprising if one looks at the crude estimate of the diffusion constant used.

It is important that the position and composition dependence of D_{L} is accounted for because otherwise the simulation results cannot be reproduced. Qualitatively dif-

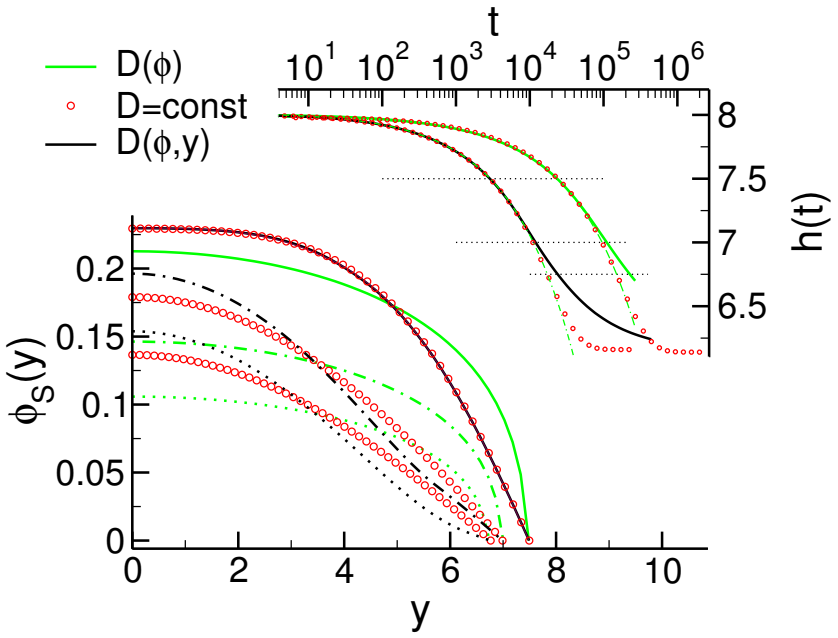

Figure 8.12: LEFT ORDINATE: The volume fraction of solvent inside a free standing film during solvent evaporation at times as marked by the horizontal dashed lines in the inset. The black lines indicate the numerical solution for a position and composition dependent diffusion constant given by equation (8.45) while the grey lines indicate the solution for an only composition dependent diffusion constant. The y-dependent term in equation (8.45) is set to 1. The circles indicate a solution using a constant diffusion value of D_L. RIGHT ORDINATE: The film thickness as a function of time during evaporation is shown. The horizontal dotted lines indicate the times for which the solvent profiles are shown in the main figure. The dash-dotted lines indicate a decrease in film thickness as the $\sqrt{t}$.

ferent density profiles are obtained along with a time scale of the evaporation which is by a factor of 10 larger than in the MD simulation, if only the composition dependence is taken into account. This can be seen in figure 8.12 where the numerical solution for a composition dependent diffusion constant is compared with that of a position and composition dependent diffusion constant. The profiles are compared at equal film thickness. Thus they do not correspond to the same time in the evaporation process. When an only composition dependent diffusion constant is used a very steep increase of solvent volume fraction followed by a flat plateau is observed. The plateau is due to the fact the solvent in the center of the film has enough time to reduce the density gradient and assume an almost constant value during the very slow evaporation because of the low mobility right at the interface. In the case of a composition and position dependent diffusion constant the evaporation is faster and initially profiles, very similar to the ones for a constant diffusion constant are recovered (compare circles and black lines in figure 8.12).

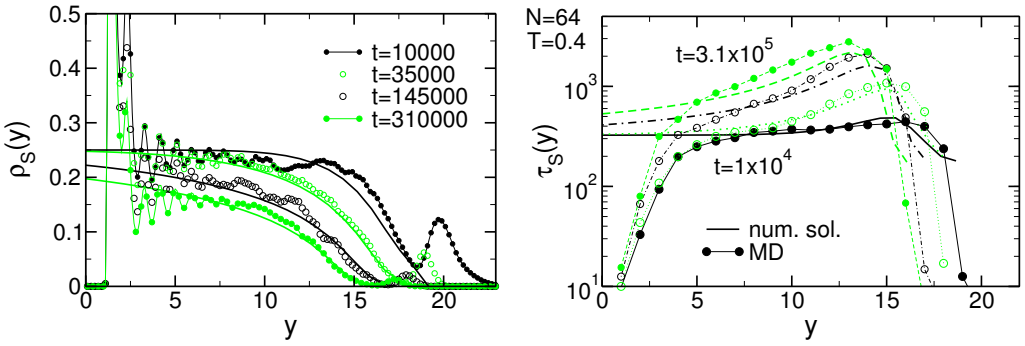

Figure 8.13: LEFT PANEL: The density profiles of the solvent at times $t = 10000$ (full black circles), $t = 35000$ (open grey circles), $t = 145000$ (open black circles) and 310000 (full grey circles) during the evaporation of the solvent from a supported film at $T = 0.4$ containing initially a volume fraction of $\phi_S = 25\%$ in an MD simulation. Also indicated is the numerical solution of the diffusion equation (lines) with the position and composition dependent diffusion constant given in equation (8.45). The film thickness was chosen very large $h_0 = 40$, $\phi_L^0 = 25\%$ and $\phi_L^{eq} = 0$. MIDDLE PANEL: The relaxation times extracted from the simulation shown in figure 8.3 (circles) are compared to the values of the diffusion constant used in the numerical solution of the diffusion equation via $\tau_S = 1/4/D_L$ (lines). $D_L[y, \phi_S(y,t)]$ was calculated from the density profile of the solvent and the local interface position using equation (8.45).

A composition and position dependent diffusion constant leads to deviation from the $\sqrt{t}$ law, but in such a thin film this is also the case for a solution employing a constant diffusion constant or an only composition dependent diffusion constant due to the importance of finite size effects. They all show similar behavior if one adjusts the time-scales. This is in agreement with our observations of solvent evaporation from free-standing films in the MD simulations, where the differences in the functional curves of the decrease in film thickness at $T = 0.5$ and $T = 0.4$ are small (see figure 8.9).

An agreement of the decrease in film thickness with simulation results for a free-standing film at $T = 0.4$, where the time evolution is altered by finite size effects very early in the evaporation process, might therefore not be convincing. Also the shape of the density profiles show systematic deviations. The profiles in the simulation show a small density gradient at the surface followed by a steep increase and a plateau in the center of the film. This shape is a mirror image of the behavior of the local mobilities which are high at the surface, decrease to a minimum at a distance of about 2 monomer diameters from the surface and increase again in the center of the film. Although the numerical solution for a position and composition dependent diffusion constant shows tendencies in this direction, the effect in the simulations is more pronounced, especially in the late stages of the evaporation process.

Therefore we also calculate the numerical solution of the diffusion equation for

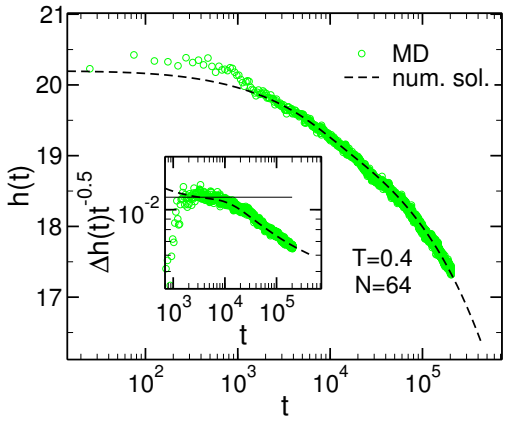

Figure 8.14: The film thickness obtained on in the MD simulations (circles) is compared to the results of the numerical solution (line). In the inset the results are replotted as a function of $\Delta h(t) = [h(0) - h(t)]/\sqrt{t}$.

a very thick film ($h_0 = 40$) where finite size effects do not play a role within the time interval accessible by simulations. The parametrization of the diffusion constant is again chosen to be given by equation (8.45). We compare these results to the MD simulations of the evaporation of solvent from a supported film at $T = 0.4$ in figure 8.13. For this film finite size did not play a role within the time window of the simulation (see section 8.3.2).

The density profiles obtained from the numerical solution of the diffusion equation are in reasonable agreement with the simulations at all times. The layering effects at the supporting wall as well as the solvent accumulation between the film and the wall are not accounted for by the theory, but the decrease of solvent in the center of the film and at the free surface are predicted correctly. Also displayed are the relaxation times extracted from the simulation in comparison with the relaxation times calculated via $\tau_{\mathrm{L}} = 1/4/D_{\mathrm{L}}$ from the position and composition dependent diffusion constant used for the numerical solution of the diffusion equation. The profiles agree semi-quantitatively and show the same qualitative trends. The growing maximum of the relaxation times is reproduced. The deviations of the thickness decrease from $h(0) - h(t) \propto \sqrt{t}$ shown in figure 8.14 is in agreement with the simulation data.

8.4.4 Possible interpretations

The model based on a numerical solution of the diffusion equation described above is sufficient to explain the observations although the parametrization of the diffusion constant used should be put on more rigorous grounds. In this simple picture the deviations from Fickian diffusion are due to the acceleration of the dynamics at the free surface. Together with the counteracting slowing down of the dynamics with decreasing solvent content close to the surface this results in a minimum of the dif-

fusion constant at a distance of about 2 from the surface. This minimum decreases with time as the solvent density decreases during evaporation. This time-dependent diffusion constant gives rise to a slower decrease of the film thickness than expected for Fickian diffusion.

Whether stresses induced in the glassy polymer alter the evaporation dynamics in addition as described by [93] is not clear. These history dependent stresses in the glassy matrix give rise to an additional gradient term in the diffusion equation of the liquid. It could play a similar role as the explicit position dependence of the diffusion constant. It has also been suggested that due to local density and/or composition fluctuations there exist faster domains [95]. If these domains percolate there could exist fast paths allowing the solvent to evaporate within an experimental timescale even below the glass transition temperature. Although we did not see any evidence of the latter in out model it cannot be excluded that local fluctuations in the mobility play a role in the process.

An argument in favor of the picture based on a composition and position dependent diffusion constant described above is the fact that no deviations from Fickian diffusion were observed upon MD simulations of solvent penetration into a glassy polymer matrix employing a very similar model for polymer and solvent [90]. If stresses or local fluctuations in the mobilities of the particles play a role in the process one would expect that it is also the case upon solvent penetration. Within the diffusion model presented above on the other hand the minimum of the diffusion constant does not develop upon solvent penetration and therefore no deviations from Fickian diffusion are expected. Further investigations are necessary to clarify these points.

8.5 Limiting-cases – Instantaneous extraction of the solvent below T_{g}

As complete solvent evaporation was only accessible above T_{g}, where we did not encounter any deviations from the equilibrium structure, it is not possible to deduce from our simulations of the solvent evaporation if there exist residual stresses in the film due to solvent evaporation below T_{g} as suggested by experiments and theory. To get a benchmark whether the system gets trapped in an out-of-equilibrium state upon very rapid solvent evaporation we resort to a method which is, of course, only possible in simulations. There it is feasible to instantaneously remove all solvent molecules by simply taking them out of the simulation box without changing the polymer conformations.

To achieve this we proceed as follows. First we set up an equilibrated polymer film of chains of $N = 64$ monomers and a volume fraction of $\phi_s = 23\%$ in the center of the film at $T = 0.35$. This configuration is cooled to $T = 0.3$, a temperature slightly above the T_{g} of the mixture at this composition and well below T_{g} of the pure

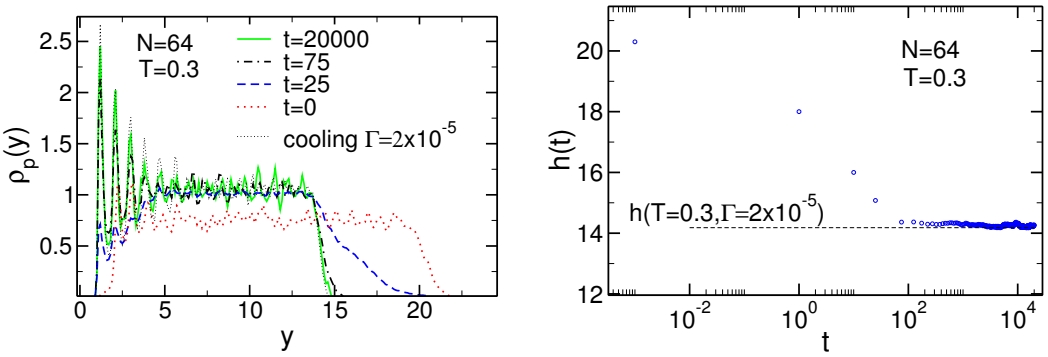

Figure 8.15: LEFT PANEL: The density profile at times $t = 0$ (full line), $t = 25$ (dashed line), $t = 75$ (dash-dotted line), $t = 20000$ (dotted line) after the deletion of all solvent molecules in the simulation at $T = 0.3$. The chain length is $N = 64$. An equilibrated configuration at $T = 0.35$ with an volume fraction of $\phi_S = 23\%$ in the center of the film was cooled to $T = 0.3$ with a cooling rate of $\Gamma_T = 2 \times 10^{-5}$ to create the initial configuration from which the solvent was deleted. Also indicated is the density profile obtained upon cooling the pure polymer film containing the same amount of chains ($n = 96$) from $T = 1$ to $T = 0.3$ with a cooling rate of $\Gamma_T = 2 \times 10^{-5}$ (thin dotted line). RIGHT PANEL: The thickness of the film as a function of time after the deletion of all solvent molecules. The initial configuration was prepared as described before.

polymer film, with a cooling rate of $\Gamma_T = 2 \times 10^{-5}$. At $T = 0.3$ we take out all solvent molecules and continue the simulation at this temperature.

As can be seen in figure 8.15 the film contracts very fast and reaches a density very similar to the density in the center of a pure polymer film cooled to this temperature with a constant rate of $\Gamma_T = 2 \times 10^{-5}$. Initially the layering at the wall is less pronounced and it increases quite slowly towards the amplitude found in a pure polymer film cooled to this temperature. The thickness nevertheless reaches a value very close to the thickness of the cooled polymer film after only 100τ.

The total structure factor and the intra-chain structure factor of the pure polymer film cooled to $T = 0.3$ and the one created by solvent deletion are compared in figure 8.16. Also the differences found in structure of a cooled film and the one created by deleting the solvent seem to be very small within the scatter of $S(q)$ due to the poor sampling of configuration space at this temperature far below the glass transition temperature $T_g = 0.4$. There is no sign of large scale inhomogeneities in the density which would correspond to holes. The film contracts closing the holes left by the solvent molecules and reaching a homogeneous density distribution. Small holes seem to be energetically very unfavorable and there is no large scale inhomogeneity in the system which could give rise to larger holes which could be more stable.

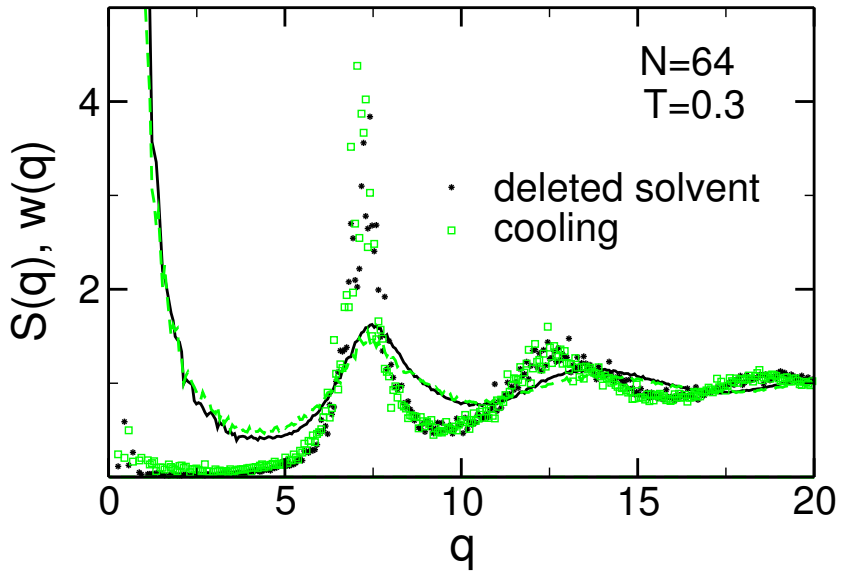

Figure 8.16: Total structure factor $S(q)$ (squares) and intra-chain structure factor $w(q)$ (black line) of a pure polymer film cooled to $T = 0.3$ with a cooling rate of $\Gamma_T = 2 \times 10^{-5}$ and $S(q)$ (filled circles) and $w(q)$ (grey line) obtained at $t = 15000$ after deletion of the solvent at $T = 0.3$ from a film containing an initial volume fraction of solvent of $\phi_S = 23\%$.

8.6 Summary

We simulated the evaporation of solvent above T_g of the pure polymer film, at T_g of the pure polymer film and also below T_g for free-standing and supported films. As initial condition a dense solution with a solvent volume fraction of about $\phi_S \simeq 20\%$ is used. Upon solvent evaporation at all temperatures a polymer rich crust is formed at the surface.

Above T_g of the pure polymer the solvent evaporation can be described by Fickian diffusion while at T_g and below deviations are observed. The decrease in film thickness follows a power law dependence. Only above T_g could the simulations be run long enough to end up with a pure polymer film. In this case we did not observe any deviations of the properties of the film from equilibrium. The evaporation from free-standing films is faster than the solvent evaporation from supported films where the solvent trapped between the polymer and the wall only leaves the film very slowly. Residual solvent trapped between the polymer and the wall could lead to a negative thermal expansion coefficient upon heating observed in experiments when the film dries completely.

Even upon an instantaneous extraction of the solvent we did not observe considerable deviations of the resulting glassy film structure from a glassy polymer film obtained by cooling a pure polymer film from high temperature. The conformation

of the chains in solution do in our model not differ strongly from the chain conformations encountered in the melt. Probably to observe out of equilibrium structures where the chains are only poorly entangled or otherwise strained, it is necessary to start the evaporation from a more dilute solution and use longer chains, so that the initially swollen conformations need to rearrange considerably to reach an equilibrium structure in the melt.

Chapter 9

Conclusions

The realization of ever smaller structures confronts nanosciences with a challenging fundamental problem: To what extent are properties and concepts, well established in the bulk, still pertinent on the nanoscale? In this respect, polymer films play an important role. Not only because of their technical significance, but also because of our increased capabilities to explore their behavior. Numerous recent studies have revealed unexpected deviations from bulk behavior for films thinner than about 10 nm. For instance, the glass transition temperature can be dramatically reduced, implying that the film is in a fluid state at temperatures where the bulk would be solid.

Within the framework of the Marie Curie Research Training Network 'POLYFILM', research groups from the United Kingdom, the Netherlands, Belgium, Germany, and France combine their efforts to study such nanoscopic polymer films. Of particular interest are questions of how the thermodynamic, structural and dynamical properties of the polymer films deviate from the bulk behavior, and of how these properties are affected by the film preparation techniques.

Our group at the Institut Charles Sadron (ICS) in Strasbourg contributed to this interdisciplinary research by computer simulations of coarse-grained polymer models [101] presented in this thesis. In a first step, a recently developed model for polymer films [32, 35] was extended to consider films with a free surface. Conformational, structural, and dynamical properties were investigated, as the polymer film is cooled towards its glass transition. In a second step, the film preparation technique ('spin-coating') was modeled by simulating the solvent evaporation from a polymer film on a substrate.

Relaxation and structure of polymer films close to the glass transition

We performed MD simulations of ultra-thin polymer films in free-standing and supported film geometries using a coarse-grained bead-spring model which retains only

the most prominent features of polymers, such as chain-connectivity, short range repulsion between the monomers, and long range attraction of the monomers ensuring the integrity of the material in the presence of a free surface.

Average and layer-resolved static and dynamic properties. We find a layering of the monomer density at the supported surface, while the density profile at the free surface monotonically decays to zero. The layering becomes more pronounced on cooling and reaches further into the film. The dynamics in our system are also altered due to the presence of the surfaces. A layer-resolved analysis clearly demonstrates that monomers at the free and solid interfaces are faster than those in the center of the film, which remain bulk-like. Furthermore, monomers at the free surface are faster than those at the solid interface. These highly mobile surface monomers transfer part of their high mobility to the next deeper layer, which in turn can accelerate the next layer, and so on until the effect is damped out if the film is thick enough (for thin films and/or low T, the perturbations emanating from both surfaces interfere with one another in the film center). The static structure is affected by the presence of the surfaces as well. We find a decrease of comparable magnitude of the first maximum of the static structure factor in the vicinity of both surfaces indicating that the packing constraints are weaker. In addition, a divergence of $S(q)$ as q^{-2} for small q due to capillary waves is observed at the free surface.

Therefore, if we consider the same temperature, we find that the dynamics of the films, averaged over the whole film, is faster than that of bulk and, furthermore, that the free-standing films relax faster than the supported films (two free surfaces instead of one). The first peak of the average static structure factor measuring local correlations in density fluctuations is also lower in the films than in the bulk and decreases with decreasing film thickness. Contrary to the dynamic properties we find the reduction in the first maximum of $S(q)$ to be comparable in size for both film geometries. This makes an interpretation within the picture of mode-coupling theory which suggest a strong coupling of the static structure on the local scale and the system's dynamics difficult. Although the general trend of weaker packing constraints and a decrease of relaxation times with decreasing thickness are in agreement with these ideas, the differences encountered for supported and free-standing films cannot be explained.

Thickness dependence of T_c and T_g. These results have an impact on characteristic temperatures, such as the glass transition temperature T_g and the critical temperature of MCT T_c. T_g was determined from the temperature dependence of the film thickness h on cooling; T_c was derived from an analysis of relaxation times in the films. Qualitatively, $T_g(h)$ and $T_c(h)$ display the same features. The values of both temperatures are depressed with respect to the bulk, and the depression becomes more pronounced with decreasing h. The thickness dependence of T_c (or T_g) can be well

described by $T_{\mathrm{c}}(h) = T_{\mathrm{c}}^{\mathrm{bulk}}/(1 + h_0/h)$. The fit yields a characteristic height h_0 that is about twice as large for free-standing films than for supported films.

This finding qualitatively agrees with experimental results on the depression of T_{g} for supported and free-standing polystyrene (PS) films [4, 40, 41]. These experiments suggest that T_{g} of a free-standing film of thickness h agrees, within the error bars, with the T_{g} of a supported film of thickness $h/2$. From this result alone it thus appears as if the substrate could be introduced in the midplane of the free-standing film with negligible perturbation of its properties. Our discussion of the layer-resolved dynamics, however, indicates that such an interpretation may be too simplified. For our model, the substrate leads to faster dynamics, similar to that found at the free interface.

Local glass transition temperature. In agreement with recent experiments on supported polystyrene films [9] we find that the free surface gives rise to a local glass transition temperature which decreases with decreasing distance to the surface. We show that this distance dependence can be understood from the average behavior of the film, that is, from the depression of T_{g} with decreasing film thickness which is well described by a parametrization suggested by Herminghaus and coworkers [4].

Dielectric relaxation in thin polymer films. We performed a complementary analysis of the dynamics in our model polymer films and the bulk, based on the autocorrelation function of the system's polarization. This method provids results, similar to the ones obtained in experiments employing broadband dielectric spectroscopy, a technique often used to study polymer dynamics and especially also the glass transition in thin polymer films. We attached dipoles locally parallel and perpendicular to the chain backbone [175] allowing to follow the segmental relaxation as well as the normal mode relaxation related to the dynamics of the whole chain. We find that the segmental mode is faster in the films than in the bulk and a fit to a VFT equation yields a lower temperature T_0 in comparison with the bulk. The segmental relaxation in the films is found to be isotropic while the normal mode relaxation becomes anisotropic in thin films. The normal mode relaxation is faster perpendicular to the plane of the film than in the plane of the film. As the interaction with the supporting wall was chosen such that the monomers at the wall remained highly mobile, we did not observe an additional confinement induced mode in our systems as suggested by [171–174].

Simulations with explicit solvent

We performed simulations of a coarse-grained polymer in solution with explicit solvent. The interaction parameters were chosen to model the solution of polystyrene and toluene. We investigated the system in the regime of high polymer concentration

(the solvent volume fraction ϕ_S is varied between 0% and 30%) at 3 different temperatures: $T = 0.5$ which is well above T_g of the pure polymer, at $T \simeq T_g = 0.4$ and at $T = 0.35$ which is below the glass transition temperature of the pure polymer. The solution becomes glassy at this temperature below a solvent volume fraction of about $\phi_S = 10\%$.

We studied two film geometries as for the pure polymer films, namely supported and free-standing films. The solvent is enriched between the polymer and the wall as well as at the free surface. The presence of the solvent reduces the glass transition temperature of the binary mixture. We find that the solvent also suppresses correlations in local density fluctuations as measured by the maximum of the static structure factor. An increasing sensitivity of the local mobility of the monomers on the solvent concentration and the proximity to the interface is observed with decreasing temperature. The solvent acts as a plasticizer accelerating the relaxation of the polymer. The closer the monomers are to the surface, the faster their dynamics. At T_g of the pure polymer the local relaxation times span three orders of magnitude as a function of composition and distance from the surface.

We simulate the evaporation of solvent above T_g of the pure polymer film, at T_g of the pure polymer film and also below T_g for free-standing and supported films. As initial condition a dense solution with a solvent volume fraction of about $\phi_S \simeq 20\%$ is used. Upon solvent evaporation at all temperatures a polymer rich crust is formed at the surface.

Solvent evaporation above T_g. At temperatures well above T_g we observe a Fickian diffusion process. The film thickness decreases as the square root of time until finite size effects become relevant in both free-standing and supported films. The complete evaporation of the solvent from a supported film is by more than an order of magnitude slower than the one from a free-standing film of the same thickness and solvent content. The solvent trapped between the polymer and the supporting wall only leaves the film very slowly prolonging the final stages of the evaporation process.

Solvent evaporation at T_g and below. If the evaporation is performed at T_g or below, we initially also observe Fickian diffusion. In this regime the results at all temperatures superimpose upon rescaling the time axis by a characteristic time τ^*. This initial short regime of Fickian diffusion is followed by a regime characterized by the decrease of the film thickness as $h(0) - h(t) \propto t^{\kappa(T)}$. The exponent $\kappa(T)$ is smaller than 0.5 which would be expected for Fickian diffusion and decreases with decreasing temperature. In free-standing films the second regime cannot be observed clearly due to the early onset of finite-size effects which alter the evaporation kinetics.

Comparison with theory. We use a simple model of solvent evaporation based on diffusion equations to describe the problem theoretically. The differential equations are solved numerically yielding the density profiles of the solvent inside the liquid film as well as the decrease of film thickness as a function of time. The results of the simulations at high temperatures can be reproduced well using a constant value of the diffusivity in the liquid phase. A possible explanation for the regime of non-Fickian diffusion observed in the simulations at lower temperatures is based on the strong dependence of the mobilities on composition and the distance from the surface. These counteracting trends, i.e. the acceleration in the vicinity of the surface and on the other hand the strong decrease of solvent concentration at the surface lead to a minimum in mobility at a distance of about two monomer diameters from the surface. This 'mobility barrier' becomes more pronounced with time slowing down the evaporation at the later stages and leading to deviations from Fickian diffusion.

Outlook

Although our simulations could shed some light on the influence of a free surface on the glass transition in our simple polymer model there remain still a lot of questions unanswered. Nevertheless our results can provide some guidelines for further investigation of the problem.

Coupling between relaxation on the local scale and capillary wave fluctuations. The theoretical basis leading to the equation $T_{\mathrm{c}}(h) = T_{\mathrm{c}}^{\mathrm{bulk}}/(1 + h_0/h)$ is still unclear. There are few theoretical guidelines how to determine the parameter h_0. By Herminghaus and coworkers [4] it was suggested that $h_0 = \gamma/E$, where γ is the surface tension and E is the elastic modulus of the bulk polymer at T_{g}. As E changes very abruptly upon approaching T_{g}, this does not allow to determine h_0 in practice. In connection with the found T_{g} reductions in thin polymer films with a free surface it would therefore be interesting to further investigate the influence of capillary waves on the relaxation in thin polymer films. Our analysis of this process did not allow to determine whether there exists a coupling between these large scale fluctuations and the local relaxation of the monomers usually thought more relevant for the glass transition. Maybe four-point correlation functions as introduced by Bouchaud [196] and Glotzer [197] might provide a means to determine whether the acceleration of the dynamics on the local scale in these thin films can be linked to the presence of capillary waves. The fact that simulations by Fathollah Varnik for confined films, where these capillary wave fluctuation should be suppressed, gave very similar results, raises doubts that the idea of a coupling between the viscous bulk flow and the capillary wave fluctuations, that lead to the derivation of $T_{\mathrm{c}}(h) = T_{\mathrm{c}}^{\mathrm{bulk}}/(1 + h_0/h)$, are correct.

Influence of chain stiffness on the thickness dependence of T_c and T_g. While our simulations so far focused on general features of polymers, experimentally also the specific structure of different polymers has a large influence on the observed results and therefore on h_0. It has also become clear that, while h_0 seems to be rather independent of chain length for low and intermediate molecular weight polymer films, this is no longer the case for very high molecular weight polymers [10, 198]. Experimentally the decrease in T_g for ultra-thin polymer films with a free surface is found to differ strongly in magnitude between different polymers, ranging from a few Kelvin for PMMA to more than forty Kelvin for PS [31, 198]. The influence of chain specific properties such as stiffness or bulky side-groups on the glass transition in confinement have not yet been investigated using computer simulations. An extension of our simulations to include for example the influence of chain stiffness on the T_g reductions in thin films could therefore provide further insight into the phenomenon.

Towards a simulation of the spin-coating process. Our simulations on the evaporation of solvent from a dense polymer solution provide a starting point for further analysis of the effects of this film preparation technique on the resulting structures. In order to come closer to the experimental scenario during spin coating, it would be desirable to carry out longer MD simulations of the evaporation at low temperature probably for polymer films containing longer chains. The influence of the solvent concentration on the entanglement length and the chain conformation itself should be stronger for longer chains. As this requires very large scale simulations, it is worthwhile to explore other paths to gain insight into the process.

Artificial preparation of non-equilibrium configurations. The question whether films prepared by spin-coating are non-equilibrium structures could only be partially addressed in this thesis. The evaporation of solvent below T_g was too slow to prepare pure glassy polymer films by this procedure. Therefore, also the relaxation of these structures could not be addressed. Another way to tackle this problem would by the artificial preparation of non-equilibrium configurations and subsequent MD simulations investigating the relaxation towards equilibrium of these structures. One suggestion from experiments was that residual stresses in films prepared by spin-coating are due to poorly entangled chains. The initially in dilute solution isolated chains are thought not to have had enough time to interpenetrate during the rapid solvent loss. Such a structure could be created in computer simulations for example by forming a film as an array of single chain globules. It would also be possible to take a very dilute system at a temperature above the θ temperature so that the chains are initially swollen and compress it very rapidly upon lowering the temperature below T_g, i. e. the change of the chains environment due to the solvent loss in this case would be modeled by a temperature change, to obtain a dense glassy film. The relaxation of these structures towards equilibrium could then be investigated.

Mesoscopic theories of solvent evaporation. MD simulations can only address a limited range of time and length scales. It is in our case desirable to be able to go to lower temperatures to observe a glass transition upon solvent evaporation. Thus even slower evaporation rates and relaxation times make it difficult to treat this problem by MD-simulations alone. It is desirable to find a method to complement our simulation results which makes larger time scales accessible. A quite common choice for such a method is the self-consistent mean field theory (SCMFT) [199–201]. This approach has been applied successfully to a wide range of problems but its biggest short-coming is that it ignores fluctuations which can become important near critical points and at interfaces. To include the effect of fluctuations and to also be able to treat the dynamical aspect of the problem it can be extended to perform single chain in mean field (SCMF) simulations [48, 202].

The knowledge we gained from MD simulations on the static and dynamic properties of the solution as a function of solvent content can provide guidelines how to model this phenomenon within the framework of SCMF theory and simulations. Also a very simple time-dependent version of SCMFT along the lines of a time-dependent Ginzburg-Landau theory [199, 203] using a square gradient expansion of the free energy could be used to further complement this study. By comparing with the results from SCMF simulations the importance of chain connectivity in the process could be assessed. Also Ginzburg-Landau theory provides a natural way to improve on our simple diffusion model treating only the solvent volume fraction in the liquid phase. While this theory is still based on diffusion equations, it includes the interfaces and therefore both phases can be accounted for, as well as the thermodynamic forces described by the gradients in the chemical potential. Work in this direction is under way.

Appendix A

Tables

$N = 10$	supported $n = 288$	free $n = 288$	supported $n = 576$	free $n = 576$	supported $n = 864$	bulk $n = 288$
T_{g}	0.341(8)	0.322(4)	0.371(2)	0.355(3)	0.384(2)	0.392(5)
T_{m}	0.347(7)	0.330(6)	0.381(5)	0.363(6)	0.396(7)	0.401(9)
T_{c}	0.361(5)	0.333(6)	0.383(8)	0.365(5)	0.392(8)	0.405(4)
γ_1	2.2(2)	2.2(1)	2.09(9)	2.1(1)	2.1(2)	1.96(8)
γ_{q^*}	3.4(2)	3.4(2)	3.0(1)	3.3(2)	2.95(10)	2.2(1)
h_0	0.80	1.47	0.76	1.47	0.74	
$h(T = 1)$	8.4	8.4	16.6	16.6	24.9	
$h(T = 0.44)$	6.9	7.0	13.85	14.0	20.5	

Table A.1: Survey of characteristic temperatures and other parameters for the system sizes n (= number of chains) and geometries studied: glass transition temperature T_{g} and inflection point of the thermal expansion coefficient T_{m} as described in section 3.1; mode-coupling critical temperature $T_{\mathrm{c}}(h)$ and exponents $\gamma_{\mathsf{A}}(h)$ (section 4.2). The error bars refer to the statistical error due to the noise in the data for a given fit interval. The parameter h_0 is found by inversion of equation (4.14).

$N = 64$	supported $n = 48$	free $n = 48$	supported $n = 96$	free $n = 96$	bulk $n = 48$
T_{g}		0.328(5)	0.379(4)	0.369(9)	0.402(4)
T_{m}		0.337(7)	0.385(6)	0.375(8)	0.416(6)
T_{c}	0.365(4)	0.331(7)	0.391(7)	0.370(5)	0.415(6)
γ_1	2.3(2)	2.35(8)	2.2(1)	2.2(1)	2.0(2)
γ_{q^*}	3.7(2)	3.6(3)	3.3(1)	3.5(2)	3.15(10)
h_0		1.67	0.93	1.69	

Table A.2: Survey of characteristic temperatures and other parameters for the system sizes n (= number of chains) and geometries studied: glass transition temperature T_{g} and inflection point of the thermal expansion coefficient T_{m} as described in section 3.1; mode-coupling critical temperature $T_{\mathrm{c}}(h)$ and exponents $\gamma_{\mathsf{A}}(h)$ (section 4.2). The error bars refer to the statistical error due to the noise in the data for a given fit interval. The parameter h_0 is found by inversion of equation (4.14).

ϕ_S	ρ_P	ρ_S^L	ρ_S^G	ρ_{tot}	h	N_S
27%	0.695	0.256	0.12	0.951	22.1	4608
22%	0.751	0.213	0.095	0.964	20.25	3072
21%	0.772	0.198	0.077	0.97	20.15	3072
15%	0.835	0.15	0.0538	0.985	18.6	2304
10%	0.892	0.098	0.031	0.99	17.3	1536
5%	0.948	0.049	0.012	0.997	15.97	768
0%	1.01	0	0	1.01	14.82	0

Table A.3: A compilation of the density of polymer ρ_P and solvent ρ_S^L in solution in the center of the film as well as the total density in the center of the film ρ_{tot} and the density of the solvent in the vapor phase ρ_G^L in the MD simulations of a supported film of lateral $L = 20$ containing $n = 96$ chains of $N = 64$ monomers at $T = 0.5$ and a number of solvent molecules as indicated in the table. The film thickness is also indicated.

ϕ_S	ρ_P	ρ_S^L	ρ_S^G	ρ_{tot}	h	N_S
35%	0.63	0.34	0.03	0.97	23.96	4608
25%	0.745	0.245	0.02	0.99	20.61	3072
19%	0.81	0.19	0.015	1.0	18.78	2304
12%	0.89	0.125	0.0105	1.015	17.12	1536
6%	0.975	0.058	0.0042	1.03	15.55	768
0%	1.03	0	0	1.03	14.61	0

Table A.4: A compilation of the density of polymer ρ_P and solvent ρ_S^L in solution in the center of the film as well as the total density in the center of the film ρ_{tot} and the density of the solvent in the vapor phase ρ_G^L in the MD simulations of a supported film of lateral $L = 20$ containing $n = 96$ chains of $N = 64$ monomers at $T = 0.4$ and a number of solvent molecules as indicated in the table. The film thickness is also indicated.

List of Figures

Bibliography

[1] J. L. Keddie, R. A. L. Jones, and R. A. Cory. Size-dependent depression of the glass transition temperature in polymer films. *Europhys. Lett.*, 27:59, 1994.

[2] J. A. Forrest and K. Dalnoki-Veress. The glass transition in thin polymer films. *Adv. Coll. Interf. Sci.*, 94:167, 2001.

[3] J. Sharp, J. Teichroeb, and J. Forrest. The properties of free polymer surfaces and their influence on the glass transition temperature of thin polystyrene films. *Eur. Phys. J.*, 15:473, 2004.

[4] S. Herminghaus, K. Jacobs, and R. Seemann. The glass transition of thin polymer films: Some questions, and a possible answer. *Eur. Phys. J. E*, 5:531, 2001.

[5] S. Herminghaus, R. Seemann, and K. Landfester. Polymer surface melting mediated by capillary waves. *Phys. Rev. Lett.*, 93:017801, 2004.

[6] R. Seemann, S. Herminghaus, C. Neto, S. Schlagowski, D. Podzimek, R. Konrad, H. Mantz, and K. Jacobs. Dynamics and structure formation in thin polymer melt films. *J. Phys.: Condens. Matter*, 17:S267, 2005.

[7] Y. Grohens, L. Hamon, G. Reiter, A. Soldera, and Y. Holl. Some relevant parameters affecting the glass transition of supported ultra-thin polymer films. *Eur. Phys. J. E*, 8:217, 2002.

[8] J. H. Kim, J. Jang, and W.-C. Zin. Thickness dependence of the glass transition temperature in thin polymer films. *Langmuir*, 17:2703, 2001.

[9] C. J. Ellison and J. M. Torkelson. The distribution of glass-transition temperatures in nanoscopically confined glass formers. *Nature Mat.*, 2:695, 2003.

[10] C. Ellison, M. Mundra, and J. Torkelson. Impacts of polystyrene molecular weight and modification to the repeat unit structure on the glass transition-nanoconfinement effect and the cooperativity length scale. *Macromolecules*, 38:1767, 2005.

[11] C. Alba-Simionesco, G. Dosseh, E. Dumont, B. Frick, B. Geil, D. Morineau, V. Teboul, and Y. Xia. Confinement of molecular liquids: Consequences on thermodynamic, static and dynamical properties of benzene and toluene. *Eur. Phys. J. E*, 12:19, 2003.

[12] G. Xu and W. L. Mattice. Monte Carlo simulation on the glass transition of free-standing atactic polypropylene thin films on a high coordination lattice. *J. Chem. Phys.*, 118:5241, 2003.

[13] F. W. Starr, T. B. Schrøder, and S. C. Glotzer. Effects of a nanoscopic filler on the structure and dynamics of a simulated polymer melt and the relationship to ultrathin films. *Phys. Rev. E*, 64:021802, 2001.

[14] R. A. Riggleman, K. Yoshimoto, J. F. Douglas, and J. J. de Pablo. Influence of confinement on the fragility of antiplasticized and pure polymer films. *Phys. Rev. Lett.*, 97:045502, 2006.

[15] K. Yoshimoto, T. S. Jain, P. F. Nealey, and J. J. de Pablo. Local dynamic mechanical properties in model free-standing polymer thin films. *J. Chem. Phys.*, 122:144712, 2005.

[16] T. R. Böhme and J. J. de Pablo. Evidence for size-dependent mechanical properties from simulations of nanoscopic polymeric structures. *J. Chem. Phys.*, 116:9939, 2002.

[17] A. R. C. Baljon, M. H. M. Van Weert, R. Barber DeGraaff, and R. Khare. Glass transition behavior of polymer films of nanoscopic dimensions. *Macromolecules*, 38:2391, 2005.

[18] A. R. C. Baljon, J. Billen, and R. Khare. Percolation of immobile domains in supercooled thin polymeric films. *Phys. Rev. Lett.*, 93:255701, 2004.

[19] P. Scheidler, W. Kob, and K. Binder. The relaxation dynamics of a supercooled liquid confined by rough walls. *J. Phys. Chem. B*, 108:6673, 2004.

[20] V. Teboul and C. Alba-Simionesco. Properties of a confined molecular glass-forming liquid. *J. Phys.: Condens. Matter*, 14:5699, 2002.

[21] H. Morita, K. Tanaka, T. Kajiyama, T. Nishi, and M. Doi. Study of the glass transition temperature of polymer surface by coarse-grained molecular dynamics simulation. *Macromolecules*, 39:6233, 2006.

[22] P. G. de Gennes. Glass transitions in thin polymer films. *Eur. Phys. J. E*, 2:201, 2000.

[23] J. D. McCoy and J. G. Curro. Conjectures on the glass transition of polymers in confined geometries. *J. Chem. Phys.*, 116:9154, 2002.

[24] J. Mittal, P. Shah, and T. M. Truskett. Using energy landscapes to predict the properties of thin films. *J. Phys. Chem. B*, 108:19769, 2004.

[25] D. Long and F. Lequeux. Heterogeneous dynamics at the glass transition in van der Waals liquids, in the bulk and in thin films. *Eur. Phys. J. E*, 4:371, 2001.

[26] K. L. Ngai. The effects of changes of intermolecular coupling on glass transition dynamics in polymer thin films and glass-formers confined in nanometer pores. *Eur. Phys. J. E*, 12:93, 2003.

[27] F. T. Oyerokun and K. S. Schweizer. Theory of glassy dynamics in conformationally anisotropic polymer systems. *J. Chem. Phys.*, 123:224901, 2005.

[28] C. A. Angell, K. L. Ngai, G. B. McKenna, P. F. McMillan, and S. W. Martin. Relaxation in glassforming liquids and amorphous solids. *J. Appl. Phys.*, 88:3113, 2000.

[29] E. Donth. *The Glass Transition*. Springer, Berlin–Heidelberg, 2001.

[30] C. B. Roth and J. R. Dutcher. *Soft Materials: Structure and Dynamics*, pages 1–38. Marcel Dekker, New York, 2005.

[31] M. Alcoutlabi and G. B. McKenna. Effects of confinement on material behaviour at nanometer size scale. *J. Phys.: Condens. Matter*, 17:R461, 2005.

[32] J. Baschnagel and F. Varnik. Computer simulations of supercooled polymer melts in the bulk and in-confined geometry. *J. Phys.: Condens. Matter*, 17:R851, 2005.

[33] P. Scheidler, W. Kob, and K. Binder. Cooperative motion and growing length scales in supercooled confined liquids. *Europhys. Lett.*, 59:701, 2002.

[34] G. D. Smith, D. Bedrov, and O. Borodin. Structural relaxation and dynamic heterogeneity in a polymer melt at attractive surfaces. *Phys. Rev. Lett.*, 90:226103, 2003.

[35] F. Varnik, J. Baschnagel, and K. Binder. Reduction of the glass transition temperature in polymer films: A molecular-dynamics study. *Phys. Rev. E*, 65:021507, 2002.

[36] F. Varnik, J. Baschnagel, and K. Binder. Static and dynamic properties of supercooled thin polymer films. *Eur. Phys. J. E*, 8:175, 2002.

[37] C. R. Nugent, H. N. Patel, and E. R. Weeks. Colloidal glass transition observed in confinement. *Submitted to Phys. Rev. Lett*, 2007.

[38] S. Peter, H. Meyer, and J. Baschnagel. Thickness dependent reduction of the glass transition temperature in thin polymer films with a free surface. *J. Polym. Sci. B: Polymer Physics*, 44:2951, 2006.

[39] S. Peter, H. Meyer, and J. Baschnagel. Slow dynamics and glass transition in simulated free-standing polymer films: A possible relation between global and local glass transition temperatures. *J. Phys.: Condens. Matter*, 19:205119, 2007.

[40] J. S. Sharp and J. A. Forrest. Free surfaces cause reductions in the glass transition temperature of thin polystyrene films. *Phys. Rev. Lett.*, 91:235701, 2003.

[41] J. A. Forrest. A decade of dynamics in thin films of polystyrene: Where are we now? *Eur. Phys. J. E*, 8:261, 2002.

[42] H. Richardson, M. Sferrazza, and J.L. Keddie. Influence of the glass transition on solvent loss from spin-cast glassy polymer thin films. *Eur. Phys. J. E.*, 12:S87, 2003.

[43] H. Richardson, C. Carelli, J.L. Keddie, and M. Sferrazza. Structural relaxation of spin-cast glassy polymer thin films as a possible factor in dewetting. *Eur. Phys. J. E.*, 12:437–441, 2003.

[44] G. Reiter and P.G. de Gennes. Spin-cast, thin,glassy polymer films: Highly metastable forms of matter. *Eur. Phys. J. E.*, 3:25–28, 2001.

[45] P.G. de Gennes. Solvent evaporation of spin cast filmd: ”Crust” effects. *Eur. Phys. J. E.*, 7:31–34, 2002.

[46] M. Tsige and G. S. Grest. Molecular dynamics study of the evaporation process in polymer films. *Macromolecules*, 37:4333, 2004.

[47] M. Tsige and G. Grest. Solvent evaporation and interdiffusion in polymer films. *J. Phys.: Condens. Matter*, 17:S4119–S4132, 2005.

[48] M. Müller and G.D. Smith. Phase separation in binary mixtures containing polymers. *J. Poly. Sci. B: Polymer Physics*, 43:934–958, 2005.

[49] T. P. Lodge and M. Muthukumar. Physical chemistry of polymers: Entropy, interactions, and dynamics. *J. Phys. Chem.*, 100:13275, 1996.

[50] M. Doi and S. F. Edwards. *The Theory of Polymer Dynamics*. Oxford University Press, Oxford, 1986.

[51] M. Rubinstein and R. H. Colby. *Polymer Physics*. Oxford University Press, Oxford, 2003.

[52] P.-G. de Gennes. *Scaling Concepts in Polymer Physics*. Cornell University Press, Ithaca, 1996.

[53] T. A. Witten. Polymer solutions: A geometric introduction. *Rev. Mod. Phys.*, 70:1531, 1998.

[54] S. F. Edwards. The size of a polymer molecule in a strong solution. *J. Phys. A: Math. Gen.*, 8:1670, 1975.

[55] M. Muthukumar and S. F. Edwards. Extrapolation formulas for polymer solution properties. *J. Chem. Phys.*, 76:2720, 1982.

[56] J. P. Wittmer, H. Meyer, J. Baschnagel, A. Johner, S. Obukhov, L. Mattioni, M. Müller, and A. N. Semenov. Long range bond-bond correlations in dense polymer solutions. *Phys. Rev. Lett.*, 93:147801, 2004.

[57] T. C. B. McLeish. Tube theory of entangled polymer dynamics. *Adv. Phys.*, 51:1379, 2002.

[58] H. Meyer and F. Müller-Plathe. Formation of chain-folded structures in supercooled polymer melts. *J. Chem. Phys.*, 115:7807, 2001.

[59] H. Meyer and F. Müller-Plathe. Formation of chain-folded structures in supercooled polymer melts examined by MD simulations. *Macromolecules*, 35:1241, 2002.

[60] G. Strobl. *The Physics of Polymers: Concepts for Understanding their Structures and Behavior*. Springer, Berlin–Heidelberg, 1997.

[61] K. Armitstead and G. Goldbeck-Wood. Polymer crystallization theories. *Adv. Poly. Sci.*, 100:219–312, 1992.

[62] M. Muthukumar. Nucleation in polymer crystallization. *Adv. Chem. Phys.*, 128:1–63, 2004.

[63] G. Strobl. From the melt via mesomorphic and granular crystalline layers to lamellar crystallites: A major route followed in polymer crystallization? *Eur. Phys. J. E*, 3:165, 2000.

[64] B. Lotz. What can polymer crystal structure tell about polymer crystallization processes? *Eur. Phys. J. E*, 3:185, 2000.

[65] G. B. McKenna. In C. Booth and C. Price, editors, *Comprehensive Polymer Science*, volume 2, pages 311–362. Pergamon, New York, 1986.

[66] P. G. Debenedetti and F. H. Stillinger. Supercooled liquids and the glass transition. *Nature*, 410:259, 2001.

[67] W. Götze. Recent tests of the mode-coupling theory for glassy dynamics. *J. Phys.: Condens. Matter*, 11:A1, 1999.

[68] W. Götze and L. Sjögren. Relaxation processes in supercooled liquids. *Rep. Prog. Phys.*, 55:241, 1992.

[69] C. B. Roth and J. R. Dutcher. Glass transition temperature of freely-standing films of atactic poly(methyl methacrylate). *Eur. Phys. J. E*, 12:S103, 2003.

[70] C. Bolline, S. Cuenot, B. Nysten, and A. M. Jones. Spinodal like dewetting of thermodynamically-stable thin polymer films. *Eur. Phys. J. E.*, 12:S87, 2003.

[71] G. Reiter, M. Hamieh, P. Damman, S. Sclavos, S. Gabriele, T. Vilmin, and E. Raphaël. Residual stresses in thin polymer films cause rupture and dominate early stages of dewetting. *Nature Materials*, 4:754, 2005.

[72] T. Miyazaki, K. Nishida, and T. Kanaya. Contraction and reexpansion of thin polymer films. *Phys. Rev. E*, 69:0220801, 2004.

[73] D. Meyerhofer. Characteristics of resist films produced by spinning. *J. Appl. Phys.*, 49:3993, 1978.

[74] J.D. LeRoux and D. R. Paul. Preparation of composite membranes by a spin coating process. *J. Membr. Sci*, 74:233, 1992.

[75] G. B. McKenna. Size and confinement effects in glass forming liquids: Perspectives on bulk and nano-scale behaviours. *J. Phys. IV*, 10:Pr7–53, 2000.

[76] D. E. Bornside, C. W. Macosko, and L. E. Scriven. On the modeling of spin coating. *J. Imag. Technol.*, 13:122, 1987.

[77] K. Dalnoki-Verress, J. A. Forrest, C. Murray, C. Gigault, and J. R. Dutcher. Molecular weight dependence of reductions in the glass transition temperature of thin, freely standing polymer films. *Phys. Rev. E*, 63:031801, 2001.

[78] J. Crank. *Mathematics of Diffusion*. Clarendon Press, Oxford, 1975.

[79] J. Crank. *Free and Moving Boundary Problems*. Clarendon Press, Oxford, 1984.

[80] J. S. Vrentas and C. M. Vrentas. Surface concentration effects in the drying of solvent coated polymer films. *J. Appl. Polym. Sci.*, 60:1049–1055, 1996.

[81] V. Mhetar and J.C. Slattery. The Stefan problem of a binary liquid mixture. *Chem. Eng. Sci.*, 52:1237–1242, 1997.

[82] S. Alsoy and J.L. Duda. Modeling of multilayer drying of polymer films. *J. Poly. Sci. B: Polymer Physics*, 37:1665–1675, 1999.

[83] R. Chebbi and M.S. Selim. The Stefan problem of evaporation of a volatile component from a binary liquid mixture. *Heat Mass Transfer*, 42:238–247, 2006.

[84] G. S. Hartley. Diffusion and swelling of high polymers. Part I: The swelling and solution of a high polymer solid considered as a diffusion process. *Trans. Farady Soc.*, 42B:6, 1946.

[85] T. K. Kwei and H. M. Zupko. Diffusion in glassy polymers. I. *J. Polym. Sci.: Part A-2*, 7:867, 1969.

[86] C.-Y. Hui and K.-C. Wu. Case-II diffusion in polymers. I. Transient swelling. *J. Appl. Phys.*, 61:5129, 1987.

[87] C.-Y. Hui and K.-C. Wu. Case-II diffusion in polymers. II. Steady front motion. *J. Appl. Phys.*, 61:5137, 1987.

[88] E. Gattiglia and T.P. Russel. Swelling behavior of an aromatic polyimide. *J. Polym. Sci.: Part B*, 27:2131, 1989.

[89] J. Janeva, B. Dünweg, and A. Milchev. Non-Fickian interdiffusion of dynamically asymmetric species: A molecular-dynamics study. *J. Chem. Phys.*, 122:204105, 2005.

[90] M. Tsige and G. Grest. Interdiffusion of solvent into glassy polymer films: A molecular dynamics study. *J. Chem. Phys.*, 121:7513, 2004.

[91] N. L. Thomas and A. H. Windle. Transport of methanol in poly(methyl methacrylate). *Polymer*, 19:255, 1978.

[92] N. L. Thomas and A. H. Windle. A theory of case II diffusion. *Polymer*, 23:529, 1982.

[93] D. A. Edwards. Non-Fickian diffusion in thin polymer films. *J. Polym. Sci. B*, 34:981–997, 1996.

[94] T. Quian and P. L. Taylor. From the Thomas-Windle model to a phenomenological description of case-II diffusion in polymers. *Polymer*, 41:7159–7163, 2000.

[95] M. Souche and D. Long. Case-II diffusion and solvent-polymer films drying: A meso-scale model. *Europhys. Lett.*, 77:48002, 2007.

[96] S. Herminghaus. Polymer thin films and surfaces: Possible effects of capillary waves. *Eur. Phys. J. E*, 8:237, 2002.

[97] M. P. Allen and D. J. Tildesley. *Computer Simulation of Liquids*. Clarendon Press, Oxford, 1994.

[98] Daan Frenkel and Berend Smit. *Understanding Molecular Simulation*. Academic Press, London, 2nd edition, 2002.

[99] J. H. R. Clarke. Molecular dynamics of glassy polymers. In K. Binder, editor, *Monte Carlo and Molecular Dynamics Simulations in Polymer Science*, pages 272–306. Oxford Univ. Press, New York, 1995.

[100] W. Paul and G. D. Smith. Structure and dynamics of amorphous polymers: Computer simulations compared to experiment and theory. *Rep. Prog. Phys.*, 67:1117, 2004.

[101] J. Baschnagel, J. P. Wittmer, and H. Meyer. Monte Carlo simulation of polymers: Coarse-greained models. In N. Attig, K. Binder, H. Grubmüller, and K. Kremer, editors, *Computational Soft Matter: From Synthetic Polymers to Proteins*, volume 23, pages 83–140. NIC Series, Jülich, 2004. (available from `http://www.fz-juelich.de/nic-series`).

[102] M. Kröger. Simple models for complex nonequilibrium fluids. *Phys. Rep.*, 390:453–551, 2004.

[103] K. Kremer. Entangled polymers: From universal aspects to structure property relations. In N. Attig, K. Binder, H. Grubmüller, and K. Kremer, editors, *Computational Soft Matter: From Synthetic Polymers to Proteins*, volume 23, pages 141–168. NIC Series, Jülich, 2004. (available from `http://www.fz-juelich.de/nic-series`).

[104] K. Binder, J. Horbach, W. Kob, W. Paul, and F. Varnik. Molecular dynamics simulations. *J. Phys.: Condens. Matter*, 16:S429, 2004.

[105] C. Bennemann, W. Paul, K. Binder, and B. Dünweg. Molecular-dynamics simulations of the thermal glass transition in polymer melts – alpha-relaxation behavior. *Phys. Rev. E*, 57:843–851, 1998.

[106] K. Kremer and G. S. Grest. Dynamics of entangled linear polymer melts: A molecular-dynamics simulation. *J. Chem. Phys.*, 92:5057, 1990.

[107] M. Pütz, K. Kremer, and G. S. Grest. What is the entanglement length in a polymer melt? *Europhys. Lett.*, 49:735, 2000. see also the Comment and Reply in Europhys. Lett. **52**, 719 (2000), Europhys. Lett. **52**, 721 (2000).

[108] R. Everaers, S. K. Sukumaran, G. S. Grest, C. Svaneborg, A. Sivasubramanian, and K. Kremer. Rheology and microscopic topology of entangled polymeric liquids. *Science*, 303:823, 2004.

[109] S. Metzger, M. Müller, K. Binder, and J. Baschnagel. Surface excess in dilute polymer solutions, and the adsorption transition versus wetting phenomena. *J. Chem. Phys.*, 118:8489, 2003.

[110] M. Müller, L. G. MacDowell, and A. Yethiraj. Short chains at surfaces and interfaces: A quantitative comparison between density-functional theories and Monte Carlo simulations. *J. Chem. Phys.*, 118:2929, 2003.

[111] G. S. Grest and K. Kremer. Molecular dynamics simulation for polymers in the presence of a heat bath. *Phys. Rev. A*, 33:3628, 1986.

[112] S. Nose. A unified formulation of the constant temperature molecular dynamics methods. *J. Chem. Phys.*, 81:511, 1984.

[113] W. Hoover. Canonical dynamics: Equilibrium phase-space distributions. *Phys. Rev. A*, 31:1695, 1985.

[114] W. Hoover. Constant-pressure equations of motion. *Phys. Rev. A*, 34:2499, 1986.

[115] S. Nose. An extension of the canonical ensemble molecular dynamics method. *Mol. Phys.*, 57:187, 1986.

[116] T. Schneider and E. Stoll. Molecular dynamics study of a three-dimensional one-component model for distortive phase transitions. *Phys. Rev. B*, 17(3):1302, 1978.

[117] T. Soddemann, B. Dünweg, and K. Kremer. Dissipative particle dynamics: A useful thermostat for equilibrium and nonequilibrium molecular dynamics simulations. *Phys. Rev. E*, 68:046702, 2003.

[118] P. Espanol and P. Warren. Statistical mechanics of dissipative particle dynamics. *Europhys. Lett.*, 30:191, 1995.

[119] G. Besold, I. Vattulainen, M. Karttunen, and J. M. Polson. Towards better integrators for dissipative particle dynamics simulations. *Phys. Rev. E*, 62:R7611, 2000.

[120] R. D. Groot and P. B. Warren. Dissipative particle dynamics: Bridging the gap between atomistic and mesoscopic simulation. *J. Chem. Phys.*, 107:4423, 1997.

[121] J. B. Gibson, K. Chen, and S. Chynoweth. The equilibrium of a velocity-Verlet type algorithm for DPD with finite time steps. *International Journal of Modern Physics C*, 10:241, 1999.

[122] I. Pagonabarraga, M. H. J. Hagen, and D. Frenkel. Self-consistent dissipative particle dynamics algorithm. *Europys. Lett.*, 42:377, 1998.

[123] Jean Pierre Hansen and Ian R. McDonald. *Theory of Simple Liquids*. Academic Press, London, 1986.

[124] S. Melchionna, G. Ciccotti, and B. Holian. Hoover NPT dynamics for systems varying in shape and size. *Mol. Phys.*, 78:533, 1993.

[125] F. Varnik, J. Baschnagel, and K. Binder. Molecular dynamics results on the pressure tensor of polymer films. *J. Chem. Phys.*, 113:4444, 2000.

[126] F. Varnik. Simulation of planar systems at constant normal pressure: Is it also possible to keep the plate separation constant? *Comp. Phys. Comm.*, 149:61, 2002.

[127] H. J. C Berendsen, J.P.M. Postma, W. F. van Gunsteren, A. DiNola, and J. R. Haak. Molecular dynamics with coupling to an external bath. *J. Chem. Phys.*, 81:3684, 1984.

[128] A. Kolb and B. Dünweg. Optimized constant pressure stochastic dynamics. *J. Chem. Phys.*, 111:4453, 1999.

[129] H. Andersen. Molecular dynamics simulations at constant pressure and/or temperature. *J. Chem. Phys.*, 72:2384, 1980.

[130] Fathollah Varnik. Dissertation, Johannes Gutenberg-Universität Mainz, 2000. (available from `http://archimed.uni-mainz.de/pub/2001/0007`).

[131] A. Jakobsen. Constant-pressure and constant-surface tension simulations in dissipative particle dynamics. *J. Chem. Phys.*, 122:124901, 2005.

[132] S. Feller, Y. Zhang, and R. Pastor. Constant pressure molecular dynamics simulation: The Langevin piston method. *J. Chem. Phys.*, 103:4613, 1995.

[133] R. Auhl, R. Everaers, G. S. Grest, K. Kremer, and S. Plimpton. Equilibration of long chain polymer melts in computer simulations. *J. Chem. Phys.*, 119:12718, 2003.

[134] J. S. Rowlinson and B. Widom. *Molecular Theory of Capillarity*. Clarendon Press, Oxford, 1982.

[135] N. Ch. Karayiannis, A. E. Giannousaki, V. G. Mavrantzas, and D. N. Theodorou. Atomistic Monte Carlo simulation of strictly monodisperse long polyethylene melts through a generalized chain bridging algorithm. *J. Chem. Phys.*, 117:5465, 2002.

[136] S.-H. Chong and M. Fuchs. Mode-coupling theory for structural and conformational dynamics of polymer melts. *Phys. Rev. Lett.*, 88:185702, 2002.

[137] T.G. Fox and P.J. Flory. Second-order transition temperatures and related properties of polystyrene. I. Influence of molecular weight. *J. Appl. Phys*, 21:581, 1950.

[138] J.M.G. Cowie and P.M. Toporowski. The dependence of glass temperature on molecular weight for poly (α-methylstyrene). *Eur. Poly. J.*, 4:621, 1968.

[139] R. Brüning and K. Samwer. Glass transition on long time scales. *Phys. Rev. B*, 46:11318, 1992.

[140] K. Vollmayr, W. Kob, and K. Binder. How do properties of a glass depend on cooling rate? A computer simulation study of a Lennard-Jones system. *J. Chem. Phys.*, 105:4714, 1996.

[141] J. Buchholz, W. Paul, F. Varnik, and K. Binder. Cooling rate dependence of the glass transition temperature of polymer melts: A molecular dynamics study. *J. Chem. Phys*, 117:7364, 2002.

[142] M. Fuchs and K. S. Schweizer. Structure of colloid-polymer suspensions. *J. Phys.: Condens. Matter*, 14:R329, 2002.

[143] A. Barbieri, D. Prevosto, M. Lucchesi, and D. Leporini. Static and dynamic density effects due to the finite length of polymer chains: A molecular-dynamics investigation. *J. Phys.: Condens. Matter*, 16:6609, 2004.

[144] M. Aichele, S.-H. Chong, J. Baschnagel, and M. Fuchs. Static properties of a simulated supercooled polymer melt: Structure factors, monomer distributions relative to the center of mass, and triple correlation functions. *Phys. Rev. E*, 69:061801, 2004.

[145] J.-P. Hansen and L. Verlet. Phase transitions of the Lennard-Jones system. *Phys. Rev.*, 184:151, 1969.

[146] C. Bennemann, W. Paul, J. Baschnagel, and K. Binder. Investigating the influence of different thermodynamic paths on the structural relaxation in a glass forming polymer melt. *J. Phys.: Condens. Matter*, 11:2179–2192, 1999.

[147] M. Nauroth and W. Kob. Quantitative test of the mode-coupling theory of the ideal glass transition for a binary Lennard-Jones system. *Phys. Rev. E*, 55:657–667, 1997.

[148] S.-H. Chong and F. Sciortino. Structural relaxation in supercooled orthoterphenyl. *Phys. Rev. E*, 69:051202, 2004.

[149] A. Tölle. Neutron scattering studies of the model glass former ortho-terphenyl. *Rep. Prog. Phys.*, 64:1473, 2001.

[150] J. Jäckle. The spectrum of surface waves on viscoelastic liquids of arbitrary depth. *J. Phys.: Condens. Matter*, 10:7121, 1998.

[151] F. Varnik and K. Binder. Shear viscosity of a supercooled polymer melt via nonequilibrium molecular dynamics simulations. *J. Chem. Phys.*, 117:6336, 2002.

[152] C. Mischler, J. Baschnagel, and K. Binder. Polymer films in the normal-liquid and supercooled state: A review of recent Monte Carlo simulation results. *Adv. Coll. Interf. Sci.*, 94:197, 2001.

[153] E. Rössler and H. Sillescu. In J. Zarzycki, editor, *Material Science and Technology*, volume IX, pages 573–618. VCH, Weinheim, 1991.

[154] B. Böddeker and H. Teichler. Dynamics near free surfaces of molecular dynamics simulated $\mathrm{Ni}_{0.5}\mathrm{Zr}_{0.5}$ metallic glass films. *Phys. Rev. E*, 59:1948, 1999.

[155] J. H. Kim, J. Jang, and W.-C. Zin. Estimation of the thickness dependence of the glass transition temperature in various thin polymer films. *Langmuir*, 16:4067, 2000.

[156] J. A. Forrest, K. Dalnoki-Veress, and J. R. Dutcher. Interface and chain confinement effects on the glass transition temperature of thin polymer films. *Phys. Rev. E*, 56:5705, 1997.

[157] M. Aichele, Y. Gebremichael, F. Starr, J. Baschnagel, and S. Glotzer. Polymer-specific effects of bulk relaxation and stringlike correlated motion in the dynamics of a supercooled polymer melt. *J. Chem. Phys.*, 119:5290, 2003.

[158] M. Tolan, O. H. Seeck, J. wang, S. K. Sinha, M. H. Rafailovich, and J. Sokolov. X-ray scattering from polymer films. *Physica B*, 283:22–26, 2000.

[159] H. Kim, A. Rühm, L. B. Lurio, J. K. Basu, J. Lal, D. Lumma, S. G. J. Mochrie, and S. K. Sinha. Surface dynamics of polymer films. *Phys. Rev. Lett.*, 90:068302, 2003.

[160] A. Werner, F. Schmid, M. Müller, and K. Binder. Anomalous size-dependence of interfacial profiles between coexisting phases of polymer mixtures in thin film geometry: A Monte Carlo simulation. *J. Chem. Phys.*, 107:8175, 1997.

[161] A. Werner, F. Schmid, M. Müller, and K. Binder. Intrinsic profiles and capillary waves at homopolymer interfaces: A Monte Carlo study. *Phys. Rev. E*, 59:728, 1998.

[162] M. Lacasse, G. Grest, and A. Levine. Capillary-wave and chain-length effects at polymer/polymer interfaces. *Phys. Rev. Lett.*, 80:309, 1998.

[163] A.O. Tuck. A simple Filon-trapezoidal rule. *Math. Comp.*, 21:239, 1967.

[164] J. Jäckle and K. Kawasaki. Intrinsic roughness of glass surfaces. *J. Phys. Condens. Matter*, 7:4351–4358, 1995.

[165] F. Kremer and A. Schönhals. *Broadband Dielectric Spectroscopy*. Springer, 2003.

[166] D. Bose and F. Kremer. Molecular dynamics in bulk cis-polyisoprene as studied by dielectric spectroscopy. *Macromolecules*, 23:829, 1990.

[167] P. Lunkenheimer, U. Schneider, R. Brand, and A. Loidl. Glassy dynamics. *Contempory Physics*, 41:15–36, 2000.

[168] C. A. Angell. Relaxation in liquids, polymers and plastic crystals–strong/fragile patterns and problems. *J. Non-Cryst. Solids*, 131-133:13–31, 1991.

[169] J. Sangmin and S. Granick. A polymer's dielectric normal modes depend on its film thickness when confined between nonwetting surfaces. *Macromolecules*, 34:8490, 2001.

[170] K. Kojio, S. Jeon, and S. Granick. Confinement-induced differences between dielectric normal modes and segmental modes of ion-conducting polymer. *Euro. Phys. J. E*, 8:167–173, 2001.

[171] F. Kremer, L. Hartmann, A. Serghei, P. Pouret, and L. Leger. Molecular dynamics in thin grafted and spin coated polymer layers. *Eur. Phys. J. E*, 12:139, 2003.

[172] A. Serghei and F. Kremer. Confinement-induced relaxation process in thin films of cis-polyisoprene. *Phys. Rev. Lett.*, 91:165702, 2003.

[173] K. Fukao. Dynamics in thin polymer films by dielectric spectroscopy. *Euro. Phys. J. E*, 12:119–125, 2003.

[174] A. Serghei, F. Kremer, and W. Kob. Chain conformation in thin polymer layers as revealed by simulations of ideal random walks. *Euro. Phys. J. E*, 12:143–146, 2003.

[175] A. Barbieri, E. Campani, S. Capacciolo, and D. Leporini. Molecular dynamics study of the thermal and the density effects on the local and the large-scale of polymer melts: Scaling properties and dielectric relaxation. *J. Chem. Phys.*, 120:437, 2004.

[176] H. Vogel. Das Temperaturabhängigkeitsgesetz der Viskosität von Flüssigkeiten. *Phys. Zeit.*, 22:645, 1921.

[177] W. Kauzmann. The nature of the glassy state and the behavior of liquids at low temperatures. *Chem. Rev.*, 43:219, 1948.

[178] K. Binder, M. Müller, P. Virnau, and L.G. MacDowell. Polymer+solvent systems: Phase diagrams, interface free energies, and nucleation. *Adv. Polym. Sci.*, 173:1–110, 2005.

[179] M. de Podesta. *Understanding the properties of matter*. CRC Press, 2002.

[180] M. Müller. Phase behavior and chain conformations in polymer blends: Monte Carlo simulation vs mean field theory. In N. Attig, K. Binder, H. Grubmüller, and K. Kremer, editors, *Computational Soft Matter: From Synthetic Polymers to Proteins*, volume 3, pages 237–274. NIC Series, Jülich, 2004. (available from `http://www.fz-juelich.de/nic-series`).

[181] L. Masaro and X.X. Zhu. Physical models of diffusion for polymer solutions, gels and solids. *Prog. Polym. Sci.*, 24:731–755, 1999.

[182] G.D.J. Phillies. Dynamics of polymers in concentrated solutions: The universal scaling equation derived. *Macromolecules*, 20:558, 1987.

[183] G.D.J Phillies, J. Gong, L. Li, A. Rau, K. Zhang, L.P. Yu, and J. Rollings. Macroparticle diffusion in dextran solutions. *J. Phys. Chem.*, 93:6219, 1989.

[184] G.D.J. Phillies, S. Ahmed, L. Li, Y. Xu, D. Rostcheck, and T. Cobb, M. Tanaka. Temperature dependence of probe diffusion in solutions of low-molecular-weight polyelectrolytes. *Macromolecules*, 24:5299, 1991.

[185] A. Bhatia and D. Thornton. Structural aspects of the electrical resistivity of binary alloys. *Phys. Rev. B*, 2:3004, 1970.

[186] A. Fick. Über Diffusion. *Poggendorff's Annalen der Physik*, 94:59, 1855.

[187] D. N. Theodorou. Molecular simulations of sorption and diffusion in amorphous polymers. In P. Neogi, editor, *Diffusion in Polymers*. Dekker, New York, 1996.

[188] L. S. Darken. Diffusion, mobility and their interrelation through free energy in binary metallic systems. *Trans. AIME*, 175:184, 1948.

[189] E. J. Maginn, A. T. Bell, and D. N. Theodorou. Transport diffusivity of methane in silicalite from equilibrium and nonequilibrium simulations. *J. Chem. Phys.*, 108:2601, 1993.

[190] M. Tsige and G. Grest. Molecular dynamics simulation of solvent-polymer interdiffusion: Fickian diffusion. *J. Chem. Phys.*, 120:2989, 2004.

[191] G. Rossi and K. A. Mazich. Macroscopic description of the kinetics of swelling for a cross-linked elastomer or a gel. *Phys. Rev. E*, 48:1182, 1993.

[192] T. Okuzono, K. Ozawa, and M. Doi. Simple model of skin formation caused by solvent evaporation in polymer solutions. *Phys. Rev. Lett.*, 97:136103, 2006.

[193] T.C. Illingworth, I.O. Golosnoy, V. Gergely, and T.W. Clyne. Numerical modelling of transient liquid phase bonding and other diffiusion controlled pahse changes. *J. Mat. Sci.*, 40:2505–2511, 2005.

[194] J. Crank and P. Nicolson. A practical method for numerical evaluation of solutions of partial differential equations of the heat conduction type. *Proceedings of the Cambridge Philosophical Society*, 43:50, 1947.

[195] Z. Wanxie and Z. Jianping. Rethinking to finite difference time-step integrations. *Applied Mathematics and Mechanics*, 16:705, 1995.

[196] C. Toninelli, M. Wyart, L. Berthier, G. Biroli, and J. P. Bouchaud. Dynamical susceptibility of glass formers: Contrasting the predictions of theoretical scenarios. *Phys. Rev. E*, 71:041505, 2005.

[197] N. Lacevic, F. W. Starr, T. B. Schroder, and Glotzer S. C. Spatially heterogeneous dynamics investigated via a time-dependent four-point density correlation function. *J. Chem. Phys.*, 119:7372, 2003.

[198] C. B. Roth, A. Pound, S. W. Kamp, C. A. Murray, and J. R. Dutcher. Molecular-weight dependence of the glass transition temperature of freely-standing poly(methyl methacrylate) films. *Euro. Phys. J. E*, 20:441, 2006.

[199] G.H. Fredrickson. *The Equilibrium Theory of Inhomogeneous Polymers*. Clarendon Press, Oxford, 2006.

[200] M.W. Matsen. Self-consistent field theory and its applications. In G. Gompper and M. Schick, editors, *Soft Matter, Volume 1:Polymer Melts and Mixtures*. Wiley-VCH, Weinheim, 2006.

[201] Ch. Lin, M. Müller, and K. Binder. Stability of thin polymer films: Influence of solvents, 2004.

[202] K.Ch. Daoulas and M. Müller. Single chain in mean field simulations: Quasi-instantaneous field approximation and quantitative comparison with Monte Carlo simulations. *J. Chem. Phys.*, 125:184904, 2006.

[203] Binder K. Collective diffusion, nucleation, and spinodal decomposition in polymer mixtures. *J. Chem. Phys.*, 79:6387, 1983.